

UNIVERSITÀ DELLA CALABRIA



UNIVERSITA' DELLA CALABRIA

Dipartimento di Fisica

**Dottorato di Ricerca in
Scienze e Tecnologie Fisiche, Chimiche e dei Materiali**

CICLO

XXXII

TITOLO TESI

Commissioning and exploitation of the μ Tomo experimental station: case studies


Settore Scientifico Disciplinare FIS/01

Coordinatore: Prof.ssa Gabriella Cipparrone


Firma oscurata in base alle linee guida del Garante della privacy

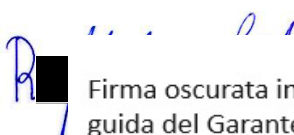
Firma

Supervisore/Tutor: Prof. Vincenzo Formoso


Firma oscurata in base alle linee guida del Garante della privacy

Firma

Dottorando: Dott. Raffaele Filosa


Firma oscurata in base alle linee guida del Garante della privacy

Firma

ABSTRACT (Ita)

All'Università della Calabria è in corso di attuazione il progetto MATERIA per la realizzazione di un'infrastruttura di ricerca su materiali e tecnologie avanzate. Il fulcro del progetto MATERIA è STAR (sorgente Thomson dell'Europa meridionale per la ricerca applicata), una sorgente Thomson avanzata di fasci di raggi X polarizzati monocromatici sintonizzabili, lunghi ps, che vanno da 20 a 140 keV. I raggi X saranno dedicati a esperimenti di scienza della materia, beni culturali, imaging radiologico avanzato con capacità di microtomografia. Attualmente le sorgenti di raggi X a Thomson Back-Scattering (TBS) stanno avendo un forte sviluppo perché sono macchine con un altro grado di flessibilità, compattezza e costi contenuti rispetto alle sorgenti di luce di sincrotrone che prevedono anelli di accumulazione. (Bacci et al. 2014).

Come prima applicazione della sorgente STAR si è deciso di realizzare una stazione sperimentale (beamline) dedicata alla microtomografia a raggi X. La microtomografia a raggi X è un tipo di tomografia assiale computerizzata (comunemente abbreviata come CT), caratterizzata da un'elevata risoluzione spaziale. Si tratta di una tecnica di imaging tridimensionale non distruttiva utilizzata per indagare la microstruttura interna di piccoli campioni (la cui dimensione è di pochi centimetri), per i quali non è richiesta una particolare preparazione del campione. Il risultato di un'indagine microtomografia a raggi X è un insieme di scansioni bidimensionali in scala di grigi del campione, che vengono elaborate da algoritmi di ricostruzione tomografica computerizzata al fine di produrre una ricostruzione 3D altamente risolta del campione, avente una risoluzione tipica dell'ordine di un micron o anche più piccoli, a seconda della dimensione del campione. La qualità delle immagini finali dipende dalle diverse proprietà di assorbimento dei raggi X dei materiali che costituiscono il campione. La microtomografia a raggi X viene utilizzata nello studio dei materiali, in particolare per i compositi, per i quali è molto importante ottenere informazioni morfologiche e densitometriche utilizzando una tecnica di indagine non invasiva e non distruttiva.

In questa tesi si descrive il lavoro svolto per lo sviluppo e l'attivazione di una stazione sperimentale di microtomografia a raggi X chiamato “ μ Tomo”. Particolare cura è stata data al conseguimento di know-how e competenza in nella tecnica di indagine per imaging.

Il primo passo ha riguardato lo sviluppo e la messa a punto dei componenti fondamentali per la costruzione della stazione sperimentale:

1. la sorgente di raggi X, che è una sorgente microfocus, che è di fondamentale importanza per ottenere immagini ad alta risoluzione;
2. il gruppo di movimentazione con motori passo-passo per la manipolazione del campione con un alto grado di precisione (dell'ordine del micron).
3. Il rivelatore di raggi X a schermo bidimensionale (flat panel), utilizzato per l'acquisizione d'immagini radiografiche (proiezioni).

Il secondo passo ha riguardato lo sviluppo di software, in linguaggio LabView (National Instruments), per il controllo remoto dell'apparato μ Tomo, necessari per l'acquisizione e la memorizzazione di immagini radiografiche. Altri programmi software sono stati sviluppati per pilotare il sistema di movimentazione del campione in modo tale da effettuare l'allineamento di quest'ultimo con la sorgente di raggi X e con il rivelatore. Tutto questo ha portato alla messa a punto della stazione sperimentale di microtomografia ed essere in grado di effettuare i primi test sperimentali. Particolarmente utili sono stati le prime misure sperimentali in fase di commissioning che hanno permesso di verificare le prestazioni della stazione sperimentale μ Tomo.

Infine, a completare il lavoro di ricerca, sono stati realizzati una serie di casi di studio su diversi campioni, aprendo collaborazioni con i vari dipartimenti dell'Università della Calabria.

ABSTRACT

At the University of Calabria, the MATERIA project for the creation of a research infrastructure on advanced materials and technologies is being implemented. The MATERIA scientific centre will have a multidisciplinary nature and will be available not only to all University researchers but will also offer advanced services to the entire national and international scientific community.

The core of the MATERIA project is STAR (Southern european Thomson source for Applied Research), an advanced Thomson source of monochromatic tunable, ps-long, polarized X-ray beams, ranging from 20 to 140 keV. The X-rays will be devoted to experiments of matter science, cultural heritage, advanced radiological imaging with micro-tomography capabilities.

Thomson Back-Scattering (TBS) X-Ray sources, nowadays, are attracting strong attention, mainly by a strong flexibility, compactness and less expensive, respect to the synchrotron sources. (Bacci et al. 2014). The TBS is the electromagnetic process in which each electron absorbs one (linear Thomson scattering) or more (nonlinear Thomson scattering) photons from a laser pulse, emitting one photon. (Curatolo et al. 2017). If the electrons are ultrarelativistic the frequency of the scattered radiation is upshifted and it is emitted forward with respect to the particles motion, with a small aperture cone, proportional to the inverse of the Lorentz relativistic factor. A TBS source driven by high quality electron beams can works in different operating modes, e.g.: the high-fluxmoderate- monochromaticity mode, suitable for medical imaging when high-flux sources are needed; the moderate-flux- monochromatic mode, suitable to improve the detection/dose performance; short-and monochromatic mode, useful for pump-and-probe experiments; further the coherence properties of the radiation have been well investigated by phase contrast imaging and diffraction enhanced imaging.

The STAR source is based on: One S-band RF Gun at 100 Hz that will produce electron bunches boosted up to 60 MeV by a 3m long S-band TW cavity. A dogleg convey the beam on a parallel line, so to shield the X-ray line from the background radiation due to Linac dark current. The peculiarity of the machine is the ability to

produce high quality electron beams, with low emittance and high stability, allowing to reach spot sizes around 15-20 microns, with a pointing jitter of the order of a few microns. The collision laser will be based on a Yb:Yag 100 Hz high quality laser system, synchronized to an external photo-cathode laser and to the RF system to better than 1 ps time jitter.

As a first application of the STAR source it was decided to build an experimental station (beamline) dedicated to X-ray microtomography.

X-ray microtomography is a kind of computed axial tomography (commonly abbreviated as CT), characterized by a high spatial resolution. It is a non-destructive 3-dimensional imaging technique used to investigate the internal microstructure of small samples (whose size is of a few centimeters), for which no particular sample preparation is required. The outcome of an X-ray microtomography investigation is a set of bidimensional grayscale scans of the sample, which are elaborated by Computed tomographic reconstruction algorithms in order to produce a highly resolved 3-D reconstruction of the sample, having a typical resolution of the order of a micron or even smaller, depending on the sample size.

The quality of the final images relies on the different X-ray absorption properties of the materials that constitute the sample. In particular, the grayscale of the outcome image, and so its contrast level, is correlated to the density, composition and thickness of the sample materials, and it is due to the detection of amplitude variations of the transmitted X-rays.

X-ray microtomography is used in materials studies, in particular for composites, for which it is very important to obtain morphological and densitometric information by using a noninvasive and a non-destructive investigation technique.

The work presented in this thesis describes the development and implementation of a compact X-ray microtomography system called μ Tomo. Particular care was given to acquiring know-how and expertise in this investigation technique.

The first step involved the development, the setup and tuning of the fundamental components for the construction of the experimental station:

- the X-ray source, which is microfocus source, capable to generate very small focal spot sizes, typically between 5 and 50 microns in diameter. This is crucial to obtain high resolution images;
- The linear stages with Stepper Motors for sample handling with a high degree of positioning accuracy (of the order of a micron).
- The Flat-panel detectors, used for the projection radiography acquisition, that combine a large- area CMOS image sensor (CCD) and a scintillator.

The second step was the development of a software package in LabView language (by National Instruments) for the remote control of the μ Tomo apparatus and the acquisition of radiographic images (projections). The software package can control the movement system, which is necessary for the alignment of the sample, the X-ray source and the detector. It also control the needed procedures for the acquisition and storage of the radiographic projections.

The first experimental tests during the commissioning were particularly useful and allowed us to verify the performances of the μ Tomo experimental station. They were followed by a series of case studies that were carried out in various fields of material science.

INDICE

| | |
|---|----|
| ABSTRACT..... | 2 |
| 1 X-RAY MICROTOMOGRAPHY | 8 |
| 1.1 INTRODUCTION..... | 8 |
| 1.2 INTERACTION OF X-RAYS WITH MATERIALS..... | 9 |
| 1.3 X-RAY ATTENUATION..... | 11 |
| 1.4 PRINCIPLES OF MICROCOMPUTED TOMOGRAPHY | 13 |
| 1.4.1 Cone Beam Configuration & Conventional Sources | 15 |
| 1.4.2 Parallel Beam Configuration & Synchrotron Light Sources | 16 |
| 1.4.3 Local Area Microtomography | 17 |
| 1.5 ABSORPTION LAW..... | 20 |
| 1.6 RECONSTRUCTION IN MICROTOMOGRAPHY | 24 |
| 1.7 PHASE CONTRAST | 28 |
| 1.7.1 Physical Principle of In-Line Phase-Contrast Imaging: | 28 |
| 2 X-RAY CONE-BEAM MICROTOMOGRAPHY..... | 32 |
| 2.1 CONE BEAM COMPUTER TOMOGRAPHY RECONSTRUCTION | 40 |
| 2.1.1 Cone-Beam CT System | 40 |
| 2.1.2 Feldkamp's Algorithm..... | 42 |
| 2.1.3 Algorithm and Mathematical Analysis | 43 |
| 3 X-RAY MICROTOMOGRAPHY STATION | 46 |
| 3.1 EXPERIMENTAL SETUP..... | 47 |
| 3.2 X-RAY SOURCE | 48 |
| 3.3 X-RAY DETECTOR | 52 |
| 3.4 POSITIONING SYSTEM..... | 53 |
| 3.5 SOFTWARE DEVELOPMENT..... | 56 |
| 3.5.1 The Main Program For Measurement..... | 57 |

| | | |
|-------|---|-----|
| 3.5.2 | Control Motors..... | 58 |
| 4 | RESULTS and CASE STUDIES..... | 63 |
| 4.1 | CASE STUDY 1: Experimental study on mechanical properties of Basalt FRCM using various matrices and validation by X-Ray micro tomography. | 71 |
| 4.2 | CASE STUDY 2: Analysis of extruded pins manufactured by friction stir forming for multi-material joining purposes. | 131 |
| 4.3 | CASE STUDY 3: Non-destructive Measurements of Single Events Induced on Power MOSFET's by Terrestrial Neutrons. | 140 |
| 4.4 | CASE STUDY 4: Studying the microvesiculation of the obsidians of Sierra de las Navajas (State of Hidalgo, Mexico). | 155 |
| 4.5 | CASE STUDY 5: Architectural terracruda sculpture of Silk Roads: new conservative insights through a diagnostic approach based on non-destructive X-ray micro-tomography. | 168 |
| | FIGURES..... | 184 |
| | BIBLIOGRAPHY..... | 187 |

1 X-RAY MICROTOMOGRAPHY

1.1 INTRODUCTION

Since the 1970s, X-ray computed tomography (CT) has become a well-established and routinely used technique in modern diagnostic radiology (Hounsfield 1973). Only a decade later, since the late 1980s, X-ray CT has emerged as a very important and widespread tool in industrial inspection as well as in material sciences (Hanke, Fuchs, and Uhlmann 2008).

Beyond medical radiology, today X-ray CT is used in three major fields of applications:

- Quantitative materials analysis of geological or biological samples, compound materials like carbon-fibre or glass-fibre reinforced plastics, advanced ceramics, composites, plastics, and alloys. Here, the accuracy of reconstructed mass densities or attenuation coefficients is crucial. Thus, for quantitative purposes, the focus lies on CT image quality in terms of homogeneity, absolute contrast, and noise, as well as on the reduction of artefacts. These groups of application include the field of materials characterization.
- Metrology measurement based on three-dimensional (3-D) volume representations of the samples, to perform nominal or actual value comparison of the sample geometry in terms of size and shape. X-ray CT is superior to alternative metrology techniques like tactile or visual systems, since it can investigate inner surfaces and hidden structures.
- Nondestructive testing and evaluation for safety purposes of, eg, critical parts of aeroplanes, cars, engines, turbines, or power generators. In safety inspections the typical task is to search and detect cracks, delaminations, blowholes, and similar defects. Thus, these applications deal with high contrast details and require high spatial resolution.

1.2 INTERACTION OF X-RAYS WITH MATERIALS

X-ray interaction with condensed matter can be explained either by considering particles as finite bodies (electrons and photons interactions) and by considering them as interacting electromagnetic waves. Both representations are described by the complex refraction index $n(x,y,z)$, which is given as

$$\mathbf{n}(x, y, z) = \mathbf{1} - \boldsymbol{\delta}(x, y, z) + i\boldsymbol{\beta}(x, y, z) \quad \text{Eq. 1.1}$$

The real part δ represents the refractive contribution (electromagnetic interaction), while the imaginary part β represents the photon attenuation. (Hanke et al. 2016)

X-rays are described by an electromagnetic wave as

$$\Psi(\vec{r}) = \Psi_0 \exp(i\vec{k} \cdot \vec{r}) \quad \text{Eq. 1.2}$$

where the wave-vector k is defined as

$$k = |\vec{k}| = \frac{n\omega}{c} \quad \text{Eq. 1.3}$$

If we assume that the wave propagates along the x-direction and we take into account the refractive index $n=n(x)$ in the same direction, then the electromagnetic wave can be written as

$$\Psi(\vec{r}) = \Psi_0 \exp\left(i \cdot n \frac{\omega}{c} \cdot x\right) = \Psi_0 \exp\left(i \frac{\omega}{c} (1 - \delta) \cdot x\right) \cdot \exp\left(-\frac{\omega}{c} \beta \cdot x\right)$$

Eq. 1.4

In radioscopic imaging, when a beam of X-rays pass through some material of thickness x in which it is partially absorbed, the X-rays intensity $I(x)$ measured after the attenuation is given by the square of absolute value of the complex wave function

$$\Psi(x) = |\Psi(x)| = I_0 \exp\left(-2 \frac{\omega}{c} \beta \cdot x\right) \quad \text{Eq. 1.5}$$

$$\text{with } \beta = \frac{\mu}{2\omega} \cdot c \quad \text{Eq. 1.6}$$

where μ represents the linear attenuation coefficient. The given dissertation hence leads to the well-known absorption law of Lambert Beer.

The next two sections make use of this result to describe photon attenuation and phase contrast imaging.

1.3 X-RAY ATTENUATION

Each material is characterized by a particular linear attenuation factor. Hence the application of X-ray micro-CT to materials characterization produces sample scans which are spatial distributions of the X-ray sensitive attenuation coefficient. It is then crucial to understand which processes are involved in X-ray interactions with condensed matter. In particular, the two dominating processes are photon absorption and incoherent Compton scattering within the energy regime between 10keV up to about 300keV.

Photons interact with matter by mean of four different processes, whose cross sections add up to give the linear attenuation factor (Hanke et al. 2016):

$$\frac{\mu(Z,E)}{\rho} = \frac{\sigma_{\text{Photoelectric}}}{\rho} + \frac{\sigma_{\text{Rayleigh}}}{\rho} + \frac{\sigma_{\text{Compton}}}{\rho} + \frac{\pi_{\text{pair}}}{\rho} \quad \text{Eq. 1.7}$$

The mass-attenuation coefficient as defined by Eq. 1.7 show a dependence on the photon energy E and the atomic number Z of the absorber.

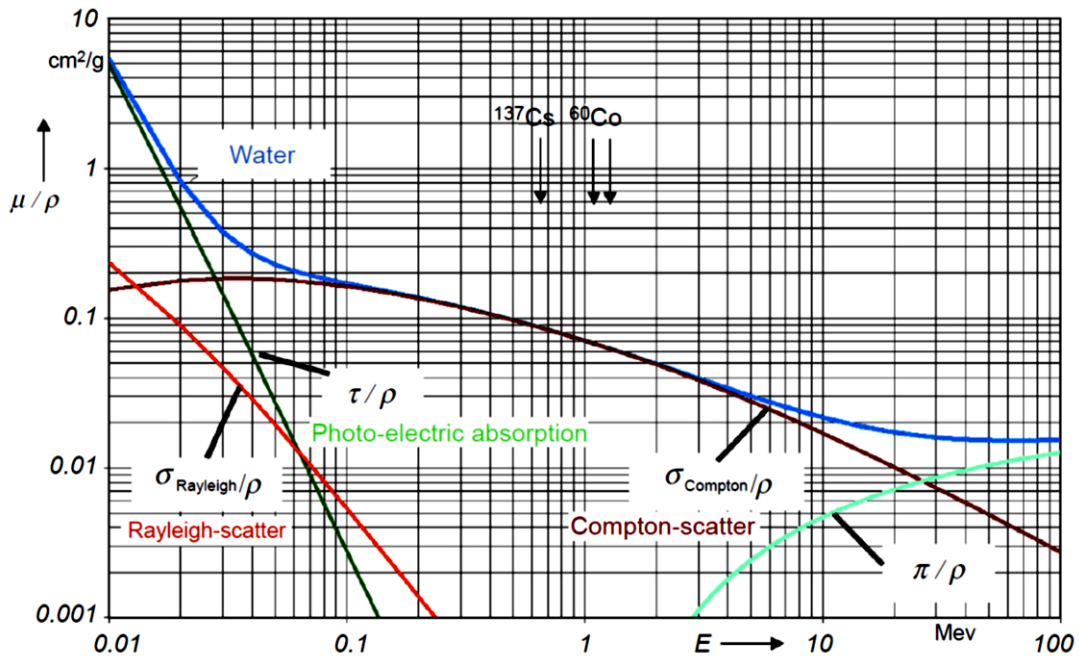
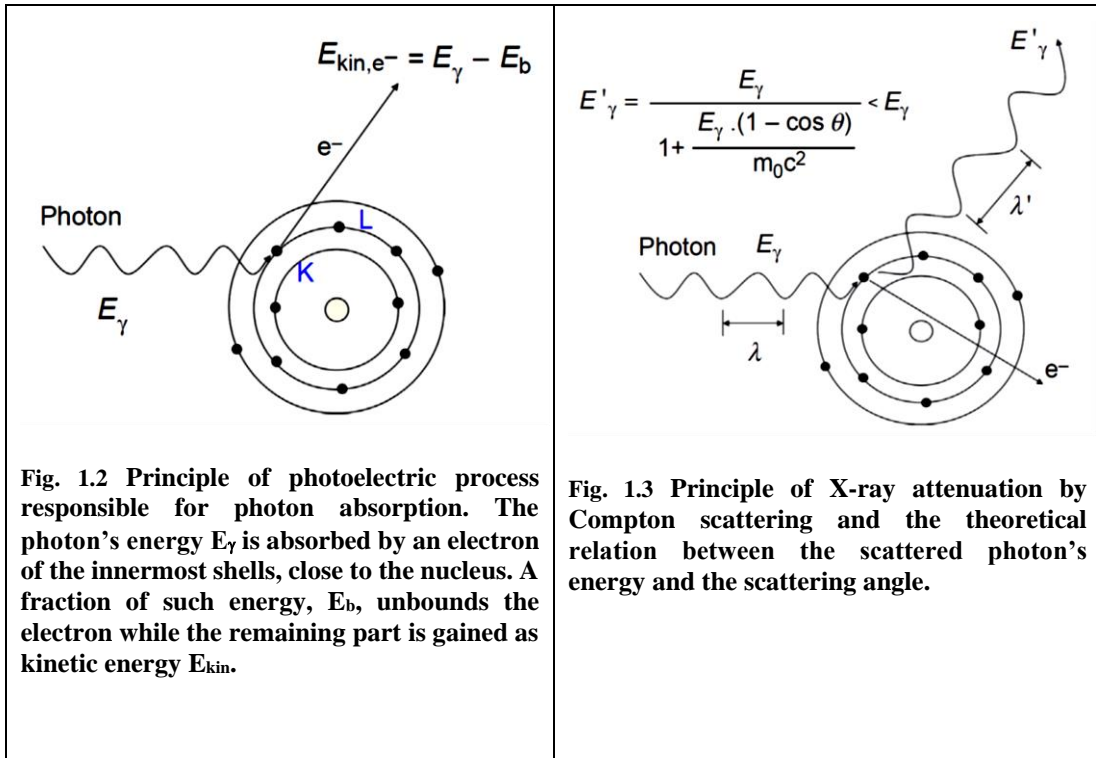


Fig. 1.1 The mass-attenuation coefficient as a function of photon energy in case of water. Based on the tables in Hubbell, J.H., Seltzer, S.M., 1989. Tables of X-Ray Mass Attenuation Coefficients and Mass Energy-Absorption Coefficients (Online). National Institute of Standards and Technology. <http://www.nist.gov/pml/data/xraycoef/>.

Numerical values for this coefficient are available and are tabulated for all known chemical elements (Hubbell and Seltzer, 1989, 1982) as functions of the photon energy. Fig. 1.1 shows the functional dependence of the different contributions to the linear attenuation factor for the case of water.

Coherent scattering (Rayleigh) and pair production are not relevant for the discussed X-ray regime and thus are not treated here.



1.4 PRINCIPLES OF MICROCOMPUTED TOMOGRAPHY

The basic principle of CT data acquisition is depicted in Fig. 3.1. The sample is positioned between a suitable X-ray source and a detection device, as for instance a two-dimensional flat panel detector. While the object rotates, a given number of its projections on the detector are recorded on the detector, at varying angles.

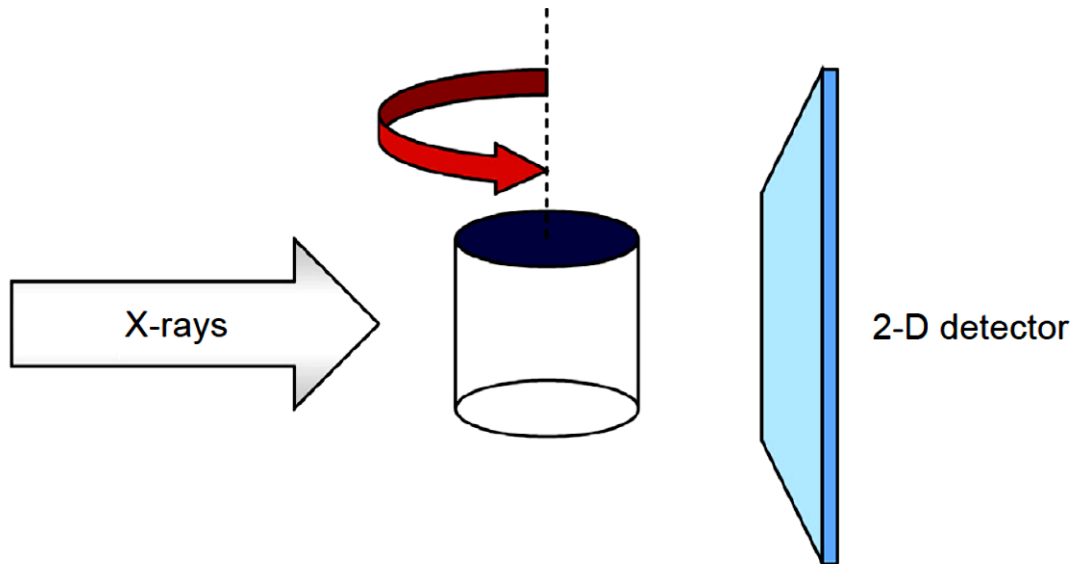


Fig. 1.4 Schematic illustration of a standard micro-CT setup. The sample is positioned on a rotational stage between the X-ray source and a two-dimensional (2-D) X-ray imaging device.

The total rotational angle depends on the system geometry but typically it is 180° when a parallel beam is used, or 360° when a cone-beam geometry is used. By using the complete set of projections, 3-D tomographic slices (which images of the internal structure of the object in a plane parallel to the beam propagation direction) are reconstructed.

Depending on the type of X-ray source, we distinguish between conventional systems based on tubes emitting X-rays with a typical conic emission and synchrotron radiation setups typically fed with intense, laminar X-ray beams having an almost parallel beam geometry. Fig. 1.4 shows a schematic representation of the main components (i.e., X-ray source, sample rotator stage, and detector) of a μ -CT setup in both cases.

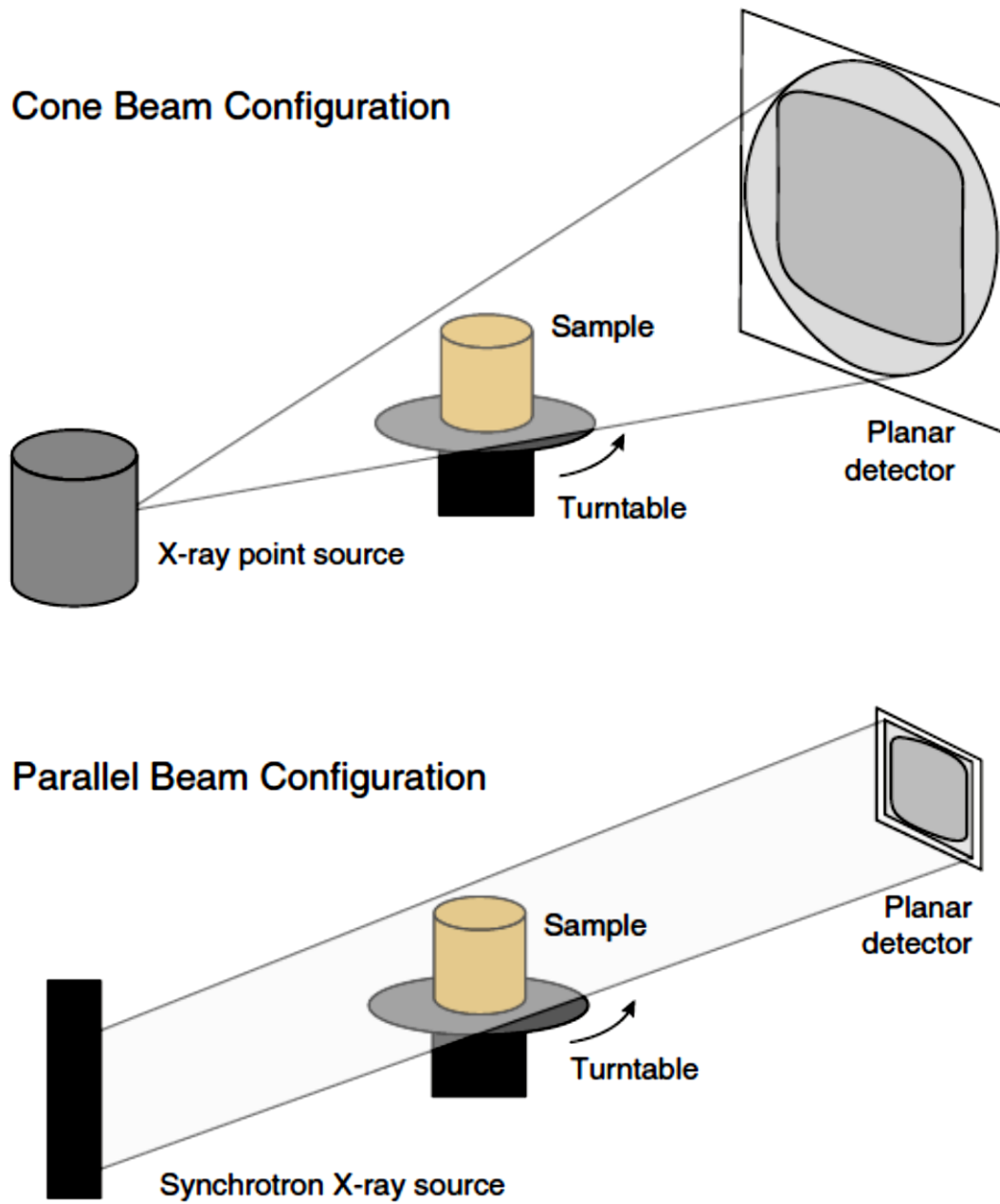


Fig. 1.5 Illustration of different beam configuration geometry. (Pacilè and Tromba 2018b)

1.4.1 Cone Beam Configuration & Conventional Sources

The most common way to perform a μ -CT makes use of a conventional microfocus based X-ray tube. Like all X-ray tubes, these sources generate X-rays when highly energetic electrons are stopped in a solid metal anode: X-rays result from the conversion of the kinetic energy of the electrons being decelerated due to a potential difference into electromagnetic radiation, as a result of collisions and radiative interactions. A polychromatic divergent beam is generated, from which a conical solid angle is selected.

Many benchtop μ -CT systems are today able to reach very high-resolution level, in the range of $1\mu\text{m}$ with a voxel size below $0.1\mu\text{m}$. The sample position respect to the source and the detector can be changed to adjust the magnification and the resolution; however, as the sample has to stay inside the field of view, the optimal position is always a compromise between sample size and spatial resolution.

The detector cameras used for μ -CT systems can be grouped into two categories, according to their ability to discriminate X-ray energy. Those that do discriminate the energy are usually referred as spectral CT, a promising technique recently introduced in last-generation μ -CT systems thanks to the progress achieved by single-photon counting detectors. In the other case, which is the most common, the detector simply integrates all the X-ray energies.

In general, μ -CT systems make use of digital flat 2-D detectors. The most commonly used are charged-coupled device (CCD) systems using scintillator screens coupled via fiberoptic bundles that convert of X-rays into visible photons.

1.4.2 Parallel Beam Configuration & Synchrotron Light Sources

Synchrotron radiation (SR) is generated by an electron bunch that travels at relativistic speed in a non-linear trajectory. SR covers a large spectrum of electromagnetic waves, from infrared to hard X-rays. Its main characteristics are the high intensity (three to four orders of magnitude higher than conventional X-ray tubes), the high brilliance, high spatial coherence, low-divergence emission and an extensive degree of freedom on tuning the radiation spectra. SR is produced in large facilities equipped with different magnetic structures (bending magnets and insertion devices) optimized to maximize the radiation production for the different experimental purposes and user requirements (see Fig. 1.5). The photon beams are generated by the bending magnet and the insertion device sources. Then the beam is manipulated (i.e. the thermal load is removed, it's monochromatized, undergoes harmonic rejection, focused, beam shaped, polarized, etc) and delivered to the experimental stations through the so-called beamlines.

The experimental stations of hard X-ray imaging beamlines are generally located at a high distance from the source and they are usually designed for specific experimental purposes. That means that they are designed according to the peculiarities of the sample of interest, taking into account the photon flux, the energy range, the focus, and the desired collimation. A SR source is characterized by a high level of spatial coherence, which allows to exploit the phase shift effects occurring to transmitted X-ray waves, and that is a further mechanism that contributes to the image formation.

Respect to the X-ray tubes, synchrotrons natively provide laminar and almost parallel geometry to the photon beam. This results in a low magnification of the sample projections on the detector, and a negligible scatter contribution to the image formation. The use of monochromatic X-rays make the beam hardening artifacts negligible, and that is fundamental to extract quantitative information about the sample (such as composition, density, morphology, etc.).

1.4.3 Local Area Microtomography

The CT is based on the analysis of the three-dimensional distribution of the refractive index of the sample, using the transmission images collected at different incident angles (see sketch A). The filtered back-projection algorithm (FBP) is the most popular reconstruction method.

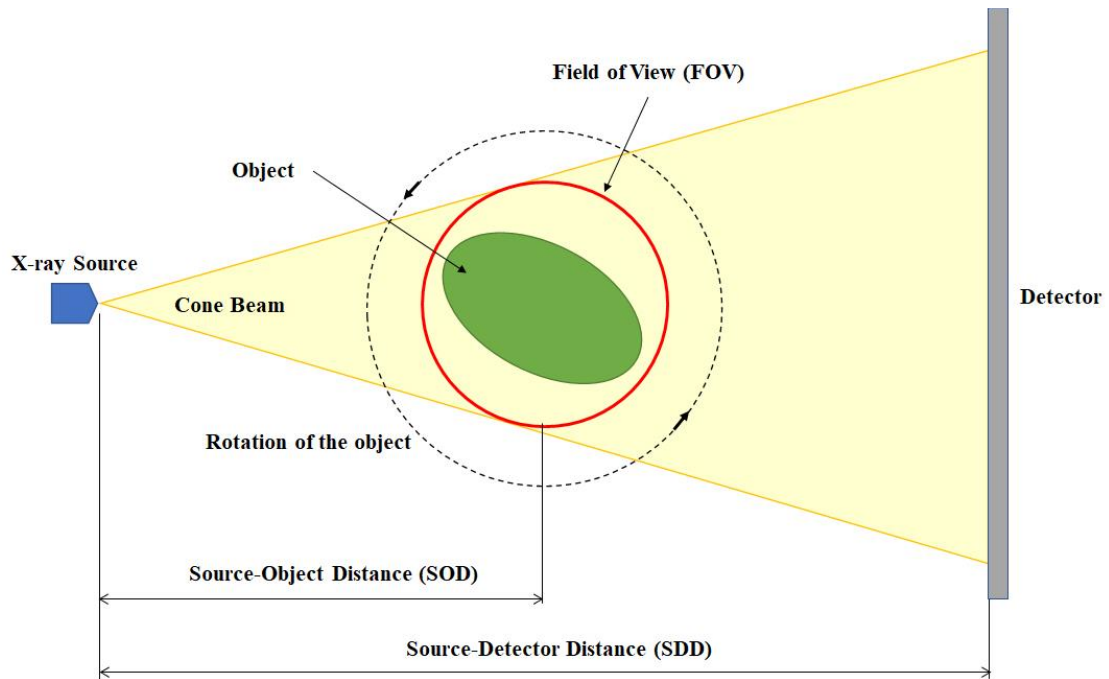
In many practical situations, it is important to minimize the Field of View (FOV) of the imaging system in order to increase the spatial resolution of the reconstructed image. However, when the region of interest (ROI) is larger than the FOV, the measured projections are truncated, which gives rise to a local tomography reconstruction problem (see sketch B), (Sodini et al. 2012).

Since the projection data do not cover the entire sample, it is said to be truncated with respect to a scan that would cover it entirely. The issue then is to reconstruct the ROI from the ‘truncated’ data. However, due to the nature of the tomography acquisition, the acquired data are not sufficient to reconstruct the ROI in general: for each angle, rays go through the entire sample, not only through the ROI. Thus, the data do not only contain information on the ROI but also contributions from the sections of the sample that are not part of the ROI. These contributions interfere with the exact reconstruction of the ROI from the acquired data in general (Paleo, Desvignes, and Mirone 2017).

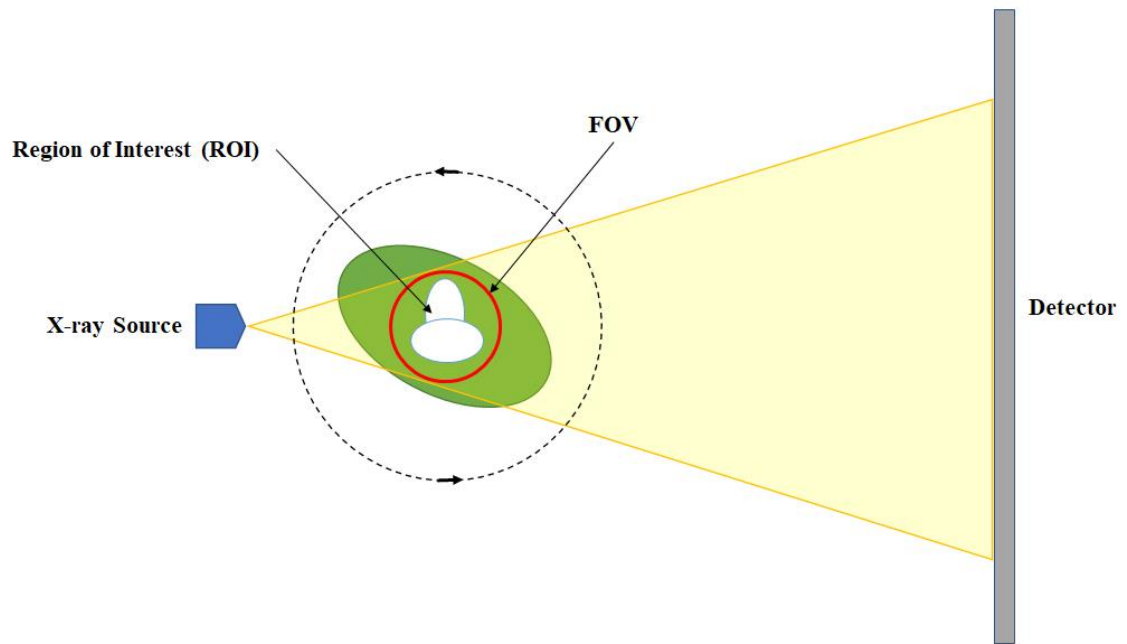
The problem of reconstructing a ROI embedded in a wider object is called the *interior problem*. It is well known that the *interior problem* does not have a unique solution in general (Paleo and Mirone 2017). As a consequence, it is generally impossible to reconstruct, with the usual experimental and mathematical methods, the distribution of the refractive index inside a sample that is larger than the FOV of the CT system. However, over the past years, analytical methods for tackling reconstructions of truncated projections have been proposed. (Gureyev, Nesterets, and Mayo 2007), (Cai et al. 2018).

An alternative method is based on a different acquisition protocol based on a continuous scan (Sodini et al. 2012), (Faridani, Ritman, and Smith 1992), (Faridani et al. 1997). While conventional tomographic acquisitions collect the sequential application of image integration and motor movement, during a continuous scan the

sample rotates at a constant speed while projections are taken during the movement. Each projection is not related to a single angular position, but corresponds to a predetermined angular integration. When applied with suitable parameters, this approach can lead to a blurring of the structures on the planar images that are positioned at larger distance from the centre of rotation of the sample, while structural details inside the FOV are not modified significantly. Choice of the angular step is critical, since details at the border of the FOV should not move by more than one pixel during a single planar acquisition. Rotation speed and acquisition time are chosen accordingly, taking into account also the characteristics of the X-ray detector. This experimental approach, rather than taking into account the mathematical features of local tomography, reduces the high frequency component of the signal related to structural details which are not in the FOV of the detector, and simplifies the reconstruction procedure needed to obtain a 3D description of the volume of interest.



Sketch A: micro-tomography scanning geometry. In a standard micro-tomography setup, the detector field of view is large enough to cover the whole sample, as all the X-rays passing through the object hit the detector for all angles.



Sketch B: Local Area tomography. In a local tomography setup, only X-rays passing through the region of interest hit the detector for all angles.

1.5 ABSORPTION LAW

Tomographic imaging consists of measuring the decrease in X-ray intensity along with a series of linear paths. This decrease is characterized by Lambert-Beer's law, which describes the decrease in intensity as a function of the X-ray energy, the length of the path, and the linear attenuation coefficient of the material.

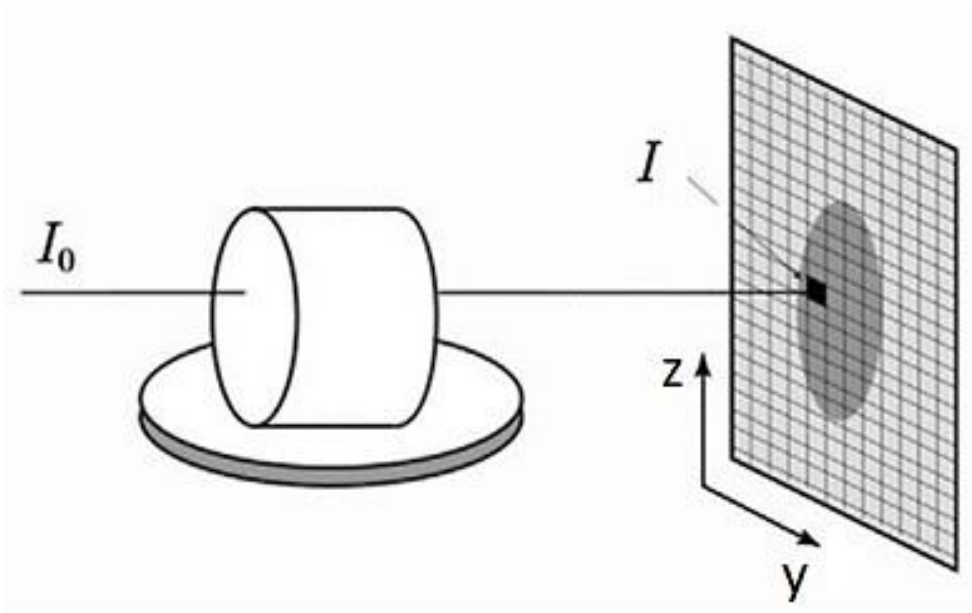


Fig. 1.6 Illustration of the incident and acquired X-ray represented as a ray passing through the sample. the acquired intensity I is modeled as a line integral of X-ray absorption along the ray path. (Landis and Keane 2010)

The simplest form of Lambert-Beer's Law for a monochromatic X-ray beam through a homogeneous material is:

$$I = I_0 e^{-\mu x} \quad \text{Eq. 1.8}$$

where I_0 and I are the initial and final X-ray intensity respectively, μ is the material's linear attenuation coefficient and x is the X-ray path length, see Fig. 1.7 (a).

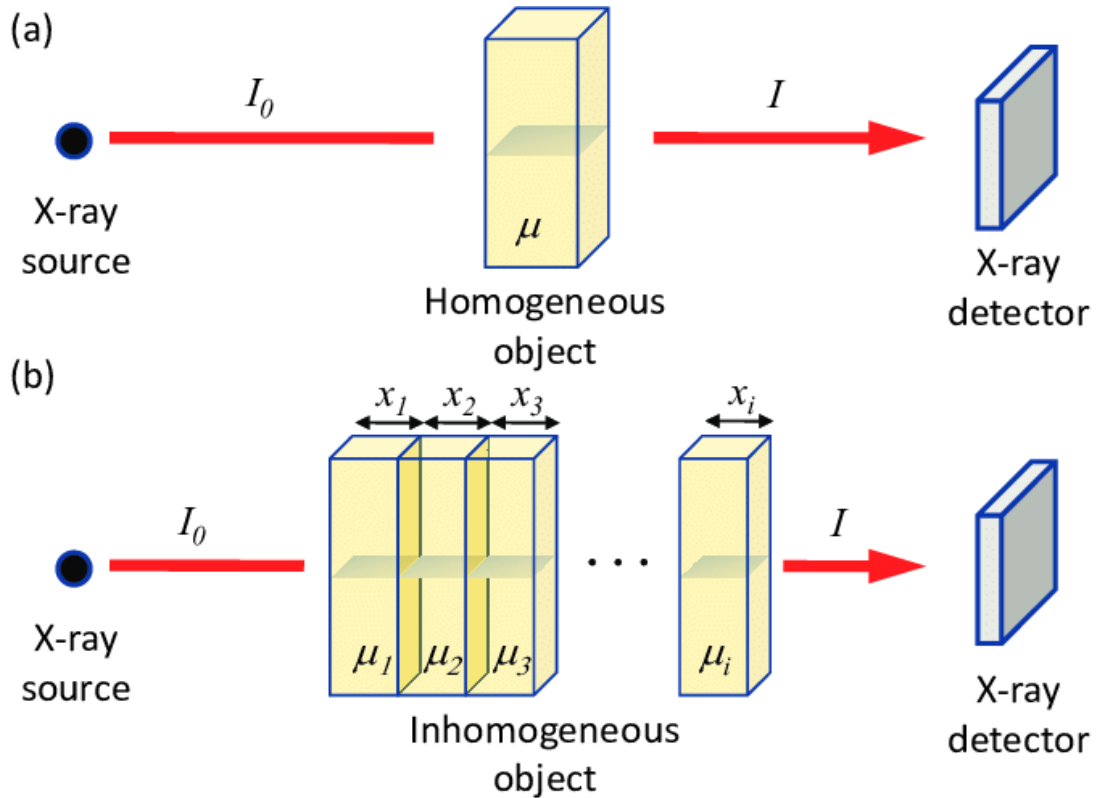


Fig. 1.7 Schematic of X-ray radiography: (a) attenuation through homogenous medium and (b) summation of attenuation through heterogeneous medium. (Tatone and Grasselli 2014)

If the scanned object is inhomogeneous (comprised of multiple materials with different attenuation characteristics), the equation is reformulated as:

$$I = I_0 \exp[\sum_i(-\mu_i x_i)] \quad \text{Eq. 1.9}$$

where μ_i and x_i are the linear attenuation coefficient and thickness of the different materials, respectively. see Fig. 1.7 (b).

In a well-calibrated system using a monochromatic X-ray source (i.e. synchrotron), this equation can be solved directly. If a polychromatic X-ray source is used (as is the case in microfocus tube systems) to take into account the fact that the attenuation

coefficient is a strong function of the X-ray energy, the complete solution would require solving the equation over the range of the entire X-ray energy (E) spectrum:

$$I = \int I_0(E) \exp\left[\sum_i (-\mu_i(E) x_i)\right] dE \quad \text{Eq. 1.10}$$

Considering a continuous and non-homogeneous medium, then the equation becomes:

$$I = \int I_0(E) \exp\left[-\int_{\mathcal{L}} \mu(s, E) ds\right] ds \quad \text{Eq. 1.11}$$

The following expression correlates the X-ray intensity I_0 that enters the sample to the outcome intensity I after traversing a path length \mathcal{L} inside the object thickness.

Under the assumption that a monochromatic X-ray beam is emitted Eq. 1.11 can be simplified. In such a case the Lambert-Beer's law state that:

$$I = I_0 \exp\left[-\int_{\mathcal{L}} \mu(s) ds\right] \quad \text{Eq. 1.12}$$

As one can observe by rearranging Eq. 1.12 a line integral of X-ray attenuation is:

$$P = \ln\left(\frac{I}{I_0}\right) = -\int_{\mathcal{L}} \mu(s) ds \quad \text{Eq. 1.13}$$

This equation shows that the logarithm of the ratio of the incident X-ray intensity over the transmitted x-ray intensity represents the line integral of the absorption coefficient along the x-ray path. The term P in CT is usually known as **projection**. (Pacilè and Tromba 2018a).

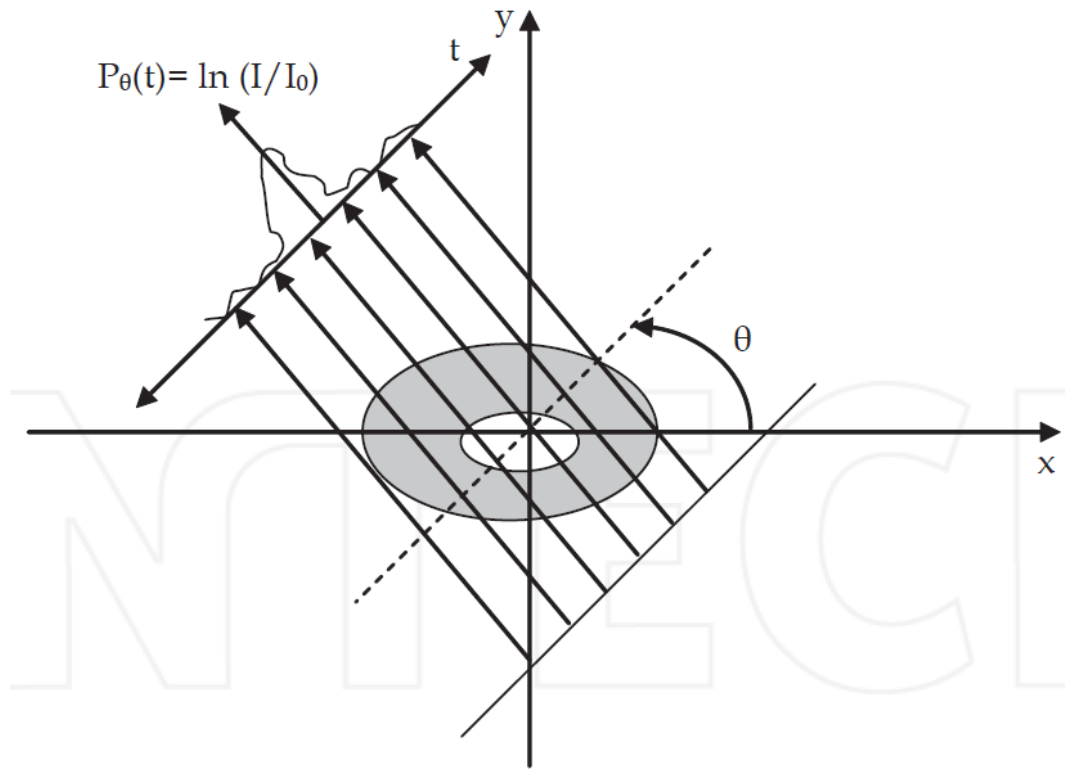


Fig. 1.8 Scanning of a single layer in the plane (x, y). Where z is the axis of rotation. (Kharfi 2013)

The projection of an object, resulting from the tomographic measurement process at a given angle θ , is made up of a set of line integrals. In Fig. 1.8 shows the scanning of a single layer in the plane (x,y). Such a projection can be defined as:

$$P_{\theta}(t) = \ln \left(\frac{I}{I_0} \right) = - \int_{path} \mu(x, y) ds \quad \text{Eq. 1.14}$$

1.6 RECONSTRUCTION IN MICROTOMOGRAPHY

We already showed how the projections of an object at a certain angle θ are made up of a series of line integrals. In X-ray computed axial tomography, the line integrals represent the total attenuation of the X-ray beam while they travel in a straight line through the object and the resulting image is a 2D (or 3D) model of the absorption coefficient i.e. the image $\mu(x,y)$. The simplest and easiest way to visualize the method of analysis is the system of parallel projections. For this, we consider the information that is collected as a series of parallel rays in the position r , through a projection in the angle θ . This is repeated for several angles. As the attenuation occurs exponentially in the medium the total attenuation p of lightning in position r with a projection on the angle θ , is given by the following integral:

$$p(r, \theta) = \ln \left(\frac{I}{I_0} \right) = - \int \mu(x, y) ds$$

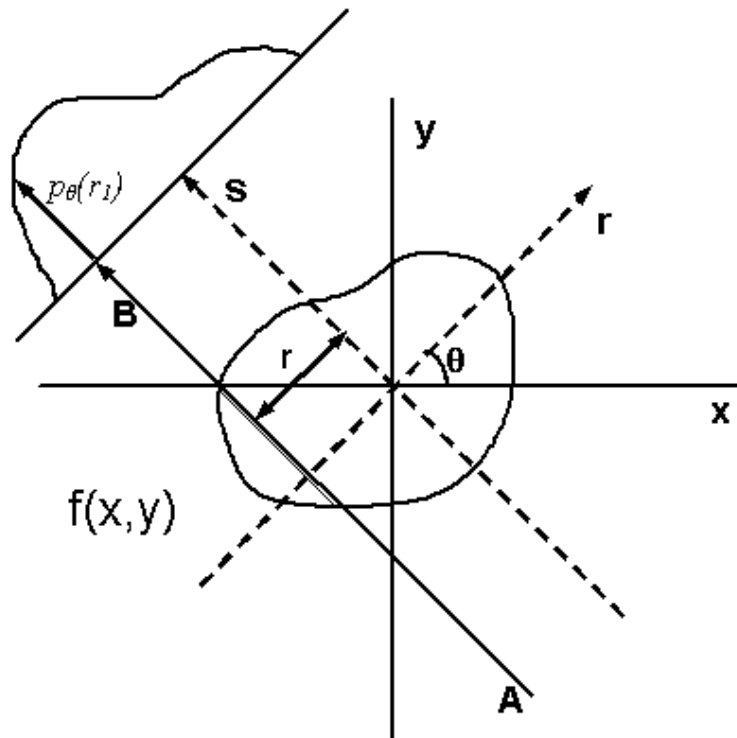


Fig. 1.9 Parallel beam geometry utilized in tomography and tomographic reconstruction. Each projection, resulting from tomography under a specific angle, is made up of the set of line integrals through the object.

Using the coordinate system of Fig. 1.9, the value of r , on the point (x, y) , will be projected in the angle θ shown by the following equation:

$$x \cos\theta + y \sin\theta = r$$

With this, we see that the equation shown above can be rewritten as follows:

$$p(r, \theta) = \iint_{-\infty}^{+\infty} f(x, y) \delta(x \cos\theta + y \sin\theta - r) dx dy$$

where $f(x,y)$ represents $\mu(x,y)$ and $\delta()$ is the Dirac delta function. This function is known as the Radon transform (or sinogram) of the object in 2D resolution. (Kak and Slaney 1988).

The Fourier section theorem states that if we have an infinite number of one-dimensional projections of an object, taken from an infinite number of angles, we can perfectly reconstruct the original object, $f(x,y)$. So, in order to obtain again $f(x,y)$ from the previous equation we must find the inverse Radon transform. However, the inverse Radon transform has proved to be very unstable with respect to noisy data. In practice, a stabilized and discrete version of the Radon inverse transform is used, which is commonly known as the filtered back-projection algorithm. Knowing the Radon transform of an object allows it to reconstruct its structure: the projection theorem actually ensures that if we have an infinite number of mono-dimensional projections of an object made from an infinite number of different angles and the reconstruction process is precise when calculating Radon's anti-transformation.

However, Radon's anti-transformation is very unstable if measured data are affected by experimental noise. In practice, a stabilized and discrete version of Radon's anti-transformation, called '*filtered back-projection algorithm*' (*FBP*), is used. A corollary to the projection theorem states that "*Radon's transformation of the two-dimensional convolution of two functions is equal to the one-dimensional convolution of their Radon transformations*". The practical consequence of this is that, in order to eliminate the noise that reduces the quality of the reconstruction, it is not necessary to physically eliminate its source, but it is possible to filter mathematically the experimental results

(i.e. the measure of the Radon transform) and then rebuild (i.e. calculate the anti-transform) directly from the a posteriori filtered data.

The reconstructed image shown by Fig. 1.10 represents one slice of a 3D object. Additional slices over the height of the object are needed to illustrate the full 3D volume. The slice thickness and the dimensions of the 2D pixels over which the back-projection is performed define rectangular prisms called voxels. With industrial cone-beam volume CT systems, including that used in the current study, voxels are cubes whose dimensions that depend on the grid size of the the CCD detector array and the selected level of magnification. Each voxel is defined by an attenuation coefficient which represents the average attenuation of the scanned object within that volume.

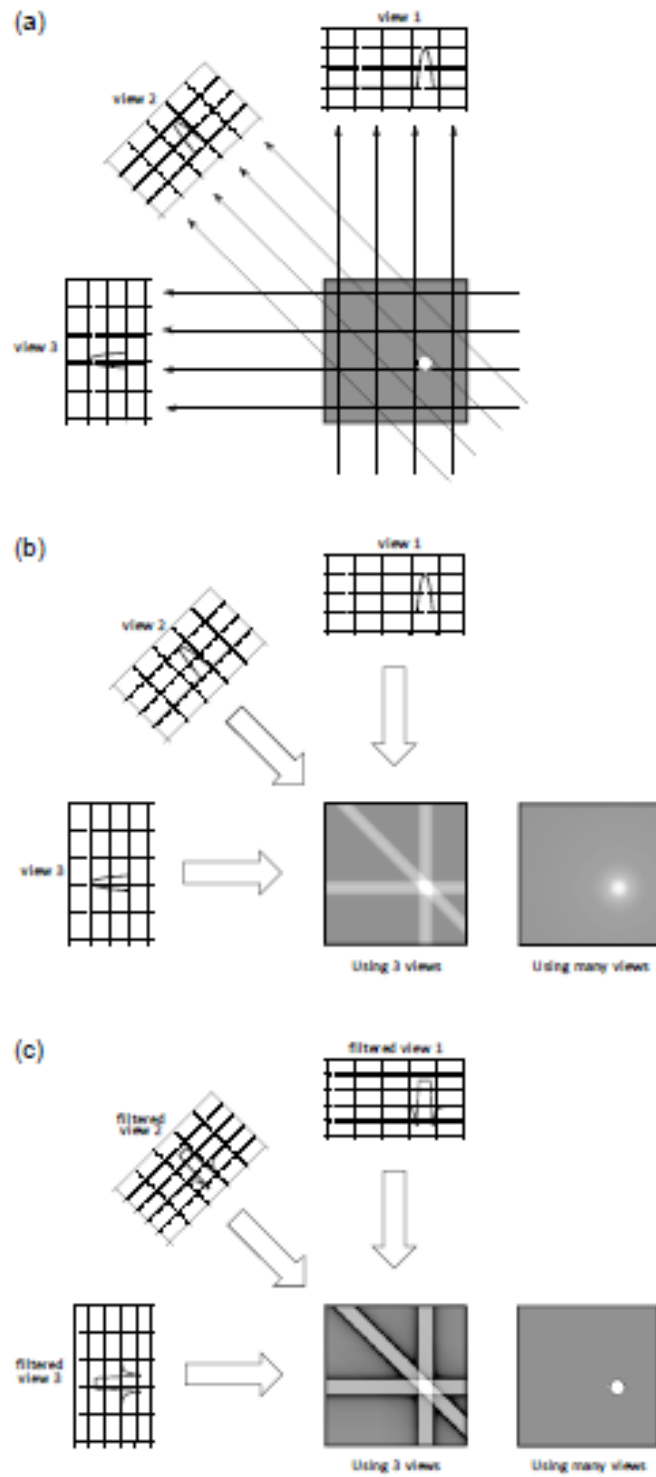


Fig. 1.10 CT volume reconstruction: (a) original X-ray projection data; (b) simple back projection; and (c) Filtered Back Projection, after (Tatone and Grasselli 2014).

However, a detailed description of such theoretical background is beyond the aim of the present thesis, and can be found in the related specific literature; (Kak and Slaney 1988), (Kharfi 2013), (Noori-Asl and Sadremomtaz 2013).

1.7 PHASE CONTRAST

X-ray phase-contrast imaging and tomography make use of the refraction of X-rays by the sample in image formation. This provides considerable additional information in the image compared to conventional X-ray imaging methods, which rely solely on X-ray absorption by the sample. Phase-contrast imaging highlights edges and internal boundaries of a sample and is thus complementary to absorption contrast, which is more sensitive to the bulk of the sample. Phase-contrast can also be used to investigate low-density materials, which do not absorb X-rays sufficiently to form a conventional X-ray image. In the context of materials science, X-ray phase-contrast imaging and tomography have particular value in the 2D and 3D characterization of low-density materials, the detection of cracks and voids and the analysis of composites and multiphase materials where the different components have similar X-ray attenuation coefficients. (Mayo, Stevenson, and Wilkins 2012).

1.7.1 Physical Principle of In-Line Phase-Contrast Imaging:

The X-ray refractive index is very close to 1, making these refractive effects weak compared to the refraction of light, therefore specialized imaging conditions are required to make use of X-ray refraction in imaging. The primary requirement is that the X-ray source illuminating the sample has high spatial coherence; a condition that is met either by having the X-ray source located some distance away, like in the typical case of a synchrotron, or by using a source of small size (a few tens of microns or less). The second significant requirement is to have a significant distance between the sample and the detector. After passing through the sample the X-ray wavefront is distorted in proportion to the phase-shift imposed by the sample. However, it is the

propagation of the distorted X-ray wavefront between the sample and detector which gives rise to Fresnel diffraction fringes in the image. An important feature for practical applications is that there is no strong requirement for chromatic coherence. In fact, in the near-field case, the Fresnel fringes are approximately coincident for different energies, enabling polychromatic radiation such as that from laboratory sources to be used. (Mayo et al. 2012).

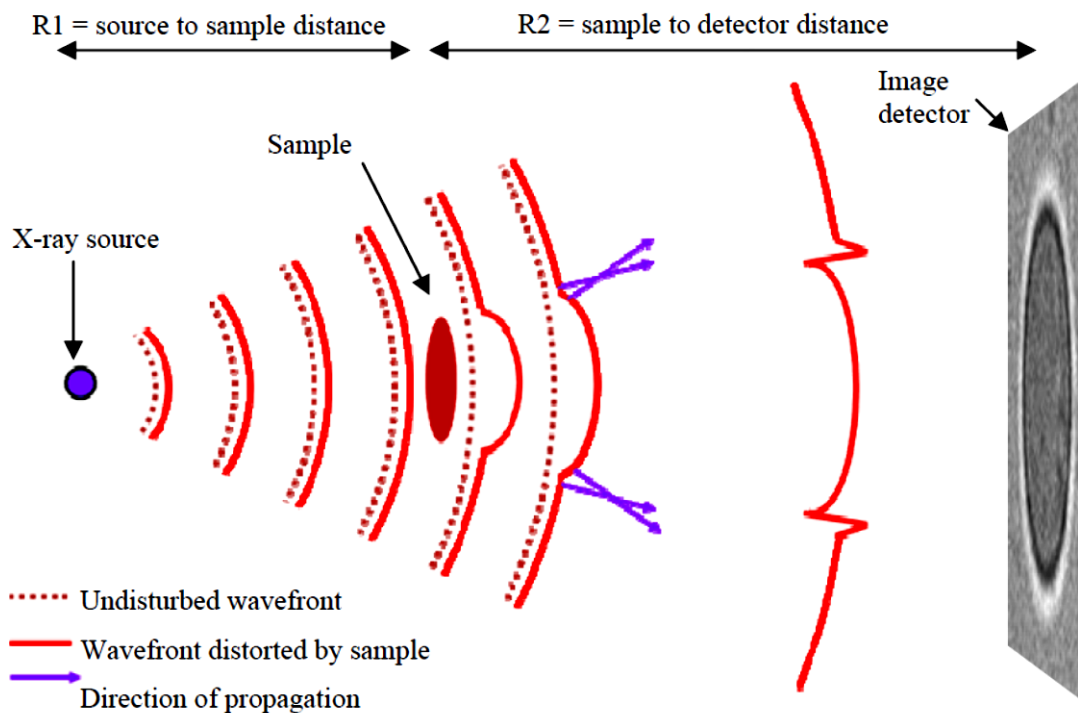


Fig. 1.11 Figure 1. Mechanism of in-line phase-contrast: A sample imposes a phase-shift on the X-ray beam, which distorts the X-ray wavefront.

A mathematical model of inline phase-contrast imaging is given by the Fresnel propagator (see Fig. 1.11).

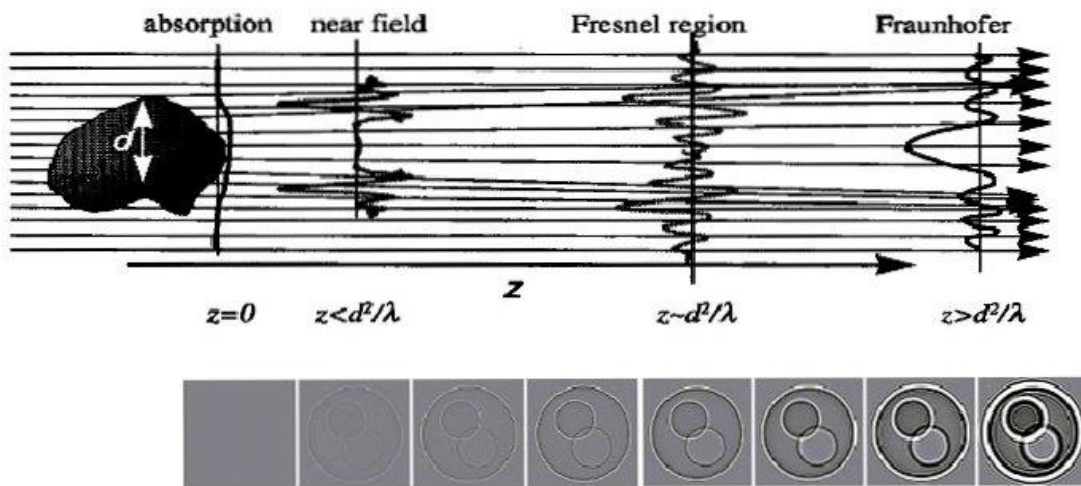


Fig. 1.12 The principle of inline phase-contrast imaging. The projection images of the computer phantom of the spheres are shown for different positions of the detector along the z axis. (Bronnikov 2006)

Assuming that the detector is in the near field of the Fresnel region:

$$z = \frac{d^2}{\lambda} \quad \text{Eq. 1.15}$$

(where λ is the wavelength, z is the distance of the detector to the sample and d is the size of the sample) we may write:

$$I(x, y) = 1 - \frac{\lambda z}{2\pi} \nabla^2 \phi(x, y) \quad \text{Eq. 1.16}$$

where,

$\phi(x, y)$: phase change due to a small slab of material

λ : wavelength

Z : distance between the sample and the detector

This equation establishes a linear relation between the phase function and the measured intensity data.

The image is edge-enhanced, and for soft tissues, it is possible to retrieve the phase projection from a single in-line image. The phase contrast technique is used for reconstructing the phase coefficient using the retrieved phase projections, (Pogany, Gao, and Wilkins 1997), (Cai 2009).

Note: In this research work, phase contrast was not used, so it will not be discussed in much detail, but it is important to know that this technique will be the spearhead when the STAR source is in operation.

2 X-RAY CONE-BEAM MICROTOMOGRAPHY

The cone beam microtomography (micro-CT) has the advantage to use a simple and versatile setup. A micro-CT system (Fig. 2.1) consists of a microfocus X-ray source, a rotational sampler holder, a flat-panel detector and a computerized processing system. All the components except the latter are mounted on an optical bench. (Lee et al. 2003)

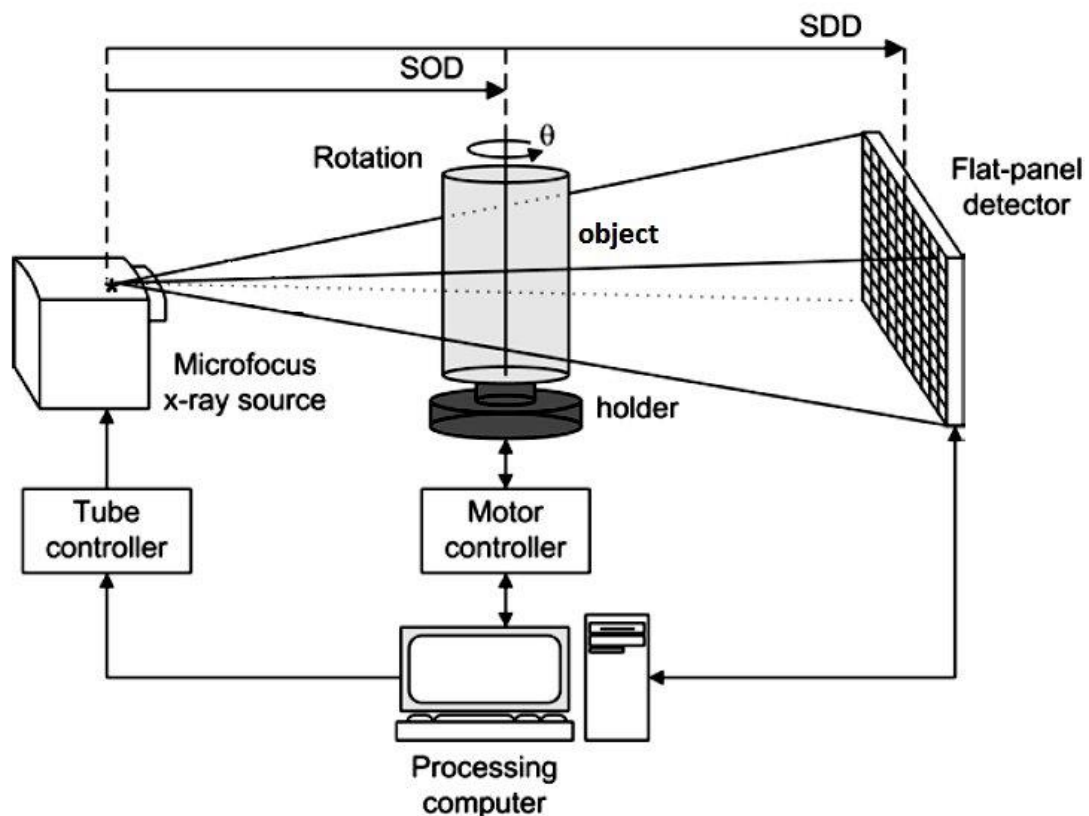


Fig. 2.1 Schematic diagram of the developed micro-CT system (Lee et al. 2003).

In order to achieve high resolution in X-ray imaging, a geometrical magnification is often the means of choice. There are two specific distances which play a key role in the determination of the system's geometric parameters such as the magnification: the Source to Object Distance (SOD) and the Source to Detector Distance (SDD). The magnification M is defined as:

$$M = SOD/SDD$$

The closer the source to the sample, the higher the magnification and the smaller the voxel size.

Fig. 2.2 shows a schematic diagram of the sequence of the operations to perform an X-ray microtomography measurement.

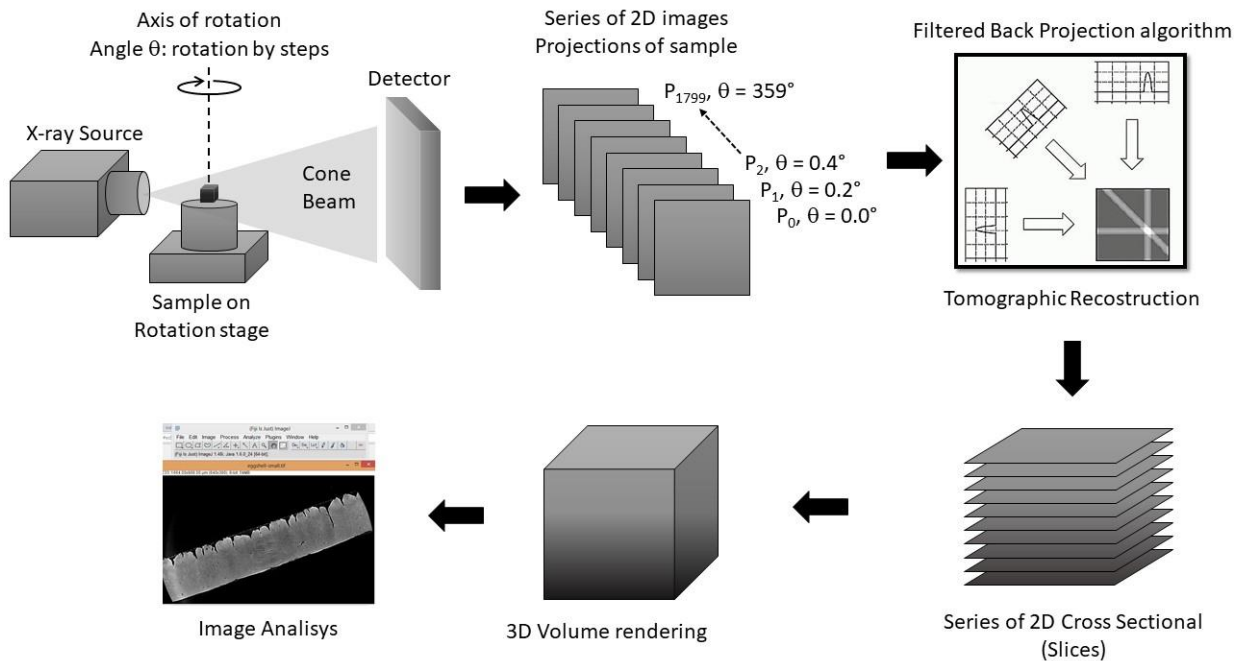


Fig. 2.2 X-ray microtomography measurement.

A complete microtomography measure consists in taking several scans of the sample while it rotates about its own axis, keeping the X-ray source and the detector in a fixed position. The microfocus X-ray source continuously irradiates a sample, while the sample rotates in a stepper motion until completing the full circle and the flat-panel detector acquires a series of 2D projections at different angles and at a fixed integration time. The angular step and integration time are computer-controlled. The acquired projections are then analyzed in order to produce a 3D digital reconstruction of the sample, using a Filtered Back-Projection algorithm (FBP).

In our case, since the micro-CT apparatus uses an X-ray cone beam source, the 3D digital reconstruction is performed using the algorithm of Feldkamp, Davis, and Kress (FDK). The 3D digital reconstruction produces a 2D dataset of cross sections, called slices. The stack of slices provides three-dimensional volumetric data. The sample can be viewed and analyzed in a virtual environment in various ways: it is possible to view a single slice of the sample or a 3D virtual volume.

To achieve high spatial resolution in the cross-sectional tomographic images, sampling has to satisfy two requirements. **First**, the projection pixel spacing must be small enough to resolve small details in the projection image of the transmitted radiation. **Second**, the angular increment while sampling the series of projection images has to dominate the spatial resolution depending on the distance of a reconstructed pixel from the axis of rotation.

The effective spatial resolution in projection imaging can be measured by the blurring (geometric unsharpness U_g) resulting from the combined influence of the focal spot size width f , the detector pixel spacing p (which is usually equal to the pixel size), and the sample's motion during data acquisition. The latter effect plays an important role for samples whose detail size is about 1 mm or smaller, since random displacement of the mechanical axes and the drift of the focal spot position are of the same magnitude during the total data acquisition time (of several minutes and more). (Hanke et al. 2016).

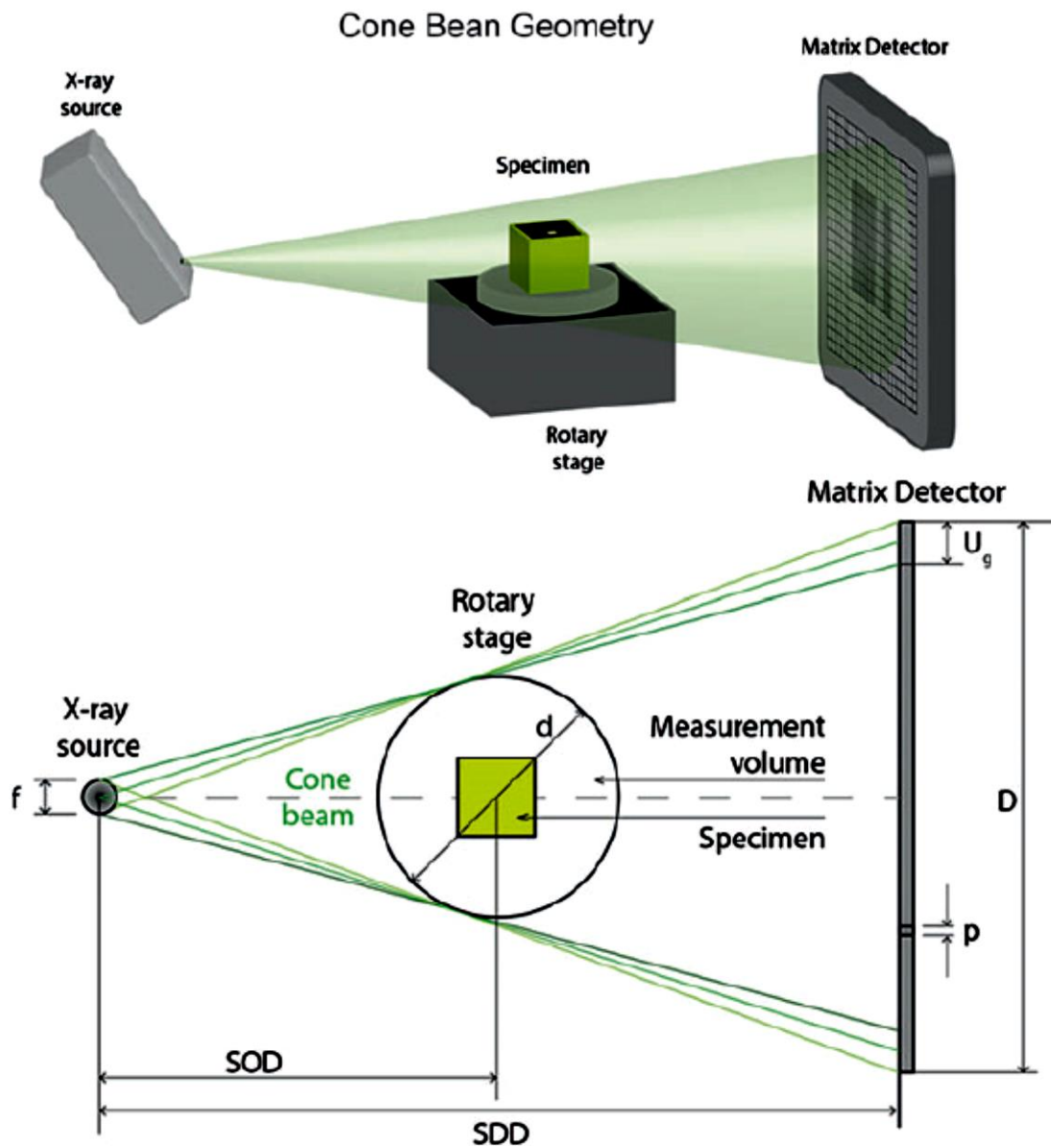


Fig. 2.3 (Top image) Main components of cone beam X-ray computed tomography: X-ray source (X-ray tube), rotary stage with specimen and a matrix detector (flat panel detector). (Bottom image) Typical geometry of cone beam micro-CT: Geometrical magnification is determined by the source-object distance (SOD) and source-detector distance (SDD), as well as the effective detector width D and the diameter d of the measuring volume. f is the focal spot size, p is the detector pixel size and U_g the geometric unsharpness in the penetration image in relation to the focal spot size f . (Kastner and Heinzl 2018)

The voxel size is then determined by the detector pixel size p according to Eq.2.1. Typical voxel sizes in the reconstructed micro-CT are in range between 1 μm and 0.2 mm. For high-resolution micro-CT systems, the minimum voxel size s can be 100 nm or even lower.

$$\mathbf{s} = \frac{p}{M} \quad \text{Eq. 2.1}$$

The voxel-size s in the reconstructed micro-CT data depends on the number of pixels N_{pixels} of the X-ray detector and the diameter d of the scanned sample and may also be computed as follows:

$$\mathbf{s} = \frac{N_{pixels}}{d} \quad \text{Eq. 2.2}$$

To accurately reconstruct the volumetric data, the entire sample must remain within the field of view (FOV) and the cone beam during the rotation. The maximum magnification of a micro-CT system is limited by the ratio of the detector width D and the sample diameter d . It can be expressed according to Eq. 2.3:

$$\mathbf{M}_{max} = \frac{D}{d} \quad \text{Eq. 2.3}$$

The geometrical unsharpness U_g depends on the focal spot size and on the magnification as given in Eq. 2.4. Since the focal spot of the X-ray source has a finite size, geometric unsharpness or image blur will always occur.

$$\mathbf{U}_g = f\left(\frac{SDD-SOD}{SOD}\right) = f(\mathbf{M} - \mathbf{1}) \quad \text{Eq. 2.4}$$

Conventional industrial X-ray tubes feature focal spots of 0.5–4 mm in size, while for mini-focus X-ray tubes they are 0.1–0.5 mm. Focal spots of industrial micro-focus X-ray tubes range from 1 to 50 μm and nano-focus from 0.4 μm to 1 μm .

With the pixel spacing p and the focal spot width f given in Fig. 2.3, the ideal magnification factor is found by setting the geometrical blurring to be equal to the effective sampling, ie, at the center of the system:

$$\frac{p}{M} = \frac{U_g}{M} \quad \rightarrow \quad \frac{p}{M} = f \left(\mathbf{1} - \frac{\mathbf{1}}{M} \right) \quad \text{Eq. 2.5}$$

Hence, the ideal magnification can be derived as:

$$\mathbf{M} = \mathbf{1} + \frac{p}{f} \quad \text{Eq. 2.6}$$

The spatial resolution in reconstructed tomographic slices depends on an additional parameter, the angular sampling distance. In general, the operator of a CT system can freely choose this parameter freely since there is no physical restriction that imposes a certain number of angular positions. Nevertheless, there exists a reasonable number of projections which are recommended to be acquired, in order not to lose spatial resolution, in particular out of the center of the image. The following “back of the envelope” consideration, sketched in Fig. 2.4 delivers a rule of thumb, which is valid for all standard filtered back-projection reconstruction algorithms. (Hanke et al. 2016)

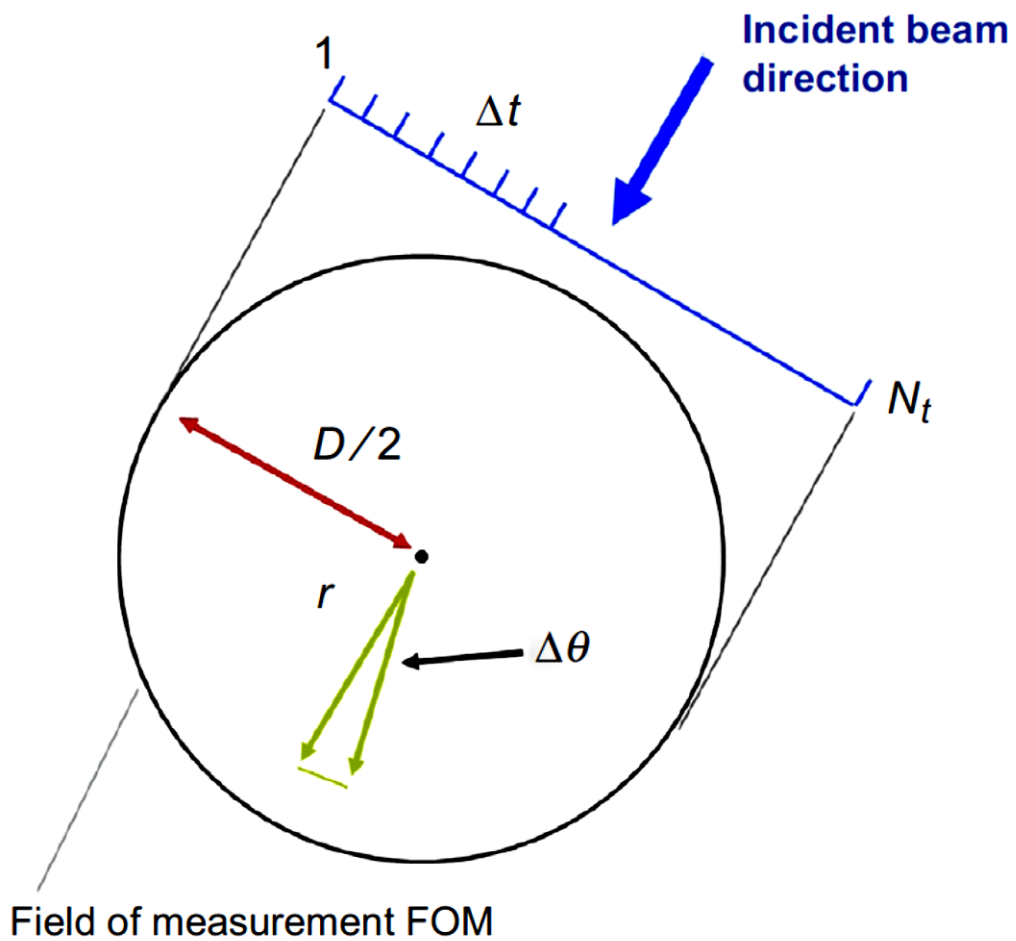


Fig. 2.4 Sketch of the field of measurement. Radial and angular sampling is illustrated within the cross-sectional tomographic plane.

Assuming parallel beam geometry and a linear detector sampling Δt in a given tangential direction given, one can put forth the condition that the same spacing of the rays is needed along a circumference of radius r . With a given angular increment $\Delta\theta$ given, it follows:

$$\Delta t = r \cdot \Delta\theta$$

This relation can be rewritten when taking into account the number of samples along the diameter D of the field of measurement:

$$D = N_t \cdot \Delta t$$

and the number of angular positions within 180 degrees, and the number of angular positions within 180 degrees, which are fully sufficient in the case of parallel beam geometry:

$$\pi = N_{\theta} \cdot \Delta t \quad \text{Eq. 2.7}$$

Putting all together we end up with a simple equation:

$$\frac{D}{N_t} = r \frac{\pi}{N_{\theta}} \quad \text{Eq. 2.8}$$

One interpretation of this equation is that the spatial resolution decreases with the increasing distance of a reconstructed pixel or voxel from the center of rotation. If we require the sampling to be adequate in the angular and tangential direction up to the edge of the field of measurement, $r=D/2$, we end up with a useful rule of thumb:

$$N_{\theta} = N_t \cdot \frac{\pi}{2} \quad \text{Eq. 2.9}$$

The number of angular positions should be about 50% higher than the number of pixels of the detector along one spatial direction. For instance, with a 2000 by 2000 pixel detector, approximately 3000 projection (angles) are necessary to allow for full spatial resolution in the whole field of measurement. Of course, each additional projection is a cost in terms of exposition to the object and measurement time to acquire the image. Besides the fact that longer measurements are more expensive, there are several practical technical reasons, which recommends a reduction of scanning time.

2.1 CONE BEAM COMPUTER TOMOGRAPHY RECONSTRUCTION

Unlike the thin fan-beam geometry, cone-beam geometry immediately captures a two-dimensional image through a three-dimensional x-ray beam, which scans in the shape of a cone.

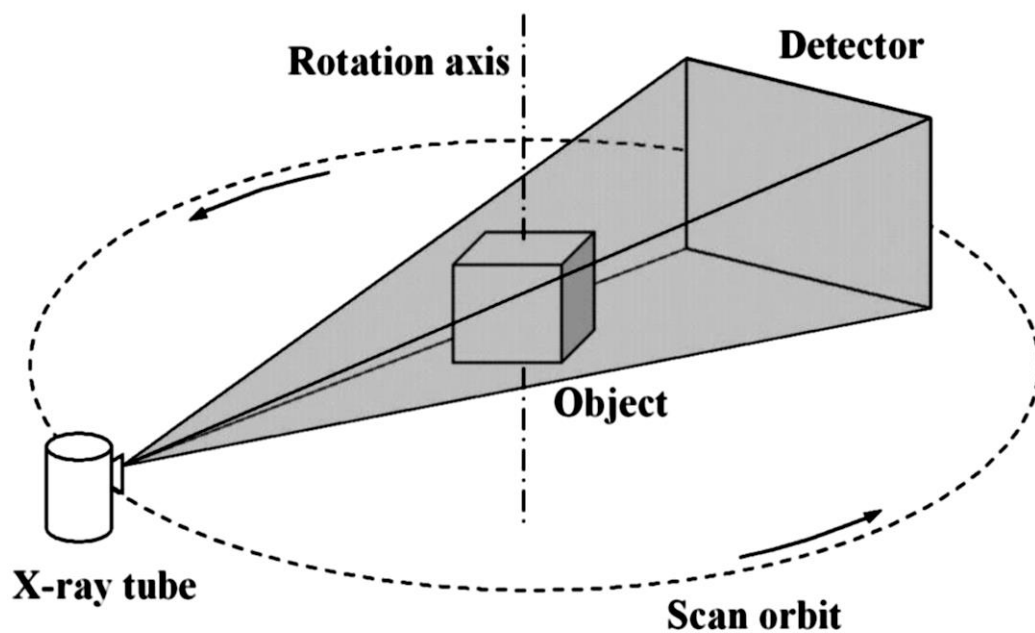


Fig. 2.5 cone-beam geometry in CT

2.1.1 Cone-Beam CT System

The image reconstruction process involves generating images from the X-ray data collected during the CT scan process, improving image quality through intense mathematical computations. X-ray images cone-beam tomography are affected by discrepancies called artefacts. These artefacts are described as errors between the numbers evaluated during the CT scan and the exact attenuation coefficients whose sum gives the amount of X-ray beam that is absorbed in the sample material per unit of area.

The most popular CT image technology today is the cone-beam imaging technology, which emits a cone-shaped x-ray beam that takes two dimensional images. These two-dimensional images are taken almost instantly in the scanning process, and they are sent to a software program to run image reconstruction algorithms. This program can run on a CPU, but will take too much time to process the large amount of data. Exploring speedups by modifying algorithms, using different languages, and relying on different hardware accelerators is well researched today.

Among the most popular algorithms used for 3D CT image reconstruction, the Feldkamp et al. (FDK)'s weighted filtered back-projection algorithm is the most used. Due to the circular trajectory required for calculating this algorithm, only an approximate reconstruction can be acquired. Yet, this algorithm remains popular due to simplicity and the ability to parallelize implementations. Weighting and filtering the two-dimensional image slices takes no time compared to the time required by the back projection step, which is the bottleneck of the algorithm.

2.1.2 Feldkamp's Algorithm

The Feldkamp et al. algorithm for CBCT image reconstruction is the most widely used today, due to the practicality and power of the approach. This algorithm uses filtered back projection, however, due to the use of a circular trajectory, it cannot provide exact reconstructions. Because of the approximate reconstruction, the reconstructed image is prone to more artefacts such as blurriness in areas far from the orbit, and missing part of the projection image.

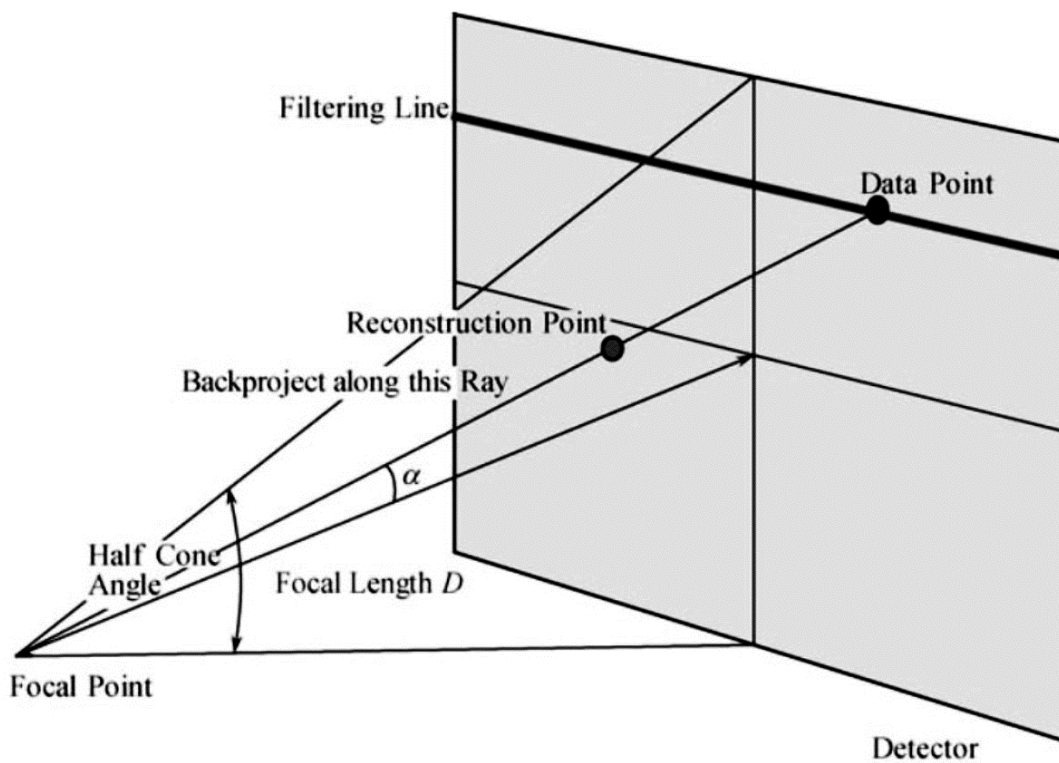


Fig. 2.6 The coordinate system for Feldkamp's cone-beam algorithm (Zeng 2010)

Figure 2.6 provides a visualization of the Feldkamp algorithm, which outlines the cone-beam projections and where the filter and back projections are applied. Feldkamp et. al (FDK) make use of the cone angle outlined in Figure 2.6 and gives exact reconstruction if the angle is less than ten degrees or if the scanned object has constant dimensions in one direction.

2.1.3 Algorithm and Mathematical Analysis

As mentioned before, the FDK algorithm implements filtered back projection, heavily relying on the conversion from a cone-beam reconstruction problem to a modified fan-beam reconstruction problem. Steps described in the FDK cone-beam algorithm may sound similar to that in fan-beam reconstruction techniques. The general algorithm (Zeng 2010) is described as follows:

1. Scale projections by cosine of the cone angle.
2. Apply ramp filtering to the data.
3. Apply weighted-filtered back projection.

The interesting part about the FDK algorithm, is its similarity to fan-beam reconstruction algorithms. The FDK algorithm implements the core of the fan-beam algorithm, with a few additions to ensure it applies to the three-dimensional reconstruction. To ensure the understanding of the differences and additions to this algorithm, let us analyze the coordinate system for the FDK algorithm with the help of the pictures in Figure 2.7.

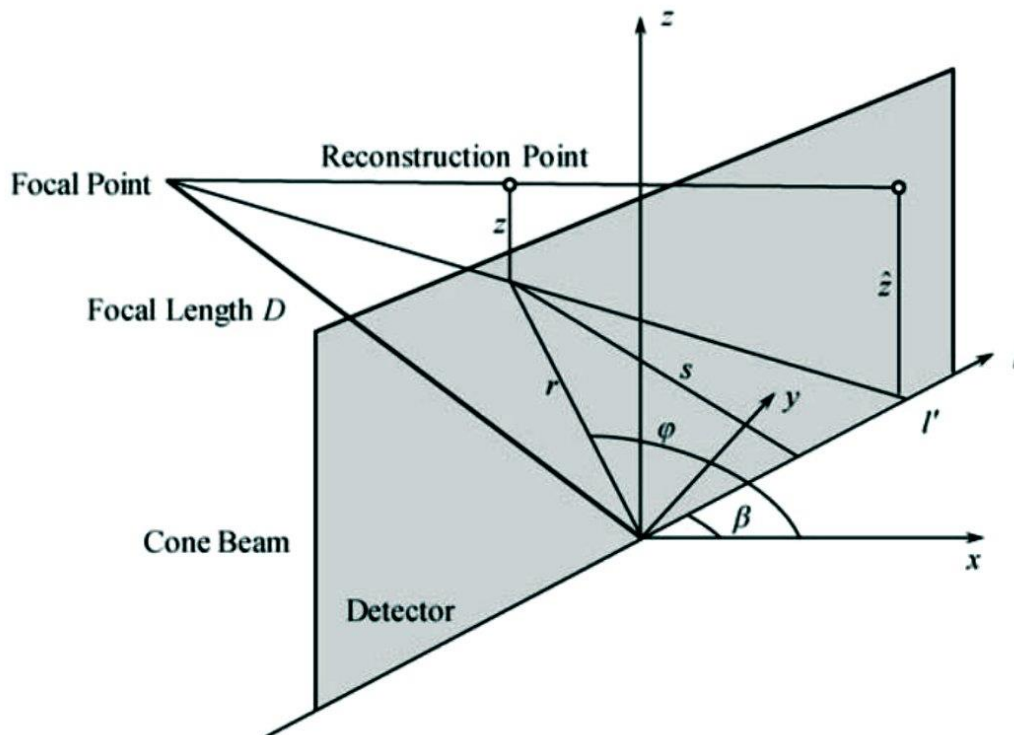


Fig. 2.7 The coordinate system for Feldkamp's cone-beam algorithm. (Zeng 2010)

The difference between the cone-beam coordinate system and the fan-beam coordinate system is the addition of a dimension in the z-direction and abstraction of the reconstruction point to fit the three dimensions. The cone-beam coordinate system is similar to the fan-beam coordinate system. However, an additional dimension - z - is added to the diagram to represent the third dimension of the cone-beam projection. An important variable to note is the length from the detector to the focal point, D, which is the main determination of a weighting function for this algorithm.

In terms of the algorithms, the only difference is that the back projection is a cone-beam back projection. CBCT also uses the Fourier transform and ramp filtering to reconstruct the CT images. Ramp-filtering is applied to the images row-by-row and then back projection is calculated on the resulting data. Zeng et al. (Zeng 2010) provide an exceptional straightforward diagram of the cone-beam coordinate systems and a clear mathematical equation to assist in understanding and expressing important aspects.

The mathematical equation is expressed as follows:

$$f(r, \varphi, z) = \frac{1}{2} \int_0^{2\pi} \frac{D}{D-s} \int_{-\infty}^{\infty} \frac{D}{\sqrt{D^2 + l^2 + \hat{z}^2}} g(l, \hat{z}, \beta) h(l' - l) dl d\beta.$$

$$s = r \sin(\varphi - \beta), \text{ and } l' = \frac{Dr \cos(\varphi - \beta)}{D - r \sin(\varphi - \beta)}$$

Fig. 2.8 FDK Reconstruction Algorithm

Where the main parts that constitute the equation are described in the following table:

| Equation Component | Description |
|--|-------------------------------|
| $f(r, \varphi, z)$ | Back Projected Image |
| $g(l, \hat{z}, \beta)$ | Cone-Beam Projection |
| $h(l' - l)$ | Ramp Filter |
| $\frac{D}{D - s}$ | Weighting Equation |
| $\frac{D}{\sqrt{D^2 + l^2 + \hat{z}^2}}$ | Cosine of the Incidence Angle |
| $\int_{-\infty}^{\infty} \frac{D}{\sqrt{D^2 + l^2}} g(l, \beta) h(l' - l) dl$ | Inverted Fourier Transform |
| $\int_0^{2\pi} \frac{D}{D - s} \int_{-\infty}^{\infty} \frac{D}{\sqrt{D^2 + l^2}} g(l, \beta) h(l' - l) dl d\beta$ | Back Projection |

Individual variables are illustrated in Figure 2.7, and the ramp filter is not described in these sections. D represents the focal length, and l is the linear coordinate on the detector. The mathematical equation may appear complex, but it is simply broken up into different steps. This equation is performed by weighting, ramp filtering (including the inverse Fourier Transform), and then performing back projection to reconstruct the three-dimensional image.

3 X-RAY MICROTOMOGRAPHY STATION

An x-ray microtomography station, named μ Tomo, is implemented at the START-Lab facility realized under the PON MaTeRiA project. It is located at the University of Calabria in Italy. The station is based on a propagation based transmission imaging setup with a microfocus source and digital x-ray area detectors. Due to its simplicity, this setup is ideal for fast, high resolution imaging and microtomography of materials research samples.

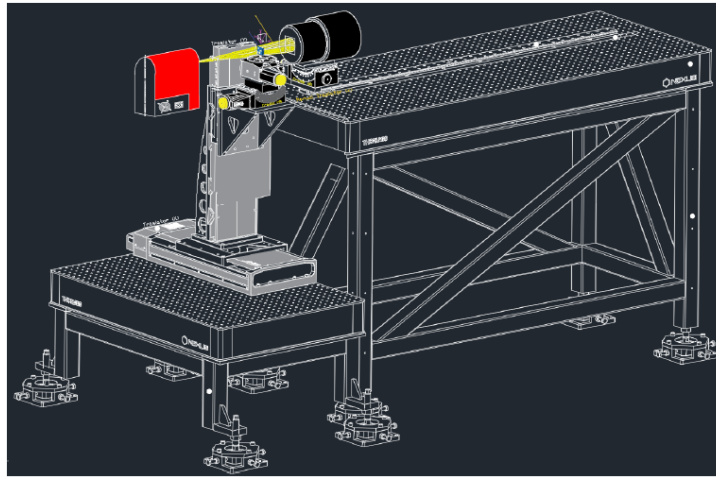


Fig. 3.1 Sketch of the μ Tomo microtomography station at STAR-LAB.

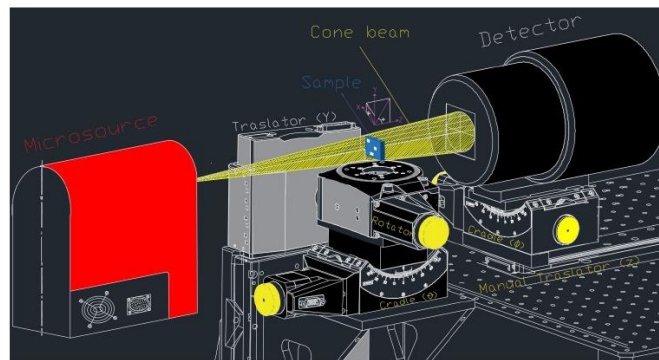


Fig. 3.2 The sketch zoomed shows in detail the alignment of the components of the tomographic system. X-ray source, sample and detector.

Details of the experimental setup, equipment, and software integration are described. Test microtomography for setup commissioning and characterization is shown.

3.1 EXPERIMENTAL SETUP

The μ Tomo experimental station, based on a cone beam geometry shown schematically in Fig. 3.3 is made of:

- a microfocus X-ray source Hamamatsu L12161-07;
- a flat panel detector Hamamatsu C7942SK-05;
- a five degree of freedom sample positioning system (linear movement and rotation stage);
- hardware and software system for control and data acquisition.

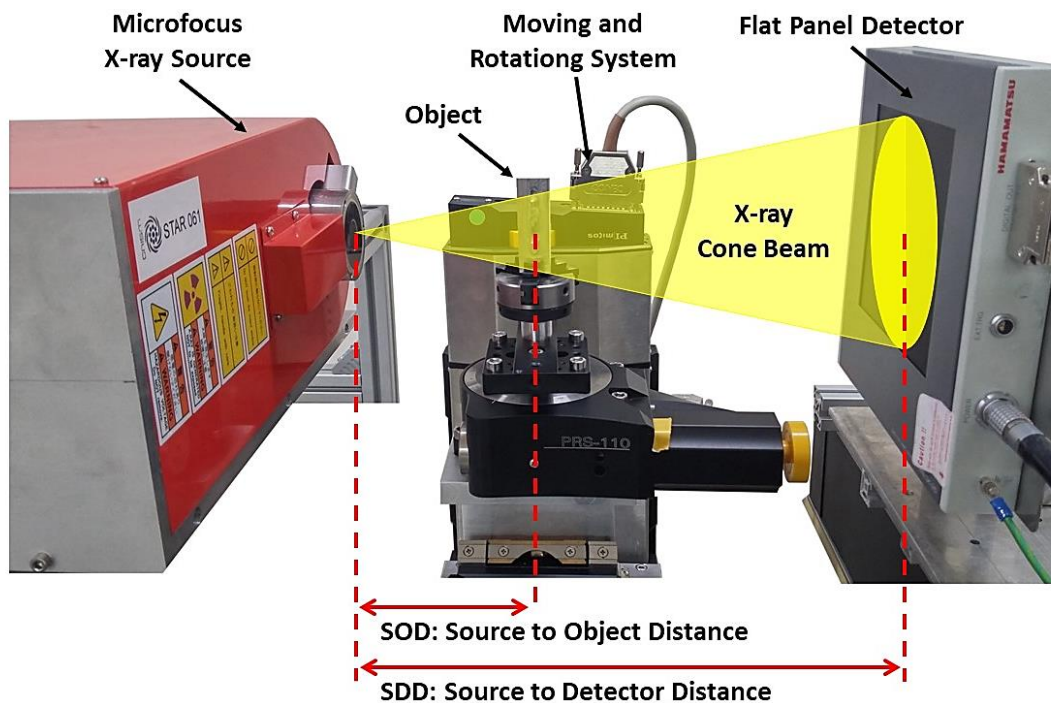


Fig. 3.3 μ Tomo@STAR-Lab. - University of Calabria.

This setup has been commissioned by Synchrotron Elettra of Trieste (Italy) and assembled in STAR-Lab. at the University of Calabria.

3.2 X-RAY SOURCE



Fig. 3.4 Microfocus X-ray source Hamamatsu L12161-07 & the external control unit.

The X-ray source is the Microfocus L12161-07 by Hamamatsu Fig. 3.4, a polychromatic source that can work at three focal spot size: $7\mu\text{m}$ (Small Focus Mode), $20\mu\text{m}$ (Middle Focus Mode), and $50\mu\text{m}$ (Large Focus Mode); the operating voltage of the tube can vary in a range between 40 and 150kV, the operating current of the tube can vary between $10\mu\text{A}$ and $500\mu\text{A}$, with a maximum output power that depends on the selected focus mode (Small, Middle, Large) which is respectively 10, 30 and 75W. If the power is 4W, it is possible to have a nominal focal spot size of $5\mu\text{m}$. The geometry of the X-ray beam is conical having an opening angle of about 43 degrees. The target anode is made of tungsten, while the exit window is a 200nm thick beryllium sheet. The main characteristics of the Microfocus X-ray source L12161-07 are shown in Tab. 3.1.

Tab. 3.1 Microfocus Hamamatsu L12161-07 characteristics

| | Parameter | Value | Unit |
|--|---------------------|----------------------------|---------------|
| X-ray tube voltage setting range | | 0 to 150 | kV |
| X-ray tube current setting range | | 0 to 500 | μA |
| X-ray tube voltage operational range | | 40 to 150 | kV |
| X-ray tube current operational range | | 10 to 500 | μA |
| Maximum output | - Small Focus Mode | 10 | W |
| | - Middle Focus Mode | 30 | W |
| | - Large Focus Mode | 75 | W |
| X-ray focal spot size (Nominal value) | - Small Focus Mode | 7 (5 μm at 4 W) | μm |
| | - Middle Focus Mode | 20 | μm |
| | - Large Focus Mode | 50 | μm |
| X-ray beam angle | | Approx. 43 | degree |
| Focus to object distance (FOD) | | Approx. 17 | mm |

From the characteristic curve shown in Fig. 3.5 it is possible to determine the maximum value of the tube current, once the tube voltage and the focal spot size have been set.

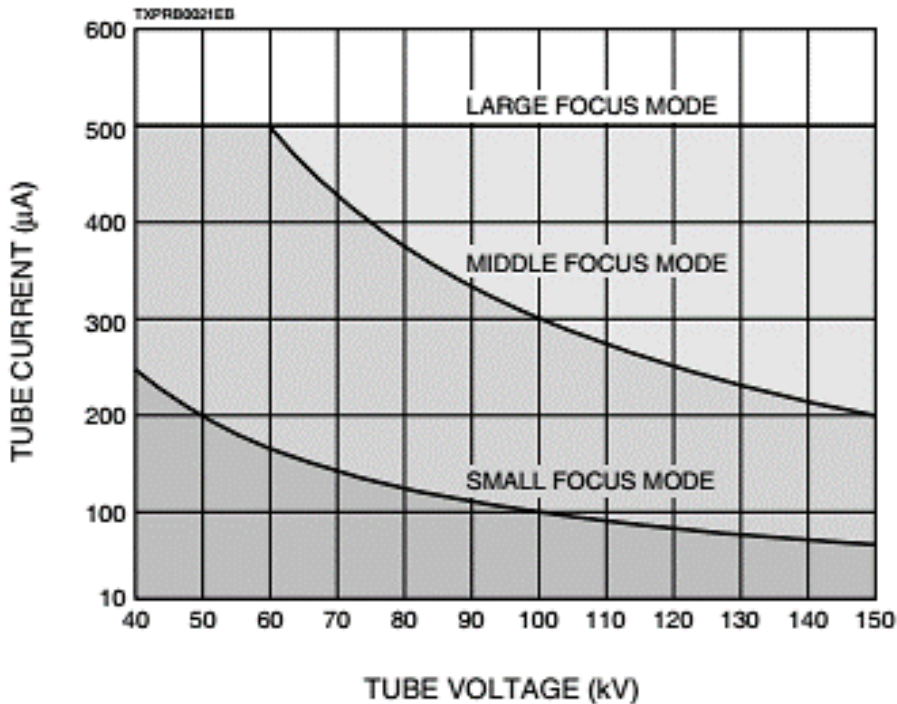
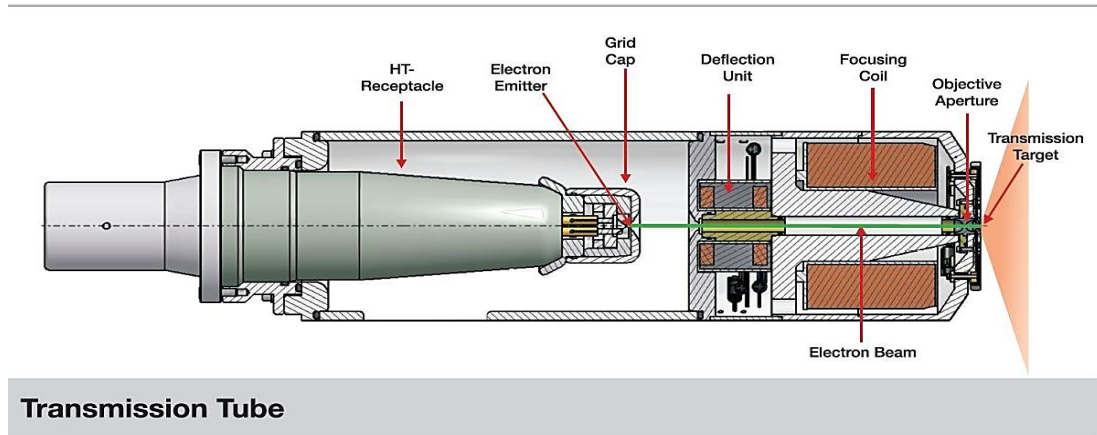


Fig. 3.5 The Graph shows the working curves of the microfocus X-ray source Hamamatsu L12161-07.

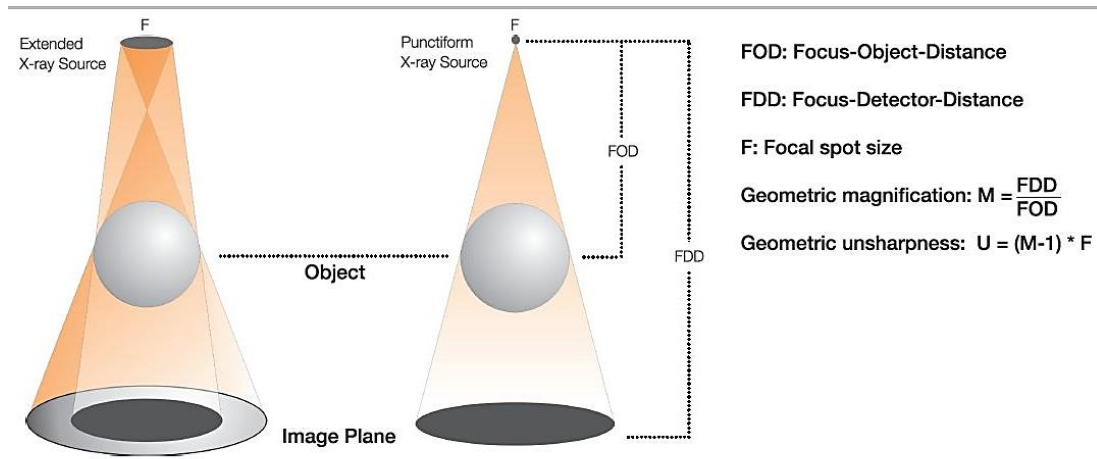
The head of an X-ray transmission tube contains a slide-like "target", which is covered with a very thin layer of tungsten. This layer has a thickness of 1-10 microns, depending on the application of the X-ray tube. For special tasks different materials can be used for this layer. The transmission target is hit by a focused electron beam in the so-called focal spot.



Transmission Tube

Fig. 3.6 Cross section of microfocus transmission x-ray tube

The size of this focal spot defines the sharpness of the resulting X-ray image. The bigger the focal spot the higher the geometric unsharpness. See Fig. 3.7 For high resolution X-ray analysis, a small focal spot is required.



FOD: Focus-Object-Distance
 FDD: Focus-Detector-Distance
 F: Focal spot size
 Geometric magnification: $M = \frac{FDD}{FOD}$
 Geometric unsharpness: $U = (M-1) * F$

Magnification and Unsharpness

Fig. 3.7 Geometric properties for a microfocus X-ray source.

- Geometric magnification (M) is required to visualize very small details. It is defined by the ratio of focus-to-detector distance (FDD) and focus-to-object distance (FOD).
- Geometric unsharpness (U) is introduced by the X-ray focal spot. A bigger focal spot size (F) leads to higher unsharpness by generating a wider half shadow (penumbra) of the object.

In X-ray microfocus source, electrons are accelerated in a vacuum tube by an electric field towards a metal target called anode. X-rays are emitted as the electrons slow down (decelerate) in the metal. The output spectrum consists of a continuous spectrum of X-rays, with additional sharp peaks at certain energies. The continuous spectrum is due to bremsstrahlung, while the sharp peaks are characteristic X-rays associated with the atoms in the target. For this reason, the X-rays spectrum is polychromatic, see Fig. 3.8

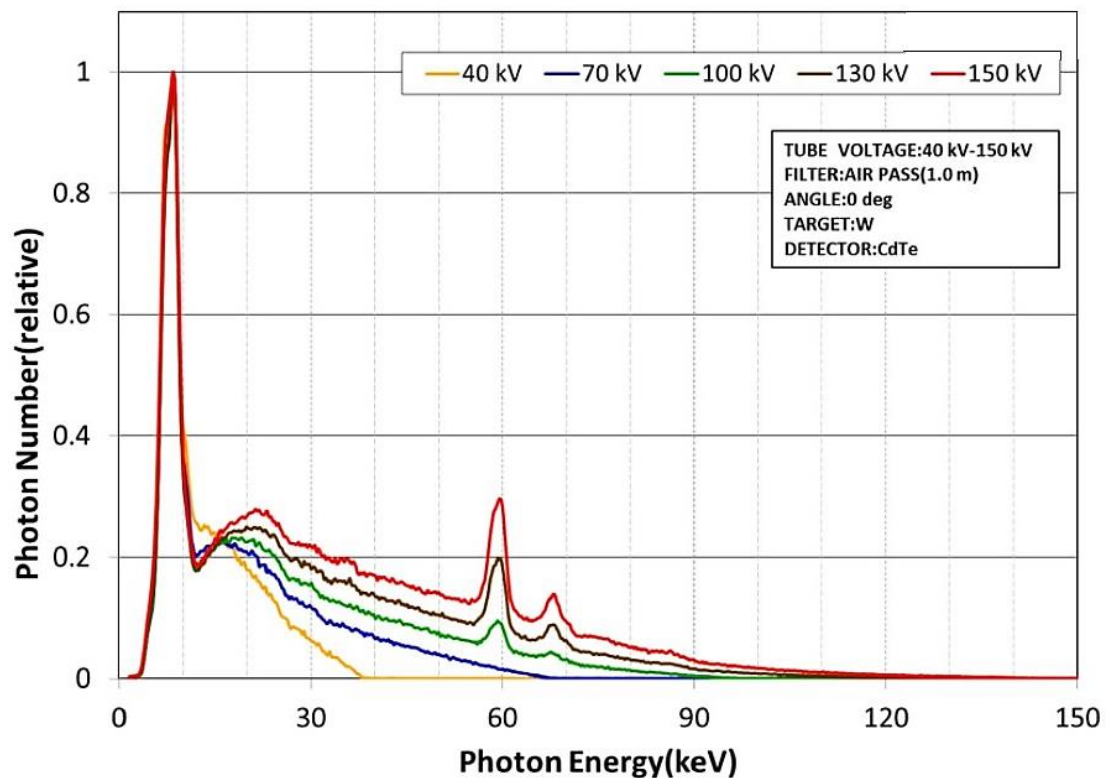


Fig. 3.8 Fig. Spectra generated by microfocus x-ray sources Hamamatsu L12161-07 at different acceleration potentials and plotted for a range of voltages between 1 and 150 kV. The photon counts were normalized to 1 (relative).

3.3 X-RAY DETECTOR

The detector is a Flat panel sensor C7942SK-05 from Hamamatsu. These detectors are based on two-dimensional arrays of photodiodes CMOS (CCD) directly coupled to a scintillator for X-ray to light conversion. Its main features are shown in the Tab. 3.2.

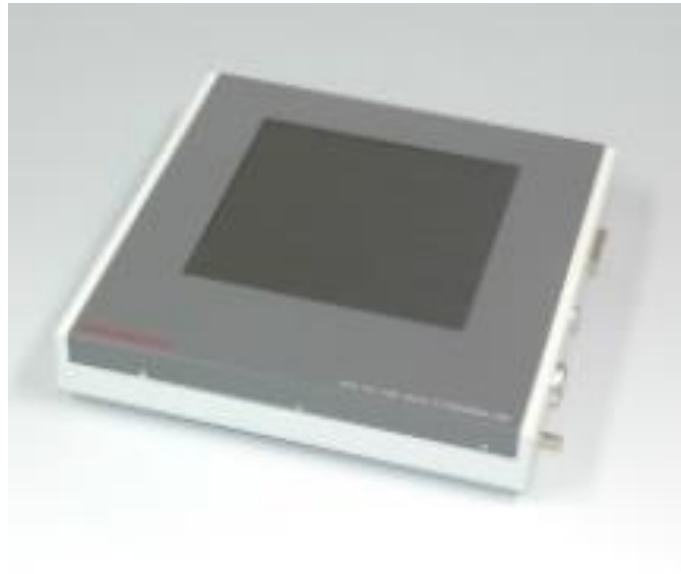


Fig. 3.9 Detector Hamamatsu C7942SK-05

The sensor is composed of a scintillator layer of Gadolinium oxysulfide (Gd_2O_2S), also called gadolinium sulfoxylate (GOS or Gadox) which is an inorganic, ceramic compound. The detector has 2316×2316 active pixels, with a pixel size of $50 \times 50 \mu m$ and the photodiode area is $120 \times 120 mm$. The acquired signal is digitalized and sent to an acquisition card (Frame Grabber). The frame rate allows to fix the signal acquisition frequency, therefore the exposure period, in a range between 0.2 and 9 fps (frames per second). The software for image acquisition control then allows you to select the number of radiographic images or projections.

Tab. 3.2: Detector features

| Parameter | Specification | Unit |
|------------------------|---------------|---------|
| Pixel size | 50×50 | μm |
| Photodiode active area | 115×115 | mm |
| Number of active pixel | 2316×2316 | pixels |
| Energy range | 150 | kVp Max |
| High quality image | 5.4 | Mpixels |
| Digital output | 12bit | |
| Scintillator | GOS | |

3.4 POSITIONING SYSTEM

The sample positioning system (by PI miCos Physik Instrumente) provides five degrees of freedom (x , y , ϕ , θ and ω). Two linear movements for x,y , one for the rotation stage omega (ω), two stages for tilt angles theta (θ) and phi (ϕ).

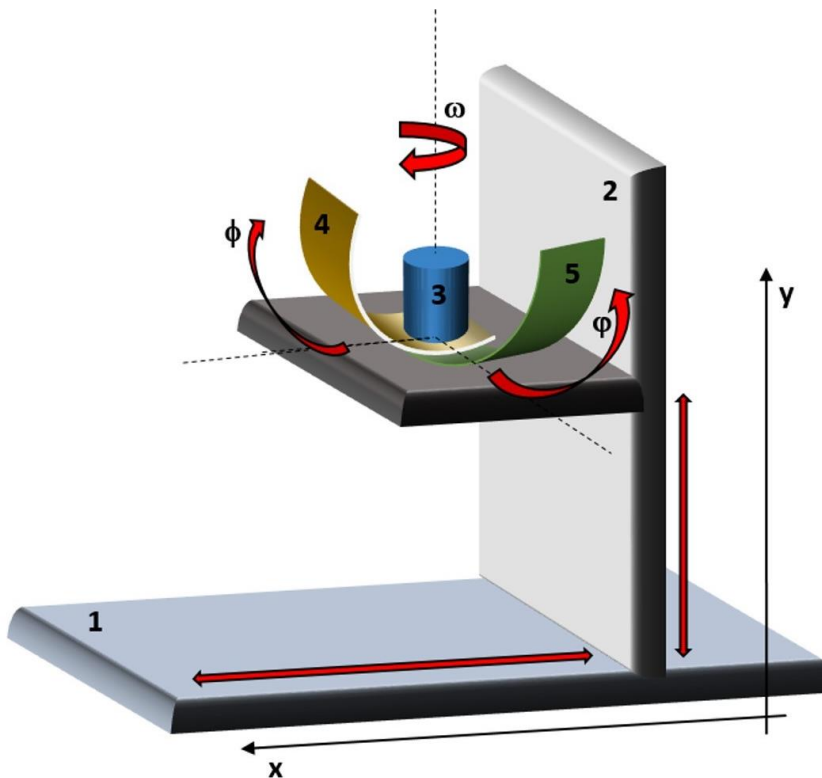


Fig. 3.10 Skecth of Sample positioning: y sample holder structure: X -translator (1), Y -translator (2), ω -rotator (3), θ -goniometer (4) and ϕ -goniometer.

Fig. 3.11 shows the mechanical assembly of the positioning system of the μ Tomo station at STAR-Lab. Types of stepper motor positioners:

1. LS-270 Linear Stage for Very High Loads, corresponds to the x-axis.
2. LS-180 Linear Stage for Heavy Loads, corresponds to the y-axis.
3. RS-110 Precision Rotation Stage, corresponds to the ω rotation angle.
4. WT-90 Goniometer, corresponds to the ϕ angle.
5. WT-90 Goniometer, corresponds to the θ angle.

This equipment can work in open loop, excellent holding torque and low speeds, low maintenance (brushless), very rugged in any environment, excellent for precise positioning control and no tuning required. The Tab.3.3 shows the characteristics of the stepper motor positioners used in μ Tomo station.

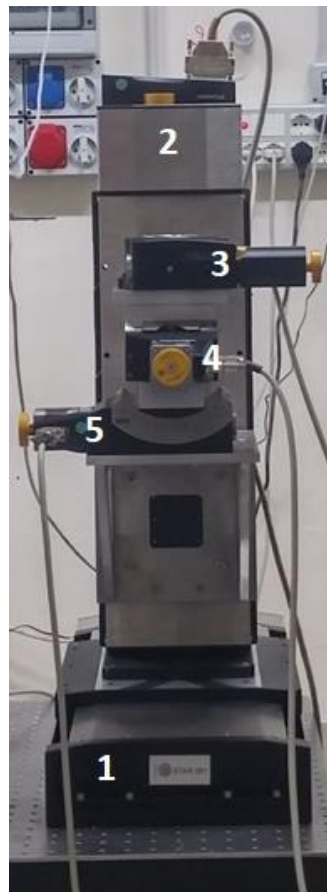


Fig. 3.11 μ tomo@STAR-Lab. Sample positioning system.

This system allows to position the sample with the required precision. In particular, the Source to Object Distance (SOD) and Source to Detector Distance (SDD) determine the system geometric parameters such as magnification ratio ($M=SOD/SDD$). The μ Tomo station is provided with a user interface that allows to control it using a computer. All the electronic hardware components are commercially available and are, in general, provided with software drivers which are LabVIEW compatible.

Tab. 3.3: Stepper Motors: Features Main (by PI miCos Physik Instrumente)

| Specifications | PI-Micos Model | | | | |
|---|--------------------|---------------------|-----------|-----------|----------|
| | LS-270 | LS-180 | WT-90 | WT-90 | PRS-110 |
| Load Capacity (Kg) | 150 | 100 | 8 | 8 | 10 |
| Load Capacity (N) | 1500 (Fz) | 200 (Fy) | 80 (Fz) | 80 (Fz) | 100 (Fz) |
| Travel range | 205 mm | 155 mm | 90° (max) | 90° (max) | >360° |
| Bi-direc. Repeatability (down to) | 0.05 μ m | 0.05 μ m | 0.001° | 0.001° | 0.0002° |
| Maximun speed (mm/s) | 150 | 200 | 15 | 15 | 200 |
| Type limit switch | Inductive (pnp) NC | mechanical (pnp) NC | npn* | npn* | npn* |
| Location on μTomo Station | X-axis | Y-axis | Phi | Tetha | Omega |

Hardware components are provided with LabVIEW compatible software drivers.

3.5 SOFTWARE DEVELOPMENT

The μ Tomo software was developed using LabVIEW to control the hardware by means of a graphical user interface (GUI). LabVIEW is a graphical programming language. It has a powerful function library and an easy-to-use multithreaded programming and graphic user interface (GUI) design. The availability of drivers, debugging, and other features make it an ideal software for instrument-oriented programming.

The developed software is flexible allowing easy changes or additions to the hardware. The RS232 serial interface is the communication standard for most of the used laboratory equipment (Microfocus X-ray source and motors).

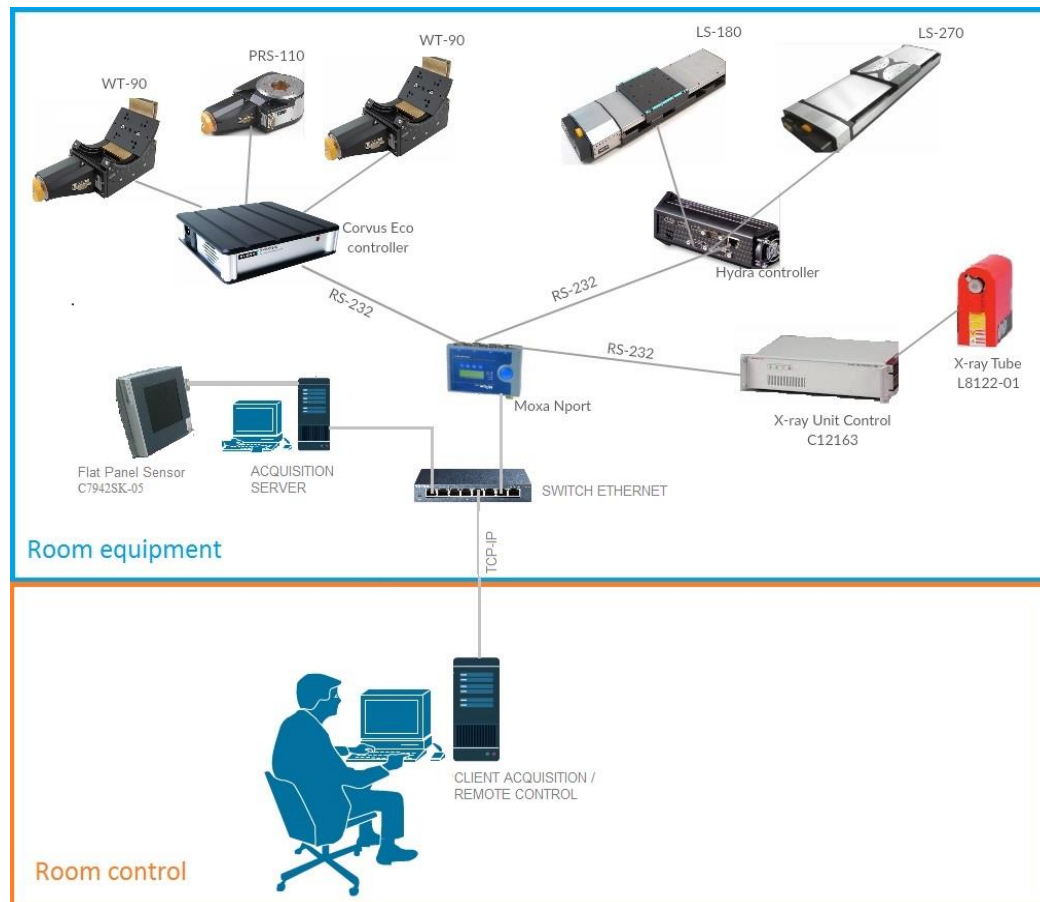


Fig. 3.12 Connection diagram for the remote control of the μ Tomo station.

3.5.1 The Main Program For Measurement

The main program was created using the 2016 version of LabVIEW. An installer is also created to be executed in computers without LabVIEW already installed or with older version of the same program. The software can be used on both 32 bits or 64 bits Windows environment. Figure 3.14 shows the front panel of the Main Program while Figure 3.15 depicts part of the Block Diagram. The front panel has a menu divided into four parts: 'Phi/Theta', 'X-Y-Rotator', 'Acquisition' and 'File Parameters' for the complete control of the μ Tomo apparatus.

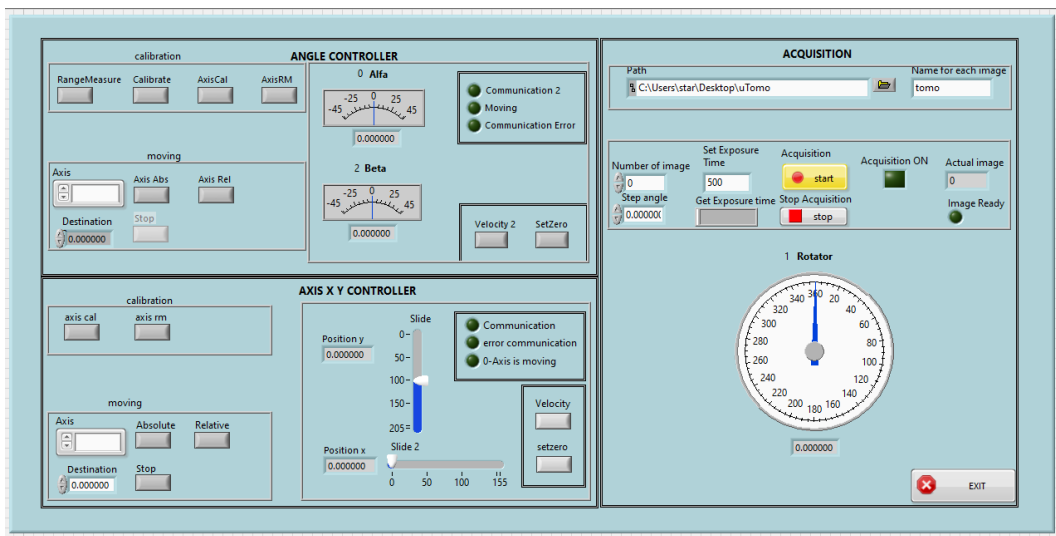


Fig. 3.13 Front Panel panel of the Main Program

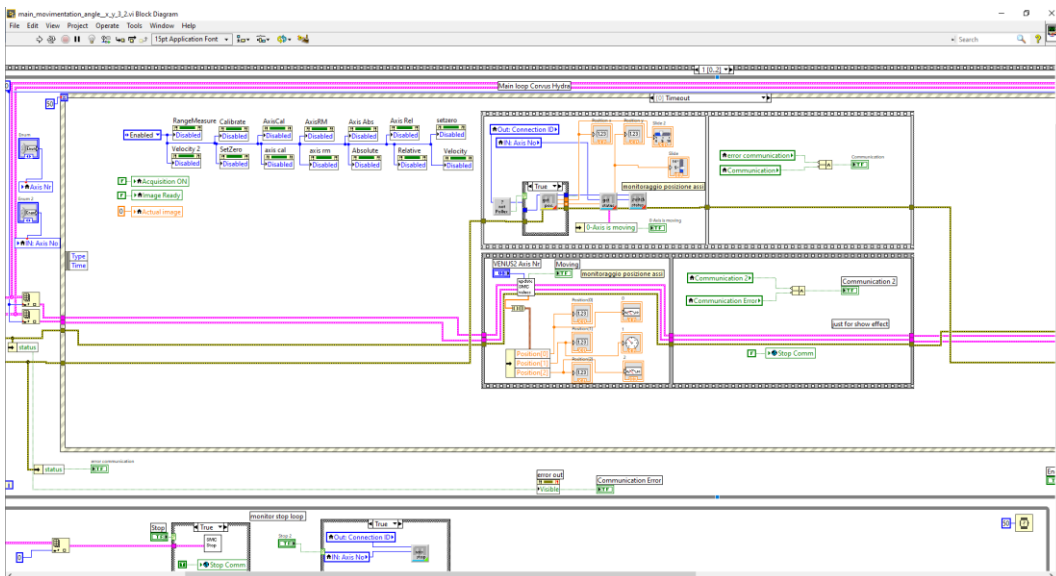


Fig. 3.14 Block Diagram

3.5.2 Control Motors

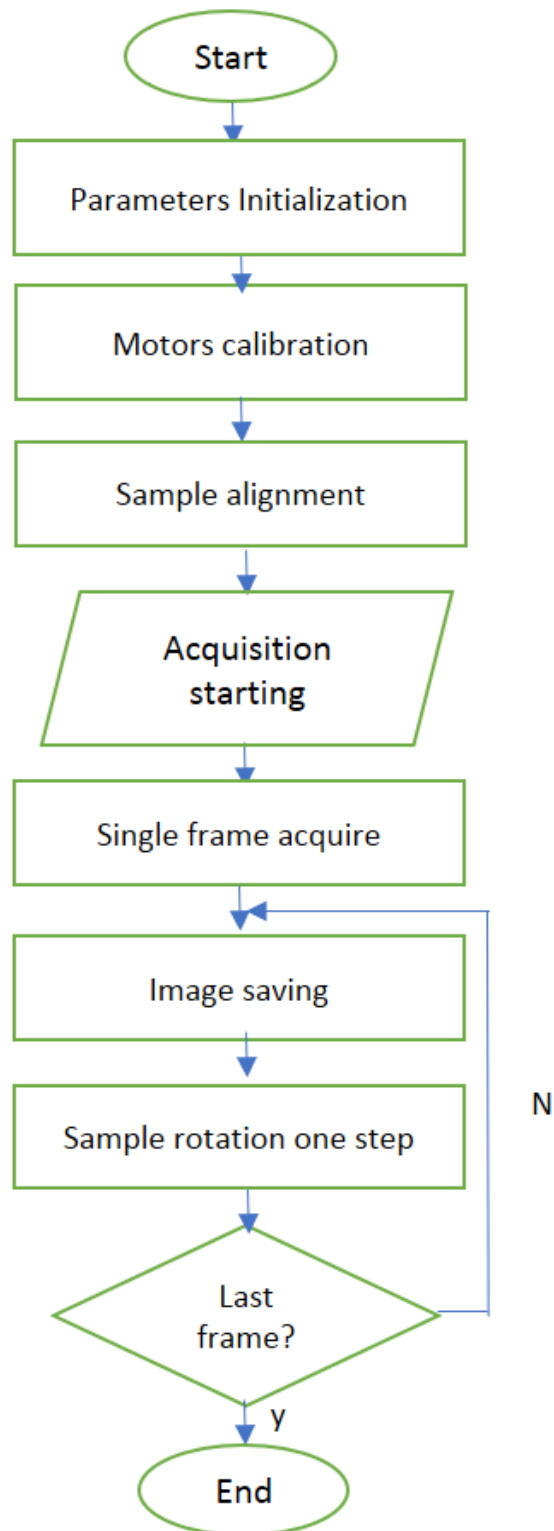
The programming of the motor control was carried out taking as reference the virtual instruments (vi) of the national instrument supplied with the Mechanische Instrument Optische System (PI Micos).

The menu depicted in Fig. 3.15 and Fig. 3.16 is relative to the Corvus controller (control of the stepper motor relative to the axis rotator: PRS-110,) and of the Hydra controller (control of the stepper motor relative to the Y-axis - LS-270 - and X-axis - LS-180).

The front panel is divided into two parts, the upper part refers to X-axis and Y-axis while the lower part is relative to the rotator. The programming is based on the virtual instruments (vi) program of LabView and allow to set the absolute and relative movements for the X-axis and Y-axis in the microtomography system by means of Ethernet and/or RS-232 communication. The characteristics of this menu are:

- Position: present position, returned from the controller for each axis.
- Relative movement: negative or positive direction.
- Absolute movement: the parameter is the target position starting at the present position.
- Stop: Stops motion of the axis
- Initializing of motors for each axis.
- Reset to zero the value of the position
- Initial Calibration: for alignment of sample.

Flow chart for data acquisition in an X-ray tomographic measurement



NOTE:

One of the most important features of the uTomo station is that it can be easily upgraded according to required experimental needs.

The crucial aspect for the commissioning was to understand how to vary the station configurations to optimize the microtomography station. For example, the control software of the uTomo station. In fact, the control software was entirely developed by Lab. staff, so we are able to modify the parameters and the control functions. One of the most important results is that we were able to modify the image acquisition mode, in addition to the standard described above. Now we can acquire at the same angle several images in order to increase the acquisition time of X-ray image without sending the detector in saturation.

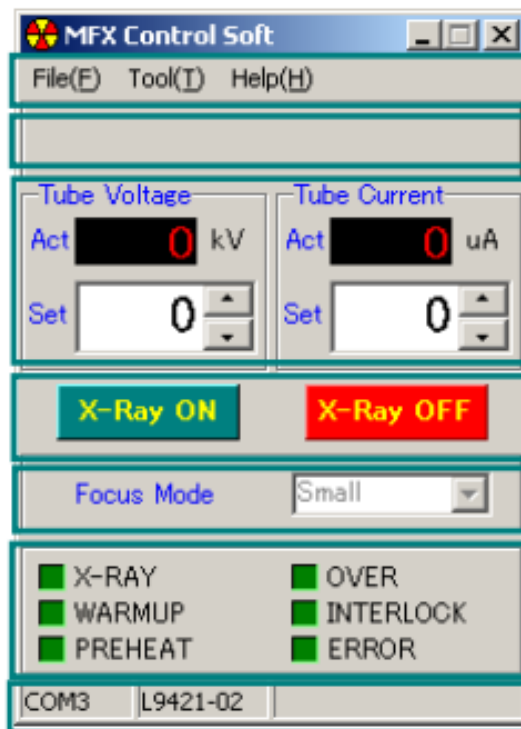


Fig. 3.15 Graphical User Interface (GUI) of the Software for X-ray source control provided by the hamamatsu company

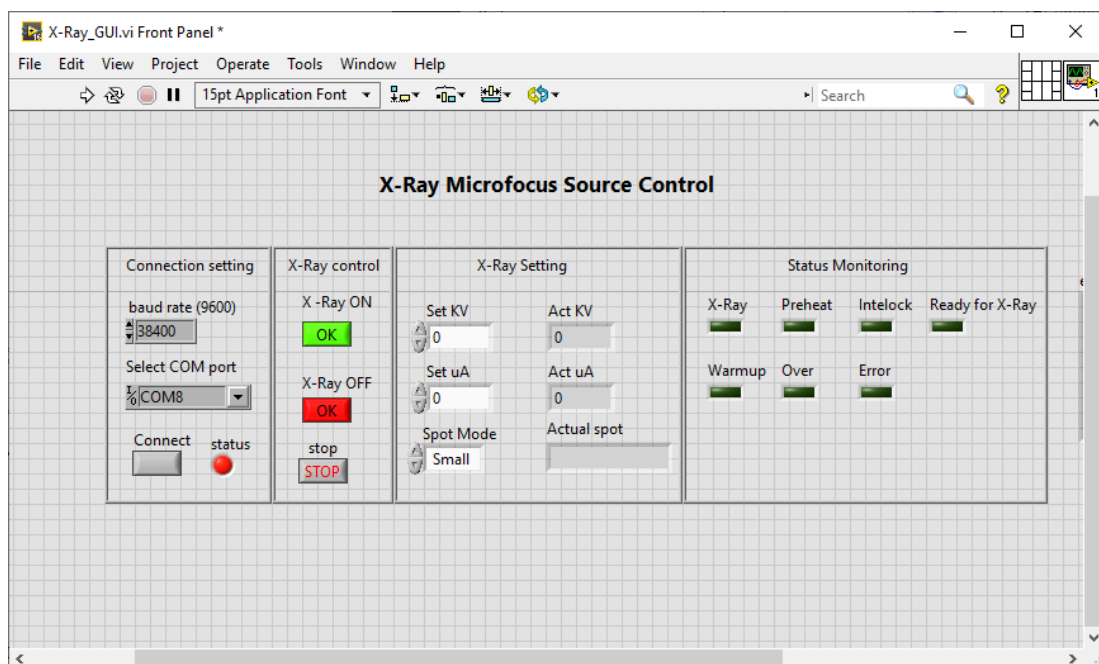


Fig. 3.16 Software for the control of the X-ray source made in the STAR-LAB laboratory.

4 RESULTS and CASE STUDIES

The installation of STAR (Southern Europe Thomson Backscattering Source for Applied Research), the compact hard X-rays source, designed and realized by INFN (Sezione di Milano and Laboratori Nazionali di Frascati, with the collaboration of Gruppo Collegato di Cosenza), for advanced applied research in Materials Science, has started at the “Polo Tecnologico” of the University of Calabria.

This source is the core of the project “MaTeRiA”, prepared jointly by the Consorzio Nazionale Interuniversitario per le Scienze Fisiche della Materia (CNISM) and the University of Calabria, and funded with 15.7 million Euro.

With its quasi-monochromatic and high collimation of X-rays beam in the adjustable energy range 10-200 keV, STAR offers a complementary source with respect to a synchrotron radiation facility, but at lower running costs.

STAR source is designed to be easily upgraded, in terms of energy, polarization, photon flux and divergence of the beam. The possibility to host several dedicated beamlines will make of STAR a reference facility in the national and international panorama of X-rays sources applied to the vast community of Materials Science.

The first beamline that will be installed at the STAR is dedicated to phase-contrast microtomography. Precisely for this purpose, my Ph.D. work was focused on the commissioning of the μ TOMO station for X-ray microtomography.

I was in charge of the project management of the micro-tomography apparatus to obtain, verify and document that the performance of the assembled system meets the objectives and criteria defined in the project specifications.

The set of activities involved the assembly, calibration and testing of the parts, the writing of the acquisition program, and all the functional tests of the complete system. The correct integration of the control systems between the different components was verified: X-ray source, motors, detector.

A detailed documentation was produced, that contains an organic and coordinated collection of all the documentation concerning the system:

the project, the use and maintenance manuals, the procedures to be adopted to keep the system efficient.

Finally, we can summarize by saying that:

- in-depth knowledge of the system made it possible to optimize its performance;
- ease of use is guaranteed thanks to the availability of updated and congruent system manuals;
- management costs are reduced;
- the collection of verification and calibration data was performed to constitute a necessary basis for future recalibration, monitoring and control activities;
- the system meets the project specifications.

The commissioning phase allowed to acquire the skills to be able to independently manage a complex system such as the STAR beamlines that will soon be operational. In practice, it was a training ground to prepare for the management of an even more demanding system. In addition, the uTomo apparatus was also used for hands-on training activities involving students and scientists from different departments of the university of Calabria.

We have developed, for the first time at UNICAL, innovative X-ray analytical tools for noninvasive studies on material science, cultural heritage and biomedical samples.

The commissioning of the μ TOMO station trained us so to acquire the know-how to manage a complex system such as the STAR beamlines that will soon be operational.

This chapter reports the most important results of the research activity carried out during my PhD. The aims achieved can be summarized as follows:

1. state of the art of cone-beam X-ray tomography (CBCT);
2. commissioning of the microtomography apparatus: the assembly of the experimental setup, development of the control software, testing of the various parts of the microtomography station;
3. image acquisition and analysis;
4. microtomographic measurements on samples of various nature: case studies.

The results obtained showed that the X-ray microtomography technique is a valid non-destructive and non-invasive method of investigation to study the internal structure of a sample.

The cases studied in this research work were about 100, of which about 50 experiments with valid results. The experiments performed using the mTOMO station involved different fields of science: engineering, geology, cultural heritage, biology, etc.

In addition to research work, I have been the supervisor of several dissertations. The table below shows the titles of the theses carried out with the students of the physics department of the University of Calabria.

| | A. A. | Students | Bachelor Thesis Title |
|-------------------------|--------------|-----------------------|---|
| Bachelor Degrees | 2016/2017 | Lucia Emanuele | MICROTOMOGRAFIA APPLICATA AI BENI CULTURALI <i>CASO STUDIO: PENDENTI IN BRONZO A COPPIE ANTROPOMORFE</i> |
| | | Sarah Siciliano | MICROTOMOGRAFIA APPLICATA A SISTEMI BIOLOGICI |
| | 2017/2018 | Simone Caputo | MICROTOMOGRAFIA APPLICATA AI BENI CULTURALI |
| | | Francesco Cianciaruso | MICRO-CT A RAGGI X SU CAMPIONI DI ACCIAIO SOTTOPOSTI AL PROCESSO DI “INFRAGILIMENTO INDOTTO DA IDROGENO |

| | | | |
|-----------------------|-----------|-----------------------|---|
| | | Filippo Dodero | STUDIO DI OSSIDIANE MEDIANTE MICROTOMOGRFIA A RAGGI X |
| | | Martina Lamacchia | MICROTOMOGRFIA A RAGGI X SU CAMPIONI DI PIETRA LECCESE TRATTATA CON TIO ₂ |
| | 2018/2019 | Michele Emanuele Lio | STUDIO DEI PARAMETRI FONDAMENTALI E DELLA QUALITÀ DELLE IMMAGINI IN MICROTOMOGRFIA AI RAGGI X |
| | | Simone Bartucci | MONETE ROMANE E GRECHE SUBERATE: UNO STUDIO ARCHEOMETRICO |
| | | Edoardo De Rose | STUDIO DEL BIOACCUMULO DI PIOMBO IN DANIO RERIO MEDIANTE MICROTOMOGRFIA A RAGGI-X |
| Master Degrees | 2016/2017 | Matteo donato | MICROTOMOGRFIA APPLICATA AI BENI CULTURALI |
| | | Erica Fuoco | MISURE MICROTOMOGRFICHE SU MOSFETS BOMBARDATI DA NEUTRONI |
| | 2017/2018 | Maria Caterina Crocco | MISURA DELLA DOSE ASSORBITA IN ESPERIMENTI DI MICROTOMOGRFIA |
| | | Amedeo Rotundo | MICROTOMOGRFIA A CONTRASTO DI FASE |
| | 2018/2019 | Alessio Bruno | MICROTOMOGRFIA APPLICATA A REPERTI DEL MUSEO DEI BRETTII E DEGLI ENOTRI |

It is important to emphasise that this work has been possible thanks to a network of scientific collaborations with other research groups. They allowed to build a multidisciplinary interest around the microtomography laboratory “ μ TOMO@STAR-LAB.”.

The case studies reported in this thesis were selected based on importance and whether they are the subject of publications in international journals, proceedings and congress highlights.

REPORT OF RESULTS:

1. Experimental study on mechanical properties of Basalt FRCM using various matrices and validation by X-Ray micro tomography.

Summary: The idea of alternative substitution to common composite materials (FRP) with sustainable composite materials is rapidly developing. The sustainable composite materials, indicated with the acronym NFRCM (Natural Fibers Reinforced Cementitious Matrix), are eco-friendly both in the reinforcing fibers that in the matrix, until today do not exist technical standards which set out their design rules or composition. For the purpose of this work, a type of natural fibers made with basalt was examined. From the obtained results, the performance of used matrices was classified and analysed in terms of compression strength, bending strength and tensile strength.

An x-ray microtomography has been carried out in order to analyse the adhesion status between the cementitious matrix and the basalt fibers. The X-ray microtomography imaging have used to obtain a non-destructive 2D and 3D characterization of the specimens and to detect cracks and voids. The 3D map permitted to identify the precise position of the voids and damage in the volume as well as to determine the components distribution in the sampled volume.

Status: Submitted at the “**Arabian Journal for Science and Engineering**” in data nov-21-2020. Manuscript number: AJSE-D-20-06304. Under Review.

2. Analysis of extruded pins manufactured by friction stir forming for multi-material joining purposes.

Summary: Nowadays the application of multi-material parts has become a standard in several sectors, such as in transportation where the use of dissimilar material contributes to reduce the weight of structural components.

To this aim and to propose an alternative joining technique, which does not require the use of additional external parts, the authors investigated a method based on the Friction Stir Forming (FSF) technology. FSF is a process, where a rotating tool moves on a metal sheet pushing the material through the holes of a forming die positioned under the worked sheet.

In the current study, the authors aimed at improving the quality of the aluminium extruded pins, which leads to the improvement of the connection with composite materials. A deep analysis has been carried out on the extruded aluminium pins in terms of internal structure. Specifically, an X-ray micro-tomographic analysis has been performed to investigate, qualitatively and quantitatively, the distribution of the material within the manufactured pins. The void content and the final height of the pins have been measured aiming at understanding how these outputs can be affected by the investigated parameters.

Status: Published Online: 02 July 2019: AIP Conference Proceedings 2113, 050026 (2019); <https://doi.org/10.1063/1.5112590>

3. Non-destructive Measurements of Single Events Induced on Power MOSFET's by Terrestrial Neutrons.

Summary: X-ray microtomography has been employed for non-destructive measurements on Power MOSFET's with the aim to investigate the damage due to "Single Events Effects (SEEs)" induced by high energy neutrons in accelerated tests. The technique allowed to investigate the spatial structure of damages induced by neutrons.

Status: Manuscript in preparation

4. Studying the microvesiculation of the obsidians of Sierra de las Navajas (State of Hidalgo, Mexico).

Summary: Sierra de las Navajas obsidian was highly exploited by the pre-colonial Mesoamerican people and highly requested for its very good quality and its characteristic green colour. The surface of these obsidian is sometimes characterized by the occurrence of a diffuse microvesiculation. In order to investigate the 2-D and 3-D distribution of vesicles and to relate it to the macroscopic aspect and to the physical properties of obsidian, we have selected three samples showing different colour, roughness, hue and fracture. We have observed their surface by electron microscopy and we have investigated small volumes of the same specimen by X-rays microtomography. The results have shown that the hue sometimes shown by obsidian is strictly related with the occurrence of abundant, elongated and iso-oriented vesicles. The occurrence of course (hundreds of microns) vesicles also give to the surface a high roughness. Finally, the shape of the vesicles controls the type of fracture (conchoidal or flat).

Status: Manuscript accepted. The proceedings will be published in the series of the Hungarian National Museum INVENTARIA PRAEHISTORICA HUNGARIAE (IPH XIV): ISSN 0865-0381

5. Architectural terracruda sculpture of Silk Roads: new conservative insights through a diagnostic approach based on non-destructive X-ray micro-tomography.

Summary: This work presents the results of the study of a fragment of architectural terracruda sculpture from the Buddhist archaeological site of Tepe Narenj (Kabul, Afghanistan, 5th-9th centuries) through X-ray micro-tomographic analysis. The results have provided useful data for the understanding of the sculpturing methodology, and which appears to be crucial for proposing suitable conservation intervention.

Status: Published on “Studies in Conservation” journal. Received 10 Oct 2020, Accepted 06 Dec 2020, Published online: 17 Jan 2021
<https://doi.org/10.1080/00393630.2020.1862605>

4.1 CASE STUDY 1: Experimental study on mechanical properties of Basalt FRCM using various matrices and validation by X-Ray micro tomography.

Experimental study on mechanical properties of Basalt FRCM using various matrices and validation by X-Ray micro tomography.

Olivito Renato S.¹, Scuro Carmelo², Codispoti Rosamaria¹, Filosa Raffaele², Crocco Maria Caterina², Formoso Vincenzo^{2,3}

¹*Dept. of Civil Engineering - University of Calabria, 87036 Rende – CS, Italy*

²*Dept. of Physics - University of Calabria, 87036 Rende – CS, Italy*

³*CNR-Nanotec, UoS di Cosenza, Dipartimento di Fisica, Universita della Calabria, Arcavacata di Rende (CS), 87036, Italy*

Abstract

The idea of alternative substitution to common composite materials (FRP) with sustainable composite materials is rapidly developing. The CO₂ emissions during the construction phase of a building, but also during the use of them, are equal to approximately 40% of all the CO₂ emissions; 15% of which are related to the energy consumption during the production of construction materials. However, the sustainable composite materials, indicated with the acronym NFRCM (Natural Fibers Reinforced Cementitious Matrix), are eco-friendly both in the reinforcing fibers that in the matrix, and to date do not exist technical standards which set out their design rules or composition. To analyse the mechanical behaviour of NFRCM, standards regarding FRP or common FRCM (Fibers Reinforced Cementitious Matrix) materials are taken into account. It is however necessary to make changes regarding the production stages of NFRCM materials respect to the common composite materials. For the purpose of this work, a type of natural fibers made with basalt was examined. Furthermore, various matrices with different composition and mechanical properties were considered during the manufacturing of composite materials in the laboratory. Specifically, two organic and one inorganic matrices were investigated. In the phase before preparation of NFRCM specimens, as the fabrics, also the matrices have been analysed from experimental point of view carrying out

compressive tests and three points bending tests. From the obtained results, the performance of used matrices was classified and analysed in terms of compression strength, bending strength and tensile strength.

An x-ray microtomography has been carried out in order to analyse the adhesion status between the cementitious matrix and the basalt fibers. The X-ray microtomography imaging has been used to obtain a non-destructive 2D and 3D characterization of the specimens and to detect cracks and voids. A complete set of 2D projections is acquired and a 3D map of the X-ray absorption in the volume is mathematically reconstructed. The 3D map permitted to identify the precise position of the voids and damage in the volume as well as to determine the components distribution in the sampled volume.

Keywords: Natural FRCM, Basalt FRCM, Structural strengthening, X-Ray micro tomography

1. Introduction

Structural materials can be divided, according to their characteristics, into four categories: metals, polymers, ceramic and composite materials. The latter differs in that it is the combination of the first three. A composite is a system consisting of two or more elements having better mechanical behaviour than the constituent materials that act independently. Contrary to alloys, each material maintains its separate chemical, physical and mechanical properties, so that it is possible to identify, within the system, a reinforcement and a matrix. In general, the reinforcement represents the discontinuous phase and is characterized by high axial stiffness and strength, while the matrix constitutes the less stiffness and weaker continuous phase; therefore, the former has the task of responding to the stresses transferred to it from the reinforced support, the second evenly distributes the stresses from the structure to the reinforcement [1], [2].

In the field of structural rehabilitation, the use of composite materials has long been consolidated thanks to their rapid evolution due to the advantages provided. Among them it is of interest to mention the high strength and stiffness, combined with a low density, which allows a reduction of the weight

in the finished part. Furthermore, the increase in the offer has led to a considerable decrease in costs, guaranteeing the availability of various solutions of composite systems: there are numerous types of fibers [3], which are distinguished by their shape, material and strength, while there are two matrix families, that is, polymer-based or hydraulic-based matrices [4], [5], [6]. Therefore, two main categories of composite materials for structural reinforcement are identified in:

- FRP (Fiber Reinforced Polymers), characterized by a polymeric matrix, usually composed of epoxy resin, in which the reinforcement is made of long carbon, glass, aramid fibers chosen according to the different project needs;

- FRG (Fiber Reinforced Grout), characterized by a hydraulic matrix, that is cement or lime mortar, in which various types of fibers are incorporated. [7]

The latter group includes FRCM (Fiber Reinforced Cementitious Matrix) systems, that is, composites made with a cement matrix to which are added, improperly, those with lime mortar [8].

To fully understand the field of application of composite materials it is necessary to take into consideration the various causes that make the reinforcement of a structure indispensable; among the most common are:

- damage due to an exceptional load, such as earthquake, explosion, impact, etc.;
- increase in permanent or accidental loads, due to regulatory adaptation or change of use of the structure;
- seismic improvement;
- degradation of materials, in particular corrosion of reinforcement in structural elements of reinforced concrete;
- design or execution errors, such as the incorrect arrangement of the reinforcement or the poor quality of the conglomerate in reinforced concrete structures. [9]

The diffusion within the restoration of the masonry structures of the FRCM is mainly due to the compatibility between support and matrices. It was less in the case of FRPs because epoxy resins could hardly meet continuity conditions with masonry structures of different types. The present study

will deal specifically with the reinforcement of masonry structures with FRCC, with particular attention to the different matrices (Organic and Inorganic) and to the study of the adhesion in the interface between them and the basalt fiber used. A further check will be provided by the realization of an x-ray tomography conducted on the tensile tested specimens in order to verify the adhesion bond between the fibers and the matrix

The paper is organized as it follows. In Section 2, information about the FRCC and the differences between the old and new Italian technical standards are provided. In Section 3 and 4, the experimental test carried out and the results obtained are presented. In Section 5, the x-ray micro tomography carried out in order to analyse the adhesion status between the cementitious matrix and the basalt fibers are exposed. Finally, in Section 5 the conclusions are drawn.

2. Properties of FRCC

The reinforcement systems made with FRCC materials are composed of an inorganic and organic matrix based on lime or cement and fibers in mesh format. Because of their mechanical properties, FRCC reinforcements are specifically indicated in applications where modest deformations are required, as typically happens for the reinforcement of masonry structures.

The mechanical behaviour of a FRCC reinforcement system depends both on the nature of the fibers used and, on the mortar, employed to make the matrix (Organic or Inorganic). The overall behaviour is influenced by the shrinkage and cracking phenomena of the cement matrix and by the phenomenon of relative sliding between the matrix and reinforcing mesh. In this regard, the study conducted by different researchers [10], [11], in which the problem of the breaking of fiber-reinforced composites based on the cementitious matrix was made, in particular, in order to evaluate the failure mode within the composite, direct tensile tests were performed under displacement control in a monotonic manner, on prismatic samples having a thickness of 10 mm and a width equal to a whole multiple of the distance between the fiber bundles. The typical stress-strain constitutive law of a

FRCM system in a monoaxial tensile test is similar to a polyline consisting of three consecutive branches as shown in figure 1:

- Step I (un-cracking),
- Step II (crack development),
- Step III (cracking).

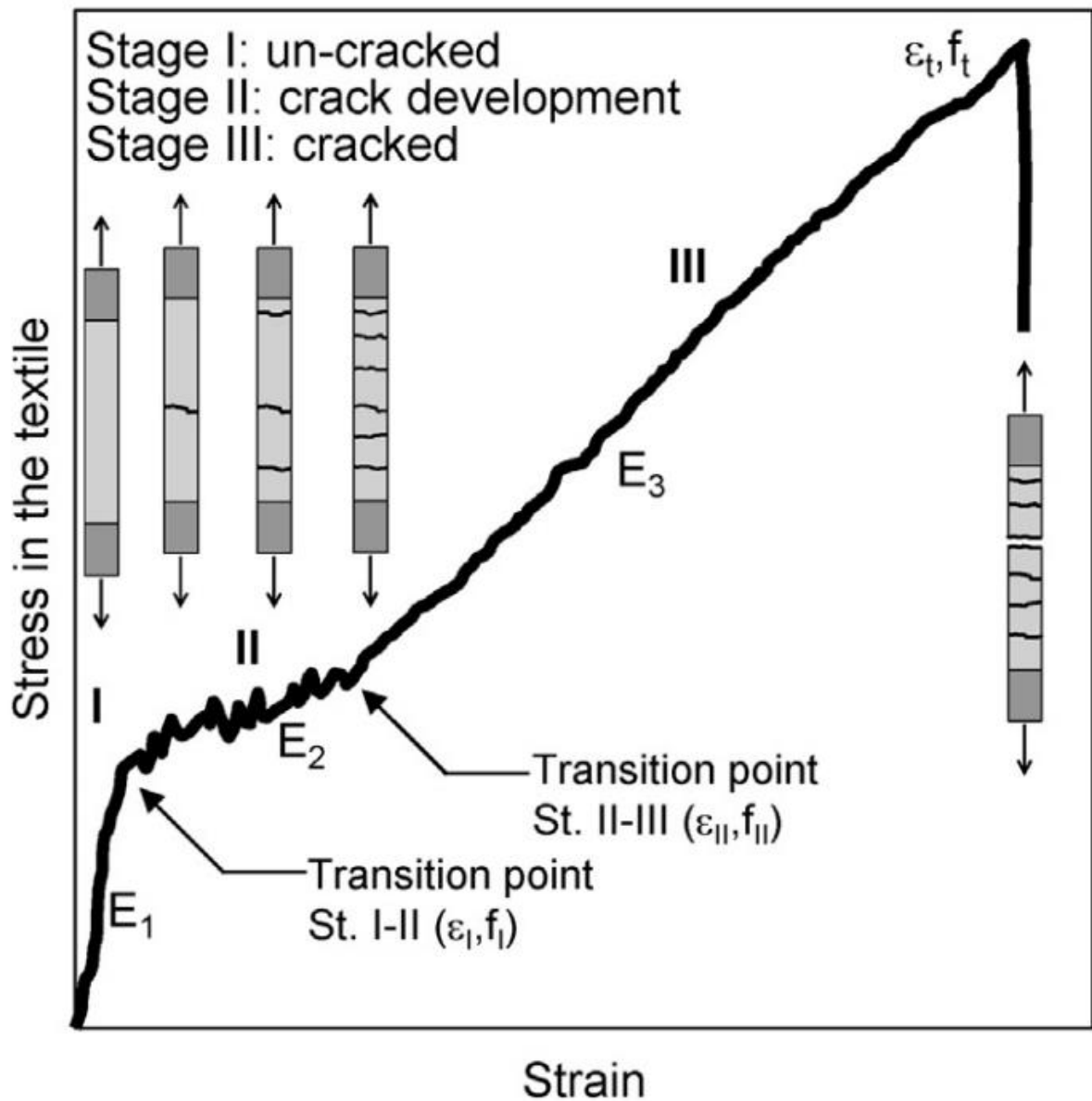


Fig.1 Stress vs Strain constitutive law of FRCM [5].

In stage I the sample is not damaged and the response is linear. The occurrence of the first crack conventionally identifies the transition to stage II, during which a decrease in stiffness can be recognized and the damage develops progressively [12]. The behaviour in the first two stages depends on the mechanical properties of the mortar and the fiber, as well as on the transfer of the stresses from fibers to matrix. These parameters influence the width and distribution of the cracks which can affect the durability of the reinforcement system when the fabric is exposed to external aggressions. When during the test the number of cracks stabilizes, an increase in stiffness normally occurs, which defines the transition to stage III, in which an additional stress imposed causes the enlargement of the existing cracks making the normal modulus of elasticity depend mainly from the fiber mesh used. In this last phase, the matrix, although cracked, can still provide a redistribution of the transverse load. Breakage of the composite generally occurs due to the tensile breakage of the matrix, which occurs in a roving and suddenly spreads to all the fibers [13], [14]. This is due to the fact that the cement matrix is not ideal for impregnating the yarns because the external filaments are in direct contact with the matrix and, theoretically, closely tied, while the internal filaments in the core of the yarn are not in direct contact with the matrix and can slide more easily due to the lower friction between the fibers. The yarn crisis mechanism begins with the breakage of the outer ring of the filament, followed by that of each adjacent layer until it reaches the core filaments. This modality of breakage, called telescopic, is influenced by the penetrability of the matrix, the geometry and structure of the fabric, the presence of a coating and by the friction between the filaments of each thread [15].

2.1 Failure modes of FRCM

The applications of FRCM composites for the consolidation of masonry structures have demonstrated the validity of these materials in the building sector, and a significant improvement in the structural capacity of the elements subjected to reinforcement has been found. However, to maximize its potential, an understanding of the interaction between FRCM and support and the adhesion in the interface that is established between matrix and fabric is essential. From this it is easy

to understand how the problem of adhesion is closely related to the mechanical, physical and chemical properties of the mortar and the fabric that is used for the FRCM system, as well as to the characteristics of the masonry that acts as a substrate.

The type of breakage found for FRCM [5], [16] reinforcements is, in general, very complex to analyse and to numerically model, but it became of primary importance in the analysis and in order to understand the mechanical behaviour. In this regard, adherence tests are introduced, called shear tests [4], [16] necessary for the determination of the breakdown mechanisms in cementitious matrix compo-sites. Both the tests defined as single lap shear tests and the double lap shear tests [13], [15], [17], [18], [19], [20] can be used. In the first case the load is unambiguously identified, but special attention is required in the alignment, to ensure that the stress applied to the reinforcement is of pure shear and prevent the result from undergoing normal external stresses at the substrate-matrix interface. In the case of double lap shear tests, the reinforcement is applied to the two sides of the sample, so that the geometry of the system is symmetrical. However, this does not guarantee that the load distribution on the two surfaces is the same, and the force applied on each side must be carefully evaluated.

The FRCM-support or matrix-fiber mesh delamination was studied in order to identify six failure modes illustrated in Fig. 2 and listed below:

- Delamination with cohesive breakage in the substrate (Figure 2 A);
- Delamination at the reinforcement-substrate interface (Figure 2 B);
- Delamination at the fiber-matrix interface (Figure 2 C);
- Sliding of the fabric inside the reinforcement thickness (Figure 2 D);
- Traction and breakage of the fabric at the extreme not glued (Figure 2 E);
- Traction and breakage in the mortar-based matrix (Figure 2 F).

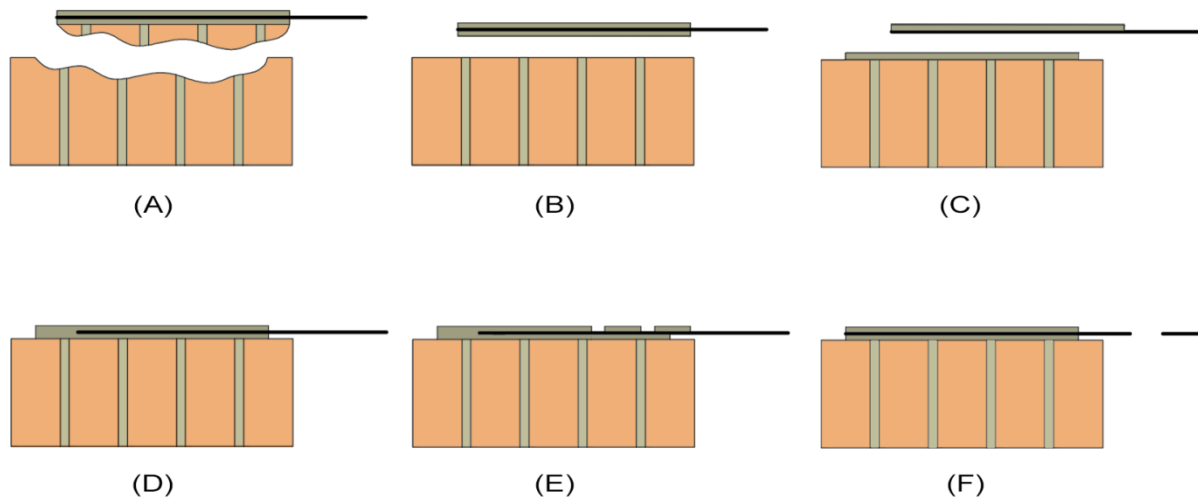


Fig.2 Failure modes of FRCM

The failure mode A occurs, generally, when a matrix with high mechanical characteristics (for example based on cement or geopolymer, with organic additives, etc.) is applied on a weak substrate (for example, tuff bricks), while B is found on relatively smooth surfaces and / or can be associated with inadequate substrate preparation or unfavourable conditions of hardening of the mortar. Delamination at the matrix-fabric interface (C) is governed by the adhesion between the matrix and the reinforcement, which occurs through the penetration of the mortar into the voids of the mesh, so this failure is often exhibited by FRCM systems that include fabrics with a reduced centre distance between the yarns. The first three failure modes (ie A, B and C) generate on a force-displacement (Slip) diagram a curve characterized by an almost flat branch, followed by a fragile break (Fig. 3 (a)). The breaking mode D occurs when dry (not impregnated) bundles of fibers are used, characterized by a relatively weak adhesion with the matrix and, in general, the force-displacement curve presents a decrease in load with softening section due to the progressive loss of friction of the fiber, which flows inside the mortar (Fig. 3 (b)). Finally, FRCM systems made with fabrics having low resistance and small equivalent thickness can trigger the failure mode E or the failure mode F, distinguishable on the force-displacement graph since the first (mode E) is associated with instantaneous load reductions caused by traction breaking of the fiber bundles, which can occur before the flat branch of

the curve is reached (Fig. 3 (c)), while the second (mode F) denotes a sudden reduction and a further slight decrease in the load; in this case, the failure is activated by the telescopic tearing of the fiber bundles and is followed by the sliding of the first portion of the fabric inside the mortar (Fig. 3 (d)) [5], [21], [22].

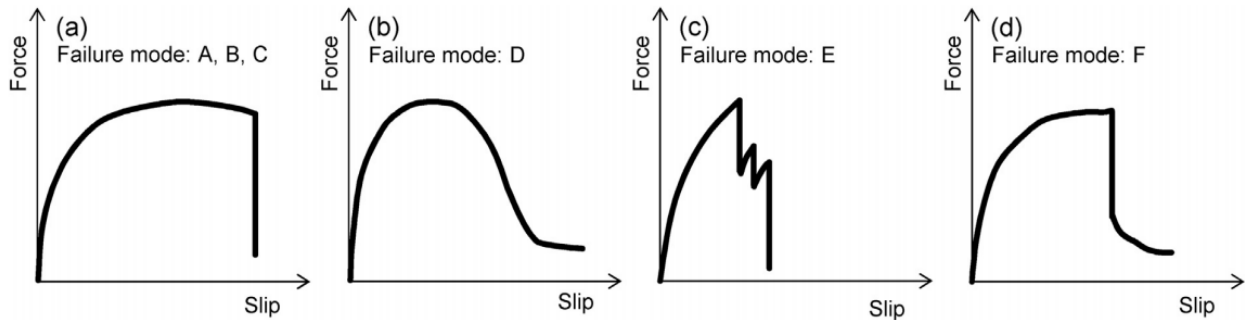


Figure 3 Typical force-slip curves observed in shear bond tests on externally bonded FRCC strengthening systems related to failure modes A, B, and C (a), failure mode D (b), failure mode E (c), and failure mode F (d). [5]

2.2 CNR DT 215/2018 Italian technical standards

By tensile testing an FRCC specimen, such as those listed in the beginning of paragraph 2, it is possible to trace its mechanical properties. This is not sufficient as the use of an FRCC composite as reinforcement of a structural element leads to considering the multiple crisis mechanisms that may occur following the support-reinforcement interaction. For this reason, the mechanical characterization must include, in addition to the tensile test of the FRCC system and of the fabric without inorganic matrix, also the detachment test from the support, and any other appropriate tests, in relation to the specific characteristics of the system [23].

A parameter of fundamental importance obtained by Single-Lap Direct Shear Tests from conventional supports is the conventional limit stress, $\sigma_{lim, conv}$, of the FRCC system; it represents the resistance of the resulting reinforcement and is obtained by dividing the characteristic value of the peaks of the pulling force F , recorded during the tests mentioned above, by the cross-sectional

area of the reinforcement, A_f , regardless of the presence of the inorganic matrix in the FRCC specimen, ie considering only the area of the dry fabric [24].

The conventional limit stress provides an essential characteristic represented by the conventional limit strain, $\varepsilon_{lim,conv}$, which can be obtained from the following relationship

$$\varepsilon_{lim,conv} = \sigma_{lim,conv} / E_f \quad (1)$$

where E_f is the elastic modulus of the fiber.

Through the conventional limit strain and the competent conventional limit stress, FRCC reinforcement interventions can be designed by avoiding explicit verification of the phenomenon of delamination from the support or sliding of the fibers in the matrix at the ends of the reinforcement, otherwise necessary in cases where such a crisis mode is possible. This happens, for example, when the stress in the reinforcement system is maximum at the ends, a situation that usually occurs in the beams subject to bending moment or column reinforcement interventions subject to horizontal actions (typically seismic actions). If, on the other hand, the FRCC can be extended up to a significant distance from the most stressed section, such as in the case of reinforcement of wall panels stressed out of the plane, the crisis due to delamination from the support, or that of sliding of the fibers in the matrix, located at the end of the reinforcement is averted.

The aforementioned damage models, due to delamination from the support or to sliding of the fibers within the matrix, can only occur for strain values significantly higher than the conventional limit strain.

The values of the parameters to be used in the checks controlled by the end phenomena are the conventional limit values just defined, $\sigma_{lim,conv}$ and $\varepsilon_{lim,conv}$.

If these phenomena were located in intermediate areas, the values to be used, and are:

$$\varepsilon_{lim,conv}^{(\alpha)} = \alpha \cdot \varepsilon_{lim,conv} \quad (2)$$

$$\sigma_{lim,conv}^{(\alpha)} = E_f \cdot \varepsilon_{lim,conv}^{(\alpha)} \quad (3)$$

α is an amplification coefficient assumed equal to 1.5 for all FRCM systems, with the exception of those for which the ordinate point σ_{lim} , falls in step I of the reinforcement stress-strain curve (Fig. 1). For the latter, a value of α equal to the unit must be assumed.

In any case, the value of the conventional limit stress must be less than or equal to the ultimate tensile strength of the FRCM composite ($\sigma_{lim, conv} \leq \sigma_u$).

The design values of the strain, ε_{fd} , and of the tensile strength, σ_{fd} , of the FRCM reinforcement system are obtained by referring to $\varepsilon_{lim, conv}$ in the case in which the expected crisis mode is due to delamination or sliding of the ends, considering $\varepsilon^{(\alpha)}_{lim, conv}$ where intermediate delamination or sliding is envisaged.

Considering the different failure modes for a FRCM composite previously exposed (§2.1), the design values are obtained through the following relationships:

- expected crisis mode due to delamination or sliding of extremities:

$$\varepsilon_{fd} = \eta_a \frac{\min(\varepsilon_{lim, conv}, \varepsilon_{u, f})}{\gamma_m} \quad (4)$$

$$\sigma_{fd} = \eta_a \frac{\min(\sigma_{lim, conv}, \sigma_{u, f})}{\gamma_m} \quad (5)$$

-expected crisis mode due to delamination or sliding in middle part:

$$\varepsilon_{fd} = \eta_a \frac{\min(\varepsilon^{(\alpha)}_{lim, conv}, \varepsilon_{u, f})}{\gamma_m} \quad (6)$$

$$\sigma_{fd} = \eta_a \frac{\min(\sigma^{(\alpha)}_{lim, conv}, \sigma_{u, f})}{\gamma_m} \quad (7)$$

where η_a is an environmental conversion factor that takes the values:

- 0.90 in internal exposure condition,
- 0.80 in external exposure condition,
- 0.70 in aggressive environment conditions.

γ_m identifies a partial factor corresponding to the characteristic value of the property and is equal to 1.5 for the Ultimate limit States and 1.0 for the Operating Limit States; $\varepsilon_{u, f}$ and $\sigma_{u, f}$ are, respectively, the strain and the ultimate stress at collapse by tensile stress of the dry fabric.

In order to delay or avoid the phenomena of detachment from the support, the technical document indicates which are the particular precautions to be taken during implementation, while following the instructions contained in the reinforcement system installation manual that the Manufacturer is required to provide.

The following detailed rules are reported in §6 of DT 215/2018:

- the edges to be reinforced by FRCM must be suitably rounded according to a minimum radius of curvature of 20 mm;
- an adequate anchoring length must be ensured, beyond the extreme section in which the FRCM reinforcement is necessary and, in the absence of more accurate investigations, it must be at least equal to 300 mm;
- if a confinement is carried out, the overlap length must be at least $\frac{1}{4}$ of the circumference/perimeter of the cross section and in any case not less than 300 mm;
- if the application of multiple reinforcement layers is necessary, the joints must be staggered; specifically, these offsets must be less than half the thickness of the reinforced element, with a minimum of 300 mm [25].

The different crisis modes, which denote the behaviour of FRP and FRCM composites, represent the main reason because it is not possible to adopt DT 200 R1 / 2013 for the implementation of reinforcement systems with a cement matrix.

The typical breaking method recorded for FRP is the delamination of a reinforcement layer with subsequent partial removal of the substrate, while for FRCM materials it is observed that the most common break occurs at the matrix-fabric interface, with sliding of the fiber mesh respect to mortar and consequent cutting of the fibers. This mechanism induces in the FRCM a ductile behaviour due to the friction phenomena that occur between the filaments and between fabric and matrix; distinctly, FRP systems are characterized by fragile behaviour, once the ultimate stress is reached, there is a sudden breakdown. It is also noted that the materials with a polymer-based matrix are extremely thin (thickness ~ 1 mm), therefore constant stresses along the thickness can be assumed, as opposed to

what happens for composites with an inorganic or organic matrix made with two layers of mortar, generally having a total thickness of about 10 mm. In this case the stresses on the external surface and on the interface between the mortar and the substrate could differ from the matrix-fabric interface [26].

From the direct comparison of the two technical documents, it is immediately evident that the most recently published Italian technical standard introduces a new mechanical characteristic for FRCM systems, that is the conventional limit stress obtained from Single-Lap Direct Shear Tests, together with the conventional strain limit derived from it. Its use allows to design reinforcement interventions avoiding the verification against delamination phenomena, otherwise indispensable where such a crisis mode is foreseen.

Therefore, being able to refer to a limit stress deduced directly from Single-Lap Direct Shear Tests, DT 215/2018 omits a calculation method for the optimal anchoring length, recommending criteria for the realization of some construction details and indicating as adequate a length of anchorage of at least 300 mm in the absence of more detailed investigations.

3. Mechanical Characterization of Materials

In this experimental investigation three types of mortar were examined, one of which inorganic and two organic types, whose composition is schematized in the table 1, and identified with the acronym M (mortar)_number of typologies.

Tab. 1: Composition of matrix use for experimental investigation

| Matrix | Mortar | Resin | Water Ratio | resin/mortar | Type |
|--------|--------------|-----------------------|-------------|--------------|-----------|
| M_1 | Kimisteel LM | Kimitech B2 | - | 30% | Inorganic |
| M_2 | Kimisteel LM | Kimicover Fix (A+B) * | 30% | 30% | Organic |
| M_3 | Kimisteel LM | Kimicover Fix (A+B) * | - | 22% | Organic |

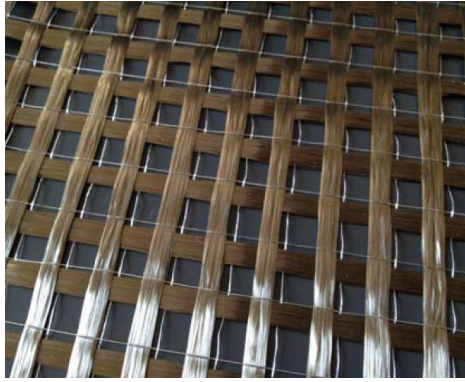
The mechanical characterization was carried out for each matrix by creating prismatic specimens with dimensions $40 \times 40 \times 160 \text{ mm}^3$ in accordance with UNI EN 1015-11 [26]. Initially, the mortar and resin were weighed separately accurately, after which they were mixed, continuously adding the resin to the powdered mortar in the mixer until a perfect amalgam was obtained. Subsequently, the specimens were packaged in wooden formwork, previously lubricated with mineral oil to avoid adhesion with the mortar and ensure the integrity of the specimens themselves (Fig. 4).



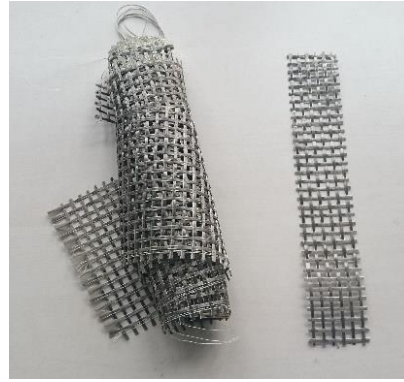
Fig. 4. Different step preparation of mortar specimens in laboratory.

After 48 hours from preparation, the specimens were extracted from the formworks and, in order to preserve the conditions of hardening from humidity and allow for complete maturation, they were covered for 28 days.

The fibers used as reinforced fibers are those of basalt (Fig. 5). Mechanical and physical parameters provided by the manufacturing company (Fidia S.r.l) and shown in table 2. The fabrics were cut according to the UNI EN ISO 13934-1 [27] standard and with a width equal to 50 mm and lengths equal to 300mm, in order to carry out for tensile tests on fabrics, corresponding to 34 basalt strips (Fig. 4). In addition, the mechanical behavior of the individual wires was studied in accordance with the UNI EN ISO 2062 [28] standard. For the following experimentation, 6 specimens were used for each fabric.



a)



b)

Fig. 5. a) Balance fabrics of basalt; b) Example of basalt specimen used

Tab. 2: Mechanical performance of basalt fabrics provided by Fidia S.r.l

| Properties | Basalt |
|--|--------|
| Tensile strength, σ [MPa] | 3080 |
| Young Modulus, E [MPa] | 95 |
| Strain at break, ε [%] | 3,15 |
| Density of fibers, r [g/cm ³] | 2,8 |

4. Experimental Investigation

For the purpose of paper, the tests have been performed in order to define the mechanical behavior of the materials used:

- Three points bending tests on the mortar;
- Compression test on mortar;
- Tensile test on basalt fibers.

4.1 Three points bending tests on the mortar

The flexural tests on the mortar were carried out as prescribed by UNI EN 1015-11 [29] on prismatic samples of dimensions 40x40x160 mm³, using a universal electromechanical machine INSTRON 1195 with a maximum capacity of 10 tons. The machine is equipped with two steel support hinges having a length of 150 mm and a diameter of 10 ± 0.5 mm placed at a distance of 100

± 0.5 mm between them and a third hinge, of the same diameter and length, positioned at the extrados of the specimen and placed in correspondence with the center section that imprints the load (Fig. 6).

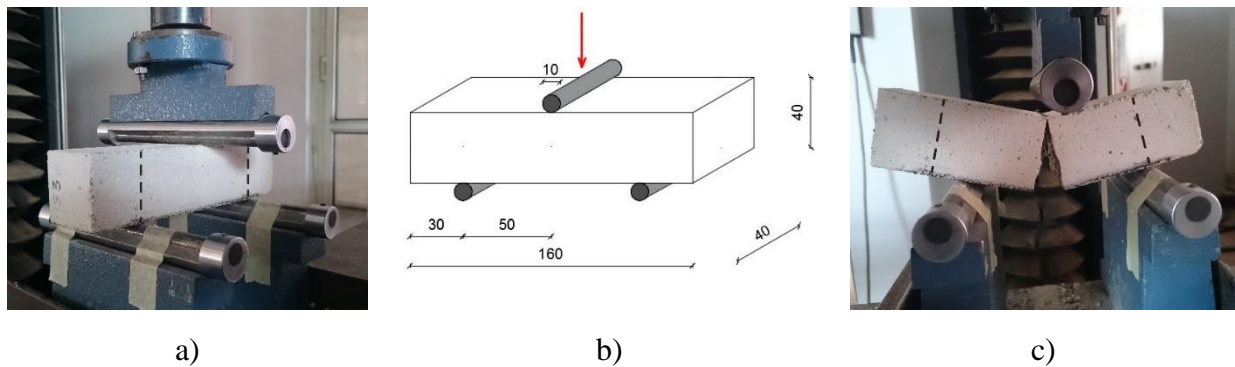


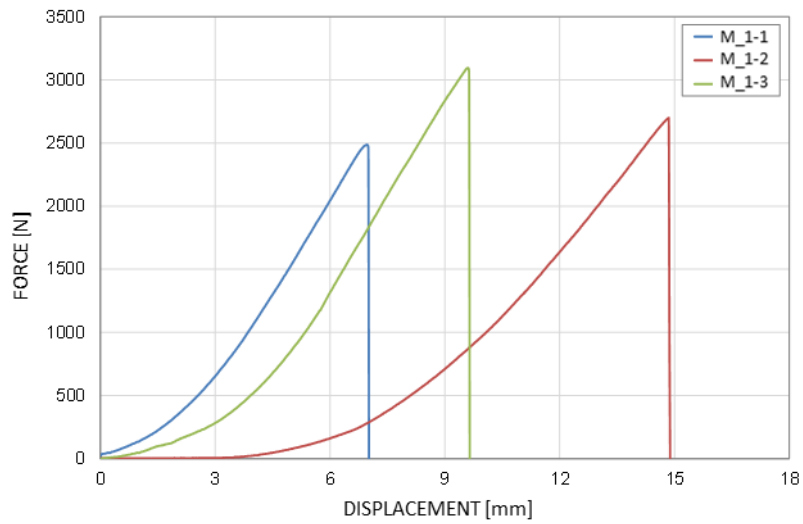
Fig. 6. Set-up of three-point bending tests: a) set-up machine; b) static scheme; c) flexural failure of the tested specimens

The tests were carried out in displacement control with a constant crosshead speed of 1 mm / min until the specimen broke, which occurs, in almost all the mortars analyzed, with a vertical lesion in the middle of the specimen (fig. 6.c).

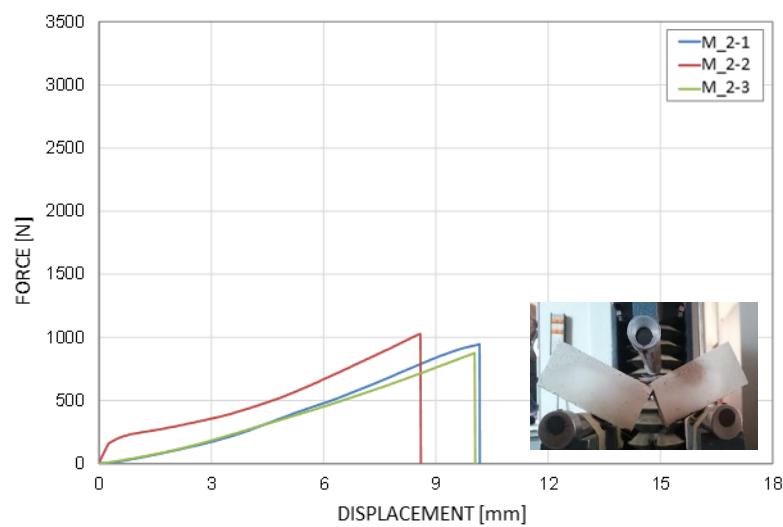
During the test, the movements of the crosspiece and the relative load levels reached by the specimen until the break were recorded. Flexural strength f_b was calculated using the following relationship:

$$f_b = 1,5 \frac{Fl}{bd^2} \quad (8)$$

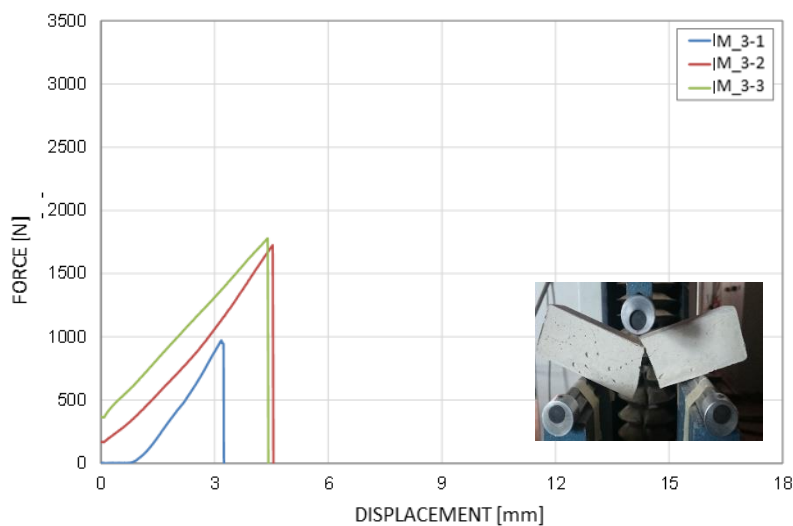
where F is the maximum load applied, l represents the clear gap between the support hinges for the specimen (100 mm), b and d represent the base and the height of the cross section of the specimen (40x40 mm²). Once the experimental tests were carried out in the laboratory, all the data obtained were processed by obtaining both the force-displacement diagrams (Fig. 7) and the mechanical parameters necessary for the purposes of the experimentation, for each of the mortars examined. The results obtained are shown below.



(a)



(b)



(c)

Fig. 7. Force-displacement diagrams obtained from 3-point bending tests: a) M₁; b) M₂; c) M₃

From the force-displacement diagrams it was possible to analyze the mechanical behavior of the individual mortars. An initial analysis of the results shows that all the mortars have a brittle type of

behavior, in fact the failures of the individual specimens occurred instantaneously and characterized by a lesion at the central hinge located in the upper edge of the specimen. Mortars with the presence of only resin (M_1; M_3), (fig. 7 a, c,) were found to be much more rigid than mortars that also have water (M_2, fig. 7 b). The mechanical parameters obtained are the maximum and average displacement (d_{max} and d_m), the maximum and average force (F_{max} and F_m), the absolute and average flexural strength (f_b and f_{bm}) and are shown in the table 3:

Tab. 3: Mechanical parameters obtained from the flexural tests for each mortar

| | d_{max} | d_m | F_{max} | F_m | f_b | f_{bm} | |
|-----|-----------|-------|-----------|---------|--------|----------|------------|
| | [mm] | [mm] | [N] | [N] | [MPa] | [MPa] | |
| M_1 | 1 | 7,00 | | 2487,00 | | 5,83 | |
| | 2 | 14,87 | 10,50 | 2700,00 | 2761,0 | 6,33 | 6,47 (11%) |
| | 3 | 9,63 | | 3096,00 | | 7,26 | |
| M_2 | 1 | 10,17 | | 948,00 | | 2,22 | |
| | 2 | 8,58 | 9,59 | 1029,00 | 951,0 | 2,41 | 2,23 (8%) |
| | 3 | 10,03 | | 876,00 | | 2,05 | |
| M_3 | 1 | 3,25 | | 972,00 | | | |
| | 2 | 4,55 | 4,07 | 1725,00 | 1492,0 | 4,04 | 4,11 (2%) |
| | 3 | 4,40 | | 1779,00 | | 4,17 | |

(Variation coefficient CoV is indicated in parentheses)

4.2 Compression test on mortar

The compression tests on the mortar were carried out after performing the flexural tests. The tests were conducted on the remaining half of the specimens used and for a number of samples equal to 6, for each mortar analyzed. A universal electro-hydraulic machine BPS 300 MFL with a maximum load capacity of up to 3000 kN was used to carry out the test.

The specimens were positioned in the center, between the two plates of the machine, by inserting square metal plates of size 40x40 mm² and thickness equal to 10 mm, as required by the standard governing the test, in order to distribute the load in a centered manner only on the surface considered (Fig. 8).

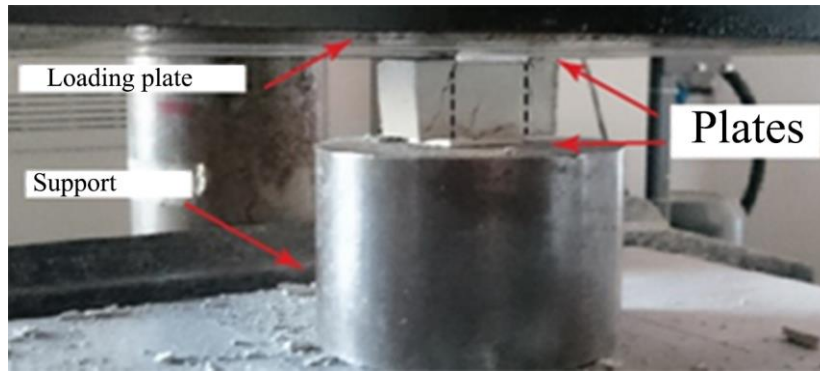


Fig. 8. Set-up machine and schematic representation.

This test was carried out in displacement control by applying a constant speed of 1 mm / min until the specimen collapse, which is manifested by the truncated-cone break in the central part of the specimen, typical of mortars (Fig. 9).

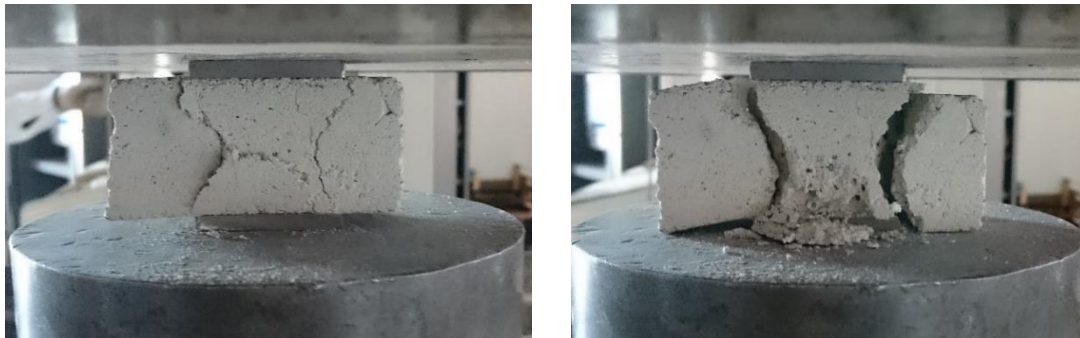
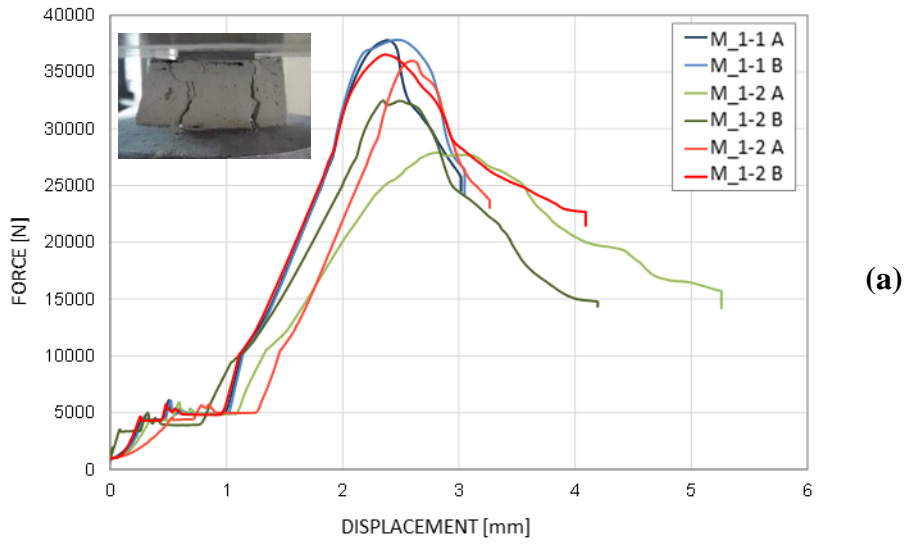


Fig. 9. Compression failure

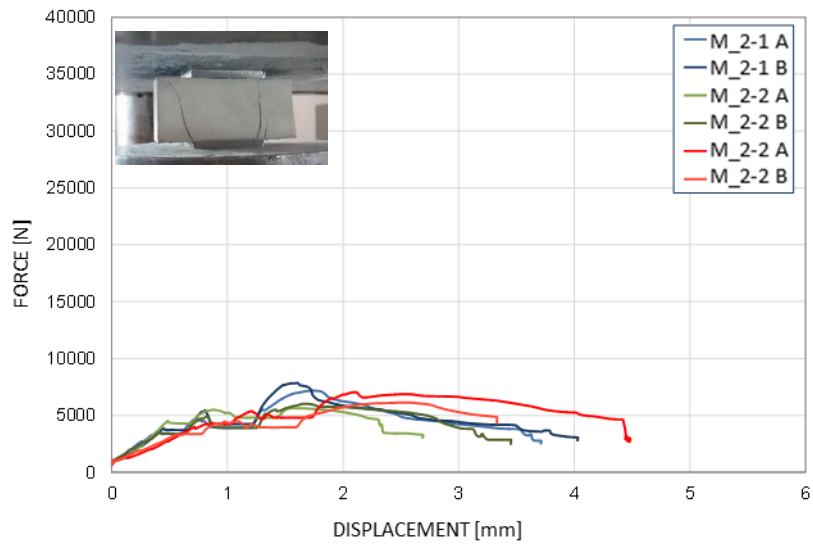
During the test, the displacement control to the crosspiece were recorded the different load levels reached by the specimen, consequently it was possible to calculate the compressive strength f_c through the following relationship:

$$f_c = \frac{F}{A_c} \quad (9)$$

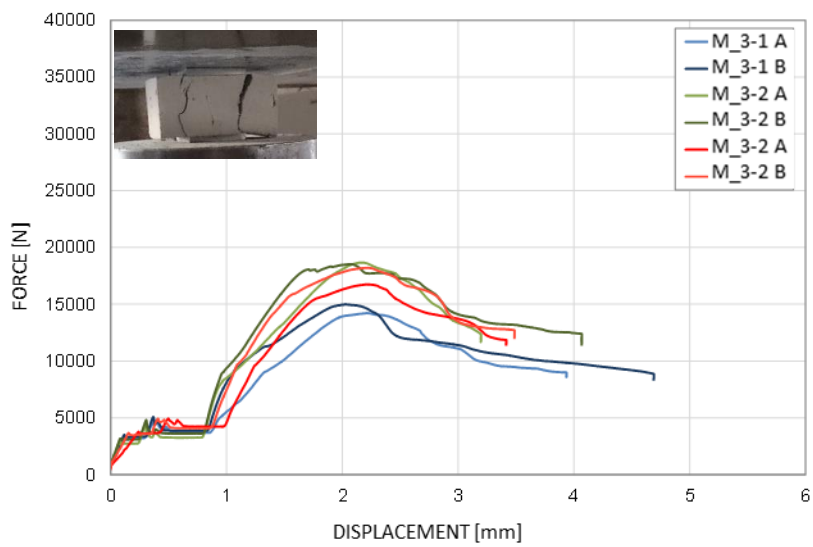
where F represents the maximum load and A_c indicates the of the specimen, defined by the steel plates. After carrying out the laboratory tests, both the force-displacement diagrams (Fig. 10) and the mechanical parameters such as the compressive strength were obtained for each mortar examined.



(a)



(b)



(c)

Fig. 10. Force-displacement diagrams obtained from compression tests: a) M_1; b) M_2; c) M_3

The mechanical parameters obtained are shown in the table 4: the displacement and the maximum force (d_{max} and F_{max}) and the absolute and average compressive strength (f_c and f_{cm}).

Tab. 4: Comparison of the results obtained from the compression tests

| | | d_{max} | | F_{max} | | f_c | | f_{cm} |
|-----|---|-----------|------|-----------|-------|-------|-------|-------------|
| | | [mm] | | [kN] | | [MPa] | | |
| | | A | B | A | B | A | B | |
| M_1 | 1 | 2,38 | 2,48 | 37,80 | 37,84 | 23,63 | 23,65 | |
| | 2 | 2,81 | 2,35 | 27,93 | 32,49 | 17,45 | 20,31 | 21,73 (11%) |
| | 3 | 2,60 | 2,37 | 36,01 | 36,55 | 22,51 | 22,84 | |
| M_2 | 1 | 1,73 | 1,61 | 7,18 | 7,85 | 4,49 | 4,91 | |
| | 2 | 1,59 | 1,66 | 5,65 | 6,04 | 3,53 | 3,77 | 4,16 (13%) |
| | 3 | 2,10 | 2,54 | 7,05 | 6,14 | 4,41 | 3,84 | |
| M_3 | 1 | 2,21 | 2,03 | 14,23 | 14,99 | 8,90 | 9,37 | |
| | 2 | 2,16 | 2,07 | 18,68 | 18,54 | 11,68 | 11,59 | 10,56 (11%) |
| | 3 | 2,21 | 2,22 | 16,75 | 18,21 | 10,47 | 11,38 | |

(Variation coefficient CoV is indicated in parentheses)

4.3 Tensile tests on fibers

The tensile tests on fibers have been carried out on fabrics with dimension equal to 50x200 mm² according to UNI EN ISO 13934-1 [27] standard and on single yarns according to UNI EN ISO 2062 standard [28]. After cutting the specimens, in order to avoid the sliding of the machine grips during the test and to have a homogeneous deformation, steel plates were glued to the ends of the specimens (Fig. 11). All tests were carried out with a universal Instron 5582 machine, in control of displacement of the crosspiece by applying a constant speed of 5 mm / min until the specimen broke, which manifests itself differently in the two examined fabrics (Fig. 12).

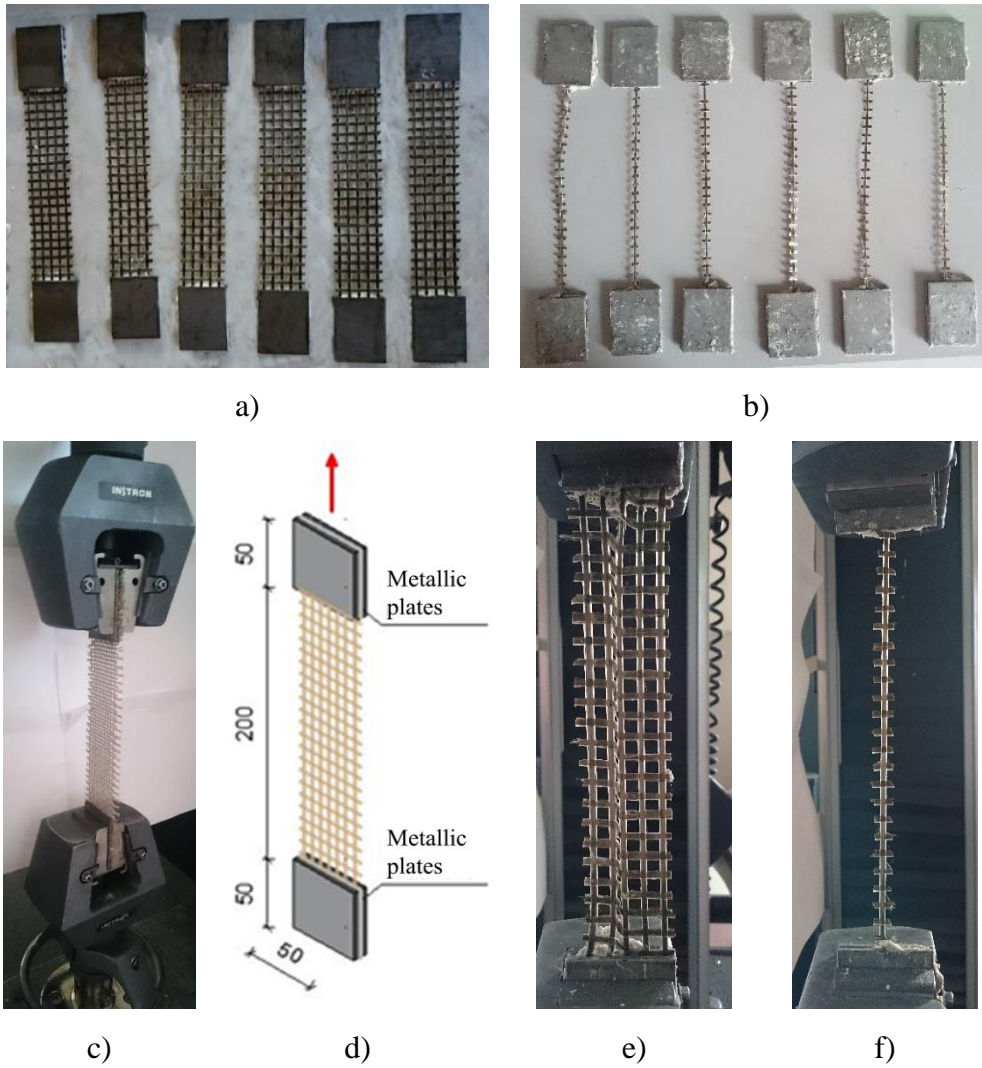


Fig. 11. Specimens used for tensile tests: a) basalt fabrics; b) yarns basalt; c) Ste-up machine; d) Schematic representation; e) Basalt fabrics; f) Yarn fabrics

To determine tensile failure of the fabric, the resistant area of the fabric obtained using the guidelines of the CNR-DT 200 R1 / 2013 [30] was used, for the case of balanced fabrics that have the same number of fibers in the weft and warp direction:

$$A_{fib} = \frac{p_t}{2 \cdot \rho_{fib}} \cdot \frac{b_f}{10^3} \quad (10)$$

In the previous formula (10), the physical characteristics of the yarn are present, in particular p_t represents the mass of unit area (weight, in g / m²), ρ_{fib} is the density of the fibers (g / cm³) and b_f indicates the width of the fabric expressed in mm. Density of the fabrics ρ was determined according to ASTM D 792 – 13 [31]:

$$\rho = \frac{w[\rho(H_2O) - 0,0012]}{0,99983 \cdot G} + 0,0012 \quad (11)$$

Formula (11) indicates w the weight of the specimen and $\rho(H_2O)$ the density of the water. Finally, in accordance with ISO 3374 -2000 [32], the mass per unit area (GSM) has been calculated for each fabric, on specimens having the dimensions of about 100 mm², through the relationship (12):

$$p_t = \frac{W_s}{A} \times 1000 \quad (12)$$

where W_s the mass, in grams, of the specimen and A the area of the specimen itself. For application purposes, it is customary to refer the resistant area of the fabric to the thickness of an equivalent sheet consisting only of the fiber material, obtained from the ratio:

$$t_f = \frac{A_{fib}}{b_f} \quad (13)$$

The results obtained are shown in the table 5.

Tab. 5. Physical and geometric properties of basalt fabrics

| | yarns | fabrics |
|-----------------------------------|--------------|---------|
| W [g] | 0,62 (5%) | 3,69 |
| p_t [g/m ²] | 326,77 | 326,77 |
| b_f [mm] | 4 | 100,00 |
| ρ_{fib} [g/cm ³] | 1,18 | 1,18 |
| A_{fib} [mm ²] | 0,55 | 13,84 |
| t_f [mm] | 0,14 | 0,14 |

By processing the data obtained from the tensile tests, the mechanical behavior of the fibers was defined; initially, force-displacement diagrams were plotted from both yarns and fabrics analyzed (Fig.12). The results obtained are listed in table 6.

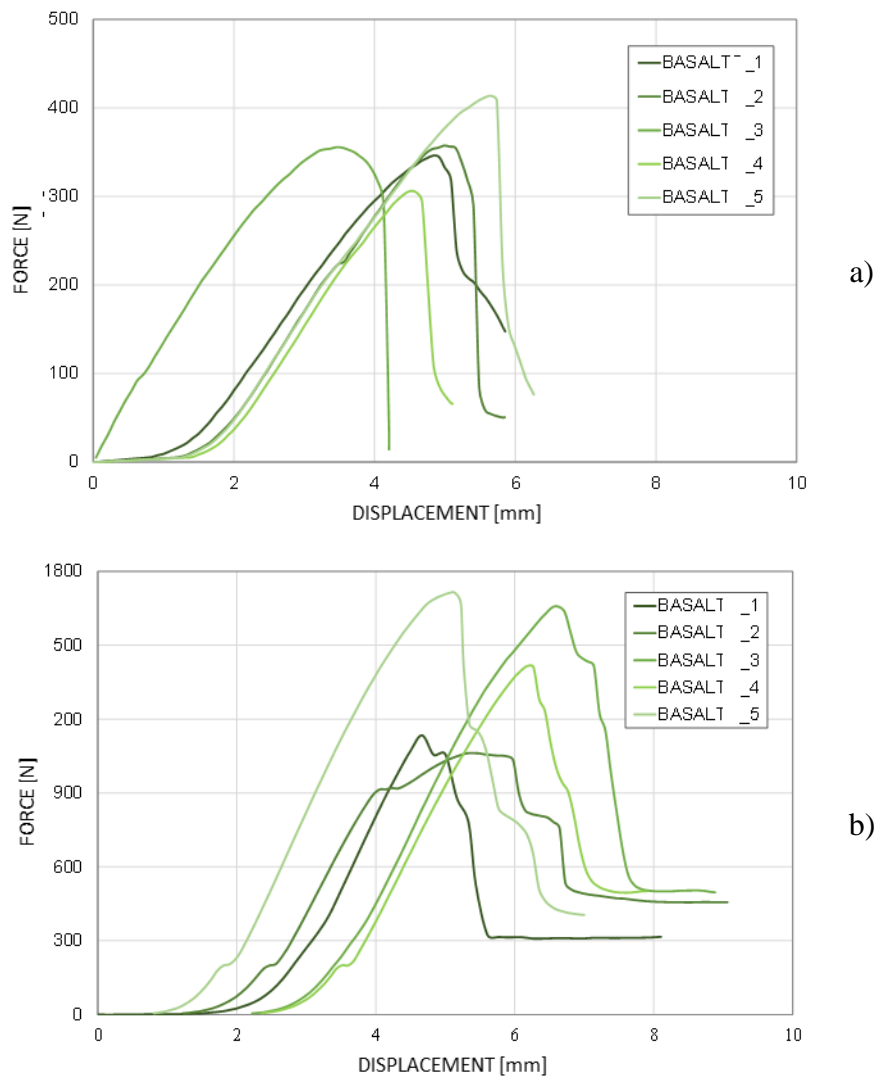


Fig. 12. Force-displacement diagrams of a) single yarns b) fabrics

The mechanical parameters obtained are shown in the table 6. Young's modulus was obtained, considering the variation of tension and deformation between 50% and 20%, in accordance with ISO TC 71 / SC 6 / WG [33].

Tab. 6. Results obtained from the tensile test on basalt fabrics

| | BASALT_1 | BASALT_2 | BASALT_3 | BASALT_4 | BASALT_5 |
|----------------------------------|----------|----------|----------|----------|----------|
| Displacement, d_{\max} [mm] | 4,67 | 5,96 | 6,55 | 6,18 | 5,14 |
| Load F_{\max} [N] | 1134,70 | 912,84 | 1657,07 | 1416,57 | 1713,40 |
| Strength, σ_{\max} [MPa] | 81,97 | 65,94 | 119,71 | 102,33 | 123,77 |
| Strain, ε_{\max} [%] | 7% | 3% | 4% | 4% | 3% |

4.4 Tensile tests on Basalt FRCM composites

In the first step, each mortar was prepared, following the doses prescribed in the technical data sheets; after reaching a good consistency, composites were made inside the formwork. A first layer of mortar of about 4 mm was applied inside the formworks, after that fabric was positioned, pre-cut and pre-impregnated by making it integrate into the matrix, and then a subsequent layer of mortar was applied which allowed the complete coverage of the fabric and regularization of the specimen (fig. 13).



Fig. 13. Preparation steps of composites specimens

The specimens were removed from the molds after 48 h and were covered to prevent shrinkage, allowing the complete curing of the cement matrix. Once the maturation has taken place, the thickness is 5-8 mm, which varies according to the type of mortar (Fig. 14).

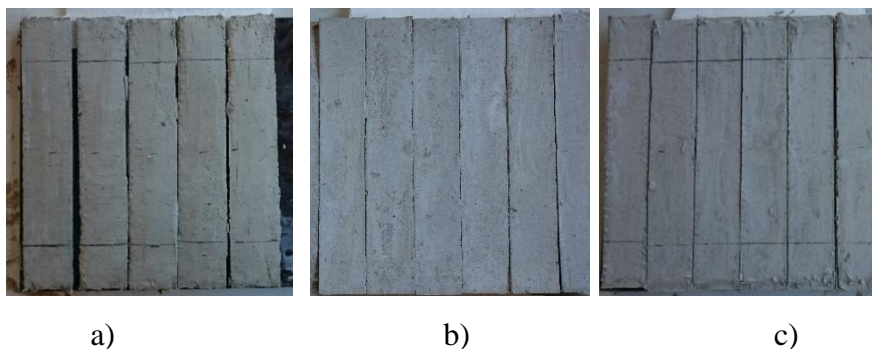


Fig. 14. Specimens Composite: a) FRCM1; b)FRCM2; c)FRCM3

The mechanical properties of the composites were analyzed by tensile tests, as described in Annex A of the AC 434_13 standard [34]. The tests were carried out with a Zwick Roell Z250 universal

machine in displacement control and a constant speed of 0.3 mm / min with no preload applied (Fig. 15).

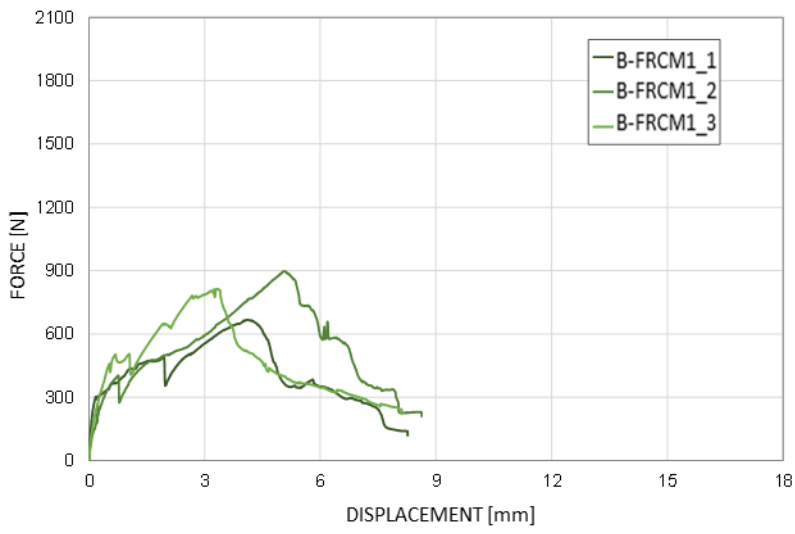


Fig. 15. Set up tensile tests and specimens with application of steel plates

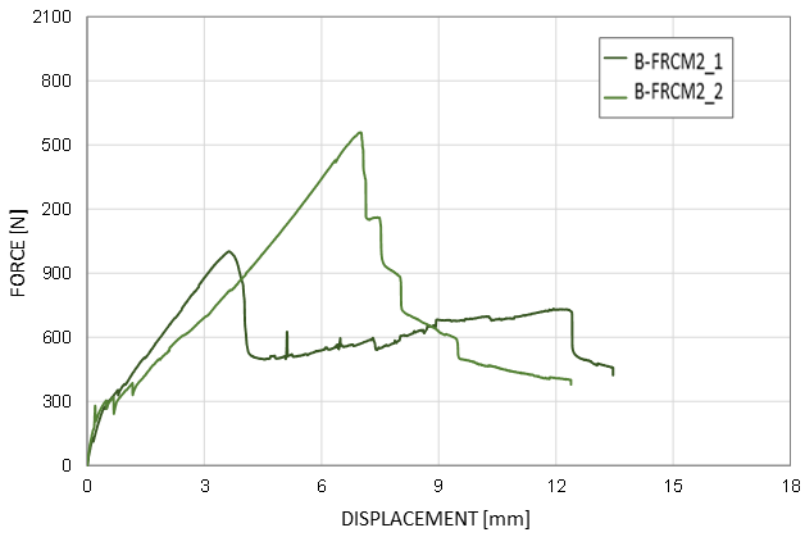
To ensure a homogeneous distribution of the stresses and to prevent the sample from slipping from the grips of the test machine, metal plates with a length of 50 mm have been applied to the ends of the specimens (Fig. 15). During the test, the displacements relating to the machine cross member were recorded by detecting the load levels reached by the specimen, also the tensile strength f_t was obtained by means of the following relationship:

$$f_t = \frac{F}{A_c} \quad (14)$$

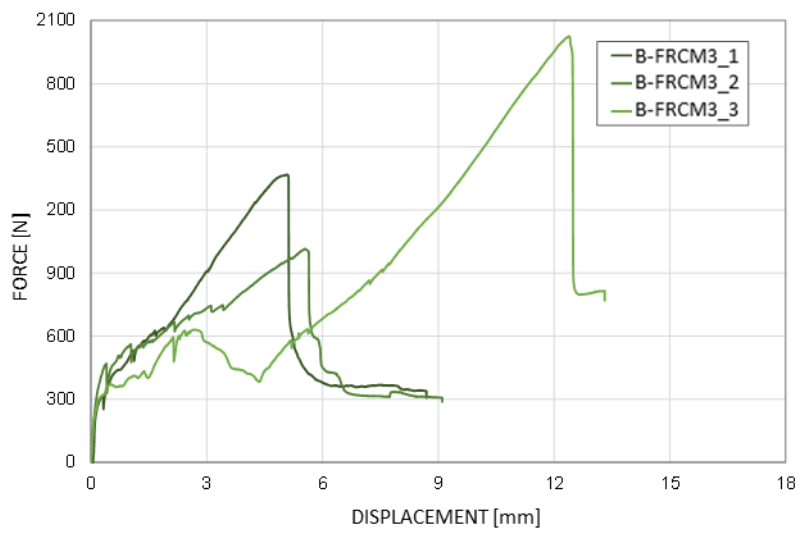
Where F represents the maximum load and A_c indicates the cross section of the composite. By processing the data obtained from the tensile tests, the mechanical behavior of the analyzed composites was defined, obtaining, also in this case, the force-displacement diagrams (Fig. 16) and the failure modes, for each specimen, observed during the tests.



a)



b)



c)

Fig. 16. Force-displacement diagrams of composites: a) B-FRCM1; b) B-FRCM2; c) B-FRCM3

The force-displacement diagrams obtained from the B-FRCM composites (Fig. 16) show a behavior with three distinct main phases: the first section corresponds to the non-cracked phase in which the matrix and the reinforcement are collaborating; in the second step, the tensile force is transferred from the mortar to the fibers with the formation of cracks and presents itself with an uneven behavior ; the third phase has a more linear stretch and the achievement of the maximum load is due solely to the resistance of the fibers. With reference to the entire matrix-fabric system, the overall behavior of the composite was defined by calculating the main parameters in terms of displacement, maximum force and stress, reported as the average value of the tests performed for each specimen in table 7.

Tab. 7: Comparison of the results obtained on the analyzed composites

| | B-FRCM1 | B-FRCM2 | B-FRCM3 |
|------------------|---------|---------|---------|
| d_{MAX} [mm] | 4,17 | 5,32 | 7,67 |
| | (21%) | (45%) | (53%) |
| F_{MAX} [N] | 793,70 | 1281,43 | 1470,10 |
| | (15%) | (31%) | (35%) |
| σ_t [MPa] | 3,17 | 5,13 | 5,88 |
| | (15%) | (31%) | (35%) |

(Variation coefficient CoV is indicated in parentheses)

4.5 Failure modes on B-FRCM

Failure modes of each sample analyzed, allow to define the bond created between matrix and reinforcement fibers. The B-FRCM composites (Fig. 17) appear to have, after deformation, few cracks located in the center line of the specimen, from which it is possible to deduce a more uniform behavior and a better bond between the matrix and the reinforcement, although there are minor deformations due to the lack of ductility basalt fibers, as already seen in the characterization of the individual fabrics.



Fig. 17 – Failure mode of a sample of B-FRCM, subjected to tensile test

In the intermediate phase (Fig. 18), at each peak there is the formation of cracks, even if small, which allow to transfer the stresses from the matrix to the fiber. The length and slope of this curve portion depends on the quality of the bond between the fabric and the matrix, and on the volume of fibers that are affected by the tensile load. It can also be seen from the stress-strain diagram, how the curves are characterized by a final softening trait, therefore by a not completely fragile behavior of the composite.

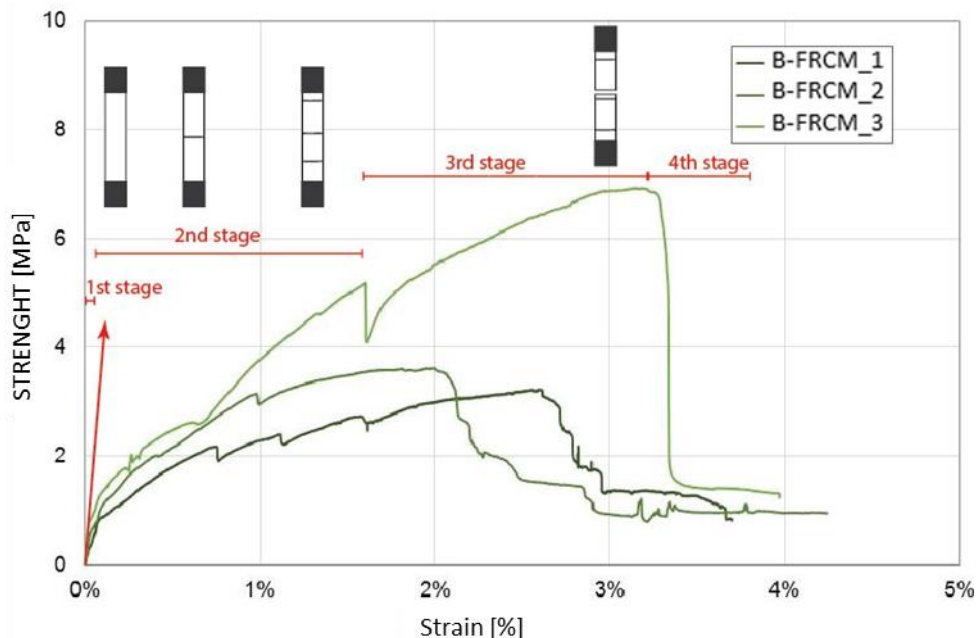


Fig.18. Analysis of the individual phases in the stress-strain diagram of a sample of B-FRCM

5. X-Ray Tomography

The micro-CT is a non-destructive technique for diagnostic imaging able to produce 3D images of the inner structure of a material with a spatial resolution in the order of the micrometers, using a set of bi-dimensional radiographic images from a sample [35], [36]. It finds application in a vast variety of fields: medicine, biology, many engineering disciplines, paleontology and earth sciences are just few examples.

The principle of micro-CT is based on the attenuation of X-rays passing through the sample being imaged as an X-ray passes through a homogeneous object, the intensity of the incident X-ray beam is reduced according to the Lambert-Beer equation (Fig. 19):

$$I = I_0 e^{-\mu x} \quad (15)$$

where I_0 is the intensity of the incident beam, x is the distance covered by the X-ray in the absorbing object and μ is the linear attenuation coefficient [37].

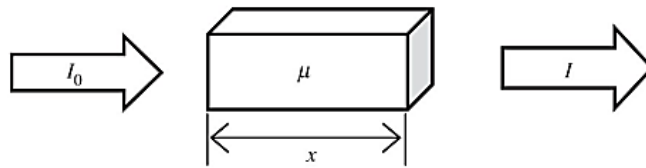


Fig. 19. Attenuation of X-rays passing through the sample according to the Beer-Lambert law.

The cone beam microtomography has the advantage to use a simple and versatile apparatus. A micro-CT system (Fig. 20) consists of a microfocus X-ray source, a rotational subject holder, a flat-panel detector and a process control system by computer. All the components except the process control system are mounted on an optical bench [38].

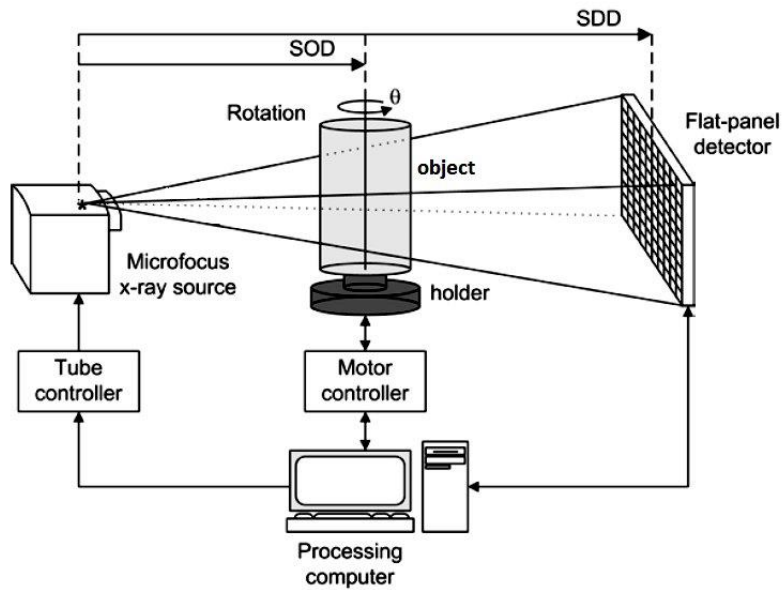


Fig. 20: Schematic diagram of the developed micro-CT system [38].

In Fig. 21 is show a schematic diagram of the sequence of the operations to perform an X-ray microtomography measurement.

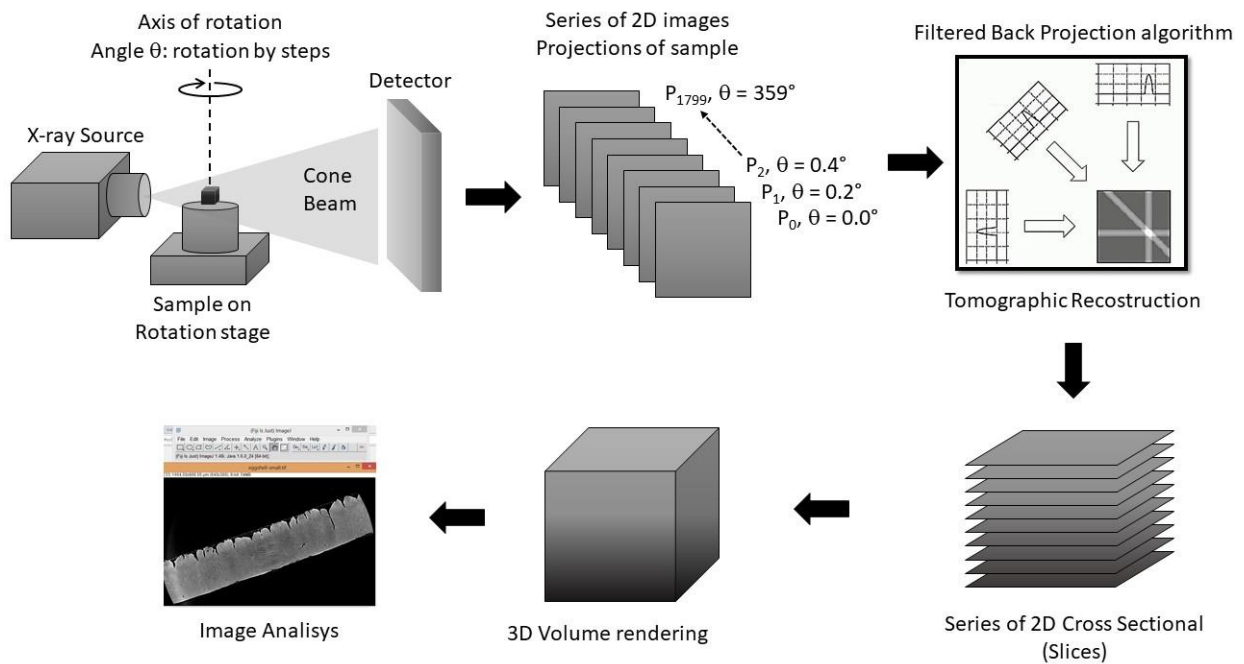


Fig. 21. Schematic representation of operations sequences to perform an X-ray microtomography measurement.

A microtomography apparatus perform a measurement rotating the sample on its own axis while the X-ray source and detector remain fixed. The microfocus X-ray source continuously irradiates an object (or a sample), which is rotated with a constant angular step until completing 360 degrees and

the flat-panel detector acquires a series of 2D projections of the object at different angles and at a fixed integration time. The angular step and integration time are computer-controlled. The next step is the 3D digital reconstruction, this is based Filtered Back-Projection algorithm (FBP) [39].

In our case, since the micro-CT apparatus uses an X-ray cone beam source, the 3D digital reconstruction is performed using the algorithm of Feldkamp, Davis, and Kress (FDK) [40]. The 3D digital reconstruction produces a 2D dataset of cross sections, called slices. The stack of slices provides three-dimensional volumetric data. The sample can be viewed and analyzed in a virtual environment in various ways: it is possible to view a single slice of the sample or a 3D virtual volume.

5.1 Experimental Setup

The micro-tomographic experimental station, named μ Tomo, is part of the STAR-Lab facility realized under the PON MaTeRiA project. It is located into the University of Calabria in Italy.

The μ Tomo experimental station, based on a cone beam geometry, used to the aim of this analysis and shown schematically in

Fig. 22, is made of:

- a microfocus X-ray source Hamamatsu L12161-07;
- a flat panel detector Hamamatsu C7942SK-05;
- a six degree of freedom sample positioning system (linear movement and rotation stage);
- hardware and software system for control and data acquisition.

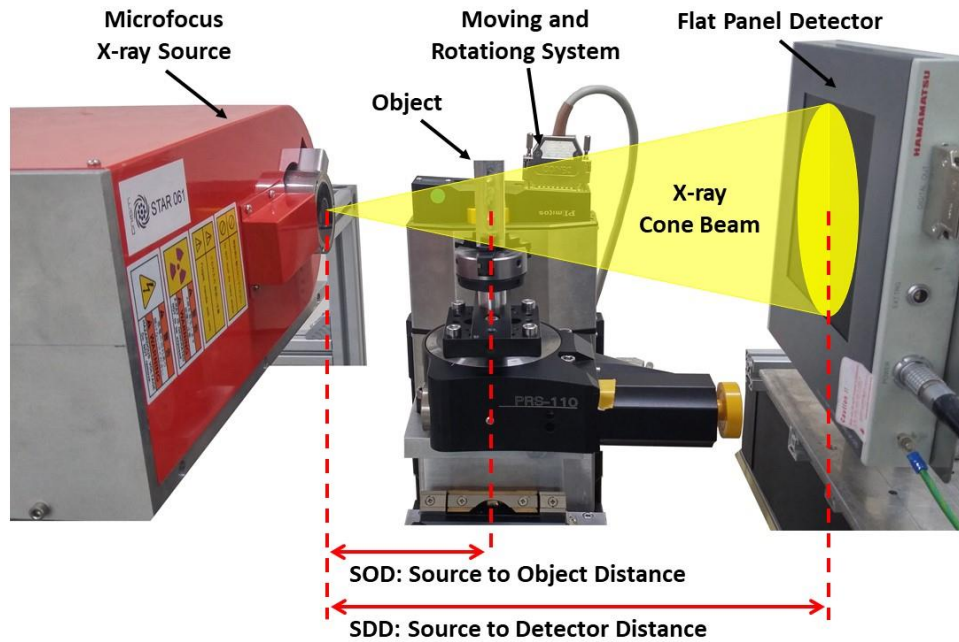


Fig. 22. μ Tomo@STAR-Lab. - University of Calabria.

The X-ray source is based on a polychromatic microfocus X-ray generator (Hamamatsu L12161-07) with a tungsten target and a minimum source size of $7\mu\text{m}$. The microfocus source can be operated with a voltage range from 40kV to 150kV and allows three power modes that determine the source size. The minimum source size ($5\mu\text{m}$) is obtained at power below 4W. The X-ray cone beam aperture is about 43 degrees.

The detector is a Flat panel sensor C7942SK-05 from Hamamatsu. These detectors are based on two-dimensional arrays of photodiodes CMOS (CCD) directly coupled to a scintillator for X-ray to light conversion. Its main features are shown in the Tab. 8:

Tab. 8: Detector features

| Parameter | Specification | Unit |
|------------------------|---------------|---------------|
| Pixel size | 50 x 50 | μm |
| Photodiode active area | 115 x 115 | mm |
| Number of active pixel | 2316 x 2316 | pixels |

The sample positioning system (by PI miCos Industry) provides six degrees of freedom. Three linear motor for x,y,z movement, one for the rotation stage tetha (ϑ) and two stages for tilt angles. This system allows to position the sample with the required precision. In particular, the Source to

Object Distance (SOD) and Source to Detector Distance (SDD) determine the system geometric parameters such as magnification ratio ($M=SOD/SDD$).

The μ Tomo station is provided with a user interface that allows its control through a computer. All the electronic hardware components are commercially available and are, in general, provided with software drivers which are LabVIEW compatible [41].

5.2 Measurement parameters

The sample were investigated by X-rays micro-CT with a conventional laboratory source at μ Tomo@STAR-Lab. The experiment setup was the following: the X-ray source operated at a voltage of 80kV, a current of 125 μ A and a focal spot size of 7 μ m; the X-ray beam was filtered for low energy components with 25 μ m of Aluminum add to 25 μ m of Copper fixed target. In this study, the SOD was set to 150mm and the SDD to 455mm, then the magnification equal to $M=3$. Considering the employed beam magnification, the equivalent pixel-size was 16.67 μ m. A set of 1800 projections were acquired over an angular range of 360° using an angular step of 0.2 degree and an exposure time of 1 s/projection. Axial slices were reconstructed with an isotropic voxel size of 16.67 μ m using the FDK algorithm for cone-beam geometry. The measurement parameters are show in the Tab. 9.

Tab. 9: Measurement parameters

| Microfocus source parameters | |
|--|-------------------------------------|
| X-ray tube voltage (kV) | 80 |
| X-ray tube current (μ A) | 125 |
| X-ray focal spot mode Small | 7 μ m |
| Power (W) | 10 |
| Energy filter | 25 μ m of Al + 25 μ m of Cu |
| Source and detector position | |
| Source to Object Distance - SOD (mm) | 150 |
| Source to Detector Distance - SDD (mm) | 455 |
| Magnification | 3 |
| Equivalent pixel-size (μ m) | 16.67 |
| Detector parameters | |
| Number of images captured | 1800 |
| Angular step (°) | 0.2 |
| Acquisition time (ms) | 1000 |

5.3 3D image analysis

Image analysis was performed with Fiji (Fiji Is Just ImageJ) [41] an open source image processing package based on ImageJ. ImageJ is an open source software developed by the National Institutes of Health of the United States [42], which allows digital image processing operations. ImageJ is designed with an “open architecture” that provides the possibility to install extensions via small subprograms "Java plugin" and the possibility to develop many macros for ad-hoc processing.

The aim of the analysis is to retrieve the morphology and topology of the constituents of the samples. The first procedure was to extract a volume of interest (VOI) from the stack of reconstructed slices. The selected VOI enclosed a representative amount of the sample heterogeneity and can be defined as Representative Elementary Volumes (REVs) [43]. The VOI was filtered with a ‘3D Gaussian-Blur filter’ [44] to reduce the image noise, and segmented by an automatic thresholding algorithm [45] to separate the different materials in the samples (basalt fibers, mortars and voids). In a first analysis, the macro structure of the sample was studied, subsequently the various components were isolated and analyzed separately.

The ‘3D ImageJ Suite’ [44] of the Fiji software library was applied to evaluate the density of the different components, which provides their volumetric fraction in the sample. A morphological and topological analysis of clay, sand and voids was performed by excluding those touching the VOI borders, since they can be truncated and their volume and morphology may not be representative of the real shape.

The 3D visualization was performed by volume rendering procedures by using the plugins of Fiji ‘Volume Viewer’ [46] and ‘3D Viewer’ [47]. This analysis allowed to determine the three-dimensional shape of the basalt fibers, mortars and voids and their distribution and orientation inside the sample.

5.4 Results

In this study were analyzed three samples composed by cement matrix and basalt fiber (Fig. 23), called B-FRCM1, B-FRCM2 and B-FRCM3 (respectively indicated with the abbreviations B2, B5,

and B6). The specimens were studied with the X-ray microtomography technique at the experimental station μ Tomo@STAR-Lab. The aim of this research is to investigate the presence of voids incorporated in the fibers that to compromise the mechanical performance.

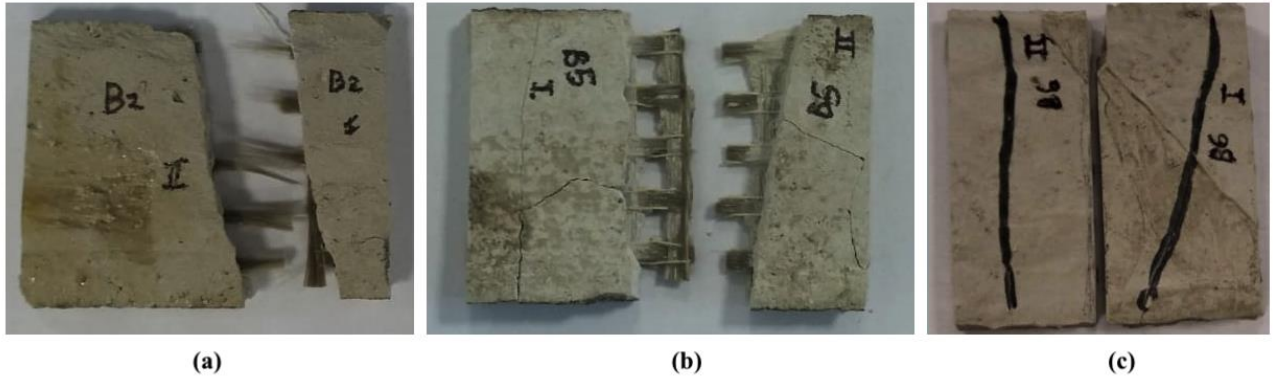


Fig. 23. Samples analyzed

By the use of the X-ray microtomography technique, it was possible to examine the three FRCM samples in basalt fibers in a non-invasive and non-destructive mode.

The analysis of the internal structure of the sample was carried out through a three-dimensional study. Once the 3D reconstruction of the samples is completed, the position and morphology of voids, cracks, and fiber into the cement matrix in 3D space are displayed.

Figs. 24, 25, and 26 shows the 3D X-ray micro-CT reconstructions of the samples analyzed, and Fig. 27 shows the cutting planes with their respective 2D orthogonal projections for each specimen.

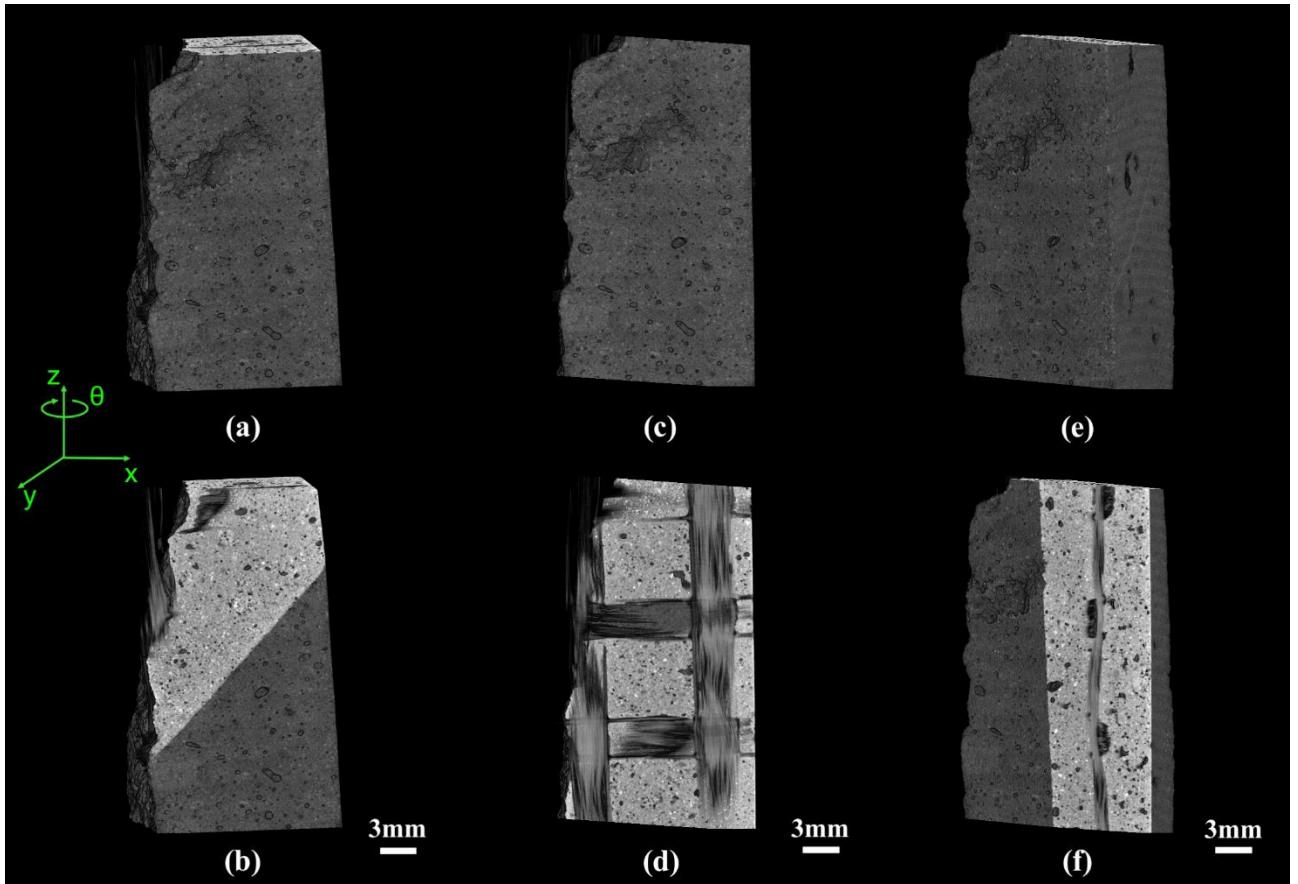


Fig. 24: 3D X-ray micro-CT reconstruction of sample B2: (a) general view in the start position, (b) view with randomly cut in start position, (c) general view rotated 15° from the start position, (d) view with randomly cut in rotate position (15°), (e) general view rotated 95° from the start position, (f) view with randomly cut in rotate position (95°),

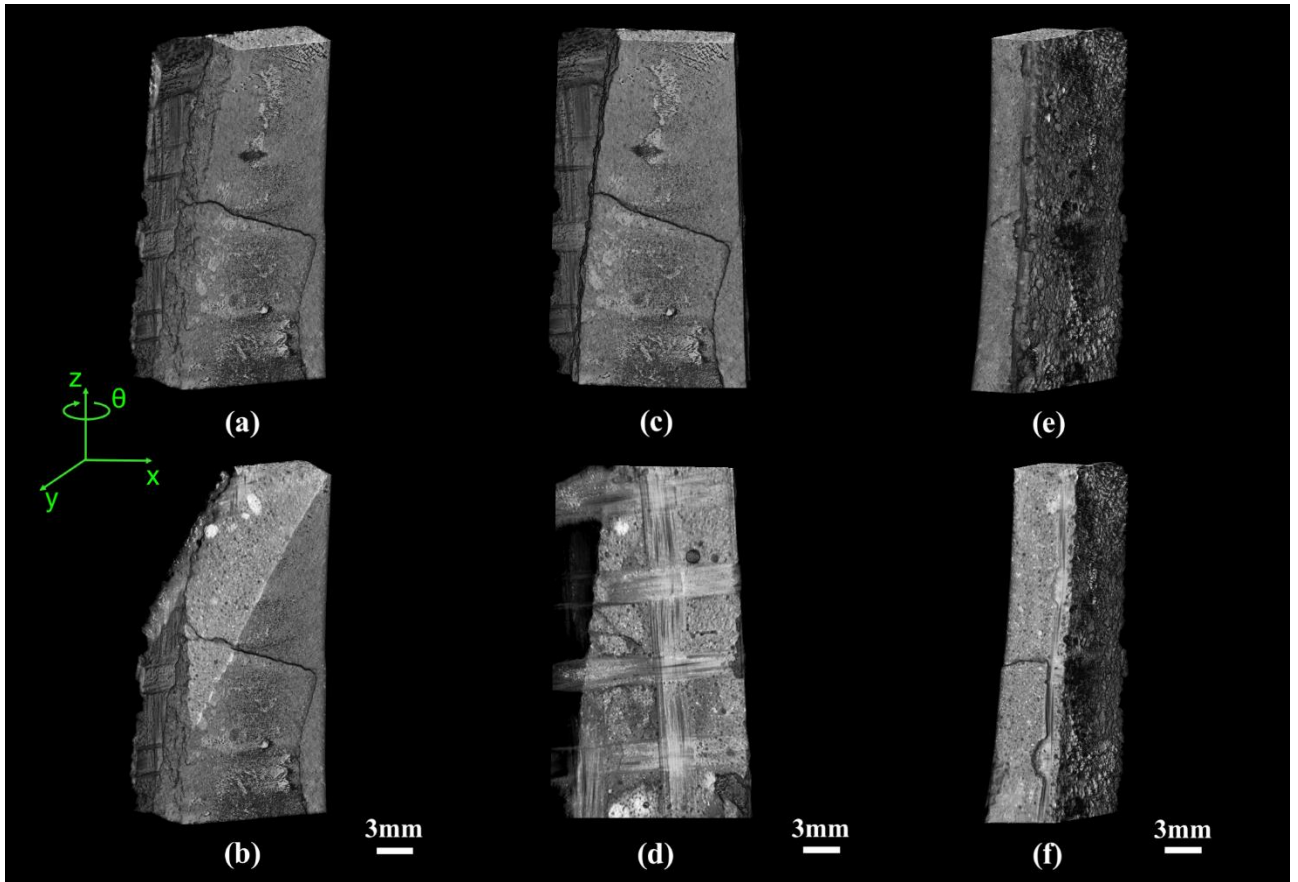


Fig. 25: 3D X-ray micro-CT reconstruction of sample B5: (a) general view in the start position, (b) view with randomly cut in start position, (c) general view rotated 15° from the start position, (d) view with randomly cut in rotate position (15°), (e) general view rotated 170° from the start position, (f) view with randomly cut in rotate position (170°),

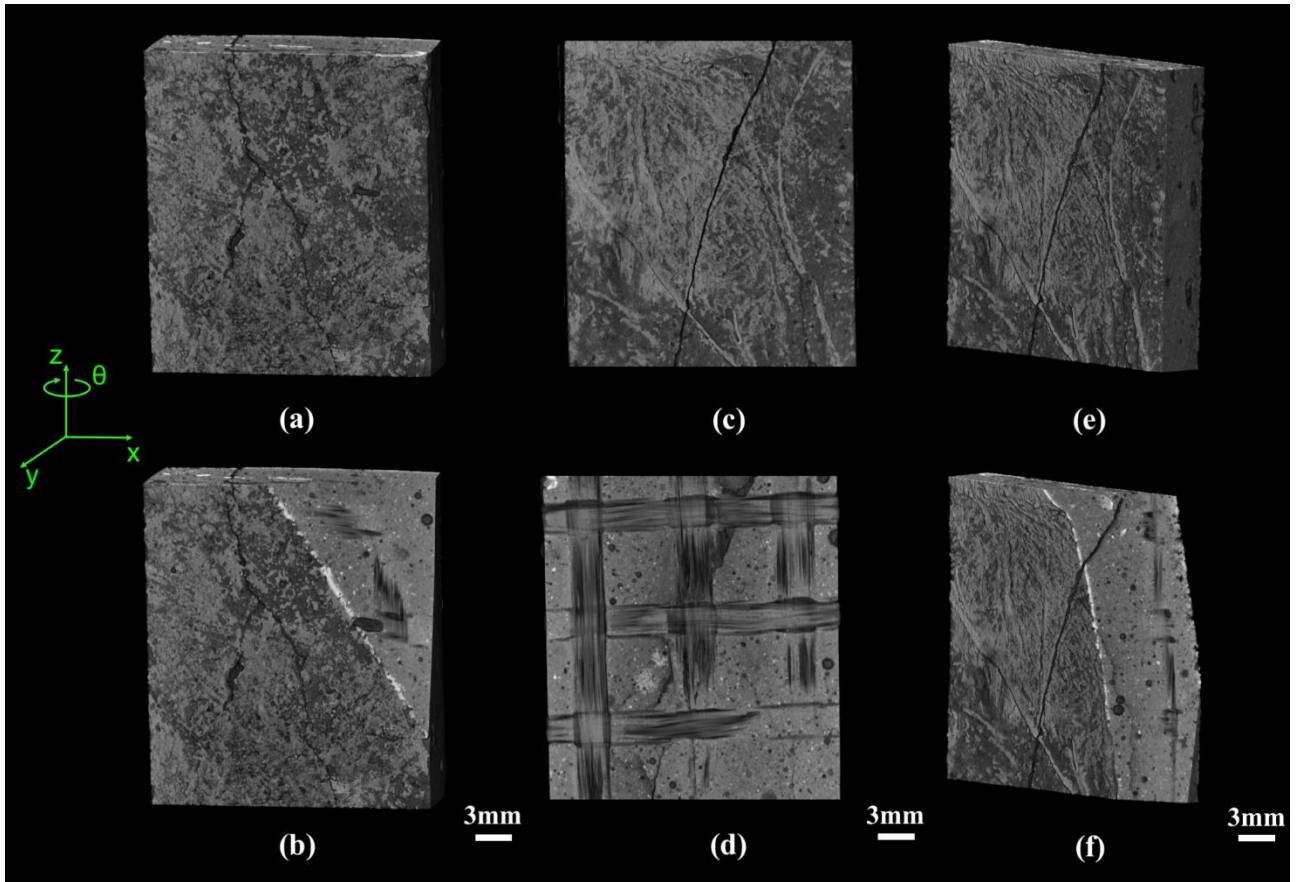


Fig. 26: 3D X-ray micro-CT reconstruction of sample B6: (a) general view in the start position, (b) view with randomly cut in start position, (c) general view rotated 5° from the start position, (d) view with randomly cut in rotate position (5°), (e) general view rotated 45° from the start position, (f) view with randomly cut in rotate position (45°),

From the 3D reconstructions it is possible to qualitatively observe the internal structure of the studied samples. In general, shape, and structural of the mortar, fibers and its textures are recognizable. In addition, in the samples it is possible to observe the presence of voids and cracks pattern.

In particularly, the basalt fibers are arranged in the two orthogonal directions to forming a grid (Figs. 24d, 25d, 26d, and Figs. 27b, 27d, and 27f):

- sample B2: the average value of the cross-sectional of one fiber bundle is 3mm wide and 0.5mm thick. The average distance between two fibers crossings is 9.2mm and the average size of a square mesh is 84.64mm^2 ;

- sample B5: the average value of the cross-sectional of one fiber bundle is 3mm wide and 0.5 mm thick. The average distance between two fibers crossings is 6.5mm and the average size of a square mesh is 42.25mm²;

- sample B6: the average value of the cross-sectional of one fiber bundle is 3mm wide and 0.5 mm thick. The average distance between two fibers crossings is 9mm and the average size of a square mesh is 81.00mm².

This value was confirmed by using of X-ray micro-CT and summarized in Tab. 10.

Tab. 10: Size of basalt fibers

| | B2 | B5 | B6 |
|---|-------|-------|-------|
| Basalt fiber width (mm) | 3.00 | 3.00 | 3.00 |
| Basalt fiber thickness (mm) | 0.50 | 0.50 | 0.50 |
| Distance between two basalt fibers (mm) | 9.20 | 6.50 | 9.00 |
| Mesh area of basalt fibers (mm ²) | 84.64 | 42.25 | 81.00 |

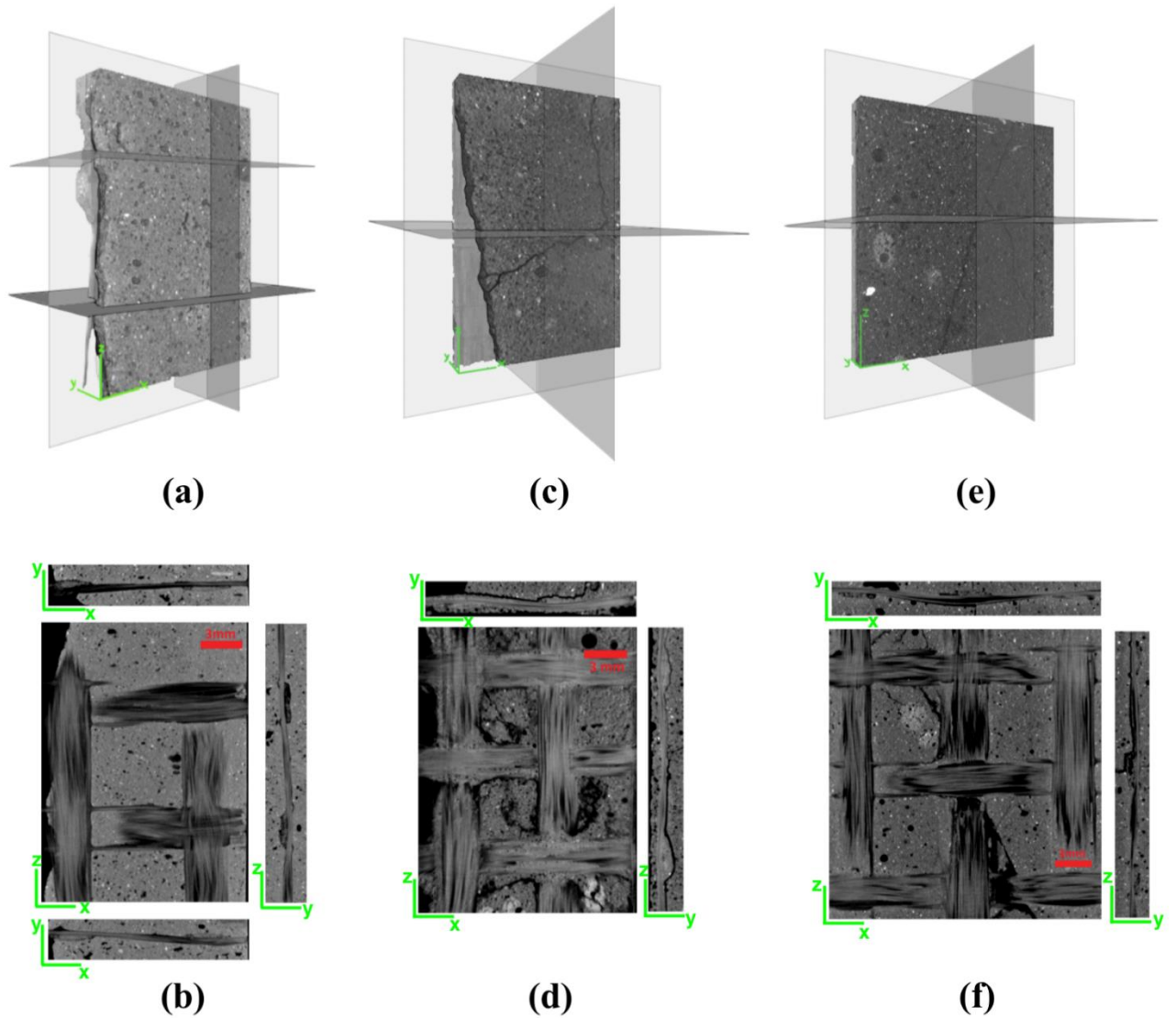


Fig. 27: cutting planes (a) with their respective 2D orthogonal projections (b) of sample B2; cutting planes (c) with their respective 2D orthogonal projections (d) of sample B5; cutting planes (e) with their respective 2D orthogonal projections (f) of sample B6.

An important tool for the analysis of 2D and 3D images is the grayscale histogram of the voxels.

A typical digital image is composed of pixels (picture elements), while an X-ray CT slice image is composed of voxels (volume elements). Each pixel has a resolution of 16 bits, therefore each of them is assigned a grayscale level value between 0 and 65535. This grayscale value represents the X-ray beam attenuation into the specimen. Pixels with value close to 0 (darker pixels) represent structures having less attenuation to the beam, i.e. soft matter (material with low Z number) or voids (bubbles air). While pixels close to 65535 (light pixels) represent structures having high attenuation,

i.e. high-density matter or material with high Z number. In practice, a grayscale histogram is a tool for the study of image contrast and for this reason gives information about the composition of the investigated sample.

In Fig. 28 are shown the histograms of the gray levels for the three samples investigated FRCM (B2, B5, B6). From a first analysis, is evident that the composition of the cement matrix and basalt fibers is similar, in fact in the histogram the grey levels of the two materials constitute a single peak.

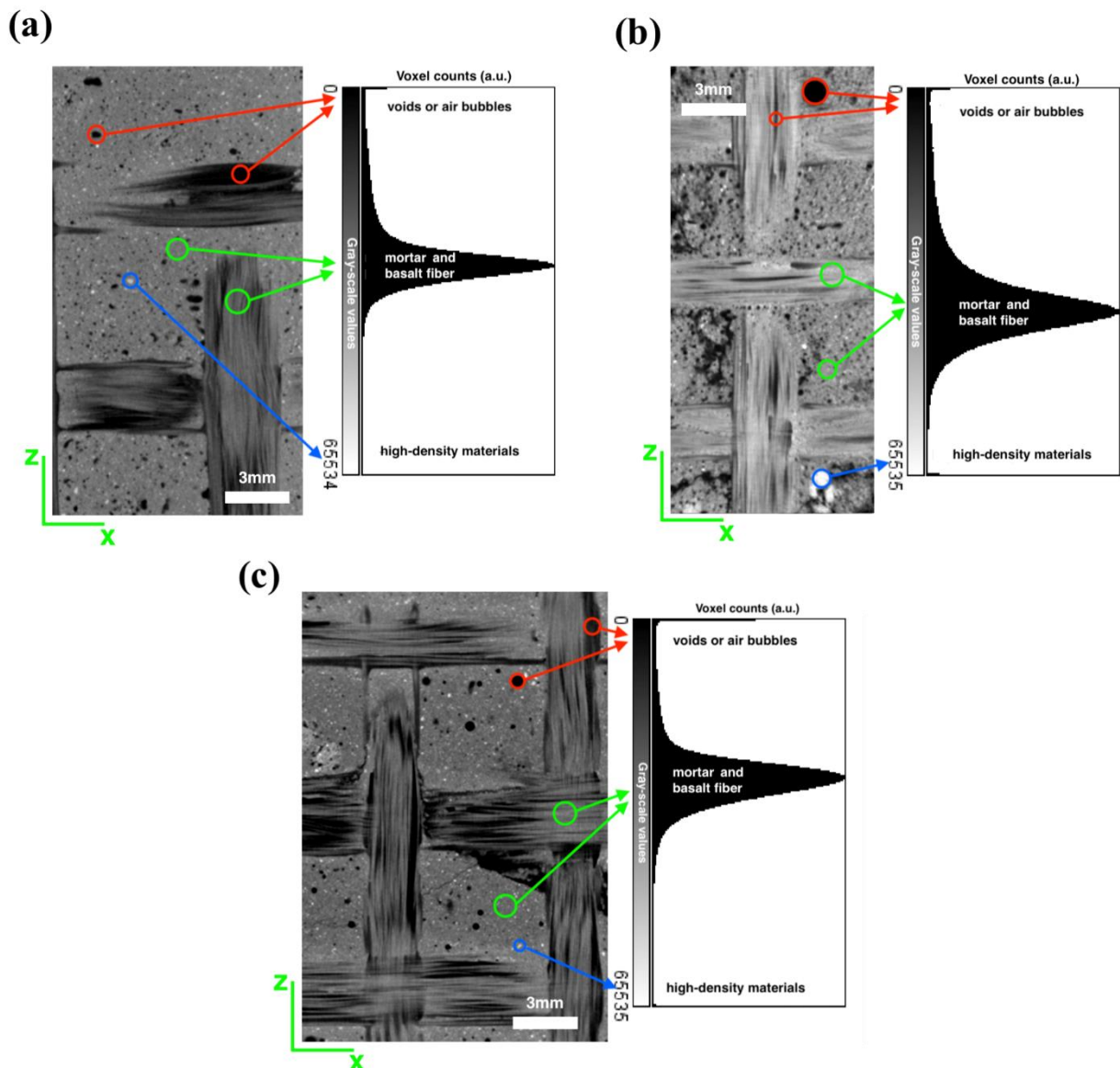


Fig. 28: X-ray micro-CT image extracted from the different samples, and its corresponding grayscale histogram: (a) sample B2; (b) sample B5; (c) sample B6. The image is composed of three different value of gray: mortar and the basalt fiber (middle gray), voids or air bubbles (dark), and high-density or inert materials (light gray).

Fig. 29 shown the graph of the intensities of pixels along the horizontal line selected (shown in yellow) within the image. The x-axis represents the distance (in micrometers) along the line selected and the y-axis is the pixel intensity in greyscale values. The grayscale values varying considerably by point to point: there are similar gray values for the cement matrix and the basalt fiber, while there are different values in the zone where there are voids. The mortar and the basalt fibers have an average gray value around 30000 for B2 and B6 samples, while for the B5 sample is around 40000. For the voids, cracks and detachment the gray value is reduced about to 0.

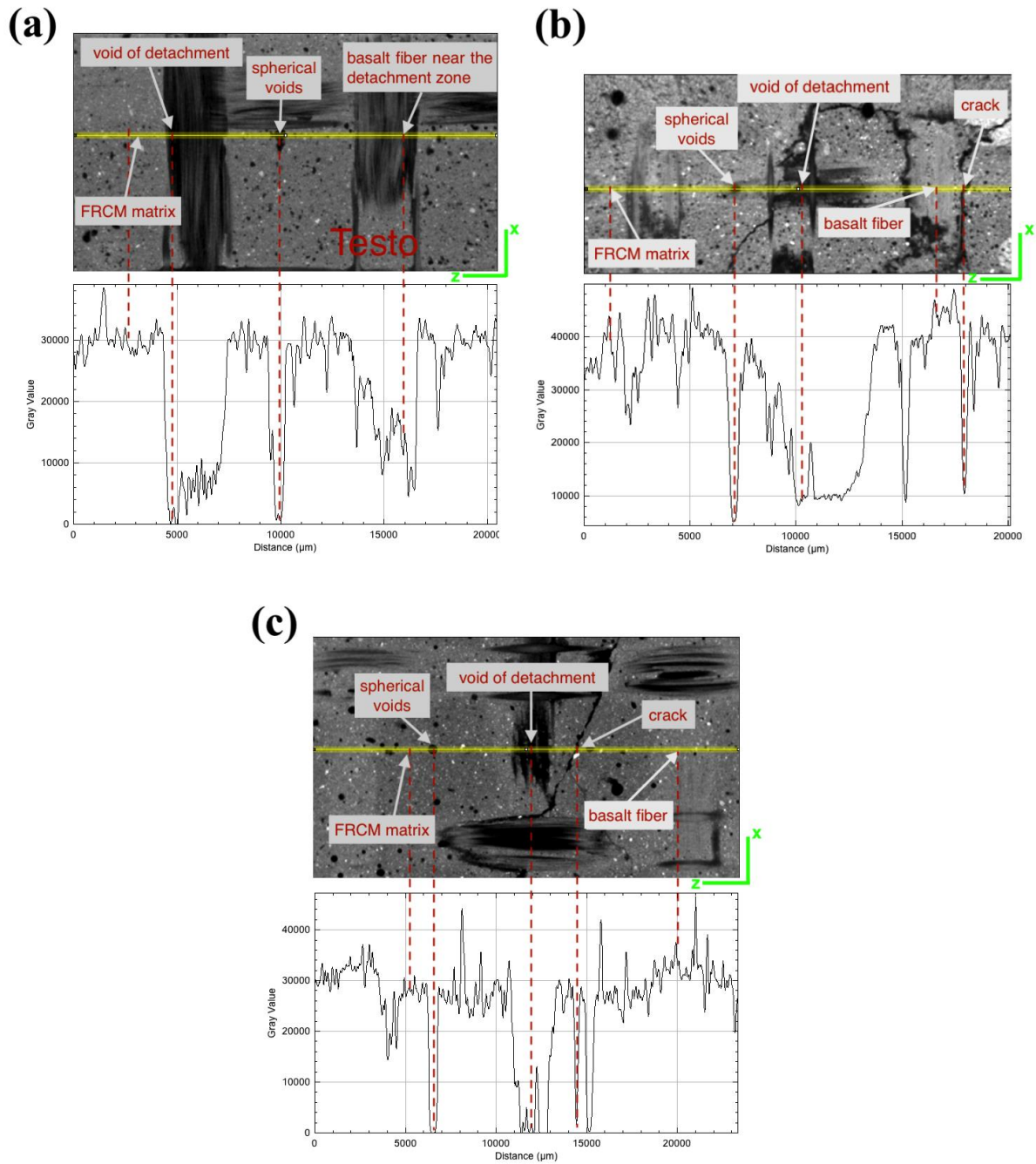


Fig. 29: Profile of grayscale levels for sample B2 (a), sample B5 (b), and sample B6 (c)

For the analysis of the detachment between the mortar and the basalt fibers, a segmentation of the gray levels was carried out to isolate the void zones (Fig. 30). The generally technique used for segmentation is the thresholding, a tool used for dividing an X-ray image into two classes of pixels. In our case, a threshold value has been selected between voids and solid part of B-FRCM, dividing

the regions with middle/high gray value intensity from those with low intensity of grey. The voids appear black, while the B-FRCM shown in white (Fig. 30).

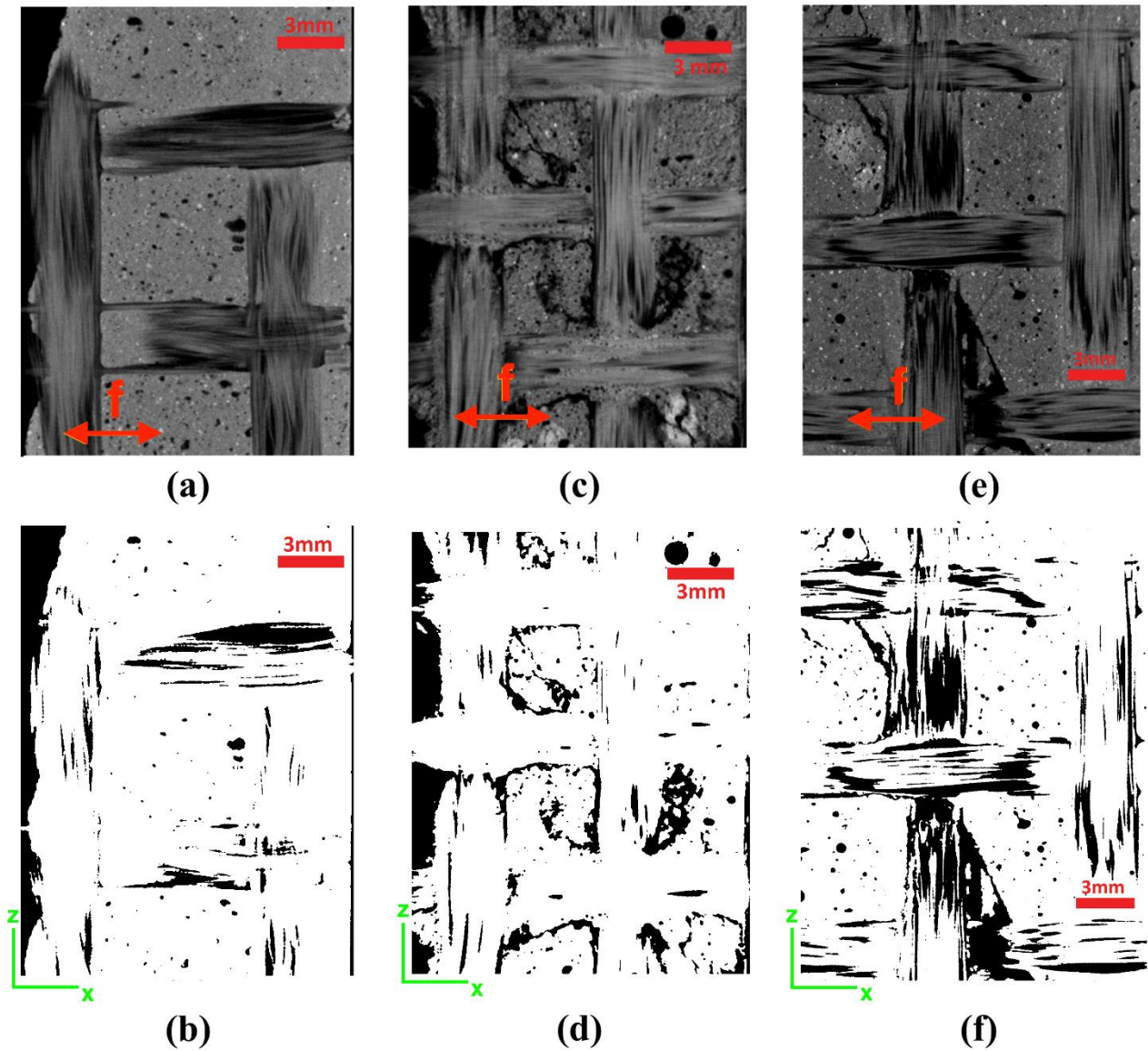


Fig. 30: 2D-images slices in the xz plane: slices and segmentation. Slice: (a) of sample B2; (c) of sample B5; (e) of sample B6. Identification of the voids (shape and distribution): (b) segmentation of sample B2; (d) segmentation of sample B5; (f) segmentation of sample B6

From Fig. 30 can argue the distribution of the voids and their nature. There are three types of voids: spherical voids, irregular voids, and crack. The first type of voids is placed inside the cement mortar with a fairly regular frequency and are due to the presence of bubbles of water and air, incorporated during the building of the specimen. As is evident from Fig. 30, Sample B5 is more porous than the

other two (B2 and B6). This because the mortar used was prepared with the addition of 30% water which, after hardening of the sample, evaporating, will leave by air bubbles (spherical voids).

The irregular voids are formed at the fiber-mortar interface and are due to the application of the tensile force, f , and at low penetration of the mortar into the basalt fibers activating a telescopic breakage. Therefore, the detachment between the two components is significant in the fibers arranged parallel to the direction of the stress, f , (Fig. 30 and Fig. 31).

The Fig. 31 show the evolution of the crack and detachments openings during tests.

In specimens B5 and B6 there are cracks, which are not present in specimen B2. This leads to the deduction that into B2 there is a better adhesion between fiber and mortar. In particular, in the specimens with cracks, occurred a local detachment between fiber and cement matrix.

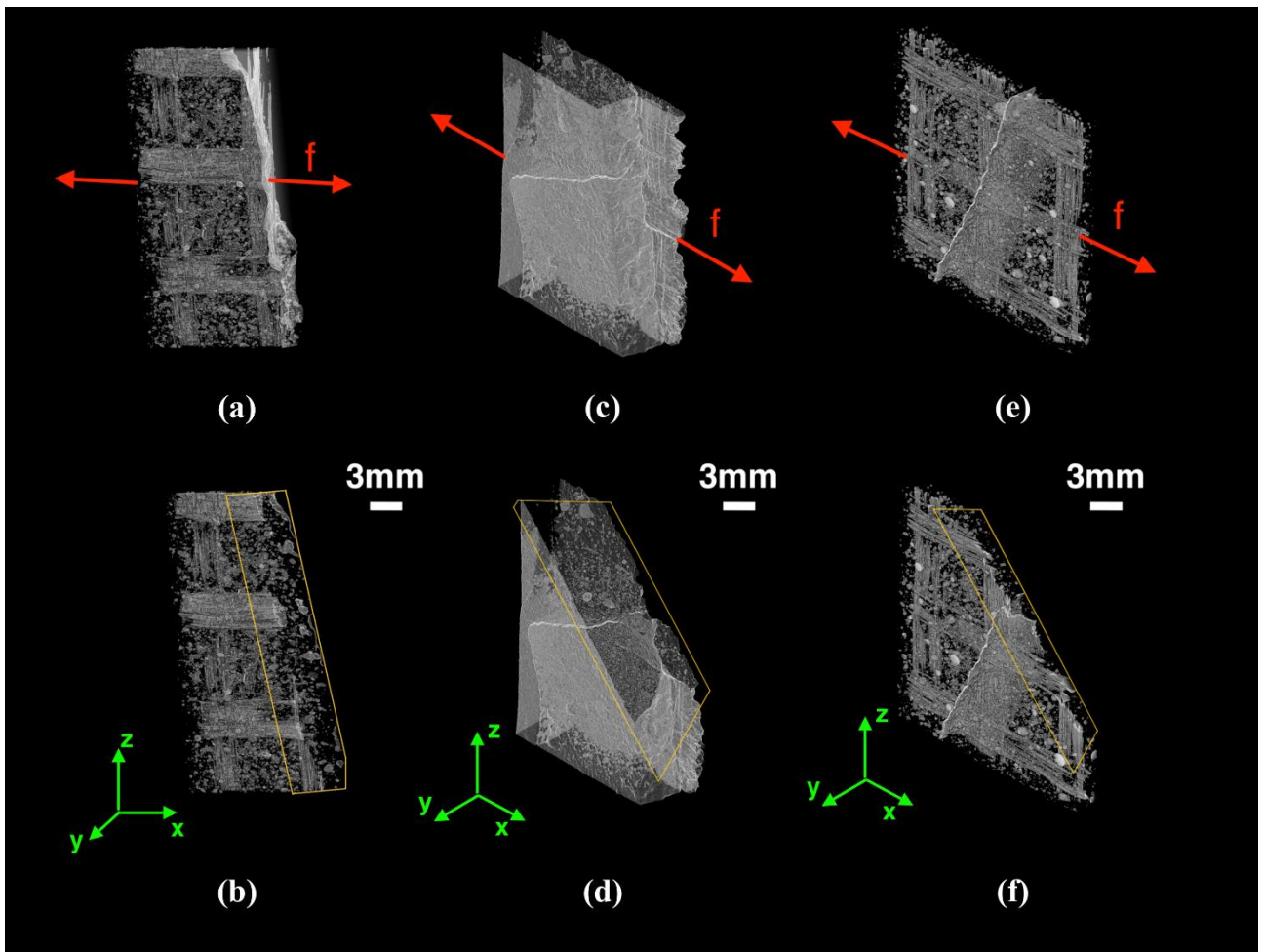


Fig. 31: 3D rendering of the voids: (a) sample B2, (c) sample B5, (e) sample B6. For each 3D-image is shown a cut: (b) sample B2, (d) sample B5, (f) sample B6. In red is indicate the direction of

the tensile force applied. The yellow line shows the cut plane. The 3D-Images show the evolution of the crack and detachments openings during tests.

The analysis of the 3D distribution of the voids allows us to understand how and where the basalt fiber detachments from the cement matrix occurred due to the traction force.

By images analysis, can be deduced that the maximum detachment occurred in the fibers arranged parallel to the applied force, while the fibers orthogonal to the direction of the force show few detachments. Furthermore, it is possible to note that the growth of the crack is about orthogonal to the direction of the applied force.

In Figs. 32, 33, and 34 are shown, respectively for the samples B2, B5, and B6, the 2D images (slices) of different scanning layers in the xy plane. For a better visualization of the voids they have been marked in red to show their structure and evolution within the various specimens.

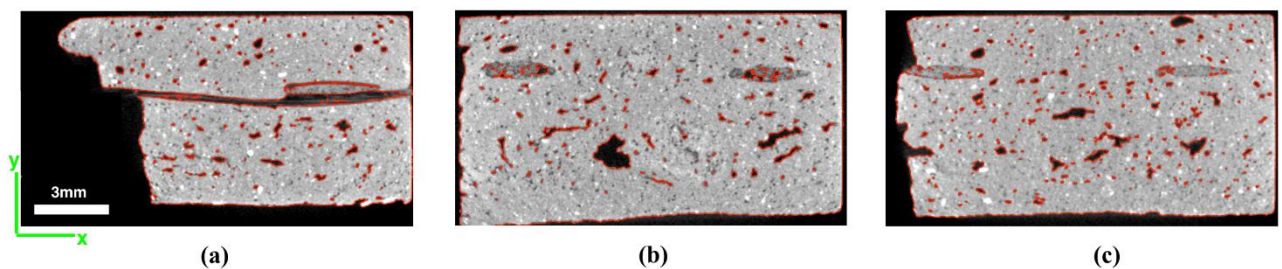


Fig. 32 Sample B2. The 2D images of different scanning layers in the xy plane. The contour of the voids is plotted in red.

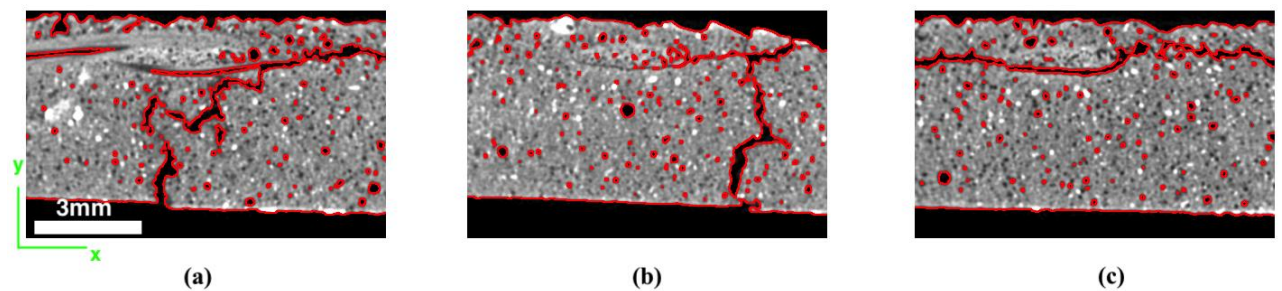


Fig. 33: Sample B5. The 2D images of different scanning layers in the xy plane. The contour of the voids is plotted in red.

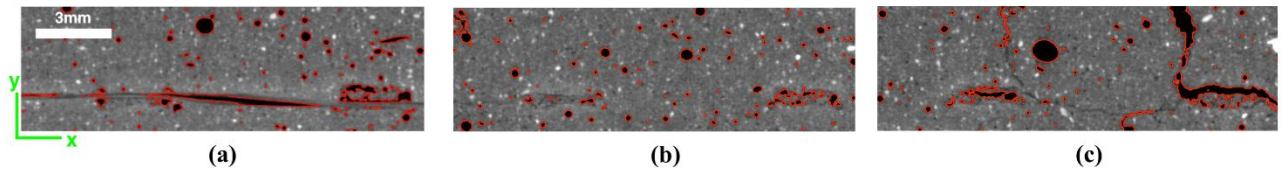


Fig. 34: Sample B6. The 2D images of different scanning layers in the xy plane. The contour of the voids is plotted in red.

Is possible to note as the materials used in the construction change the distribution and the density level of the voids inside the cement matrix.

In specimen B2 (Fig. 32) there is a uniform distribution of voids. It is possible to note the presence of other types of voids. In particular, in correspondence with the fiber positioned parallel to the direction of the traction force (directed along x-axis), there is a clear separation between the mortar and the basalt fiber (Fig. 32 a). The same type of detachment, but to a minor level, can be seen in the fiber positioned perpendicularly to the direction of the tensile force. In Fig. 32 b and 32 c are show the basalt fibers placed perpendicular to the traction force. In Fig. 32 b can see the presence of voids within the basalt fiber. In Fig. 32 c can see the presence of minimum detachment between the fiber and the mortar.

In sample B5 (Fig. 33) the quantity of voids is major respect B2 (Fig. 32) and B6 (Fig. 34) samples because the specimen was prepared with the addition of water. The B5 present a crack near the detachment between mortar-fiber, this crack is evident in all slices shown. In particular, in Fig. 33a is shown detachment between the fiber positioned parallel to the direction of the traction force (directed along x-axis) and the cement matrix. In Figs. 33 b and 33 c show the basalt fibers placed perpendicular to the traction force. The slice shown in Fig. 33 b is present the crack line and the voids within the basalt fiber. In Fig. 33 b shows the detachment between mortar and the basalt fiber positioned perpendicularly to the direction of the tensile force.

Also for the specimen B6 (Fig. 34) are shown: the spherical voids, the detachment voids between the cement matrix and the basalt fiber positioned parallel to the tensile force (directed along x-axis)

(Fig. 16a), the voids inside of the basalt fiber (Fig. 34 b), the detachment between mortar and fiber perpendicular to the traction force (Fig. 34 c). The slice shown in Fig. 34 c it is possible to observe the presence of the crack line near the fiber.

In this part, a study is reported on the fibers placed orthogonally to the direction of the traction force. By analyzing the micro-CT images, it is possible to evaluate the percentage of voids present.

The study on the specimens is carried out by choosing the volume of interest, VOI, indicated with the letters a, b, c in Fig. 35. The aim is to quantify the percentage of voids of spherical type (called voids inside the mortar), irregular (called voids inside the basalt fiber), and detachments (called voids of detachment). This study has been carried out in order to analyse the adhesion status between the cementitious matrix and the basalt fibers in the analyzed B-FRCM composites. The results are shown in Tab. 11.

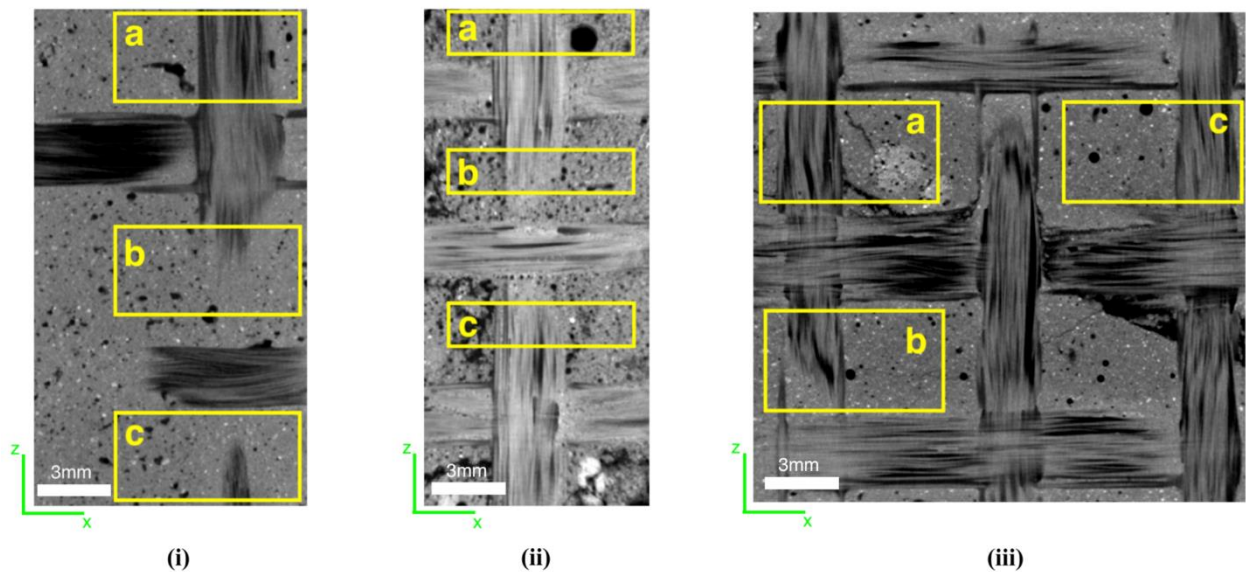


Fig. 35: Volume of Interest in B-FRCM with the relative VOI a, b, c: (i) Sample B2. (ii) Sample B5. (iii) Sample B6. (Note: in this figure the cross section of the volume is shown, but the analysis has been made on VOI).

Tab. 11: Voids volume percentage in the VOI a, b, c for the different samples B2, B5, and B6.

| Zone | B2 | | | B5 | | | B6 | | |
|-----------------------------------|------|------|------|-------|-------|-------|-------|------|------|
| | a | b | c | a | b | c | a | b | c |
| Voids inside the mortar (%) | 9.03 | 7.44 | 7.63 | 15.36 | 11.88 | 17.96 | 6.05 | 2.73 | 3.46 |
| Voids inside the basalt fiber (%) | 1.11 | 0.37 | 1.68 | 1.05 | 3.94 | 2.26 | 2.69 | 1.22 | 2.84 |
| Voids of detachment (%) | 0.01 | 0.01 | 0.02 | 1.55 | 2.88 | 9.93* | 8.82* | 3.29 | 4.13 |

*the sample presents a crack

For the sample B2, the voids inside the mortar volume percentage are equal to 9.03% of the volume a-VOI of Fig. 35i, 7.44% of the volume b-VOI of Fig. 35i, and 7.63% of the volume c-VOI of Fig. 35i. The voids inside the basalt fiber volume percentage are equal to 1.11% of the volume a-VOI of Fig. 35i, 0.37% of the volume b-VOI of Fig. 35i, and 1.68% of the volume c-VOI of Fig. 35i. The voids of detachment volume percentage are equal to 0.01% of the volume a-VOI of Fig. 35i, 0.01% of the volume b-VOI of Fig. 35i, and 0.02% of the volume c-VOI of Fig. 35i.

For the sample B5, the voids inside the mortar volume percentage are equal to 15.36% of the volume a-VOI of Fig. 35ii, 11.88% of the volume b-VOI of Fig. 35ii, and 17.96% of the volume c-VOI of Fig. 35ii. The voids inside the basalt fiber volume percentage are equal to 1.05% of the volume a-VOI of Fig. 35ii, 3.94% of the volume b-VOI of Fig. 35ii, and 2.26% of the volume c-VOI of Fig. 35ii. The voids of detachment volume percentage are equal to 1.55% of the volume a-VOI of Fig. 35ii, 2.88 % of the volume b-VOI of Fig. 35ii, and 9.93% of the volume c-VOI of Fig. 35ii. The volume percentage of the c-VOI detachment voids is larger than the a,b-VOIs, because in the volume of interest in which the calculation was made, sample B5 presents a crack that changes the result.

For the sample B6, the voids inside the mortar volume percentage are equal to 6.05% of the volume a-VOI of Fig. 35iii, 2.73% of the volume b-VOI of Fig. 35iii, and 3.46% of the volume c-VOI of Fig. 35iii. The voids inside the basalt fiber volume percentage are equal to 2.69% of the volume a-VOI of Fig. 35iii, 1.22% of the volume b-VOI of Fig. 35iii, and 2.84% of the volume c-VOI of Fig. 35iii. The voids of detachment volume percentage are equal to 8.82% of the volume a-VOI of Fig. 35iii, 3.29% of the volume b-VOI of Fig. 35iii, and 4.13% of the volume c-VOI of Fig. 35iii. The volume

percentage of the a-VOI detachment voids is larger than the b,c-VOIs, because in the volume of interest in which the calculation was made, sample B6 presents a crack that changes the result.

A summary of the results is shown in Tab. 12, and plotted in Fig.36, where the average values of the volume percentage of the voids for each individual sample are reported. This calculation was made by averaging the results obtained in the a,b,c-VOIs.

Tab. 12: Average voids volume percentage for the different samples B2, B5, and B6.

| | B2 | B5 | B6 |
|-----------------------------------|------|-------|------|
| Voids inside the mortar (%) | 8.03 | 15.07 | 4.08 |
| Voids inside the basalt fiber (%) | 1.05 | 2.42 | 2.25 |
| Voids of detachment (%) | 0.01 | 4.25 | 5.75 |

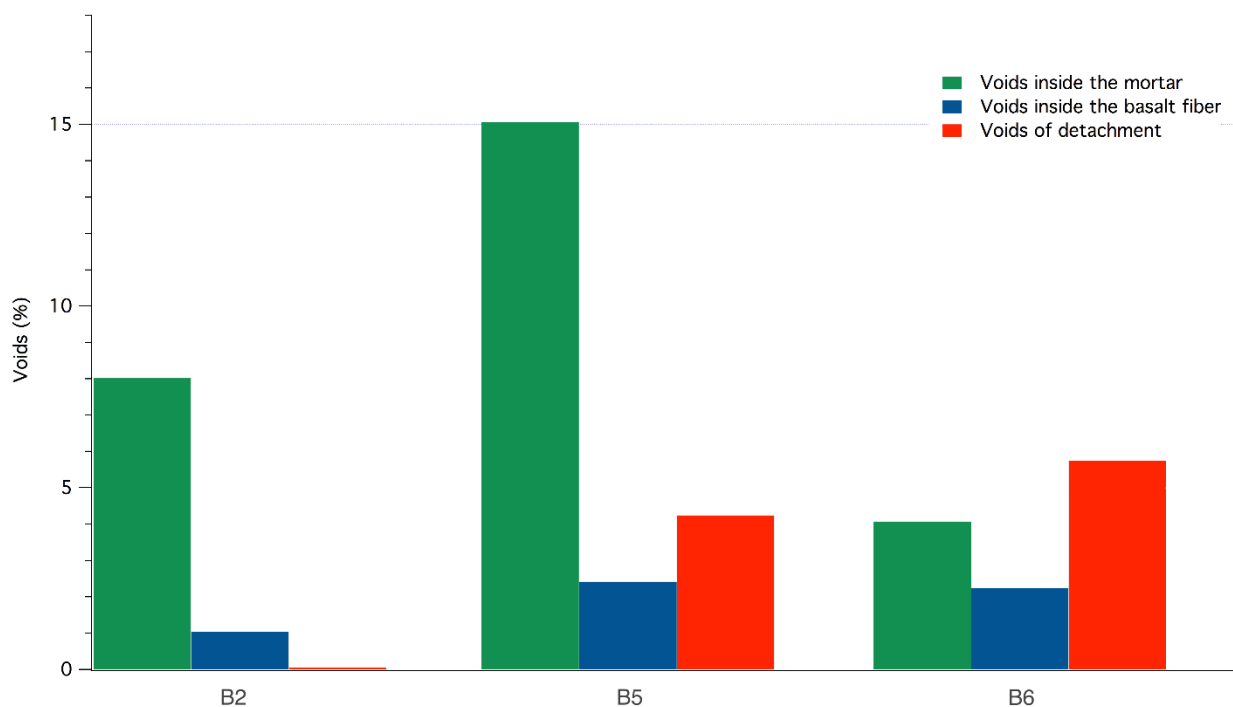


Fig. 36: Average voids volume percentage for the different samples B2, B5, and B6. Voids inside the mortar (green), voids inside the basalt fiber (blue), voids of detachment (red).

It follows that:

- Sample B5 has more voids inside the mortar than other samples due to the presence of water in the cement matrix. As the water evaporates, it leaves regular voids typically spherical in shape.

- In samples B5 and B6 the detachment voids are greater than those present in sample B2, due to the stress test.
- Sample B2 has a low percentage of voids within the basalt fiber and almost zero detachment voids. This means that in sample B2 the basalt fiber is more compact and forms a better bond with the mortar.

Conclusions

The advantages of using FRCM for the restoration and rehabilitation of masonry structures are many. Among them, certainly, the greater compatibility with the masonry support compared to the use of resins and FRP is one of the most important and guarantees a longer life and a better result. In addition, the choice of using fabrics of natural origin such as basalt allows the reduction of CO₂ emissions during their production. B-FRCM applied to masonry walls or vaults improves their strength to dynamic and static stresses without however significantly increasing their structural stiffness.

To date, the technical standards have not yet regulated the application parameters related to this type of structural reinforcement as done in the past for FRPs. The documents are nearing completion and several manufacturers of these materials are experimenting with the products before starting to go on sale.

This article used for the first time an innovative and totally experimental technique to evaluate what really happens inside FRCMs after they have been tested. Microtomography allowed to accurately highlight the presence of voids inside the samples and the real behaviour of the fiber-matrix interface. All the measurements showed a large presence of voids in the fiber FRCM and the non-perfect adherence between the parts. From this experimentation it was possible to deduce the crisis modes manifested in the three samples according to the classification drawn up by DT 215/2018 and shown in figure 2. In particular, it follows that:

- slip of the yarn in the mortar bed (breaking mode D) for all samples;

- yarn slipping and cracking of the outermost layer of mortar for specimen B5 only;
- detachment at the matrix-fabric interface for specimens B5 and B6.

Furthermore, the presence of voids in the mortar-fiber interface is minimal in the specimens made with inorganic mortar M1 (0.01%) (B2) while it is excessive (4.25%) in those made with organic M2 mortar with the addition of water. The presence of voids in a lower percentage inside the fiber incorporated in the mortar is instead found for the specimens made with M3 mortar (organic mortar without water) (2.25 %) but they are characterized, on the other hand, by a percentage of voids in the interface equal to 5.75%.

The aim of this research is to investigate the presence of voids incorporated in the fibers that to compromise the mechanical performance of the FRCM. By the use of the X-ray microtomography technique, it was possible to examine the samples in a non-invasive and non-destructive mode.

The analysis of the internal structure of the sample was carried out through a three-dimensional study. Once the 3D reconstruction of the samples is completed, the real position and morphology of voids, cracks, and fiber into the cement matrix in 3D space are displayed which was previously impossible. This is only a preliminary study and for future works new analyzes will be carried out on new innovative materials based always on cement mortars with the aim of increasingly reducing the presence of voids.

Reference

- [1] Gibson, R. F. (2016). Principles of composite material mechanics. CRC press.
- [2] Constantinides, G., Chandran, K. R., Ulm, F. J., & Van Vliet, K. J. (2006). Grid indentation analysis of composite microstructure and mechanics: Principles and validation. *Materials Science and Engineering: A*, 430(1-2), 189-202.
- [3] Codispoti, R., Oliveira, D. V., Olivito, R. S., Lourenço, P. B., & Figueiro, R. (2015). Mechanical performance of natural fiber-reinforced composites for the strengthening of masonry. *Composites Part B: Engineering*, 77, 74-83.

- [4] Cevallos, O. A., Olivito, R. S., Codispoti, R., & Ombres, L. (2015). Flax and polyparaphenylene benzobisoxazole cementitious composites for the strengthening of masonry elements subjected to eccentric loading. *Composites Part B: Engineering*, 71, 82-95.
- [5] L. Ascione, G. De Felice, S. De Santis. A Qualification Method For Externally Bonded Fiber Cementitious Matrix(FRCM) Streghtening System. *Composites: Part B:78* (2015) pp.497-506.
- [6] F. G. Carozzi, G. Milani, C. Poggi. Mechanical properties and numerical modeling of Fabric Reinforced Cementitious Matrix (FRCM) systems for strengthening of masonry structures. *Composites Structures* 107 (2014) pp. 711-725.
- [7] Menna, C., Asprone, D., Ferone, C., Colangelo, F., Balsamo, A., Prota, A., ... & Manfredi, G. (2013). Use of geopolymers for composite external reinforcement of RC members. *Composites Part B: Engineering*, 45(1), 1667-1676.
- [8] Yang, F., Zhang, B., & Ma, Q. (2010). Study of sticky rice– lime mortar technology for the restoration of historical masonry construction. *Accounts of chemical research*, 43(6), 936-944.
- [9] Tiberti, S., Scuro, C., Codispoti, R., Olivito, R. S., & Milani, G. (2017). Post-cracking FRCM strengthening of an arch composed by hollow clay elements embedded in mortar: experimental investigations and numerical analyses. In *Key Engineering Materials* (Vol. 747, pp. 142-149). Trans Tech Publications Ltd.
- [10] L. Ascione, G. De Felice, S. De Santis. A Qualification Method for Externally Bonded Fiber Cementitious Matrix (FRCM) Streghtening System. *Composites: Part B:78* (2015) pp.497-506.
- [11] R. S. Olivito, R. Codispoti, C. Scuro, S. Porzio, “Experimental evaluation of the adhesion of a FRCM-tuff strengthening system”, AIAS – Associazione Italiana Analisi delle Sollecitazioni, Villa San Giovanni, Italy, 5-8 Settembre 2018.
- [12] F. G. Carozzi, P. Colombi, G. Fava, C. Poggi. A cohesive interface crack model for the matrix-textile debonding in FRCM composites. *Composite Structures* 143 (2016) pp.230-241.
- [13] A. D’Ambrisi, L. Feo, F. Focacci. Bond slip relations for PBO-FRCM materials externally

bonded to concrete. *Composites: Part B* 43 (2012) pp. 2938-2949.

- [14] L. Ombres. Analysis of the bond between Fabric Reinforced Cementitious Mortar (FRCM) strengthening systems and concrete. *Composites: Part B* 69 (2015) pp.418-426.
- [15] D.B. Dittenber, H.V.S. GangaRao, “Critical review of recent publications on use of natural composites in infrastructure”, in *Composites: Part A* 43, 2012, pp. 1419-1429.
- [16] Olivito, R.S., Codispoti, R., Cevallos, O.A. Bond behavior of Flax-FRCM and PBO-FRCM composites applied on clay bricks: Experimental and theoretical study (2016) *Composite Structures*, 146, pp. 221-231, DOI: 10.1016/j.compstruct.2016.03.004
- [17] E. Grande, M. Imbimbo, E. Sacco. Modeling and numerical analysis of the bond behavior of masonry elements strengthened with SRP/SRG. *Composites: Part B* 55 (2013) pp.128-138.
- [18] A. Razavizadeh, B. Ghiassi, D.V. Oliveira. Bond behavior of SRG-strengthened masonry units: Testing and numerical modeling. *Construction and Buildings Materials* 64 (2014) pp.387-397.
- [19] K. Nakaba, T. Kanakubo, T. Furuta, H. Yoshizawa. Bond Behavior between Fiber-Reinforced Polymer Laminates and Concrete. *ACI Structural Journal*/May-June 2001.
- [20] J. Yao, J. G. Teng, J. F. Chen. Experimental study on FRP-to-concrete bonded joints. *Composites. Part B* 36 (2005) pp.99-113.
- [21] A. Bellini, C. Mazzotti, “Bond Behavior of FRCM Composites Applied on Concrete and Masonry”, in *Proceedings of Italian Concrete Days 2018*, pp. 347-359.
- [22] L.H. Sneed, “A comparison of the bond behavior of PBO-FRCM composites determined by double-lap and single-lap shear tests”, in *Cement and Concrete Composites* 64, 2015, pp. 37-48.
- [23] D.M. 03/12/2019, n.627, Linea Guida per la progettazione, l’esecuzione e la manutenzione di interventi di consolidamento strutturale mediante l’utilizzo di sistemi di rinforzo FRCM.
- [24] CNR-DT 200 R1/2013 - Istruzioni per la Progettazione, l’Esecuzione ed il Controllo di Interventi di Consolidamento Statico mediante l’utilizzo di Compositi Fibrorinforzati.

- [25] CNR-DT 215/2018 – Istruzioni per la Progettazione, l’Esecuzione ed il Controllo di Interventi di Consolidamento Statico mediante l’utilizzo di Compositi Fibrorinforzati a Matrice Inorganica.
- [26] Carozzi, F. G., Colombi, P., Fava, G., & Poggi, C. (2016). A cohesive interface crack model for the matrix–textile debonding in FRCM composites. *Composite Structures*, 143, 230-241.
- [27] EN ISO 13934-1 and EN ISO 13934-2:1999, "Tensile properties of fabrics, Part 1: Determination of maximum force and elongation at maximum force using the strip method, Part 2: Determination of maximum force using the grab method".
- [28] NP EN ISO 2062 "Textile yarn winding in the form of determination of strength of break and elongation at break".
- [29] BS EN 1015-11:1999 "Methods of test for mortar for masonry - Part 11: Determination of flexural and compressive strength of hardened mortar".
- [30] CNR, 2012. CNR-DT 200 R1/2013, Istruzioni per la Progettazione, l’Esecuzione ed il Controllo di Interventi di Consolidamento Statico mediante l’utilizzo di Compositi Fibrorinforzati Materiali, strutture di c.a. e di c.a.p., strutture murarie.
- [31] Standard Test Methods for Density and Specific Gravity (Relative Density) of Plastics by Displacement
- [32] ISO 3374- 2000, Reinforcement products — Mats and fabrics — Determination of mass per unit area.
- [33] ISO TC 71/SC 6 N - 2003, "Non-traditional reinforcing materials for concrete structures", Testing methods for fibre-reinforced cementitious composites/FRP reinforcement material specifications.
- [34] AC 343 Design Document - Cement based carbon fiber strengthening system.
- [35] D. Wildenschild and A. P. Sheppard, “X-ray imaging and analysis techniques for quantifying pore-scale structure and processes in subsurface porous medium systems,” *Adv. Water Resour.*, 2013.

- [36] J. D. Boerckel, D. E. Mason, A. M. McDermott, and E. Alsberg, “Microcomputed tomography: approaches and applications in bioengineering,” *Stem Cell Res. Ther.*, vol. 5, no. 6, p. 144, 2014.
- [37] E. N. Landis and D. T. Keane, “X-ray microtomography,” *Mater. Charact.*, vol. 61, no. 12, pp. 1305–1316, 2010.
- [38] S. C. Lee, H. K. Kim, I. K. Chun, M. H. Cho, S. Y. Lee, and M. H. Cho, “A flat-panel detector based micro-CT system: Performance evaluation for small-animal imaging,” *Phys. Med. Biol.*, 2003.
- [39] A. C. Kak and M. Slaney, “Principles of computerized tomographic imaging IEEE Press,” New York, 1988.
- [40] L. A. Feldkamp, L. C. Davis, and J. W. Kress, “Practical cone-beam algorithm,” *Josa a*, vol. 1, no. 6, pp. 612–619, 1984.
- [41] C. N. Ionita, K. R. Hoffmann, D. R. Bednarek, R. Chityala, and S. Rudin, “Cone-beam micro-CT system based on LabVIEW software,” *J. Digit. Imaging*, vol. 21, no. 3, pp. 296–305, 2008.
- [42] J. Schindelin et al., “Fiji: an open-source platform for biological-image analysis,” *Nat. Methods*, vol. 9, no. 7, pp. 676–682, 2012.
- [43] T. J. Collins, “ImageJ for microscopy,” *Biotechniques*, vol. 43, no. S1, pp. S25--S30, 2007.
- [44] M. S. Costanza-Robinson, B. D. Estabrook, and D. F. Fouhey, “Representative elementary volume estimation for porosity, moisture saturation, and air-water interfacial areas in unsaturated porous media: Data quality implications,” *Water Resour. Res.*, vol. 47, no. 7, 2011.
- [45] J. Ollion, J. Cochenec, F. Loll, C. Escudé, and T. Boudier, “TANGO: a generic tool for high-throughput 3D image analysis for studying nuclear organization,” *Bioinformatics*, vol. 29, no. 14, pp. 1840–1841, 2013.
- [46] N. Otsu, “A threshold selection method from gray-level histograms,” *IEEE Trans. Syst. Man. Cybern.*, vol. 9, no. 1, pp. 62–66, 1979.
- [47] K. U. Barthel, “3D-data representation with ImageJ,” in *ImageJ Conference*, 2006.

- [48] B. Schmid, J. Schindelin, A. Cardona, M. Longair, and M. Heisenberg, “A high-level 3D visualization API for Java and ImageJ,” *BMC Bioinformatics*, vol. 11, no. 1, pp. 1–7, 2010.

4.2 CASE STUDY 2: Analysis of extruded pins manufactured by friction stir forming for multi-material joining purposes.

Analysis of extruded pins manufactured by friction stir forming for multi-material joining purposes

Cite as: AIP Conference Proceedings **2113**, 050026 (2019); <https://doi.org/10.1063/1.5112590>
Published Online: 02 July 2019

Romina Conte, Raffaele Filosa, Vincenzo Formoso, Francesco Gagliardi, Raffaele G. Agostino, and Giuseppina Ambrogio



View Online



Export Citation

ARTICLES YOU MAY BE INTERESTED IN

[Modelling of extrusion welding conditions for EN AW-7020 aluminium alloy](#)

AIP Conference Proceedings **2113**, 050027 (2019); <https://doi.org/10.1063/1.5112591>

[Joining by laser induced shock waves of aluminum and plastics](#)

AIP Conference Proceedings **2113**, 050029 (2019); <https://doi.org/10.1063/1.5112593>

[Friction press joining of dissimilar materials: A novel concept to improve the joint strength](#)

AIP Conference Proceedings **2113**, 050031 (2019); <https://doi.org/10.1063/1.5112595>

AIP | Conference Proceedings

Get **30% off** all
print proceedings!

Enter Promotion Code **PDF30** at checkout



Analysis of Extruded Pins Manufactured by Friction Stir Forming for multi-material joining purposes

Romina Conte¹, Raffaele Filosa^{2,3}, Vincenzo Formoso^{2,3,4}, Francesco Gagliardi¹,
Raffaele G. Agostino^{2,3,4}, Giuseppina Ambrogio^{1, a)}

¹ *Department of Mechanical, Energy and Management Engineering - University of Calabria – Ponte P. Bucci Cubo 45/C, Rende (CS) – 87036, Italy*

² *Department of Physics - University of Calabria – Ponte P. Bucci Cubo 31/C, Rende (CS) – 87036, Italy*

³ *Sistema Tecnologico MaTeRiA, Università della Calabria, via Pietro Bucci, 87036 Arcavacata di Rende (Cosenza), Italy*

⁴ *Consiglio Nazionale delle Ricerche, Istituto di Nanotecnologia, Cosenza Unit, I-87036 Arcavacata Di Rende (Cosenza), Italy.*

a) Corresponding author: g.ambrogio@unical.it

Abstract. Nowadays the application of multi-material parts has become a standard in several sectors, such as in transportation where the use of dissimilar material contributes to reduce the weight of structural components, as well as to decrease fuel consumption and CO₂ emissions. The scientific literature proposes various methods for combining dissimilar materials, but when there are too incompatible, the process becomes a real challenge.

To this aim and to propose an alternative joining technique, which does not require the use of additional external parts, the authors investigated a method based on the Friction Stir Forming (FSF) technology. FSF is a process, where a rotating tool moves on a metal sheet pushing the material through the holes of a forming die positioned under the worked sheet.

In the current study, the authors aimed at improving the quality of the aluminium extruded pins, which leads to the improvement of the connection with composite materials. To this aim, a specific equipment has been manufactured and installed on a general purpose milling machine and an experimental plan has been designed. Both process (i.e. spindle speed, forming velocity) and geometrical parameters (i.e. hole diameter and the distance between the holes) have been considered. A deep analysis has been carried out on the extruded aluminium pins in terms of internal structure. Specifically, an X-ray micro-tomographic analysis has been performed to investigate, qualitatively and quantitatively, the distribution of the material within the manufactured pins. The void content and the final height of the pins have been measured aiming at understanding how these outputs can be affected by the investigated parameters.

INTRODUCTION

The combination of dissimilar materials has become a standard in several fields, in particular in those where the lightweight performance plays a fundamental role.

Adhesive bonding, mechanical fastening and fusion bonding can be involved in the connection of materials that are chemically and mechanically different, such as metals and fiber reinforced composites [1].

Adhesive bonding allows the joint of parts by using a binder. It is a low cost technique, that does not cause the weight increase of the assembled part and furthermore, when composites are involved in the process, fibers are not damaged. Nonetheless, the low temperature resistance and the difficulties related to the disassembly are the main drawbacks [2, 3].

Many techniques belong to the mechanical fastening category. They require or not external elements for performing the joint [4]. In the first case, the use of rivets or bolts provides strengths for long term-application, but causes an increase in weight and a decrease in the maximum load-bearing capacity due to the drilled holes that also reduce the cross section area [5, 6]. On the other hand, clinching is one of those technologies that does not need further

components to perform the joint. In case of metal and composites, for instance, a punch is used to force the metal into the predrilled composite [7]. The main problems that may arise are delamination and cracks around the pierced area [1].

Fusion bonding methods require the use of a heating source for melting the parts and, according to that, several techniques may be distinguished, such as laser assisted welding [8], friction lap joining [9], friction lap welding [10]. Recently, the combination of friction stir welding and friction stir forming (FSF) process was experimented to connect metal and composite [11, 12]. The FSF process is based on a rotating rigid tool, plunged into a metal sheet, that moves horizontally pushing the material through a forming die extruding pins [13]. After that, the metal plate with pins is placed on a predrilled composite sheet and pressed on it [12]. Further studies will focus on piercing directly the composites with the pins.

Based on the preliminary study [12], to the aim of this work, a new investigation has been carried out in order to understand in more depth the influence of the process parameters on the extruded pins and hence at improving their quality. The voids inside the formed pins have been measured by x-ray micro tomography and their size has been connected to the process and geometrical parameters investigated in the performed research. Considerations on the final pin height achievable for each specific working condition have been also provided.

MATERIAL AND METHOD

Material

FSF process was carried on aluminium EN AW-1050A-H111 sheets, which dimensions are 180x80x3 mm. The material properties are reported in the following Table 1.

Table 1. Mechanical and thermal properties of aluminium EN AW-1050A-H111

| Material | Young's Modulus (GPa) | Yield Strength (MPa) | Tensile Strength (MPa) | Elongation (%) | Thermal Conductivity (W/mK) | Spec. Heat Capacity (J/Kg °C) |
|------------------|-----------------------|----------------------|------------------------|----------------|-----------------------------|-------------------------------|
| EN AW-1050A-H111 | 69 | 30 | 65-90 | 30 | 230 | 900 |

Method

To perform the FSF method, a new equipment was designed, manufactured and finally installed on a Mazak Nexus 410A vertical CNC machine according to defined tilt angles and aiming at evaluating the material flow into the die. Figure 1 displays all the details of the used equipment. The forming die is made of two lines of holes that are characterized by a diameter \varnothing of 4 mm and 6 mm, respectively. On each line, the holes have been drilled at three different distances (d) (Fig. 1 b). The shape of the forming tool was chosen according to [13] with a shoulder of 15 mm and a probe of 5 mm.

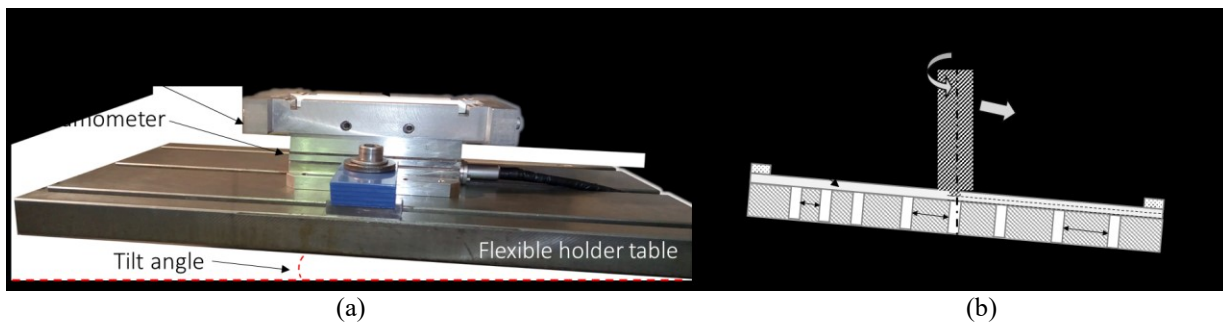


Figure 1. Details of the FSF equipment

The first tests were carried out fixing a spindle speed (S) of 3000 RPM and a penetration depth (p) equal to 0.1 mm. Forming velocity (F) and tilt angle (α) were, instead, the variable parameters (Fig. 1). Values of 25 and 300 mm/min and of 5° and 7.5° were used according a preliminary screening performed in [12]. The process was performed on the aluminium sheet, manufacturing two lines of eight pins each time. The second line was manufactured after having cooled down in air the sheet.

A X-ray micro-tomographic analysis (micro-CT) was executed on the extruded pins. The micro-CT is a non-destructive technique of radiographic imaging able to produce 3D images of the inner structure of a material with a micro spatial resolution, exploiting a set of bi-dimensional radiographic images from a sample [14, 15]. The principle of micro-CT is based on the attenuation of X-rays. As an X-ray passes through a homogeneous object, the intensity of the incident X-ray beam is reduced according to the Lambert-Beer equation: $I = I_0 e^{-\mu x}$, where I_0 is the intensity of the incident beam, x is the distance covered by the X-ray in the absorbing object and μ is the linear attenuation coefficient [16].

The μ Tomo experimental station, based on a cone beam geometry, used to the aim of this analysis and shown schematically in Fig. 2, is made of:

- a microfocus X-ray source Hamamatsu L12161-07
- a flat panel detector Hamamatsu C7942SK-05
- a five degree of freedom sample positioning system (linear movement and rotation)
- a hardware and a software system for data acquisition and analysis.

The X-ray source and the detector system are stationary and the object rotates around the rotation centre. Indeed, the sample to be scanned is positioned and rotates of 360° around an axis perpendicular to the incident beam. The transmitted signal is recorded at regular intervals during rotation using the flat panel detector. The projected X-ray images, characterized by a magnification of 3 ($M=SDD/SOD$), are acquired and mathematically reconstructed to produce a 3D map presented as a series of 2D slices [14].

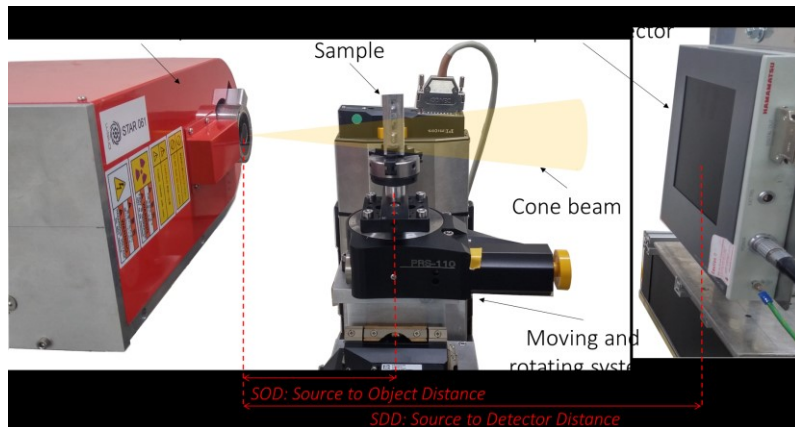


Figure 2. μ Tomo experimental station

DISCUSSION OF THE RESULTS

An upper and a lower side of a formed sheet is depicted in Fig. 3. Looking at the upper side, two grooved lines, owing to the forming tool, can be observed. Their depth and width depend on the set p value and tilt angle. On the lower side, instead, the manufactured pins are visible. From a pure qualitative standpoint, the pin height is influenced by the hole diameters and from the distance, d .



Figure 3. Example of a manufactured sample: (a) upper side and (b) lower side

The X-ray micro-CT provided a 3D reconstruction of all the manufactured pins with a lateral resolution of about 15 μm . An example is displayed in Fig. 4 a), where structural defects can be observed on the external surface of the extruded part. These defects were quantified in terms of void distribution within the whole pin volume (an example is displayed in Fig. 4 b) and measured as percentage of the total volume.

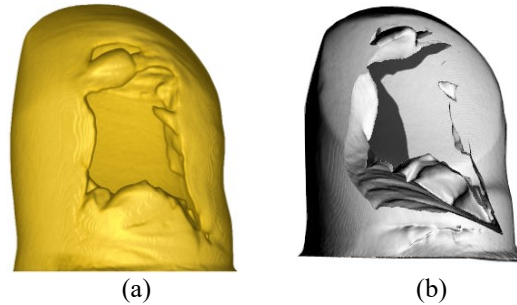


Figure 4. (a) Rendering of a 3D pin ($S=3000$ RPM, $p=0.1$ mm, $F=25$ mm/min, $\varnothing=6$ mm) reconstructed by micro-CT, (b) rendering of the void content (12.69%)

The quantification of pin height and void content for each combination of the investigated geometrical and process parameters is reported in the following Fig. 5 and Fig. 6. The first phase of the research was focused on the analysis of influence of the forming velocity using a constant tilt angle ($\alpha=5^\circ$). Specifically, looking at the configurations with $\varnothing=4$ mm, the forming velocity does not influence either the pin height or the void content, significantly. This suggests that the extrusion force, owing to a higher extrusion ratio, should result adequate to push and compact the material thorough hole. Actually, the same effect should be higher for $F=300$ mm/min, but, for this velocity, the forming temperatures are lower reducing, therefore, the material flow. The two opposite effects are balanced and, hence, the pins look quite similar. On the other side, in the case of $\varnothing=6$ mm, F becomes relevant on the quality of the formed parts. Indeed, the extrusion ratio is lower and, as a consequence, the forces should be reduced if compared to the previous condition. The combination of lower forces and higher material temperature ($F=25$ mm/min) causes an easier aluminium flow into the hole leading to higher pins with a consistent void content. On the contrary, an F increment reduces the material temperature and, hence, the process forces. This state allows a proper material squeezing obtaining smaller pins, but more compacted (Fig. 5).

A second step of the study was based on the investigation of the tilt angle influence. The forming velocity was fixed in this case ($F=300$ mm/min). If the tilt angle increases ($\alpha=7.5^\circ$), the punch moves more material hence its shoulder pierces through the sheet in more depth. As a consequence, the extruded pins are higher and with a reduced void content. This effect is more evident when pins with a small diameter are shaped (Fig. 6).

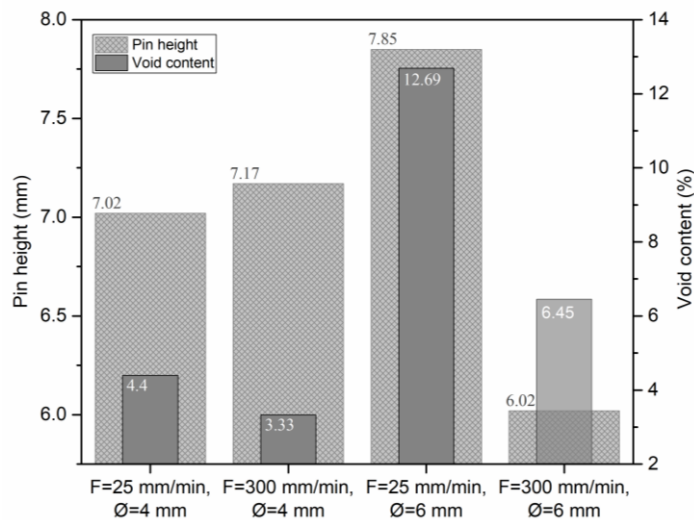


Figure 5. Pin height and void content for different combination of F and \varnothing and fixed tilt angle ($\alpha=5^\circ$).

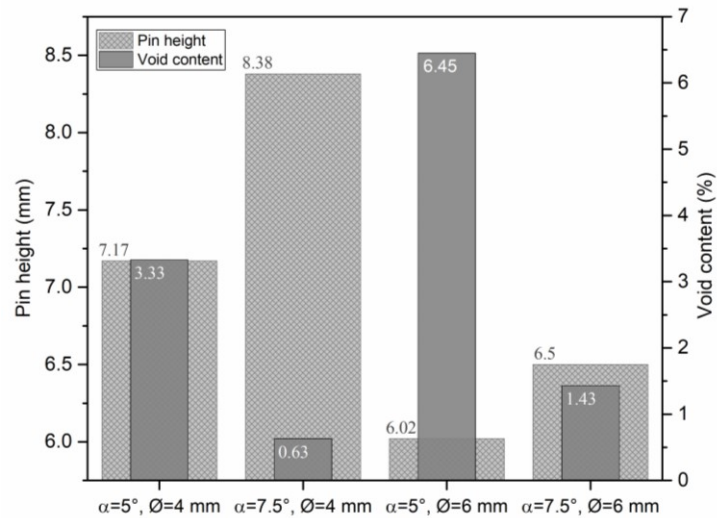


Figure 6. Pin height and void content for different combination of α and ϕ and fixed forming velocity ($F=300\text{mm/min}$).

Finally, the distance, d , between the pins is another important parameter that has to be considered. This distance is proportional to the material that is moved between two consecutive forming steps. Therefore, d has to be set as function of the pin size affecting both its final height and void content. Specifically, for $\phi=4 \text{ mm}$, the process needs a distance between 20 mm and 25 mm to work at full performance. In this range, the maximum height is reached and the void content decreases. For $\phi=6 \text{ mm}$, instead, the steady state condition was not reached at 25mm, yet. Indeed, for this value, the void content measured inside the pin is still consistent recommending an increment of d to achieve better pins.

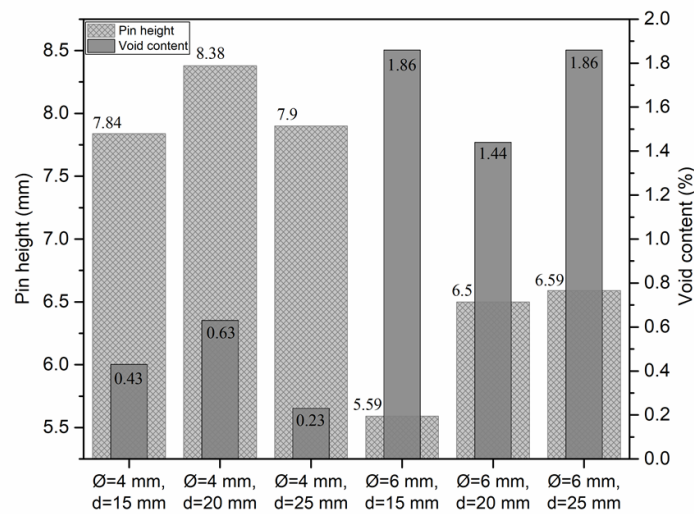


Figure 7. Pin height and void content for different distances (d) between the extruded pins ($F=300\text{mm/min}$, $\alpha=7.5^\circ$).

CONCLUSIONS

The friction stir forming was investigated focusing the attention on the quality of the extruded pins looking at their height and void content. Some geometrical and process variables were selected and their influence was highlighted.

Forming velocity, tilt angle, pin diameter and distance between two holes were the analysed variables. Their ranges were chosen starting from data available in literature.

The influence of the forming velocity on the pin quality is more evident for lower extrusion ratios, where the material could flow too easily due to the material heating and no relevant blocking hole effect. This leads to a consistent void content into the manufactured pins. The tilt angle, instead, affects the material volume that the forming tool is able to move. An increment of α , at constant depth penetration, pushes more aluminium through the holes. However, an increment of this variable should also affect the forces on the tool reducing its working life. Finally, the minimum distance between two pins, fixing all the other geometrical and process parameters, depends on the diameter of the pin that has to be extruded. Indeed, there is a strong relationship between the mass that is moved from the tool translation and the achievable pin size.

Further researches have to be still carried out to obtain a full correlation among several process parameters. Once the process optimisation will be completed, FSF could be proposed as a valuable joining solution to make multi material components.

REFERENCES

1. Pramanik A, Basak AK, Dong Y, Sarker PK, Uddin MS, Littlefair G, Dixit AR, Chattopadhyaya S (2017) Joining of carbon fibre reinforced polymer (CFRP) composites and aluminium alloys – A review. [Compos Part A Appl Sci Manuf](#) 101:1–29
2. Banea MD, da Silva LFM, Campilho RDSG (2017) Principles of Adhesive Bonding. In: *Join. Polym. Hybrid Struct.* John Wiley & Sons, Inc, Hoboken, NJ, pp 3–27
3. Araújo HAM, Machado JJM, Marques EAS, da Silva LFM (2017) Dynamic behaviour of composite adhesive joints for the automotive industry. [Compos Struct](#) 171:549–561
4. Groche P, Wohletz S, Brenneis M, Pabst C, Resch F (2014) Joining by forming—A review on joint mechanisms, applications and future trends. [J Mater Process Technol](#) 214:1972–1994
5. Xiao Y, Ishikawa T (2005) Bearing strength and failure behavior of bolted composite joints (part I: Experimental investigation). [Compos Sci Technol](#) 65:1022–1031
6. Choi J-I, Hasheminia SM, Chun H-J, Park J-C, Chang HS (2018) Failure load prediction of composite bolted joint with clamping force. [Compos Struct](#) 189:247–255
7. Lee C-J, Lee S-H, Lee J-M, Kim B-H, Kim B-M, Ko D-C (2014) Design of hole-clinching process for joining CFRP and aluminum alloy sheet. [Int J Precis Eng Manuf](#) 15:1151–1157
8. Katayama S, Kawahito Y, Mizutani M (2012) Latest Progress in Performance and Understanding of Laser Welding. [Phys Procedia](#) 39:8–16
9. Esteves JV, Goushegir SM, dos Santos JF, Canto LB, Hage E, Amancio-Filho ST (2015) Friction spot joining of aluminum AA6181-T4 and carbon fiber-reinforced poly(phenylene sulfide): Effects of process parameters on the microstructure and mechanical strength. [Mater Des](#) 66:437–445
10. Liu FC, Liao J, Nakata K (2014) Joining of metal to plastic using friction lap welding. [Mater Des](#) 54:236–244
11. Ohashi T, Tabatabaei HM, Nishihara T (2017) Fastenerless-Riveting Utilizing Friction Stir Forming for Dissimilar Materials Joining. [Key Eng Mater](#) 751:186–191
12. Conte R, Buhl J, Ambrogio G, Bambach M (2018) Joining of aluminum sheet and glass fiber reinforced polymer using extruded pins. In: [AIP Conf. Proc.](#) p 050008
13. Ohashi T, Tabatabaei HM, Nishihara T (2017) Cylindrical extrusions on A5083 aluminum alloy plate fabricated by friction stir forming. p 080002
14. Landis EN, Keane DT (2010) X-ray microtomography. [Mater Charact](#) 61:1305–1316
15. Boerckel JD, Mason DE, McDermott AM, Alsborg E (2014) Microcomputed tomography: approaches and applications in bioengineering. [Stem Cell Res Ther](#) 5:144
16. Stauber M, Müller R (2008) Micro-Computed Tomography: A Method for the Non-Destructive Evaluation of the Three-Dimensional Structure of Biological Specimens. pp 273–292

**4.3 CASE STUDY 3: Non-destructive
Measurements of Single Events Induced
on Power MOSFET's by Terrestrial
Neutrons.**

Non-destructive Measurements of Single Events Induced on Power MOSFET's by Terrestrial Neutrons

Raffaele Giuseppe Agostino, Jose Brito del Pino, Raffaele Filosa, Vincenzo Formoso, Nicolo Marchese, Calogero Pace, Elio Angelo Tomarchio

Abstract—X-ray microtomography has been employed for non-destructive measurements on Power MOSFET's to investigate the damage due to "Single Events Effects (SEEs)" induced by high energy neutrons in accelerated tests. The technique allowed to investigate the spatial structure of damages induced by neutrons. The results show that the technique and the methodologies employed to investigate SEEs in electronic devices could represent a suitable non-destructive investigation tool for the post-failure analysis.

Index Terms—Power MOSFETs, SEB, SEGR, SEE, Terrestrial neutrons, tomography.

I. INTRODUCTION

ELECTRONIC devices are employed in several applications and they are subjected to effects of the environment in which they work. In some of these applications (space, aircraft or ground), these components are subjected to the Natural Radiation Environment (NRE), composed of heavy ions, protons or neutrons [1]. The interaction of these particles with the devices causes damages that could change the features of the device or could destroy them. Power MOSFET's, largely employed in avionics, automotive and energy production and transformation, are sensitive to the interaction of high-energy terrestrial neutrons. The interaction of a "single" neutron with the device could cause the so-called Single Event Effects (SEEs) [2]. Single Event Burnout (SEB) and Single Event Gate Rupture (SEGR) are destructive SEEs that affect Power MOSFET's during their work [3] [4] [5] [6] [7]. Literature provides models of SEB and SEGR that describe how the interaction of a single high energy neutron could cause the device destruction [8] [9]. Up to now, investigations on the structure of the SEEs have been performed employing destructive (

R. G. Agostino, Jose Brito del Pino, Raffaele Filosa, and Vincenzo Formoso are with the Department Physic, University of Calabria, Rende, CS 87036. Italy, (e-mail: raffaele.agostino@fis.unical.it, jfranbripi79@hotmail.com, raffaele.filosa@fis.unical.it, vincenzo.formoso@fis.unical.it). Nicolo` Marchese and Calogero Pace are with the DIMES, University of Calabria, Rende, CS 87036, Italy, (e-mail: n.marchese@dimes.unical.it, calogero.pace@unical.it). Elio Angelo Tomarchio is with DEIM, University of Palermo, 90128 – Palermo, Italy (e-mail: elio.tomarchio@unipa.it).)

tests. X-ray microtomography with flat-panel matrix detectors and X-ray micro-focused source is a non-destructive technique able to provide advanced 3D-images. The microtomography technique requires appropriate tomographic methods, scanning geometries, photon energies and resolutions [10] [11], and it allows obtaining information on the internal structure of the

sample and to investigate and characterize several features of interest. Taking that into consideration and concerning the models of SEB and SEGR discussed above, a non-destructive investigation on Power MOSFET's went to a burnout event during accelerated tests with high-energy neutron has been performed. Methods and results are reported below.

II. SUBJECT AND METHODS

For the investigation, two sets of Power MOSFET's (N-channel STP20N95K5, STMicroelectronics) have been investigated. The first set of 7 devices underwent an accelerated test in the Neutron Irradiator facility of the DEIM department of the University of Palermo. The neutron irradiator consists of $^{4241}\text{Am-Be}$ sources that provide neutron in the energy range from thermal up to about ≈ 12 MeV. The purpose of the experiment is to verify the device reliability over a while, equivalent to 20 years of terrestrial neutrons exposure. The devices have been irradiated with Gate and Source at the ground and Drain biased with growing voltage to reach the devices burnout [12]. The second set of 8 fresh devices has been investigated with μ -CT to obtain comparative results. Then the second set has been irradiated in the same conditions of the first set to obtain the devices burnout. In the end, a post-failure investigation has been carried out with μ -CT to compare the results "before-and-after" from analysis and to confirm the results obtained on the first set of devices.

A. Scanning Electron Microscopy

Power MOSFET's devices were preliminarily investigated using a Scanning Electron Microscopy (SEM) equipped with an X-ray fluorescence detector to determine the dimensions and the typical composition of the used materials [13]. Power MOSFET external package has been removed applying a heat gun and then after with hydrochloric acid diluted at 60% in distilled water. The contrast of SEM combines imaging and chemical microanalysis permitted to give qualitative information such as the materials form, quality, colour, and location into the device. And it's quantitative information as dimensions and chemical composition of materials [14]. Taking into consideration the information carried out by SEM investigation, the system μ -CT was optimized its geometry for shows less degradation of the X-rays permitted to show some internal layers due to the absorption the X-ray on the metal sink and drain-source metallic contact when the sample is put in the vertical position. See Fig. 1.

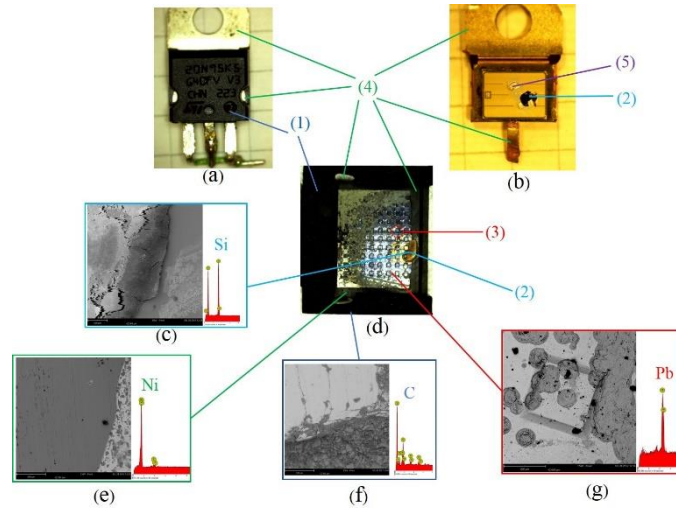


Fig. 1: SEM Results: (a) The current Power MOSFET. Figures (b) and (c) represent of unpackaging Power MOSFET. (d) Silicon layer. (e) Nickel layer. (f) Carbon layer. (g) Lead solder layer. (1) External package. (2) Silicon layer. (3) Solder layer. (4) Metallic drain. (5) Source metal contact.

B. μ -TOMO Laboratory μ -CT scan was made on μ -Tomo Laboratory part of the STAR-Lab facility from PON MaTeRiA located at the University of Calabria in Italy. As in Fig. 2, the μ -Tomo Experimental Station consists of three precision optical tables Thorlabs mod. B6090B. Equipped with a microfocus X-ray source Hamamatsu L12161-07 with a range voltage from 0 kV to 150 kV and variable focus mode which can reach 5 μ m at 4 W on small focus operation. The motorized structure consists of two motion cradles, a rotator, and two motors for linear translation. A flat panel detector Hamamatsu C7942SK05 with a maximum value of 150 kVp and a pixel size of 50 μ m. The whole system allows to control the X-rays test source managing; the sample-under-test (SUD) moving, using five high precision stepper motors; the image acquisition, employing a flat panel detector, subsequently made the 2D and 3D image reconstruction, thanks to a freeware reconstruction tool.

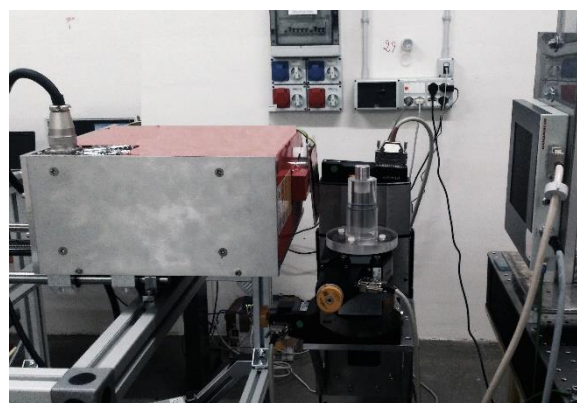


Fig. 2: μ -Tomo Experimental Station

C. Microtomography Technique

Micro-focal CT (microtomography) in cone-beam geometry is advantageous for obtaining directly reconstructed 3D images from a set of 2D projection images recorded by the detector [15] [16]. The reconstruction process transforms the raw acquisition data into a stack of 2D cross-sections through the sample, resulting in a 3D dataset [17]. The destructive analysis techniques such as physical cross-sectioning and chemical decapsulation may induce damage, not relevant to the defect site, or remove the evidence of a defect or damaged site. The 3D X-ray micro-computed tomography provides a powerful non-invasive alternative solution for these problems facing failure analysis. [18] The microtomography is a technique which permits non-destructive inspection of a certain class of electronic devices without cause damage to them and allows their subsequent utilization. The modern cone beam μ -CT used a wide range of energy and resolution of few microns permit of investigating the inner structure of electronic permitted a fast look inside at 2D x-ray projections and from 2D slices obtained quantitative analysis and 3D rendering of object [19].

Before the operation of the microtomography system, it is necessary to align source, specimen and detector: this consists of placing the specimen within the FOV (field of view) making an individual acquisition at 0 and 180 degrees, verifying the correct position of the specimen. Also, the user should set the magnification of the system considering the focal spot, the pixel size and the detector area.

Besides, we previous μ -CT test was determined the magnification, energy and position of Power MOSFET on the setup for obtaining the best contrast. The Power MOSFET was placed in a suitable sample holder, verifying the dimensions of the sample and the area of interest of MOSFET's (internal package) to be irradiated by x-rays with a magnification 6 and small spot size. At least 15 per cent of photon transmission was verified in the region of interest (inner package) of the MOSFET, for which was set a suitable current, voltage, and exposure time for optimal results. The motors were calibrated previous acquisition, alignment the system, set the exposure time and path for saving images; the acquisition consists acquire of dark and flat images previous and after scanning of the sample.

As in Fig. 3 shows the first scan of Power MOSFET was conducted on the horizontal position of the sample. The parameters used show in the Table 1 scan was made at 150 kV, 66 μ A, 1200 ms of exposure time, 0.1 mm rotation step, 6 of magnification, a filter of 3 mm Al and a filter of 0.025 mm Cu. The reconstruction shows the degradation of the X-rays due to the absorbent materials of the package as C and the metal heatsink as Ni, that do not allow to show the internal details of interest in Si substrate.

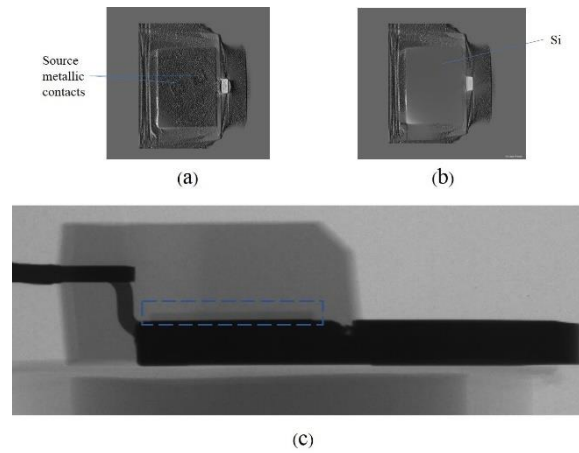


Fig. 3: Scan Power MOSFET on horizontal position:(a) 3D show the top view clamping to the external package and sour metallic contacts, (b) Si-layer shows the top view a flat section that does not evidence details or defect and (c) projection of Power MOSFET on horizontal position also show on blue dash rectangle the region of interest.

The vertical scan of Power MOSFET was made at 140 kV, 71 μ A, 2000 ms of exposure time, 0.2 mm rotation step, 6 of magnification, a filter of 3 mm Al and a filter of 0.025 mm Cu. The reconstruction shows internal details of interest into Si substrate, for this reason, this geometry is used in the μ -CT of the devices. As in Fig. 4 shows Power MOSFET scan on vertical position on the sample holder, For the reasons explained this geometry of scan will be used in μ -CT experiments.

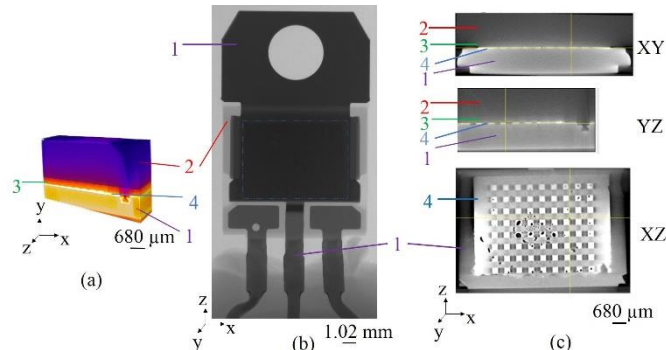


Fig. 4: Scan Power MOSFET on vertical position: with metallic drain (1), the external package (2), silicon layer (3), and lead solder layer (4). (a) depicts the 3D rendering of a part of the region of interest of projection (b) on blue dash rectangle, (c) shows it's the orthogonal view.

III. RESULTS

Fig. 5 depicts the structure of Power MOSFET N-channel STP20N95K5 with MDmesh K5 technology. The μ -CT permitted evidence the dimensions of lead solder tab and bulk of silicon, however the μ -CT no evidence the dopant regions into silicon bulk, gate and source which

were included according to the other theoretical models [20] [21] [22] and corroborating the results of μ -CT.

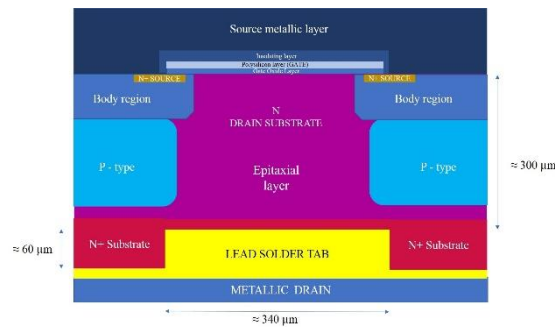


Fig. 5: MDmesh Power MOSFET Structure

As in Fig. 6 shows the region of interest of the SEB μ CT Model from the irradiated Power MOSFET slice where is located the SEB.

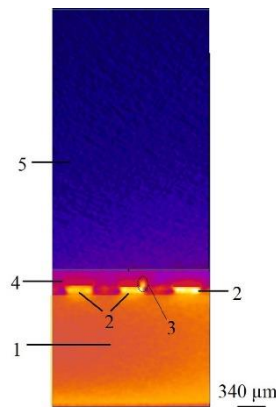


Fig. 6: SEB Model μ -CT: The drain metal backplate layer 1 of Ni material is located lower Pb solder layer 2. The SEB is a protrusion in-dash circle 3 into the silicon layer. The silicon epitaxial surface is region 4 is between the external package layer 5 and drain metal backplate layer 1.

Figures 7 and 6 depict the first and second cases of SEB, these indicate which effect the parasitic current after over lead solder layer on one tab, after reaching the melting point represents with a protrusion on a corner of the tab on alignment with any sources of the device leaving a depletion zone. The third case of SEB depicts the Fig. 9, the protrusion is near to corner tab on alignment with any of the sources of the device leaving a depletion zone. Fig. 10 shows the SEB in form of protrusion near any lead tab but on alignment any source of a single device.

As in Fig. 11 shows the region a SEGR μ -CT Model from the irradiated Power MOSFET.

As in Fig. 12 depicts the first case of SEGR indicating the effect of parasitic current on the centre of the lead tab after reaching the melting point represents with a protrusion of lead on alignment with tab gate leaving a depletion zone in form of a hole.

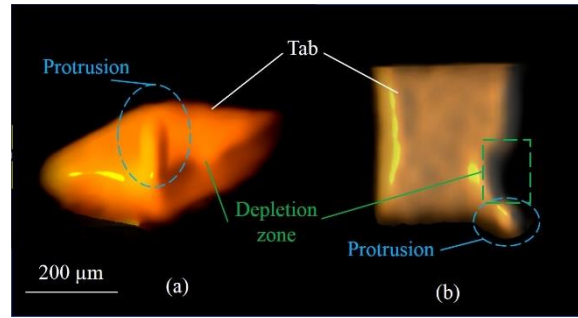


Fig. 7: SEB – Case 1: (a) Perspective view of a lead tab. (b) Top view of a lead tab.

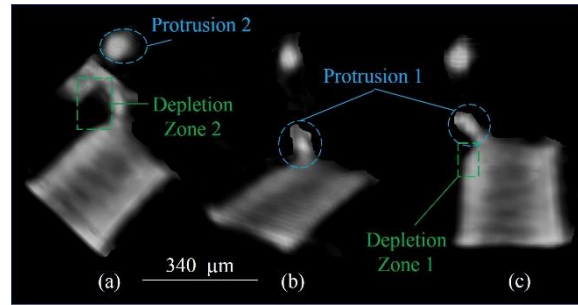


Fig. 8: SEB – Case 2: Figures (b) and (c) depict the protrusion 1 on a tab corner on alignment with an of sources of the device producing a depletion zone 1, the figure in (a) shows the protrusion 2 is alignment with the same sources, and producing a depletion zone 2.

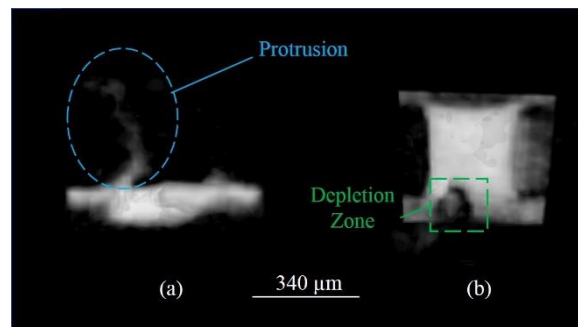


Fig. 9: SEB – Case 3: (a) Side view of a lead tab. (b) Top view of a lead tab.

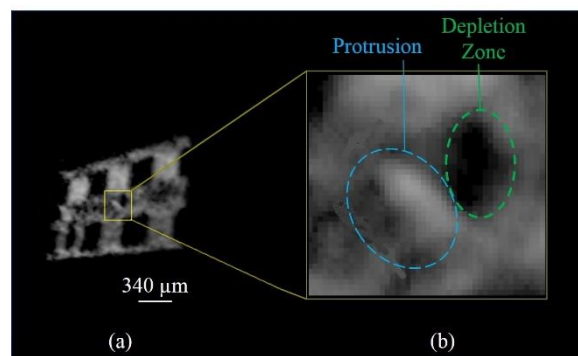


Fig. 10: SEB – Case 4: (a) Perspective view of a region of interest. (b) Zoom view of SEB and depletion zone.

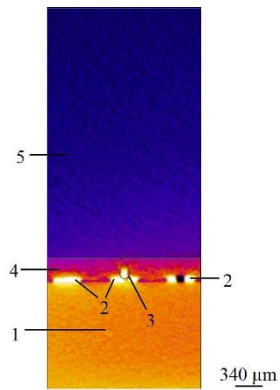


Fig. 11: SEGR Model μ -CT: The drain metal backplate layer 1 of Ni material is located lower lead solder layer 2. The SEGR is a protrusion in-dash circle 3 into the silicon layer. The silicon epitaxial surface is region 4 is between the external package layer 5 and drain metal backplate layer 1.

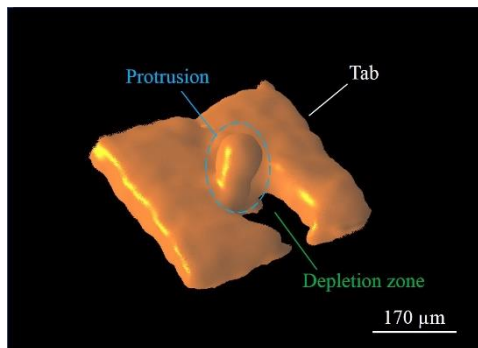


Fig. 12: SEGR – Case 1: As in Fig. 13 depicts the second case of SEGR indicating the effect of parasitic current on the centre of the lead tab after reaching the melting point represents with a protrusion of lead on alignment with gate tab and leaving some depletion zones in form of holes.

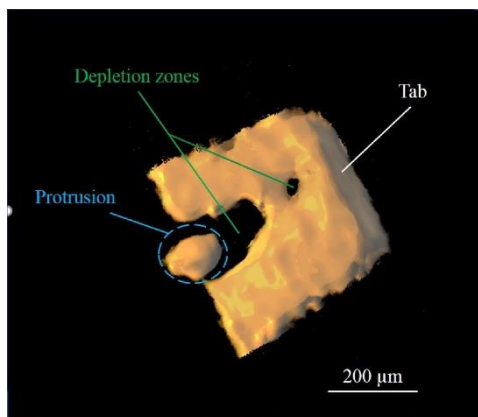


Fig. 13: SEGR – Case 2: As in Fig. 14 and Fig. 15 show the more relevant cases in fresh μ -CT of Power MOSFET's. Although after neutron irradiation show more clearly on (c') and (d') the protrusions into a blue dash circle and depletion zones into a polygon to the dotted red line.

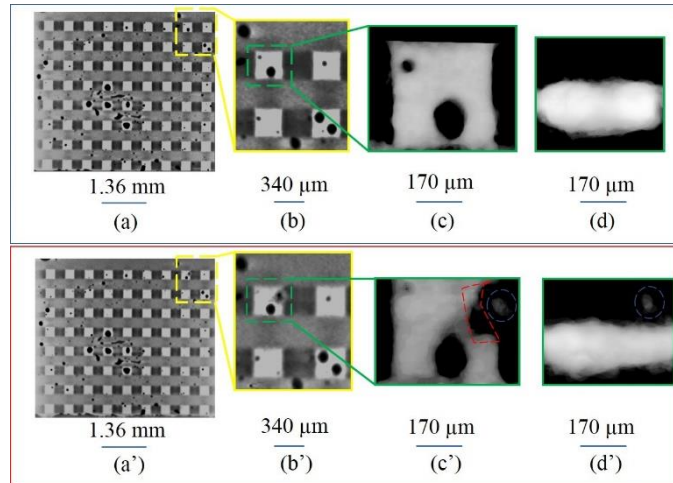


Fig. 14: SEB in fresh Power MOSFET - Case 1: On top are the figures previous neutron irradiation while the bottom is the figures after neutron irradiation. As in Figures (a) and (a') show the 3D front view of lead solder layer, The Figures (b) and (b') refer to a region of interest from lead solder layer. The Figures (c) and (c') depict the lead tab after segmentation. The Figures (d) and (d') depict the side view of the lead tab after segmentation.

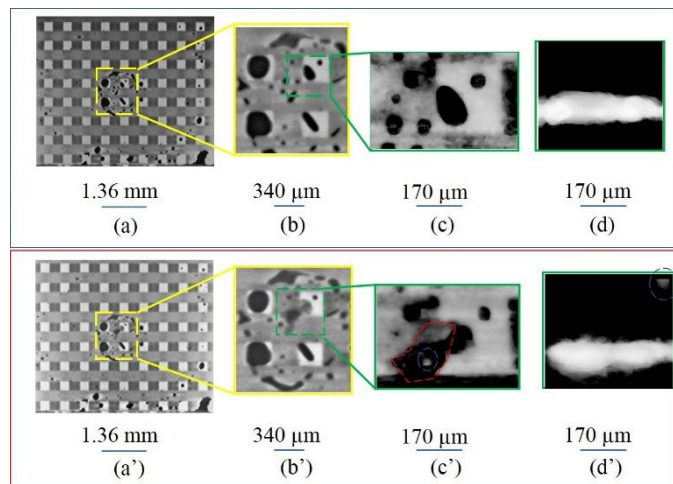


Fig. 15: SEB in fresh Power MOSFET - Case 2: On the top are the figures previous neutron irradiation while the bottom is the figures after neutron irradiation. As in Figures (a) and (a') show the 3D front view of lead solder layer, The Figures (b) and (b') refer to a region of interest from lead solder layer. The Figures (c) and (c') depict the lead tab after segmentation. The Figures (d) and (d') depict the side view of the lead tab after segmentation.

IV. CONCLUSIONS

We performed two tests, the first test was used 15 Power MOSFET's, 7 with neutron radiation and 8 fresh devices. The second test consisted put on neutron radiation the 8 fresh devices from the first test. The appropriate geometry and acquisition parameters for μ -CT have been developed with the aim of evidence SEEs occurred in the neutron-irradiated devices. The SEEs were determinate using filtering, segmentation, and 3D rendering with the ImageJ software. The methodology developed and applied has allowed to individuated SEEs inside the inner structure of devices with a good correspondence by the SEB and SEGR models.

The microtomography can evidence measurable micro destructive SEEs on Power MOSFET's N-channel STP20N95K5 with MDmesh K5 technology occur when a fast neutron with high energy induce reactions with silicon nucleus into epitaxial layer, producing secondary ionizing particles which deposit high density of electron-hole pairs along their track in the silicon collected at the p-n bipolar junction when parasitic BJT turns ON and produce parasitic current and created a fusion on lead solder layer able to lead the SEEs.

The SEB is evidence in μ -CT when the high current density in presence of large drain-to-source voltage produces a current trace with effects into the solder layer leaving a depletion zone and producing a fusion on any theirs the corners or near theirs in form of protrusion into silicon epitaxial layer in alignment with the tab source near to the p-base region of a discrete transistor.

The SEGR is evidence for μ -CT when are separated radially the electrons to drain and holes to the oxide gate along the neutron track are separate under influence of drain bias induce a charge on the gate electrode, leading to a transient increase of the electric field in the gate dielectric, producing a parasitic current trace with effects into solder layer, creating a fusion on its centre leaving a depletion zone and generating a protrusion into silicon epitaxial layer in alignment with the centre of the gate in corresponds to a discrete transistor.

The μ -CT evidence the response to sensitivity of the device when occurs the SEB, the sensitivity decreases when a neutron trace is more near to the centre of the gate, resulting in a protrusion with less density from solder tab with relation to single transistor but more difficult of evidence the 3D reconstruction. For another hand, the sensitivity in SEGR increases when the neutron trace is nearer to the centre of gate resulting in a protrusion with more density and increasing of depletion zone on lead solder layer.

However, the microtomography is a technique which permits to see the form and size on the micro level of SEB and SEGR on lead solder layer located on lower the silicon bulk and over the metallic drain, these SEEs had a different size and density which are proportional to BJT parasitic current.

The second test μ -CT in fresh of Power MOSFET's confirm the first μ -CT SEEs test. The second test only evidence SEB with low density, due to a weak secondary effect of parasitic current on lead solder layer for producing the SEEs on the Power MOSFET.

The investigation performed on Power MOSFET's intending to study the SEEs demonstrate the power of the microtomography technique in this field of application. Nondestructive techniques as the X-ray micro-tomography described above allow investigated the structure of a sample without the necessity to use chemical or mechanical procedures. This work demonstrates that the μ -CT demonstrates could be employed in industrial applications as the post-failure analysis and the characterization of the constructive process. Therefore, the information obtained with this technique represents a good guide to design innovative devices, more reliable about the environmental effects to improve the industrial process and the construction quality of the devices.

REFERENCES

- [1] A. Luu, F. Miller, P. Poirot, R. Gaillard, N. Buard, T. Carriere, P. Austin, M. Bafleur, and G. Sarrabayrouse, "Seb characterisation of commercial power mosfets with backside laser and heavy ions of different ranges," in Proceedings of the European Conference on Radiation and its Effects on Components and Systems, RADECS, vol. 55, DOI 10.1109/RADECS.2007.5205543, pp. 1–7, Oct. 2007.
- [2] A. Hands, P. Morris, K. Ryden, C. Dyer, P. Truscott, A. Chugg, and S. Parker, "Single event effects in power mosfets due to atmospheric and thermal neutrons," IEEE Transactions on Nuclear Science, vol. 58, DOI 10.1109/TNS.2011.2168540, no. 6, pp. 2687–2694, Dec. 2011.
- [3] F. Miller, A. Luu, F. Prud'Homme, P. Poirot, R. Gaillard, N. Buard, and T. Carriere, "Characterization of single-event burnout in power mosfet using backside laser testing," IEEE Transactions on Nuclear Science, vol. 53, DOI 10.1109/TNS.2006.885376, no. 6, pp. 3145–3152, Dec. 2006.
- [4] T. Bajenescu and M. Bazu, Reliability of Electronic Components: A Practical Guide to Electronic System Manufacturing, 1st ed. New York, USA: Springer-Verlag, 1999, DOI 10.1007/978-3-642-58505-0.
- [5] F. Kenneth, Galloway, and M. Bassiouni, "A brief review of heavyion radiation degradation and failure of silicon umos power transistors," in Radiation Effects Data Workshop (REDW), vol. 3, DOI 10.1109/REDW.2014.7004598, pp. 582–593, Jan. 2014.
- [6] K. Rashed, R. Wilkins, A. Akturk, R. C. Dwivedi, and B. B. Gersey, "Terrestrial neutron induced failure in silicon carbide power mosfets," in 2014 IEEE Radiation Effects Data Workshop (REDW), vol. 3, DOI 10.1109/REDW.2014.7004598, pp. 1–4, Jul. 2014.
- [7] L. Scheick, Testing Guideline for Single Event Gate Rupture (SEGR) of Power MOSFETs. NASA, Oct. 2017. [Online]. Available: <https://nepp.nasa.gov/files/16408/081634JPLScheick.pdf>
- [8] J. Hohl and G. Johnson, "Features of the triggering mechanism for single event burnout of power mosfets," IEEE Transactions on Nuclear Science, vol. 36, DOI 10.1109/23.45433, no. 6, pp. 2260–2266, Dec. 1989.

- [9] M. Allenspach, J. R. Brews, I. Mouret, R. D. Schrimpf, and K. F. Galloway, "Evaluation of segr threshold in power mosfets," *IEEE Transactions on Nuclear Science*, vol. 41, DOI 10.1109/23.340557, no. 6, pp. 2160–2166, Dec. 1994.
- [17] J. Vlassenbroeck, M. Dierick, B. Masschaele, V. Cnudde, L. V. Hoorebeke, and P. Jacobs, "Software tools for quantification of x-ray microtomography at the ugct," *Nuclear Instruments and Methods in Physics Research Section A: Accelerators, Spectrometers, Detectors and Associated Equipment*, vol. 580, DOI <https://doi.org/10.1016/j.nima.2007.05.073>, no. 1, pp. 442 – 445, 2007.
- [10] N. Kotwal, L. Hunter, J. Gelb, and S. H. L. A. Gu, "X-ray computed tomography for non-destructive testing and materials characterization," 2012.
- [11] J. Kastner and C. Heinzl, *Integrated Imaging and Vision Techniques for Industrial Inspection: Advances and Applications*, ch. 8, pp. 227–250. Springer London, 2015.
- [12] G. Consentino, M. Laudani, G. Privitera, A. Parlato, N. Marchese, E. Tomarchio, C. Pace, C. Giordano, M. Mazzeo, and J. L. H. Ambato, "Dangerous effects induced on power mosfets by terrestrial neutrons: A theoretical study and an empirical approach based on accelerated experimental analysis," in *AEIT Annual Conference 2013*, DOI 10.1109/AEIT.2013.6666813, pp. 1–6, Oct. 2013.
- [13] D. Holt and D. Joy, *SEM Microcharacterization of Semiconductors*, 1st ed., vol. 12. San Diego, CA 92101: Academic Press Inc., 1989, an optional note.
- [14] D. Donovan., G. Chandler, and S. Seraphin, *Characterization of Materials*, 2nd ed. John Wiley & Sons Inc., 2003, doi: 10.1002/0471266965.
- [15] K. Machin and S. Webb, "Cone-beam x-ray microtomography of small specimens," *Physics in Medicine & Biology*, vol. 39, no. 10, p. 1639, 1994.
- [16] H. Turbell, *Cone-Beam Reconstruction Using Filtered Backprojection*. UniTryck, Linköping, Oct. 2017. [Online]. Available: <http://citeseerx.ist.psu.edu/viewdoc/download?doi=10.1.1.134.5224&rep=rep1&type=pdf>
- [18] T. Pendleton, L. Hunter, and S. Lau, "Noninvasive failure analysis of passive electronic devices in wireless modules using x-ray microtomography (microct)," in *Conference Proceedings from the 34th International Symposium for Testing and Failure Analysis*, vol. 7, DOI 10.1361/cp2008istfa092, pp. 92–98, Jan. 2008.
- [19] R. Hanke, T. Fuchs, and N. Uhlmann, "X-ray based methods for non-destructive testing and material characterization," *Nuclear Instruments and Methods in Physics Research Section A*, vol. 591, DOI 10.1016/j.nima.2008.03.016, no. 1, pp. 14–18, Jun. 2008.
- [20] V. Giuffrida, *The avalanche issue: comparing the impacts IAR and EAS parameters*. STMicroelectronics, Oct. 2017. [Online]. Available: <http://www.st.com/content/ccc/resource/technical/document/application>

note/c8/6a/a4/10/00/80/48/af/DM00090672.pdf/files/DM00090672.pdf/
jcr:content/translations/en.DM00090672.pdf

[21] S. Havanur and P. Zuk, Power MOSFET Basics - Understanding Superjunction Technology. Vishay Siliconix, Oct. 2017. [Online]. Available: <https://www.vishay.com/docs/66864/an849.pdf>

[22] J. L. Titus and C. F. Wheatley, "Experimental studies of single-event gate rupture and burnout in vertical power mosfets," IEEE Transactions on Nuclear Science, vol. 43, DOI 10.1109/23.490899, no. 2, pp. 533–545, Apr. 1996.

4.4 CASE STUDY 4: Studying the microvesiculation of the obsidians of Sierra de las Navajas (State of Hidalgo, Mexico).

Studying the microvesiculation of the obsidians of Sierra de las Navajas (State of Hidalgo, Mexico)

Paola Donato¹; Luis Barba²; Maria Caterina Crocco³; Mariano Davoli¹; Rosanna De Rosa¹; Sandro Donato^{3,4}; Raffaele Filosa³; Gabriele Lanzafame^{4,5}; Giancarlo Niceforo¹; Alejandro Pastrana⁶; Gino Mirocle Crisci¹

¹: Department of Biology, Ecology and Earth Sciences, University of Calabria, Rende, Italy;

²: Instituto de Investigaciones Antropológicas, Universidad Nacional Autónoma de México, Mexico;

³: Department of - University of Calabria, Rende, Italy;

⁴: Elettra Sincrotrone S.C.p.A, Basovizza, Trieste, Italy;

⁵: Department of Biological, Geological and Environmental Sciences, University of Catania, Catania, Italy;

⁶: Instituto Nacional de Antropología e Historia- México, Mexico.

Keywords: Mesoamerican obsidians; X-ray micro-CT; conchoidal fracture; microvesiculation.

Abstract

Sierra de las Navajas obsidian was highly exploited by the pre-colonial Mesoamerican people and highly requested for its very good quality and its characteristic green colour. The deposit from which most of the archaeological obsidians come contains fragments with very variable macroscopic aspect, with colour ranging from very light to very dark green and variable hue. Physical properties, such as roughness and fracture are variable as well. The surface of these obsidian is sometimes characterized by the occurrence of a diffuse microvesiculation. In order to investigate the 2-D and 3-D distribution of vesicles and to relate it to the macroscopic aspect and to the physical properties of obsidian, we have selected three samples showing different colour, roughness, hue and fracture. We have observed their surface by electron microscopy and we have investigated small volumes of the same specimen by X-rays microtomography. The results have shown that the hue sometimes shown by obsidian is strictly related with the occurrence of abundant, elongated and iso-oriented vesicles. The occurrence of coarse (hundreds of microns) vesicles also gives to the surface a high roughness. Finally, the shape of the vesicles controls the type of fracture (conchoidal or flat). Aspect and physical characteristic, in their turn, influenced the use of obsidians by ancient and modern populations. Poorly or

not vesiculated obsidian with perfect conchoidal fracture was highly requested for the production of blades, while vesiculated obsidian, showing a beautiful golden hue, seems to have been preferred for the production of ornaments or magical and ritual objects.

Introduction

Obsidian was a strategic material in ancient times before the use of metals, and it was widely used both for the production of weapons and cutting tools and for ornamental or magical-religious objects. The main characteristics determining the “quality” of obsidian for the production of blades are its conchoidal fracture and the possibility to obtain sharp edges. On the other side, its attractiveness is the main feature determining its use for jewellery or in the magical traditional medicine.

Most of the obsidian found all around the world is black. Obsidian from Sierra de las Navajas (State of Hidalgo, Mexico) is unique throughout the world for its particular green colour and gold/silver shine. These features, together with the perfect conchoidal fracture and the absence of crystals, made it particularly useful for the manufacture of tools, ornaments, sculptures and weapons by the pre-colonial Mesoamerican people. Several attempts have been made to explain the characteristic colour and hue of Sierra de las Navajas obsidians, relating it to chemical, structural or microstructural aspects. The green colour of Sierra de las Navajas obsidians was attributed to a high abundance of Zn and Zr by Argote- Espino et al. (2012) and to the high Fe content by Donato et al. (2018). Other studies demonstrated that the surface of the Sierra de las Navajas obsidian is characterized by the occurrence of a diffuse microvesiculation, a feature never observed in other obsidians, that could be responsible of the gold/silver shine of the surface (Tenorio et al., 1998; Lighthart Ponomarenko, 2004; Donato et al., 2018). The main purpose of this paper is to investigate the 2-D and 3-D distribution of vesicles in obsidians from Sierra de la Navajas with different aspect, in order to determine if and how it influences the macroscopic aspect and the physical properties of obsidians, which, in their turn, can determine the different use by ancient populations. In order to achieve this purpose, we have investigated three obsidian samples showing different colour, roughness, hue and fracture by electron microscopy, in order to observe the distribution of the vesicles on the natural breakage surface, and by X-rays microtomography, in order to investigate the 3-D shape and distribution of the vesicles inside the obsidian.

Sierra de las Navajas obsidian

Sierra de Las Navajas (“the mountain of the blades”) is an extinct volcanic complex situated on the north-eastern edge of the Trans-Mexican Volcanic Belt, just north of the city of Pachuca (Hidalgo, Mexico) and was one of the major sources of high quality volcanic glass in Mesoamerica. Most of the Sierra de las Navajas archaeological obsidian (also known as “Pachuca obsidian”) probably comes from a single volcanic deposit, only sporadically outcropping, consisting of big obsidian blocks set in a clay-like matrix (Fig. 1a.). This deposit was interpreted as a lahar or block and ash flow by Pastrana (1996) and as a partially weathered lava flow by Lighthart Ponomarenko (2004). It was highly exploited and the obsidian widely used all over the Mesoamerican territory over a long period of time (Pastrana and Carballo, 2016). The intense exploitation started with the development of Teotihuacan, the first pre-Hispanic urban development in Central Mexico (ca. AD 200–600), and continued irregularly, following the major changes in the political order, during the Toltec culture (AD 950–1100) and during the Aztec military Empire (AD 1325–1521) (Pastrana and Dominguez, 2009). The extraction and use of obsidian had a sudden decrease in the Early Colonial Period (17th century), due to the availability of metals. Further limits to the use of obsidians came from the Spanish, who prohibited its use in order to prevent indigenous rebellions with obsidian weapons, and from the Catholic Inquisition, for whom the obsidians were associated with witchcraft (Pastrana and Fournier 1998; Pastrana, 2019). Obsidian was used to produce several kinds of handicraft, including weapons, jewels, and magic-religious objects that are directly associated with some of the main pre-Hispanic warrior gods (Hirth, 2003; Pastrana and Domínguez, 2009, Pastrana and Athie, 2014).

The colour of Sierra de las Navajas obsidian ranges from light to very dark green; the surface often shows a characteristic gold/silver hue (Fig. 1b.). As stated by several previous studies (Cobean et al., 1991; Lighthart Ponomarenko, 2004; Argote Espino et al., 2012; Donato et al., 2018) the composition of the Sierra de las Navajas obsidians is rhyolitic with a peralkaline affinity, but the trace element content is rather variable. The obsidian is almost completely aphyric and only rarely contains small (10-20 µm) quartz crystals (Donato et al., 2018). A feature often observed in the Sierra de las Navajas obsidians is the common occurrence of small, elongated vesicles, often iso-oriented on

the surface of the natural cut surface (Tenorio et al., 1998; Lighthart Ponomarenko, 2004; Donato et al., 2018). A preliminary study of the three-dimensional (3-D) morphology and distribution of vesicles was performed on one sample of Sierra de las Navajas green obsidian by high-resolution SR micro-CT in phase-contrast mode on the SYRMEP beamline of the Elettra synchrotron light source (Trieste, Italy) (Donato et al., 2018). This allowed to measure the total vesicularity, which was in the order of 2 vol.%, and to verify that vesicles are almost totally isolated, elongated and mostly iso-oriented and with major axis lengths in the order of tens of micrometers.

Methods

In this work we have selected three obsidians showing different aspect and fracture, all coming from the deposit previously described: sample “A” has a flat, not conchoidal fracture surface, rough to the touch and with homogeneous, almost «metallic» hue (Fig. 2a.). Sample “B” has conchoidal fracture and shows alternating concentric bands: some are light green, with a marked hue and rough surface, other are dark and smooth (Fig. 2b.). Small fragments (ca 1 cm each) were cut from each sample for 2-D and 3-D analyses. A further sample (“E”) was used only for 2-D observation: it is very dark green in colour, with perfect conchoidal fracture and no hue at all (Fig. 2c.).

The natural fracture surface of the three samples was observed at high magnification under Electron Microprobe (EPMA), in order to see the size and 2-D distribution of vesicles on the surface. The used instrument is the JEOL JXA-8230 of SILA-CM2 lab at the University of Calabria. Before the analyses the investigated surface was coated with a thin (ca 5nm) graphite film in order to make it conductive. Images were acquired in Secondary Electrons (SE) and Back-Scattered Electrons (BSE).

Samples “A” and “B” were investigated by X-rays microtomography (micro-CT) with a conventional laboratory source at μ Tomo experimental station @ STAR Lab at the University of Calabria. The experiment setup was the following: the X-ray source operated at a voltage of 100 kV, a current of 100 μ A and a focal spot size of 10 μ m; the X-ray beam was filtered for low energy components with 50 μ m of Molybdenum fixed target. The detecting system consists in a Hamamatsu Flat-panel detector (C7942SK-05) with a pixelsize of 50 μ m and an active area of 2316² pixels². Considering the employed beam magnification equal to 5, the equivalent pixelsize was 10 μ m with a field of view

of nearly 23*23 mm². A set of 1800 projections were acquired over an angular range of 360° using an exposure time of 3 s/projection. Axial slices were reconstructed with an isotropic voxel size of 10 µm using the FDK algorithm (Feldkamp et al. 1984) for cone-beam geometry.

Image analysis was performed with the freeware ImageJ suite. Firstly, a denoising filter was applied to reduce image noise and to perform a digital image segmentation. The last operation was done by means of an automatic thresholding algorithm (Ostu, 1979) and it allowed to separate the vesicles from the bulk rock. Then from the reconstructed volume of both samples, we extracted a Volume Of Interest (VOI). This volume enclosed a representative amount of the sample heterogeneity and the size was defined by a representative elementary volume analysis (Costanza-Robinson et al., 2011).

The '3D ImageJ Suite' was applied to evaluate the density of the vesicles, which provides their volumetric fraction in the sample. A morphological and topological analysis of vesicles was performed by excluding those touching the VOI borders, since they can be truncated and their volume and morphology may not be representative of the real shape. Major axis length of each vesicle and the relative three-dimensional array were then obtained via the '3D Geometrical measurements plugin'. The major axis represents the length of the longest segment among all the segments fully included in an object and passing through its centre of mass. The '3D Geometrical measurements' was then used to estimate, for each vesicle: i) the volume; ii) the elongation, defined as $E=1-(w/l)$, where w is the width and l the length of the vesicle, this value varying from 0 (not elongated) to 1 (very elongated). The 3D visualization was performed by volume rendering procedures by using the 'Volume Viewer plugin' of ImageJ.

This analysis allowed to determine the 3-D shape of the vesicles and their distribution and orientation inside the sample.

Results

Under the EPMA the surface of obsidian type "A" revealed the occurrence of many flat vesicles, displaced with the two major axes parallel to the natural breakage surface (Fig. 3a.). The shape of the vesicles is highly irregular and sometimes they seem to be formed by several layers (Fig 3b.). The size of the vesicles is highly variable; the maximum dimension of the major axis is about 250 µm. The micro-CT analyses confirmed that the

shape of the vesicles is highly irregular, but always flattened, i.e. mainly developed in a 2D space (Fig. 3c.). Moreover, it is evident that vesicles are displaced on preferential planes, all parallel to the surface of natural breakage. The image analysis revealed that total vesiculation (calculated as the ratio between the volume occupied by vesicles and the total investigated volume) is about 0.5%; the volume of vesicles ranges from 10^3 to $10^7 \mu\text{m}^3$. Elongation (E) of the vesicles in sample "A" is very variable, and both sub-rounded and highly elongated vesicles occur. The average E is 0.45.

The observation of sample "B" under the EMPA showed that bands with variable hue and roughness correspond to zones with different vesiculation. The transition from lighter, rougher bands to smoother and darker parts is marked by a sharp decrease in vesicularity (Fig. 4a.). Vesicles seem to have a rather regular, elliptic shape, with the major axis elongated in a direction parallel to the bands. They all seem isolated, without evidence of coalescence; however, vesicles occurring very close to each other seem to be plastically deformed. The length of the major axis of the vesicles ranges from few tens to several hundreds of microns (Fig 4b.). The micro-CT confirmed that the strong anisotropy in the vesicles distribution observed on the surface extends through the whole sample and they are concentrated in parallel bands (Fig 4c.). The total vesicularity is higher than the previous case and was calculated as 2.26%; however, this is an average value that considers both vesiculated and not vesiculated bands. The volume of vesicles is similar to sample "A", ranging from 10^3 to $10^7 \mu\text{m}^3$. Image analysis revealed that most vesicles are highly elongated, with average value of $E= 0.72- 0.74$. Spherical or sub-spherical vesicles are very rare.

In sample "E" BSE images showed that most of the surface has no vesicles, and only in some zones a few small and sub-rounded vesicles occur. They are randomly distributed on the analysed surface, without a preferential orientation. No micro-CT analysis was carried out on this sample.

Discussion

The deposit representing the main source for the archaeological obsidians of Sierra de las Navajas contains obsidians that, though homogeneous in composition, show very variable macroscopic aspect and physical properties. 2-D and 3-D observations clearly demonstrate that such variability is closely correlated to a different microvesiculation:

obsidian with flat, rough surface and homogeneous, “metallic” hue (sample “A”) contains flat vesicles displaced with the two major axes on the breakage surface, while in dark green, smooth samples with perfect conchoidal fracture (sample “E”) vesiculation is almost absent. Bands with different hue and roughness in sample “B” correspond to zones with different vesicle content. Therefore, the occurrence, shape, and orientation of vesicles are the main factors determining:

1) Hue and colour: abundant, isooriented vesicles give to the obsidian surface a beautiful golden/silver changing shine, probably related to light diffraction on the vesicles surface. Moreover, non-vesiculated obsidians appear very dark green or almost black (sample “E” or not vesiculated bands in sample “B”), and the green colour can only be appreciated in very thin fragments. On the contrary, the occurrence of vesicles on the surface extols the green colour of the obsidian, making it lighter.

2) Smoothness: it seems related to the occurrence and dimension of vesicles: sample “B” has rough bands with abundant, big vesicles (hundreds of microns), and smooth bands, where vesicles are smaller and less abundant. A rough surface is also shown by Sample “A”, where large flattened vesicles occur on the surface. Sample “E”, almost completely not vesiculated, has a homogeneously smooth surface.

3) Fracture: it is strongly controlled by the shape and disposition of the vesicles: in sample “A”, the flattened vesicles, displaced on preferential planes, create flat weakness surfaces along which the obsidian naturally breaks. The absence of vesicles (sample “E”) or their elongated shape and iso-orientation (sample “B”) are the necessary conditions for the formation of conchoidal fracture.

Aspect and physical characteristic, in their turn, are the main parameters determining the use of obsidians by ancient and modern populations. Poorly or not vesiculated obsidian with perfect conchoidal fracture, enhances the possibility to obtain very sharp blades with very low friction because of its homogeneous vitreous texture, and was therefore highly requested for the production of weapons and cutting tools (Pastrana and Athie, 2014). The absence of vesicles also gives a homogeneous, very dark and perfectly reflecting surface. These features make this kind of obsidian particularly useful for the production of mirrors used for divination. Many obsidian preforms for ritual mirrors have been found in one particular workshop area in Sierra de las Navajas (Pastrana, 2007; Otis Charlton and Pastrana, 2016) and all of them are made of very dark, not vesiculated obsidian.

On the other side, the vesiculation extolls the green colour of Sierra de las Navajas obsidians and gives it a beautiful hue, thus making it particularly requested for the production of ornaments or magical and religious objects. In the Aztec conception, in fact, the green obsidian was considered the most precious type and was called “*toltecaliztli* (obsidian of the masters) or *quetzalitzli* “a green stone the same green as the feathers from the quetzal bird’s tail transparent and dense as the obsidian without stain, gleaming that sweats and attracts” (Thouvenot 1982; Pastrana and Athie, 2014). The green colour of Sierra de las Navajas obsidian, particularly evident in the vesiculated variety, probably expressed notions of fertility and regeneration and was related to the rain god Tlaloc (or its Mixtec cognate Dzahui), as witnessed by multiple green blade fragments of Sierra de las Navajas obsidian found atop Mount Tlaloca and in Late postclassic Tututepec, in the State of Oaxaca, probably used for ritual activities and sacrifices (Levine, 2014 and references therein). The green, vesiculated variety of Sierra de las Navajas obsidian was also preferred for the realization of body ornaments and jewels, such as ear-spools, lip plugs and flat beads in Otumba (Otis Charlton, 1993). The vesiculated variety of obsidian is particularly used still today for the production of craft items and jewels.

In conclusion, the preliminary results of this study demonstrate that the macroscopical aspect and the physical properties of Sierra de las Navajas obsidians, on which the use of the obsidian by ancient Mesoamerican population depends, is closely relates to its microscopic and physical features.

Acknowledgements

Part of this work was carried on in the framework of the project “Messa a punto di nuove procedure analitiche LA-ICP-MS per l'individuazione della provenienza delle materie prime usate nell'edilizia storico-archeologica di monumenti precolombiani del Messico” (2011-2013), carried out by the University of Calabria and the National Autonomus University of Mexico and financially supported by Ministero degli Esteri- MAE.

Authors are thankful to the STAR LAB staff of University of Calabria for their help in performing the micro-CT experiments.

References

- Argote-Espino, D., Solé, J., López-García, P., Sterpone, O. (2012). Obsidian subsource identification in the Sierra de Pachuca and Otumba Volcanic regions, Central Mexico, by ICP-MS and DBSCAN statistical Analysis. *Geoarchaeology* 27, 48-62.
- Cobean, R.H., Vogt, J.R., Glascock, M.D., Stocker, T.L. (1991). High-precision trace-element characterization of major Mesoamerican obsidian sources and further analyses of artifacts from San Lorenzo Tenochtitlan, Mexico. *Lat. Am. Antiq.* 2, 69-91.
- Costanza-Robinson, M. S., Estabrook, B. D., & Fouhey, D. F. (2011). Representative elementary volume estimation for porosity, moisture saturation, and air-water interfacial areas in unsaturated porous media: Data quality implications. *Water Resources Research*, 47(7).
- Donato, P., Barba, L., De Rosa, R., Niceforo, G., Pastrana, A., Donato, S., Lanzafame, G., Mancini, L., Crisci, G.M. (2018). Green, grey and black: a comparative study of Sierra de las Navajas (Mexico) and Lipari (Italy) obsidians. *Quaternary International*, 467, 369-390.
- Feldkamp, L.A., Davis, L.C., Kress, J.W. (1984). Practical cone-beam algorithm. *Journal of the Optical Society of America*, A1, 1 (6), 612-619.
- Hirth, K. G. (2003). *Mesoamerican Lithic Technology*. The University of Utah Press, Salt Lake City.
- Levine, M.N. (2014). Obsidian obsessed? Examining Patterns of chipped-stone procurement at Late Postclassic Tututepec, Oaxaca. In: Levine, M.N. and Carballo, D.M. (eds) *Obsidian Reflections: Symbolic Dimensions of Obsidian in Mesoamerica*. University Press of Colorado, Boulder, Colorado, pp. 159-191.
- Lighthart Ponomarenko, A. (2004). The Pachuca obsidian source, Hidalgo, Mexico: a geoarchaeological perspective. *Geoarchaeology* 19, 71–91.
- Otis Charlton, C.L. (1993). Obsidian as jewelry- Lapidary production in Aztec Otumba, Mexico. *Ancient Mesoamerica*, 4, 231-243.
- Otis Charlton, C.L. and Pastrana, A. (2016). Aztec lapidaries. In: Nichols, D.L. and Rodríguez-Alegria (eds) *The Oxford handbook of the Aztecs*. Oxford University Press, New York, NY.
- Otsu, N. (1979). A threshold selection method from gray-level histograms. *IEEE transactions on systems, man, and cybernetics*, 9(1), 62-66.

- Pastrana, A. (1996). La explotación azteca de la obsidiana en la Sierra de las Navajas. Colección Científica 383. INAH, México, D.F.
- Pastrana, A., Fournier, P. (1998). Explotación colonial de obsidiana en el yacimiento de Sierra de Las Navajas. In: Davila, E.F. and Gomez Serafin S. (eds). Memoria del Primer congreso nacional de arqueología histórica. México, D.F., pp. 486-496.
- Pastrana, A. (2007). La distribución de la obsidiana de la Triple Alianza en la Cuenca de México. Colección Científica, Serie Arqueología, Universidad Nacional Autónoma de México, Mexico City.
- Pastrana, A., Domínguez, S. (2009). Cambios en la estrategia de la explotación de la obsidiana de Pachuca: Teotihuacan, Tula y La Triple Alianza. *Ancient Mesoam.* 20, 129-148.
- Pastrana, A., Athie, I. (2014). The Symbolism of Obsidian in Postclassic Central Mexico. In: Levine, M.N. and Carballo, D.M. (eds) *Obsidian Reflections: Symbolic Dimensions of Obsidian in Mesoamerica*. University Press of Colorado, Boulder, Colorado, pp. 75-110.
- Pastrana, A., Carballo, D. (2016). Aztec Obsidian Industries. In: Nichols, D.L. and Rodríguez-Alegría, E. (eds). *The Oxford Handbook of the Aztecs*. Oxford University Press, Oxford, U.K., pp. 329-342.
- Pastrana, A., Fournier Garcia P., Parry W.J., Otis Charlton C. L. (2019). Obsidian production and use in central Mexico after the Spanish invasion. In: Alexander, R.T. (ed) *Technology and Tradition in Mesoamerica after the Spanish Invasion*. University of New Mexico Press, Albuquerque pp. 15-33.
- Tenorio, D., Cabral, A., Bosch, P., Jimenez-Reyes, M., Bulbulian, S. (1998). Differences in coloured obsidians from Sierra de Pachuca, Mexico. *J. Archaeol. Sci.* 25, 229-234.
- Thouvenot, M. (1982). Chalchihuitl- Le jade chez les Aztèques. *Muséum national d'Histoire naturelle, Paris*, 357 p. (Mémoires de l'Institut d'Ethnologie; 21).

Figure captions:

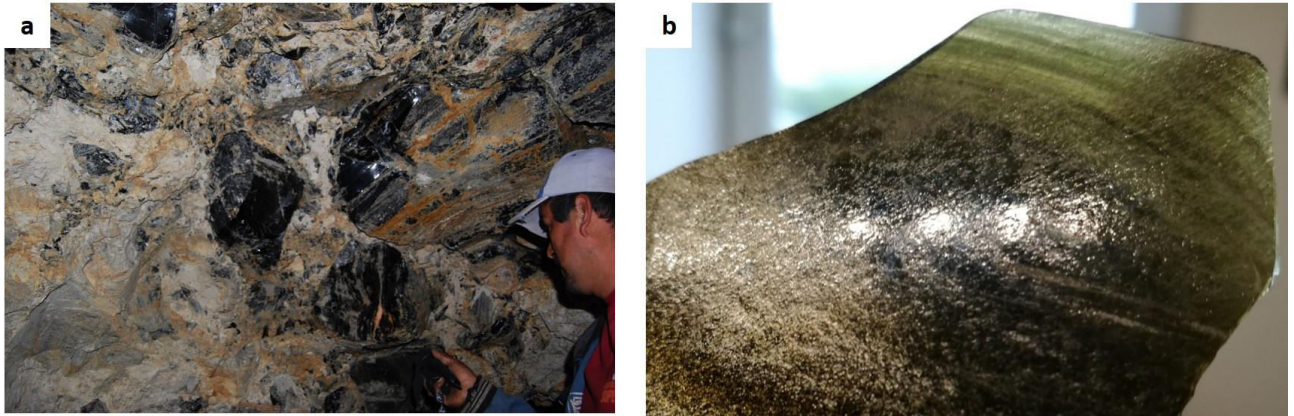


Fig. 1.: a) Obsidian tunnel mine in Sierra de las Navajas; b) the green obsidian of Sierra de las Navajas

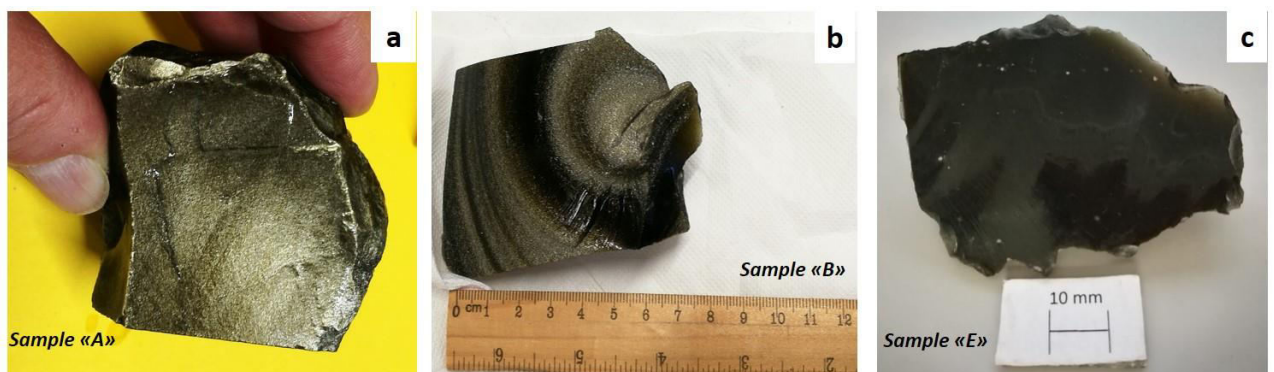


Fig. 2.: Obsidian samples used for microvesiculation studies: a) Sample “A”, with flat, rough surface (no conchoidal fracture) and homogeneous hue; b) Sample “B”, with concentric bands with different hue and roughness and conchoidal fracture; c) Sample “E”, homogeneous, dark green, with perfect conchoidal fracture, without hue.

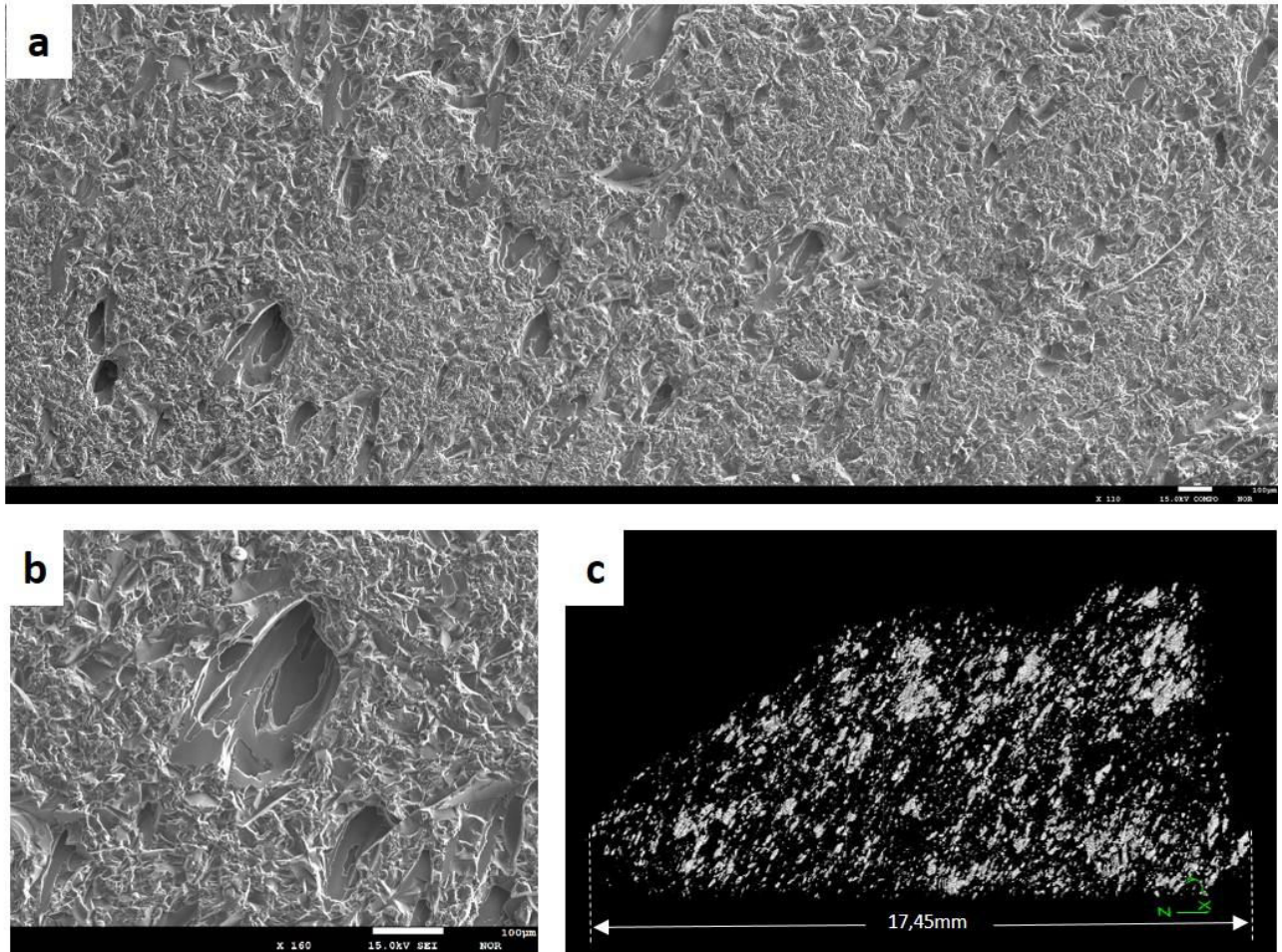


Fig. 3.: Microvesiculation of sample “A”: a) Surface of natural breakage seen under the EMPA (image acquired in Secondary Electrons); b) detail of Fig. a showing one of the multi-layered, flat vesicles; c) 3D reconstruction of vesicles by X-rays microtomography.

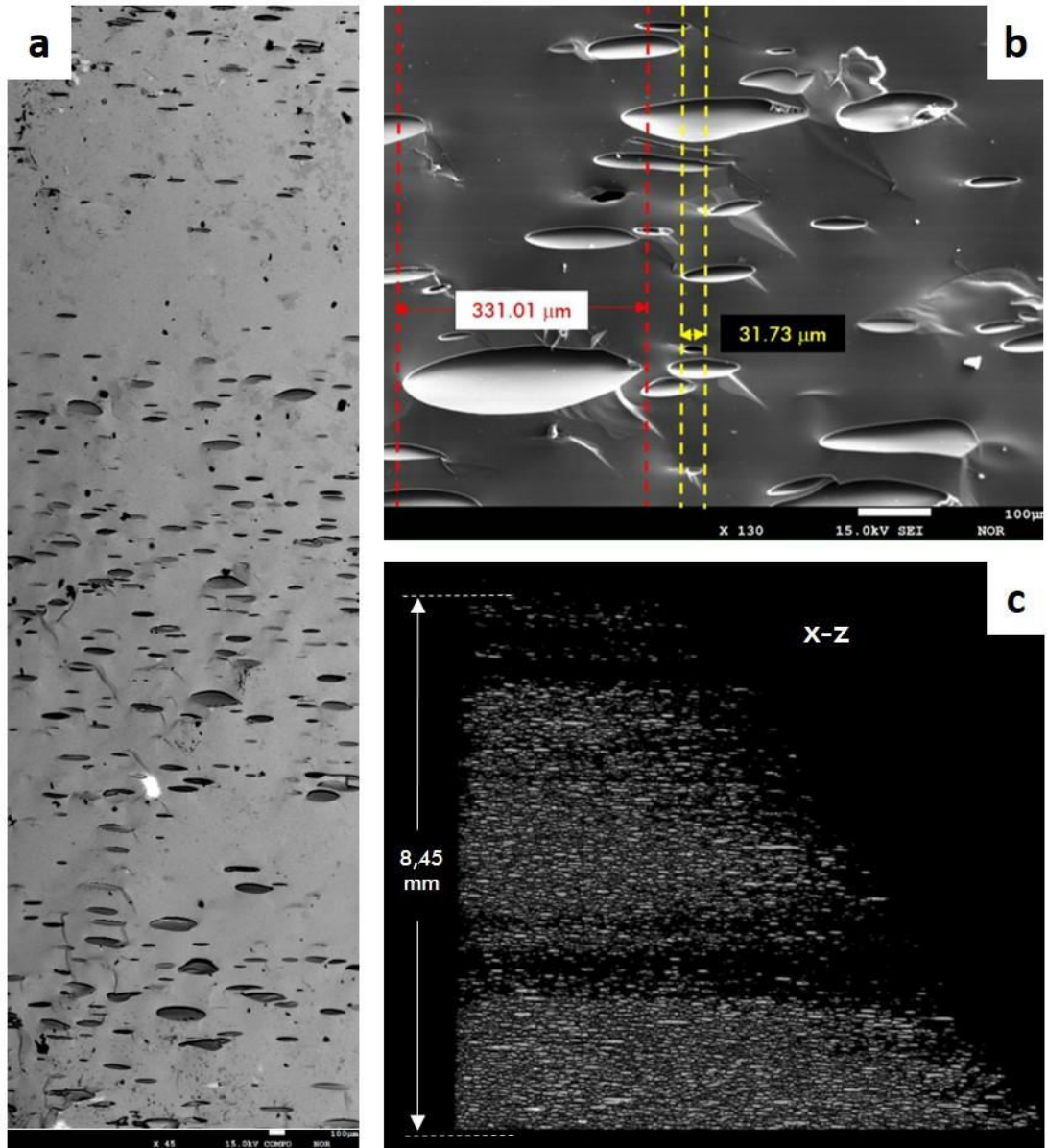


Fig. 4.: Microvesiculation of sample “B”: a) Surface of natural breakage seen under the EMPA, showing the alternation of bands with different vesicularity (image acquired in Back-Scattered Electrons); b) detail of vesicles with the size of their major axis (image acquired in Secondary Electrons); c) 3D reconstruction of vesicles by X-rays microtomography.

**4.5 CASE STUDY 5: Architectural
terracruda sculpture of Silk Roads: new
conservative insights through a
diagnostic approach based on non-
destructive X-ray micro-tomography.**





Architectural *Terracuda* Sculptures of the Silk Roads: New Conservation Insights Through a Diagnostic Approach Based on Non-Destructive X-ray Micro-Computed Tomography

Mònica López-Prat , Raffaele Giuseppe Agostino , Sudipa Ray Bandyopadhyay , Begoña Carrascosa , Maria Caterina Crocco , Raffaella De Luca , Raffaele Filosa , Vincenzo Formoso , Carla Lancelotti , Noor Agha Noori , Alessandra Pecci , José Simón-Cortés & Domenico Miriello

To cite this article: Mònica López-Prat , Raffaele Giuseppe Agostino , Sudipa Ray Bandyopadhyay , Begoña Carrascosa , Maria Caterina Crocco , Raffaella De Luca , Raffaele Filosa , Vincenzo Formoso , Carla Lancelotti , Noor Agha Noori , Alessandra Pecci , José Simón-Cortés & Domenico Miriello (2021): Architectural *Terracuda* Sculptures of the Silk Roads: New Conservation Insights Through a Diagnostic Approach Based on Non-Destructive X-ray Micro-Computed Tomography, *Studies in Conservation*, DOI: [10.1080/00393630.2020.1862605](https://doi.org/10.1080/00393630.2020.1862605)

To link to this article: <https://doi.org/10.1080/00393630.2020.1862605>

 View supplementary material [↗](#)



 Published online: 17 Jan 2021.

 Submit your article to this journal [↗](#)

 View related articles [↗](#)

 View Crossmark data [↗](#)

Architectural *Terracuda* Sculptures of the Silk Roads: New Conservation Insights Through a Diagnostic Approach Based on Non-Destructive X-ray Micro-Computed Tomography

Mònica López-Prat ¹, Raffaele Giuseppe Agostino², Sudipa Ray Bandyopadhyay³, Begoña Carrascosa¹, Maria Caterina Crocco², Raffaella De Luca⁴, Raffaele Filosa², Vincenzo Formoso², Carla Lancelotti ⁵, Noor Agha Noori⁶, Alessandra Pecci⁷, José Simón-Cortés¹ and Domenico Miriello⁴

¹Departament de Conservació i Restauració de Béns Culturals, Universitat Politècnica de València, Valencia, Spain; ²Dipartimento di Fisica and STAR-Lab, Università della Calabria, Arcavacata di Rende, Italy; ³Department of Ancient Indian History and Culture, University of Calcutta, Calcutta, India; ⁴Dipartimento di Biologia, Ecologia e Scienze della Terra, Università della Calabria, Arcavacata di Rende, Italy; ⁵CaSEs Research Group, Universitat Pompeu Fabra, Barcelona, Spain; ⁶Archaeology Institute of Afghanistan, Kabul, Afghanistan; ⁷ERAAUB Research Group, Universitat de Barcelona, Barcelona, Spain

ABSTRACT

This work presents the results of the study of a fragment of architectural *terracuda* sculpture from the Buddhist archaeological site of Tepe Narenj (Kabul, Afghanistan, fifth-ninth centuries CE) through X-ray micro-computed tomographic analysis. This technique offers great potential for the study of artworks that, due to their nature, condition, or relevance, are not suitable for sampling. The results have provided useful data for understanding the making of the sculpture showing for the first time the relevance of materials of plant origin used in the composition of the clay-based body, a feature that had not been previously highlighted and which appears to be crucial for proposing suitable conservation interventions.

ARTICLE HISTORY

Received October 2020
Accepted December 2020

KEYWORDS

Conservation; *terracuda* sculptures; X-ray micro-computed tomography; sculpting technique; ethnographic data; clay

Introduction

The practice of modelling architectural *terracuda* sculptures is a very specific artistic technique that presents no known examples outside of South, Central, and Eastern Asia. These sculptures, which can be smaller than human size or reach several meters in height, are skilfully modelled *in situ* starting from a core skeleton of wood, brick, or stone attached to the architecture, modelled with different clay-based layers, frequently covered with stucco and, finally, gilded and/or polychromed (Varma 1970; Tarzi 1986; Luczanits 2004). Historic examples of this artistic expression are mainly linked to the spread of Buddhist art from the north west Indian subcontinent through what is known today as the 'Silk Roads'. The first Buddhist instances are found, at the beginning of the common era, in the area of present-day Pakistan, Afghanistan, south of Uzbekistan, and Tajikistan. Later, they spread to the Himalayas and Eastern Asia, where examples can be identified up to modern times.

Despite their extraordinary interest, this type of sculpture has received little attention from the scientific community dedicated to heritage conservation. The technical studies carried out so far have usually focused on investigating the mineral and chemical

composition of the pastes and polychromies (Bayerová, Gruber and, and Krist 2010; Blaensdorf and Tao 2010; Lluveras et al. 2011; Singh Gill, Priego Rendo, and Menon 2014; Wang et al. 2014, 2020). Conversely, the precise methods employed to model sculptures that usually exceed human size and where the use of organic material of plant origin mixed with the clay plays an extremely important role, has been little studied. Two main issues can be identified to account for the limited research on these sculptures: either they are still *in situ*, usually in regions difficult to access, or they have already been extensively treated by a number of techniques that have largely changed their morphology. Additional motives may be related to the fact that these sculptures are produced with a modelling technique unknown outside Asia and made of raw or unfired clay, a material that has traditionally been little used in the West for the production of artworks intended to 'remain'.

In this context, interdisciplinary collaborative research work is being carried out between the Polytechnic University of Valencia (Spain), the University of Calabria (Italy), and the Archaeological Institute of Afghanistan, with the contribution of the National Geographic Society. The aim is to fully understand the artistic technique used to make architectural

terracruda sculptures and then explore new conservation treatments more in line with current frameworks using ecological and sustainable materials. For this research, we hypothesise that this ancient technique is still used in some areas of India, such as West Bengal, where an ancient caste of artists continues to produce large clay-based sculptures following a century-old tradition described in Sanskrit ritual texts, the oldest dating back to the eighth century CE (López-Prat et al. 2021, in press).

The broader project combines the characterisation of the raw materials used in the manufacture of these ancient sculptures with data obtained during the ethnographic field work. The aim is to compare the production methods by means of qualitative analysis of archaeological and ethnographic data, as well as geochemical, mineralogical, and botanical analysis of samples of clay-based sculptures, both from modern Hindu examples and from fragments collected from a selection of different archaeological sites in Afghanistan where *in situ* architectural *terracruda* sculptures are still found. In this regard, although the research is based on the comparison of two extremes of the same technology and there will undoubtedly be variations caused by the time lag and geographic difference, there are clear parallels that point to similar patterns based on the use of a core group of materials with specific properties, and layered applications in predetermined steps, which allow the creation of large sculptures of unfired polychromed clay.

In this paper we present the first results of the non-destructive analysis of a sculpture fragment (part of a finger), sample named TN7 (Figure 1), from the archaeological site of Tepe Narenj (Kabul, Afghanistan). The site, whose current name literally means ‘Hill of orange trees’, is located on the route that connected the historical regions of Gandhara and Bactria or, in other words, India with Central Asia. It lies on the eastern slopes of the Hindukush mountain chain, only a few kilometres south of the present-day city of Kabul (Figure 2). According to archaeological research,



Figure 1. Macro-photo of sample TN7.

Tepe Narenj was the location of a Buddhist monastery that was active between the fifth and ninth centuries CE. The excavations uncovered an architecturally complex system with three levels (lower, middle, and upper) interconnected by a system of steps and platforms (Paiman 2017). On the terraces in the middle portion of the site stood a series of cult chapels where the remains of multiple examples of architectural *terracruda* sculptures are preserved (Figure 3). Tepe-Narenj is today one of the best surviving examples of Afghan Buddhist archaeological complexes, especially because of the importance of the architectural *terracruda* sculptural decoration preserved *in situ*.

These sculptures were modelled following the aforementioned technique, which in this case involved the use of a core skeleton of wood, followed by layers of different clay-based plasters, finally covered with a thin layer of white stucco that in some cases retains traces of colour. Even though the sample studied in this work represents only a small part of a whole figure, its analysis is representative of the technique and the main materials used for the rest of the sculpture that, according to what we know so far, only vary in the proportion between the inert, organic, and clay fractions depending on the part of the body being processed. In addition, we hope to be able to reintegrate it to the statue of origin; this implies that during the analytical phase the sample must be preserved without performing destructive operations. However, *terracruda* materials are very brittle and difficult to treat, even during the phase aimed to investigate the chemical, mineralogical, petrographic, and textural composition. Unfortunately, the analytical procedures that allow one to obtain detailed compositional information are predominantly destructive, as they require cutting and pulverising the sample. Thus, X-ray micro-computed tomography (micro-CT) was chosen as a very suitable technique. Although it does not provide chemical or mineralogical information, it is extremely valuable for discovering important information on the internal structure of the sample. In addition, it could provide data on the number of layers that formed the finger, on the distribution and dimensions of the different materials in the different layers, on the possible presence of completely degraded organic materials used in the mixture, and on the volumetric distribution of the voids, clay, and inert material in the different layers.

Methodology

Object of the study

Sample TN7 (Figure 1) is, as mentioned, a fragment of a finger, with maximum length of 21 mm and a diameter of 36 mm. It was recovered from a wicker basket



Figure 2. Location of the archaeological site of Tepe Narenj (Kabul, Afghanistan). Aerial Photo of the site: Z. Paiman ©.

located inside Chapel 5 – Zone III. According to the archaeological excavations, this area belongs to the second period of occupation of the monastery, dated to the mid-sixth century.

Analytical techniques

Preliminary macro- and microscopic observations with a LEICA-EZ4W microscope were followed by micro-CT, a non-destructive technique of radiographic imaging, able to produce 3D images of the inner structure of a solid material with a spatial resolution in the order of micrometers, based on a set of two-dimensional radiographic images from a sample (Wildenschild and Shepard 2013; Boerckel et al. 2014). This technique is applied in a vast diversity of fields: medicine, biology, engineering, palaeontology, and earth sciences are just a few examples. Applied to cultural heritage, the technique has been mainly used for the study of stone and metal artefacts, but also in an exploratory fashion in the technological study of ceramics and bricks (Kahl and Ramminger 2012; Kulkova and Kulkov 2014; Agostino et al. 2016; Coletti et al. 2016; Kozatsas et al. 2018; Park et al. 2019; and Reedy 2020). To the best of our knowledge, micro-CT has been only applied to unfired clay objects to read the

inscriptions on ancient clay tablets that had been sealed in clay envelopes and in the technological study of unfired Neolithic clay figurines from the ancient Near East (Applbaum and Applbaum 2005). However, the use of non-destructive techniques becomes crucial in the case of very friable artefacts, like unfired clay-based ones, because destructive analyses that break or cut the clay sample to study its various components contribute to the loss of textural and spatial information (Bukreeva et al. 2016).

The principle of micro-CT is based on the attenuation of X-rays passing through the sample being imaged. As the X-ray passes through a homogeneous object the intensity of the incident X-ray beam is reduced according to the Beer-Lambert equation (Figure 4):

$$I = I_0 e^{-\mu x}$$

where I_0 is the intensity of the incident beam, x is the distance covered by the X-ray in the absorbing object and μ is the linear attenuation coefficient (Landis and Keane 2010).

Cone beam microtomography has the advantage of using a simple and versatile apparatus.

In general, a micro-CT system is composed of an X-ray source, a detector, a sample holder, and a process



Figure 3. Examples of architectural *terracuda* sculptures preserved in the archaeological site of Tepe Narenj (Kabul, Afghanistan).

control system by computer for moving the sample, or detector, or X-ray source (Lee et al. 2003). There are also computational systems for the acquisition, processing, and reconstruction of tomographic images, to carry out qualitative and quantitative analyses.

Figure 5 shows a schematic diagram of the operational sequence used to perform micro-CT measurements. A micro-CT apparatus performs an initial

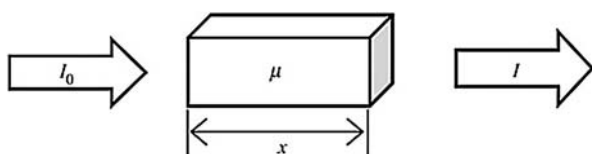


Figure 4. Attenuation of X-rays passing through the sample according to the Beer-Lambert law.

measurement rotating the sample on its own axis while the X-ray source and detector remain fixed, or *vice versa*. The microfocus X-ray source continuously irradiates the object (or the sample), while the flat-panel detector acquires a series of 2D projections of the object at different angles with a constant angular step until completing 360 degrees and at a fixed integration time. The angular step (typically a fraction of degree) and integration time are computer-controlled.

Lastly, the 3D digital reconstruction is based on a filtered back-projection algorithm (FBP) (Kak and Slaney 1988). In our case, since the micro-CT apparatus uses an X-ray cone beam source, the 3D digital reconstruction is performed using the algorithm by Feldkamp, Davis, and Kress (FDK) (Feldkamp, Davis, and Kress 1984). The 3D digital reconstruction produces a 2D dataset of cross-sections perpendicular to the

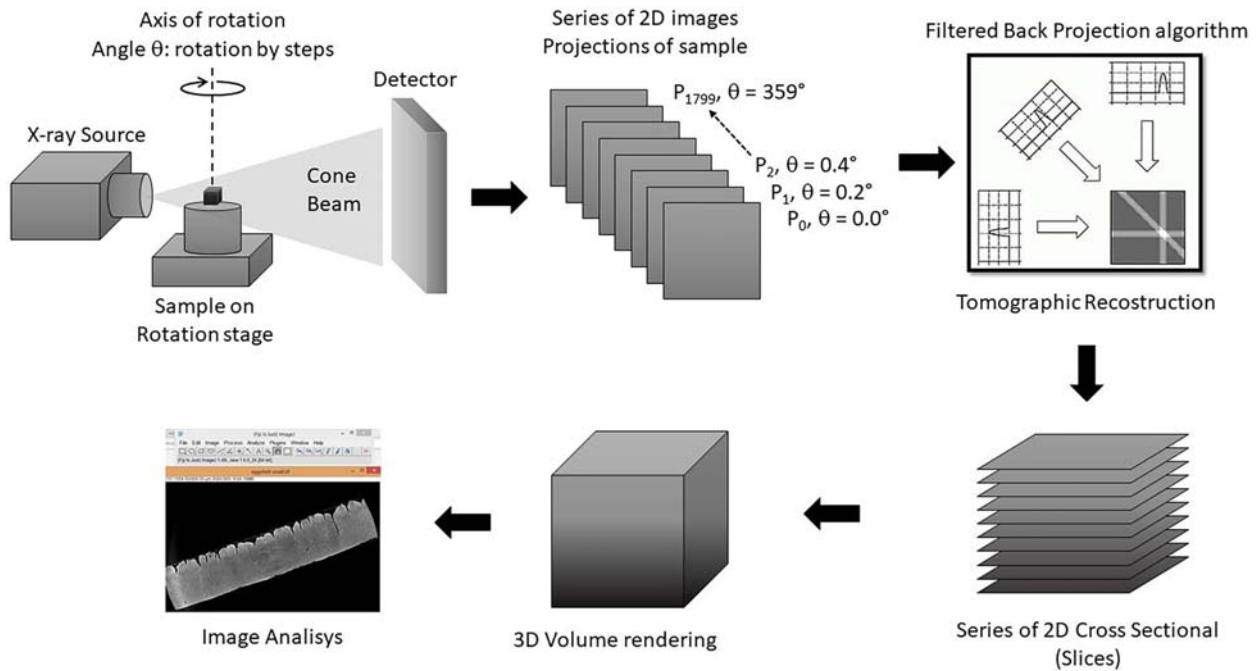


Figure 5. Schematic representation of operations sequence to perform a micro-CT measurement.

rotation axis, called slices. The stack of slices provides three-dimensional volumetric data. The sample can be then viewed and analysed in a virtual environment in various ways, either by viewing a single slice of the sample or the 3D virtual volume where each volume unit, called voxel, contains information on the X-ray absorption coefficient.

Experimental setup

The micro-CT experimental station used in this work (μ Tomo- supplied by Sincrotrone Trieste SCPA) is part of the STAR-Lab facility realised under the PON MaTeRiA project. It is located at the University of Calabria in Italy.

The μ Tomo experimental station, based on a cone beam geometry, shown schematically in Figure 6, is composed of:

- a microfocus X-ray source Hamamatsu L12161-07;
- a flat panel detector Hamamatsu C7942SK-05;
- a six degree of freedom sample positioning system (linear movement and rotation stage);
- hardware and software system for control and data acquisition.

All the components except the process control system are mounted on an optical bench. The micro-focus X-ray source continuously irradiates the object (or the sample), which is rotated with a constant angular step until completing 360 degrees and the flat-panel detector acquires a series of 2D projections

of the object at different angles and at a fixed integration time.

The X-ray source is a polychromatic microfocus X-ray generator (Hamamatsu L12161-07) with a tungsten target. The microfocus source can be operated with a voltage range from 40 to 150 kV and allows three power modes that determine the source size. The minimum source size (5 μ m) is obtained at power below 4W. The X-ray cone beam aperture is about 43 degrees.

The detector is a flat panel sensor C7942SK-05 from Hamamatsu. These detectors are based on 2D arrays of photodiodes CMOS (CCD) directly coupled to a scintillator for X-ray to light conversion. Its main features are shown in Table 1.

The sample positioning system (by PI miCos Industry) provides six degrees of freedom: three linear motors for x, y, z movement, one for the rotation stage theta (θ), and two stages for tilt angles. This system allows one to position the sample with the required precision. In particular, the Source-to-Object Distance (SOD) and Source-to-Detector Distance (SDD) determine the system geometric parameters such as magnification ratio ($M=SOD/SDD$).

The μ Tomo station is provided with a user interface that allows its control through a computer. All the electronic hardware components are commercially available and are, in general, provided with software drivers which are LabVIEW compatible (Ionita et al. 2008; Conte et al. 2019).

The sample object of this study was investigated at the μ Tomo experimental station with the following experiment setup: the X-ray source operated at a voltage of 130 kV, a current of 76 μ A (source power

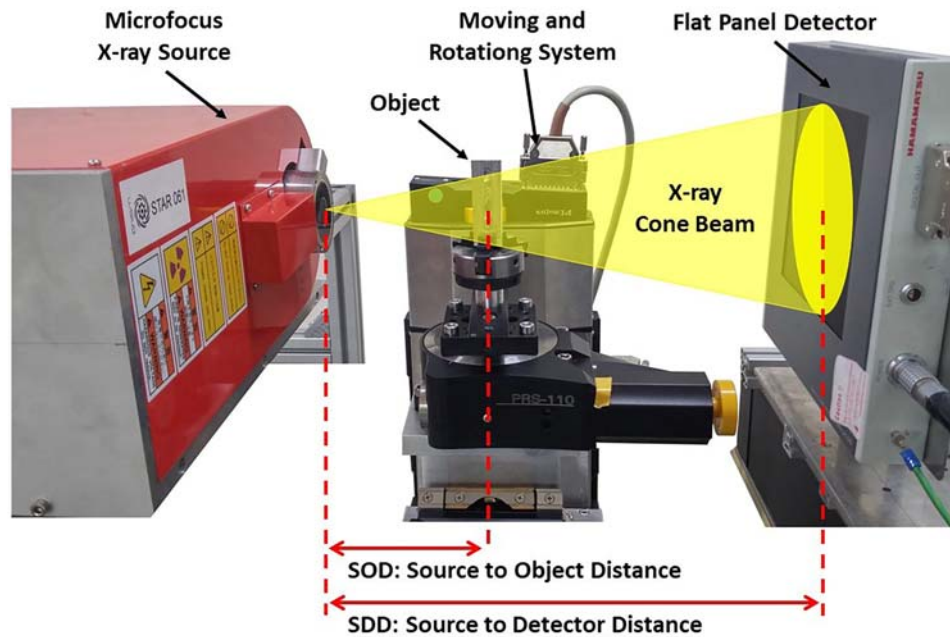


Figure 6. μ Tomo experimental station @Lab. STAR (University of Calabria, Italy).

10 W), and a focal spot size of 7 μm ; the low energy components of the X-ray beam were filtered by 100 μm -thick copper foil. In this study, the SOD was set to 200 mm and the SDD to 500 mm, and the magnification is equal to $M=2.5$. Considering the employed beam magnification, the equivalent voxel side was 20 μm . A set of 1800 projections were acquired over an angular range of 360° using a 0.2-degree angular step and an exposure time of 2 s/projection. Axial slices were reconstructed with an isotropic voxel size of 20 μm using the FDK algorithm for cone-beam geometry. The measurement parameters are shown in Table 2.

3D image analysis

Image analysis was performed with Fiji (Schindelin et al. 2012), an open source image processing package based on ImageJ. ImageJ is an open source software package developed by the National Institutes of Health of the United States (Collins 2007), which allows digital image processing operations. ImageJ is designed with an ‘open architecture’ that provides the possibility to install extensions via small subprograms as ‘Java plugins’ and the possibility to develop many macros for ad-hoc processing, working in 2D and 3D space.

The aim of the analysis is to retrieve the morphology and topology of the constituents of the

sample. The first step consisted in extracting a volume of interest (VOI) from the stack of reconstructed slices. The selected VOI enclosed a representative amount of the sample heterogeneity and can be defined as representative elementary volumes (REVs) (Costanza-Robinson, Estabrook, and Fouhey 2011). The VOI was filtered with a ‘3D Gaussian-Blur filter’ (Ollion et al. 2013) to reduce the image noise and segmented by an automatic thresholding algorithm (Otsu 1979) to separate the different materials in the sample (clay, sand, and voids).

Following the study of the macro structure of the sample, the various components were isolated and analysed separately. The ‘3D ImageJ Suite’ (Ollion et al. 2013) of the Fiji software library was applied to evaluate the density of the different components, which provides their volumetric fraction within the sample. A morphological and topological analysis of clay, sand, and voids was performed by excluding those touching the VOI borders, since they can be truncated, and their volume and morphology may not be representative of the real shape. For volumetric analysis, the sample was

Table 1. Detector features.

| Parameter | Specification | Unit |
|------------------------|---------------|---------------|
| Pixel size | 50 × 50 | μm |
| Photodiode active area | 115 × 115 | mm |
| Number of active pixel | 2316 × 2316 | pixels |

Table 2. Measurement parameters.

| | |
|---|-------------------------|
| Microfocus source parameters | |
| X-ray tube voltage (kV) | 130 |
| X-ray tube current (μA) | 76 |
| X-ray focal spot mode Small | 7 μm |
| Power (W) | 9.88 |
| Energy filter | |
| Source and detector position | 100 μm of Cu |
| Source to Object Distance – SOD (mm) | 200 |
| Source to Detector Distance – SDD (mm) | 500 |
| Magnification | 2.5 |
| Equivalent pixel-size (μm) | 20 |
| Detector parameters | |
| Number of images captured | 1800 |
| Angular step ($^\circ$) | 0.2 |
| Acquisition time (ms) | 2000 |

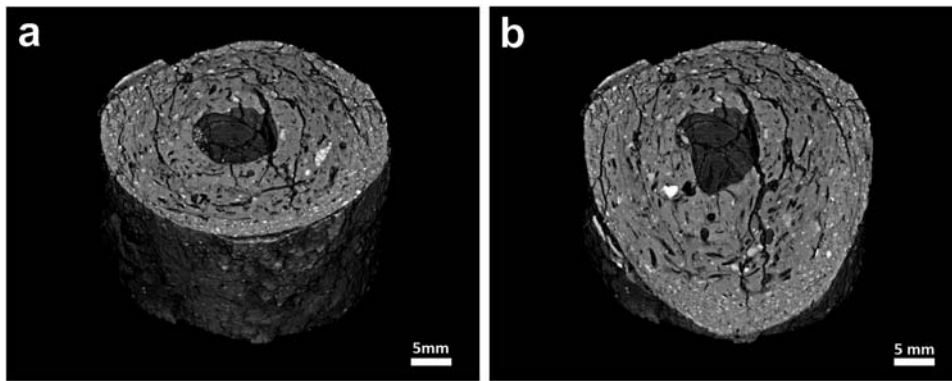


Figure 7. (a) 3D rendering of the bulk sample; (b) 3D rendering of the bulk sample, cut through an oblique plane.

divided into three parts identified as internal layer, intermediate layer, and external layer.

The volume of different components was obtained via the '3D Geometrical measurements' and '3D Object Counter' (Bolte and Cordelières 2007), plugins of Fiji. The 3D visualisation was performed by volume rendering procedures using the plugins 'Volume Viewer' (Barthel 2006) and '3D Viewer' (Schmid et al. 2010). This analysis allowed us to determine the three-dimensional shape of the clay, sand, and voids and their distribution and orientation inside the sample.

Results and discussion

The preliminary visual observation allowed us to detect that the fabrication of the fragment studied follows the practice documented in technical studies of this type of sculpture (Varma 1970; Tarzi 1986; Luczanits 2004). In fact, it was observed that the finger was made of superimposed layers of greyish brown (Munsell 10YR 6/3) clay material, layered around a rigid element (today decomposed), and finished with a thin layer of white stucco only partially preserved.

Macropores and impressions left by organic material, most probably of plant origin, mixed with the clayey paste are visible in the section to the naked eye. The identification of the various layers also highlights the different phases of the modelling process and the preparation of layers with different compositions.

The first result of the micro-CT work is shown in Figure 7, where it is possible to observe the 3D rendering of a cylindrical section of the bulk sample (Figure 7 (a)) and a cut through an oblique plane (Figure 7(b)). The three-dimensional reconstruction of the bulk sample from different points of view can be found in the video available in the supplementary material (Supplementary Video 1). The bulk image shows that there are three main layers superimposed around the central cavity. The equatorial section of the sample shows the precise details of the three principal layers (Figure 8). The inner layer (layer 1), the one closest to the cavity, and the intermediate layer (layer 2) have a thickness of c. 5 mm. The outer layer (layer 3) is the thinnest (c. 2 mm). Some fragments of white stucco on the surface are visible on the external-most layer, whose thickness is approximately 1.8 mm (Figure 8).

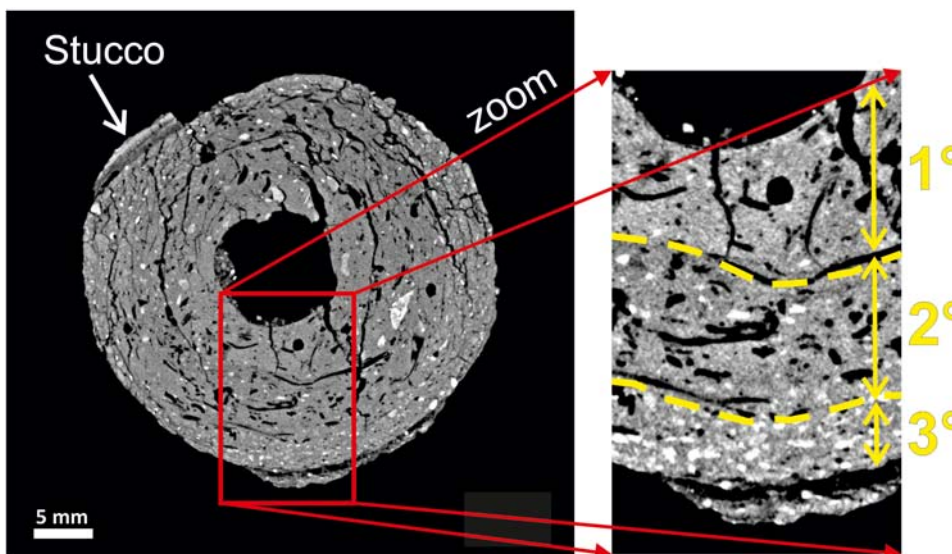


Figure 8. Equatorial section of the sample, with a close-up of the three main layers.

Table 3. Estimation of the percentage of the clay material, inert material, and voids in the layers 1, 2, and 3 of the sample TN7.

| Sample TN7 | Inert materials (% 3D volume) | Clay material (% 3D volume) | Void (% 3D volume) | Max. size of the inert materials (μm) | Mean size of the inert materials (μm) |
|------------|-------------------------------|-----------------------------|--------------------|--|--|
| Layer 1 | 1.81% | 92.71% | 5.48% | 1500 | 264 |
| Layer 2 | 1.64% | 87.29% | 11.07% | 1280 | 166 |
| Layer 3 | 4.53% | 90.38% | 5.09% | 1660 | 202 |

From the 3D reconstruction of sample TN7 it was possible to segment and perform the thresholding of the three main components of the sample: the clay fraction, the inert material, and the voids. The morphology of the voids is very particular; it does not correspond to that usually observed in clayey mixtures. These voids are not spherical or elliptical but have shapes that fit with traces of decomposed organic material, which is most likely of plant origin. The idea was to perform the thresholding of the voids to reconstruct the morphology of the organic material in three dimensions and verify this hypothesis. Table 3 shows the estimation of the percentage of the clayey material, inert material, and voids in the layers 1, 2, and 3. All three layers are mainly made of clayey material, comprising 92.71% in layer 1, 87.29% in layer 2, and 90.38% in layer 3. The 3D reconstruction of the clay fraction is shown in Figure 9. A video with the full three-dimensional reconstruction of the

clayey fraction can be found in the supplementary material (Supplementary Video 2). The inert fraction is the least abundant compared to the voids and the clayey fraction; it represents 1.81% of layer 1, 1.64% of layer 2, and 4.53% in layer 3 (Table 3). The mean size of the inert fraction in the three layers is very similar: c. 264 μm in layer 1, 166 μm in layer 2, and 202 μm in layer 3 (Table 3). However, in all three layers it is possible to find rare larger fragments of inert material varying between 1280 and 1660 μm . Figure 10 shows the 3D rendering of the inert material of the sample TN7 from different points of view and a video of the full three-dimensional reconstruction of the inert fraction can be found in the supplementary material (Supplementary Video 3). The cumulative frequency curves of the particle size distribution for the inert material inside layers 1, 2, and 3 are very similar; this suggests that the same inert material was used for the three layers (Figure 11). However, it is

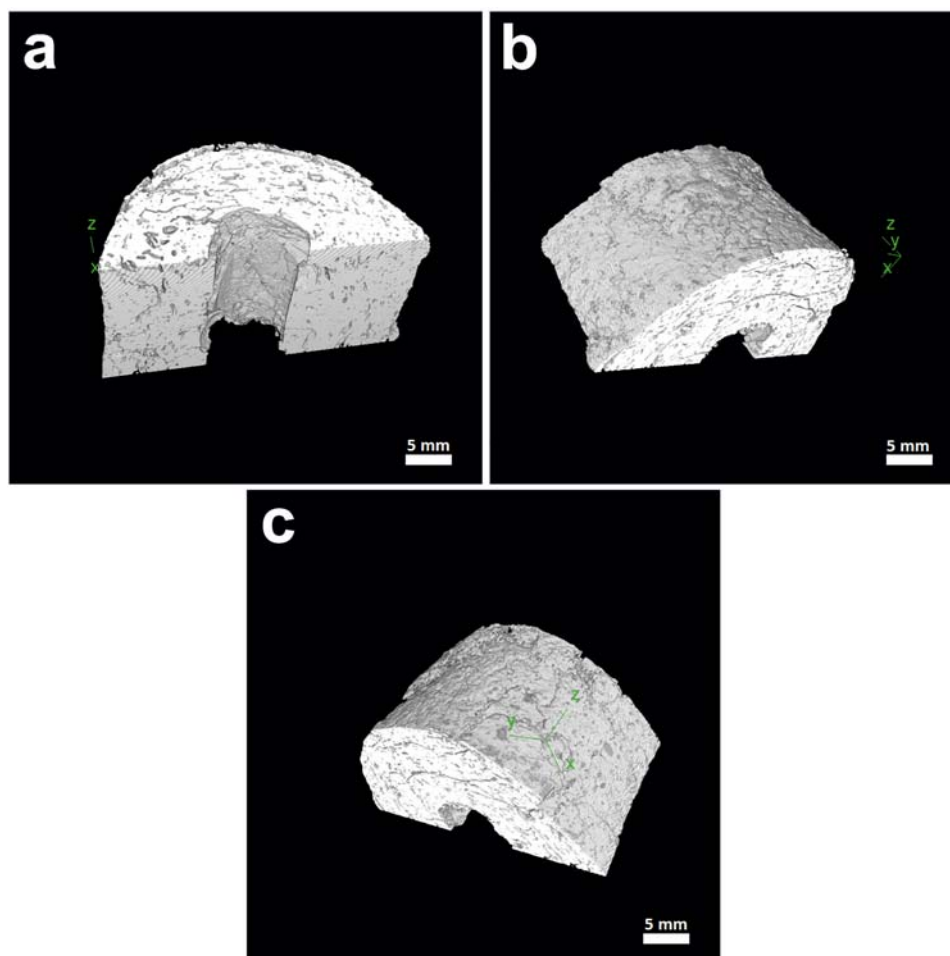


Figure 9. (a) 3D rendering of a portion of the clay material (0° position); (b) 3D rendering of a portion of the clay material, rotated 143 degrees from the start position; (c) 3D rendering of a portion of the clay material, rotated 234 degrees from the start position.

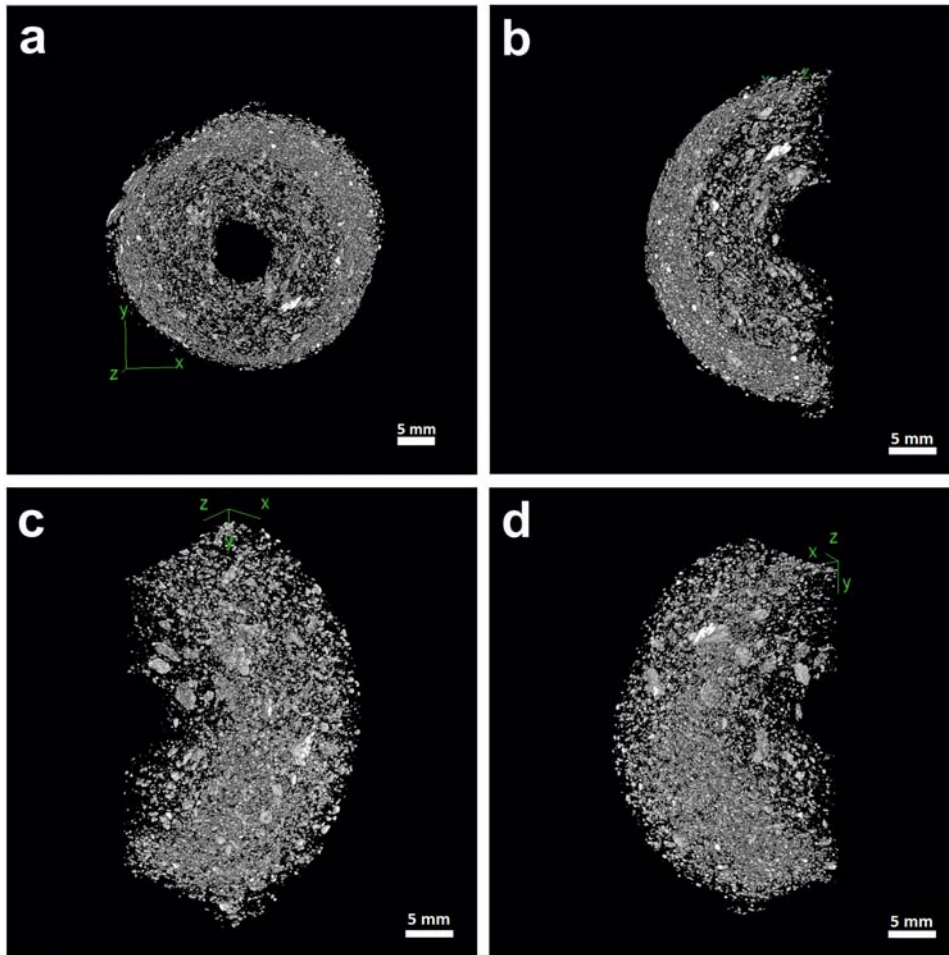


Figure 10. (a) 3D rendering of the inert material shown in the equatorial section; (b) 3D rendering of a portion of the inert material (0° position); (c) 3D rendering of a portion of the inert material rotated 40 degrees from the start position; (d) 3D rendering of a portion of the inert material rotated 146 degrees from the start position.

difficult to establish at this stage if the inert material is naturally present in the clay or if it was added later to reduce the plasticity of the clays. The distinct volumetric content of inert material in the various layers could support the second hypothesis or point to a separate origin for the clay materials in order to obtain different properties related to the plasticity and stickiness of the clay, as shown by some technical studies done on *terracruda* sculptures from the Buddhist temple complex at Nako (Bayerová, Gruber, and Krist 2010) and in the ethnographic research done in 2019 in West Bengal (López-Prat et al. 2021, in press). This showed the same principle and noted the employment of two different clays extracted from different places and used mixed or separately depending on the layers or parts to be modelled in the general step-by-step process necessary for the entire creation of a sculpture. These clays are used as needed: one is stickier and harder, and the other is sandier and more malleable. In this sense, the results of the micro-CT work showing the presence of different amounts of inert materials could indicate similar purposes.

Among all the data obtained from the micro-CT analyses, the one relating to voids is perhaps the

most interesting and surprising. The 3D segmentation of the voids shows a perfect cast of vegetal material, which is present only in the first two inner layers, while it is completely absent in the third layer (Figures 12 and 13). In the first layer the voids created by plant material represent about 5.48% while in the second layer about 11.07% of the layer (Table 3). In the third layer, 5.09% of voids are due to small shrinkage cracks and not to the presence of vegetal material. The voids left by decomposed material can reach a length of 1.5 cm (Figure 13(b)) and present diameters ranging from $200\ \mu\text{m}$ to 1.7 mm. (Figure 13(b)). In Figures 12 and 13 it is also possible to observe how the voids wind around the central cavity and are oriented in the same direction, which in all probability indicates a modelling process around a central rigid and perishable structure. A video with the full three-dimensional reconstruction of the voids can be found in the supplementary material (Supplementary Video 4). The use of plant-based materials in the inner layers of TN7 shows a clear parallel with the process of modelling fingers in the Bengali sculptures observed during the ethnographic work, which are performed in series separately

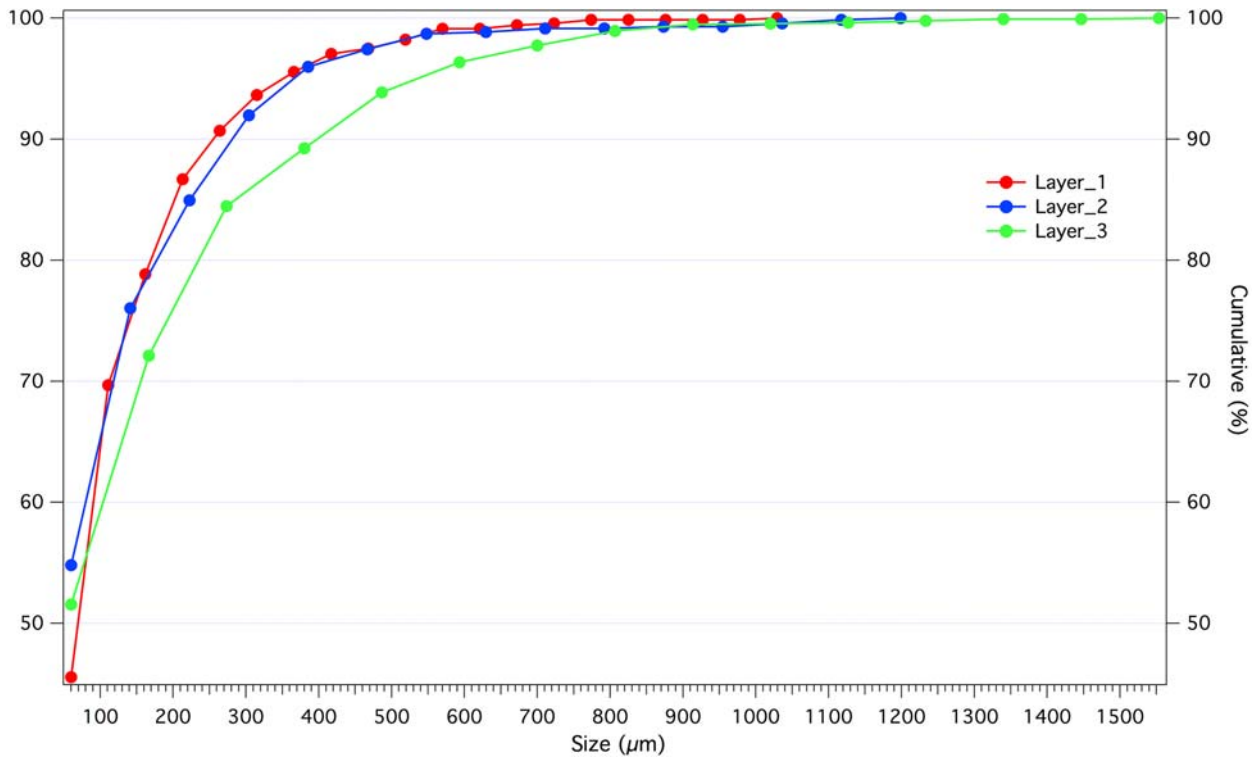


Figure 11. Cumulative frequency curves of the particle size distribution for the inert material inside layers 1, 2, and 3.

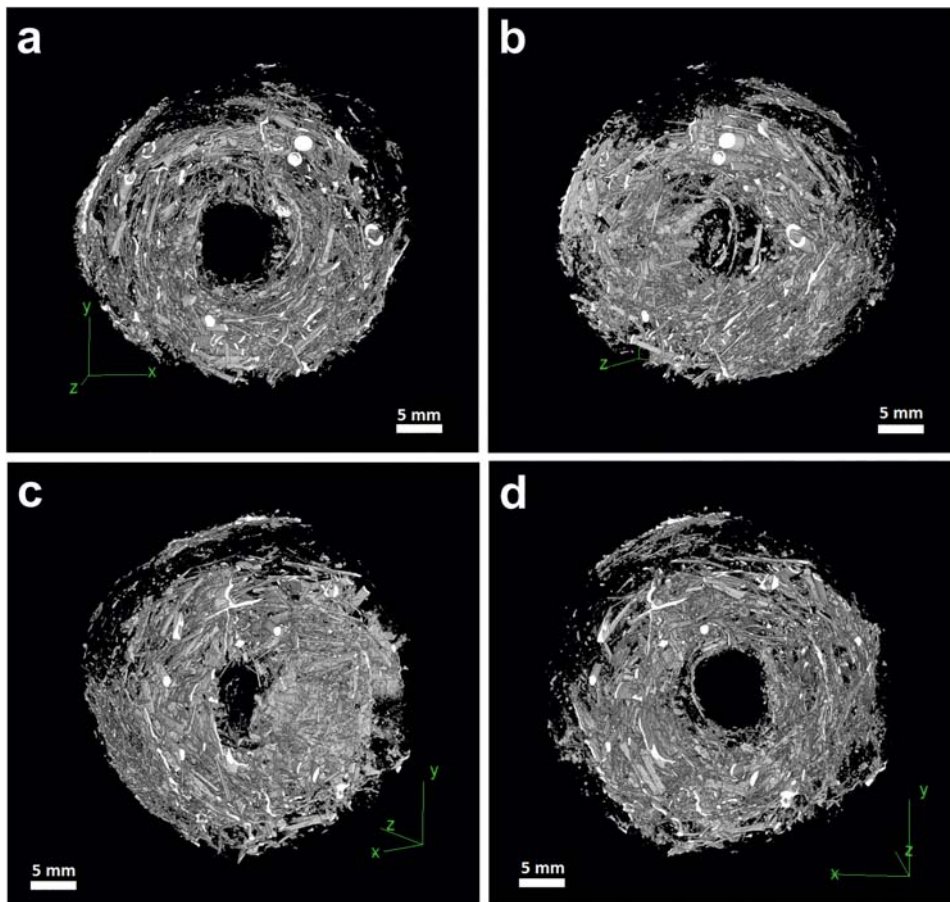


Figure 12. (a) 3D rendering of the voids shown in the equatorial section (0° position); (b) 3D rendering of the voids rotated 35 degrees from the start position; (c) 3D rendering of the voids rotated 160 degrees from the start position; (d) 3D rendering of the voids rotated 193 degrees from the start position.

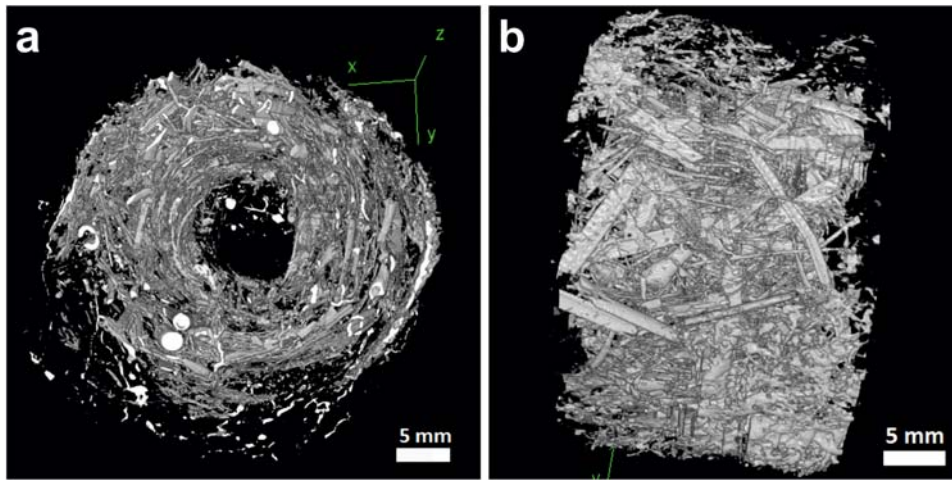


Figure 13. (a) 3D rendering of the voids shown in the equatorial section; (b) 3D rendering of the voids rotated 90 degrees from the equatorial position.



Figure 14. Dayal Pal, sculptor from the Kumortuli clay artists' quarter (Kolkata, West Bengal) showing the finger modelling process. On the right, detail of the fingers next to the clay and jute fibres used in the procedure.

by adding a large amount of jute fibres to the clay mass (product of the mixture of the two aforementioned clays), to increase its rigidity without adding any internal structure in this case (Figure 14). Moreover, the absence of voids detected in the outermost layer of TN7, together with the greater presence of inert material, also presents an analogy with current Bengali sculptors, who, in order to finish the modelling process of the different layers of clay, apply a denser and more liquid paste, prepared exclusively with the most sticky clay, to which cotton textiles are adhered. This last layer of clay prepares the sculpture to receive the white stucco coating, necessary to polychrome the sculpture. In the micro-CT work, the micrometric space left between layer 3 and the areas where the stucco layer has been preserved (see Figure 8) might indicate the presence of a similar fabric, now missing but documented in other sculptures on the site (Paiman 2005; Paiman and Alram 2010).

Conclusions

The elaboration of architectural *terracruda* sculptures through the superimposition of various layers of clay

mixed with plant material starting from a rigid skeleton mirrors a technique documented in multiple Buddhist archaeological sites and historical temples along the Silk Roads, from the north-western part of the Indian subcontinent to eastern Asia crossing the Himalayas. In this perspective, micro-CT has proved to be of great value in understanding this artistic technique, especially by unravelling in a non-destructive manner the stratigraphy and the proportions between the mineral components and the organic material present in the modelling pastes, mainly decomposed and often disregarded during destructive analyses. As far as we know, this is the first time that an imaging technique has indicated the presence of the high proportion of organic material that was originally added to the clay and that technically made it possible to produce large *terracruda* sculptures. Knowing the proportion of organic material is crucial from a conservation point of view, especially for developing compatible treatments in the consolidation and reintegration phases aimed at reproducing grouts to fill gaps and cracks, that are light enough, so their weight and the shrinkage caused by drying do not lead to the appearance of new breaks and detachments in the originals.

After this research, the question that arises is what type of plant material was used in ancient times and whether this use was random or whether specific properties were sought, as is the case today in West Bengal where rice husk and chopped straw as well as jute fibres are added with particular purposes in almost every stage of the manufacture of a clay idol. These purposes include increasing the stickiness, lightening the weight, facilitating drying while avoiding cracks, and increasing the rigidity of the clay layers. Finding the right material to reproduce the essential role of the fibres in the modelling process will be an important step towards the complex final objective of preserving architectural *terracruda* sculptures found in an archaeological context.

In this sense, within the framework of this research project, phytolith and DNA analyses are being carried out on different samples from various Afghan sites with examples of architectural *terracruda* sculpture. The results are being compared with current Bengali methodology, which has inspired the exploration of the possibilities of adding to clay micronized rice husk as a possible component in the manufacture of compatible and light enough filling mortars in the restoration process.

Acknowledgements

This research is part of Mònica López Prat's ongoing doctoral research conducted in the Polytechnic University of Valencia in collaboration with the University of Calabria and has been supported by a National Geographic Society Early Career Grant (EC-59568C-19). The activity of Carla Lancelotti has been supported by the Generalitat de Catalunya with grant SGD2017-212. The activity of Alessandra Pecci is part of the activities of the ERAAUB grant SGR 2017-01173. The μ Tomo experimental station was acquired using PON MaTeRiA project – PONa3_00370 – funds. We gratefully acknowledge Zafar Paiman, who explained the details of his studies in Tepe-Narenj and Susan S. Bean, for always being available to share their knowledge about the tradition of modelling *terracruda* sculpture in southern Asia, and all the Bengali artists (specially the *kumors* of Kumortuli) who, in keeping with their ancient tradition, have collaborated to understand the process of modelling *terracruda* sculptures. Many thanks to all the people and institutions involved in this transboundary east–west research and specially to an explorer met in Samarkand.

Disclosure statement

No potential conflict of interest was reported by the author(s).

Funding

This work was supported by Agència de Gestió d'Ajuts Universitaris i de Recerca [grant number SGD2017-212]; National Geographic Society [grant number EC-59568C-19].

ORCID

Mònica López-Prat  <http://orcid.org/0000-0002-7026-5720>

Carla Lancelotti  <http://orcid.org/0000-0003-1099-7329>

References

- Agostino, R. G., S. Donato, T. Caruso, E. Colavita, F. Zanini, A. D'Alessio, D. Pisarra, and A. Taliano Grasso. 2016. "Microtomographic Studies as a Tool in the Identification of a New Ceramic Class: The Metal-Imitating Pottery as Grave Goods among Brettians and Lucanians." *Microchemical Journal* 126: 138–148.
- Applbaum, N., and Y. H. Applbaum. 2005. "The Use of Medical Computed Tomography (CT) Imaging in the Study of Ceramic and Clay Archaeological Artifacts from the Ancient Near East." In *X-Rays for Archaeology*, edited by M. Uda, G. Demortier, and I. Nakai, 231–245. Dordrecht: Springer.
- Barthel, K. U. 2006. "3D-Data Representation with ImageJ." In ImageJ Conference.
- Bayerová, T., M. Gruber, and G. Krist. 2010. "Technical Study of Polychrome Clay Sculptures from the Buddhist Temple Complex at Nako." In *Multidisciplinary Conservation: A Holistic View for Historic Interiors, Rome 23–26 March 2010. Joint Interim Meeting of Five ICOM-CC Working Groups: Sculpture, Polychromy, and Architectural Decoration*, edited by Elsje Janseen, Mariabianca Paris, Malgorzata Sawicki, Kate Seymour, and Andrew Thorn, 1–11. ICOM-CC (International Council of Museums - Committee for Conservation).
- Blaensdorf, C., and M. Tao. 2010. "A Chinese-German Cooperative Project for the Preservation of the Cultural Heritage of Shaanxi Province. Conservation of the Polychrome Clay Sculpture and Investigation of Painting Materials in the Great Hall of the Shuilu'an Buddhist Temple." In *Conservation of Ancient Sites on the Silk Road. Proceedings of the Second International Conference on the Conservation of Grotto Sites, Mogao Grottoes, Dunhuang, People's Republic of China, June 28–July 3, 2004*, edited by Agnew Neville, 203–211. The Getty Conservation Institute.
- Boerckel, J. D., D. E. Mason, A. M. McDermott, and E. Alsberg. 2014. "Microcomputed Tomography: Approaches and Applications in Bioengineering." *Stem Cell Research & Therapy* 5 (6): 144.
- Bolte, S., and F. P. Cordelières. 2006. "A Guided Tour into Subcellular Colocalization Analysis in Light Microscopy." *Journal of Microscopy* 224 (3): 213–232.
- Bukreeva, I., A. Mittone, A. Bravin, G. Festa, M. Alessandrelli, P. Coan, V. Formoso, R. G. Agostino, M. Giocondo, F. Ciuchi, et al. 2016. "Virtual Unrolling and Deciphering of Herculaneum Papyri by X-ray Phase-Contrast Tomography." *Scientific Reports* 6: 27227. doi:10.1038/srep27227.
- Coletti, C., G. Cultrone, L. Maritan, and C. Mazzoli. 2016. "Combined Multi-Analytical Approach for Study of Pore System in Brick." *Materials Characterization* 121: 82–92.
- Collins, T. J. 2007. "ImageJ for Microscopy." *Biotechniques* 43 (S1): S25–S30. doi:10.1111/j.1365-2818.2006.01706.x.
- Conte, R., R. Filosa, V. Formoso, F. Gagliardi, R. G. Agostino, and G. Ambrogio. 2019. "Analysis of Extruded Pins Manufactured by Friction Stir Forming for Multi-Material Joining Purposes." *AIP Conference Proceedings* 2113: 050026. doi:10.1063/1.5112590.

- Costanza-Robinson, M. S., B. D. Estabrook, and D. F. Fouhey. 2011. "Representative Elementary Volume Estimation for Porosity, Moisture Saturation, and Air-Water Interfacial Areas in Unsaturated Porous Media: Data Quality Implications." *Water Resources Research* 47 (7). doi:10.1029/2010WR009655.
- Feldkamp, L. A., L. C. Davis, and J. W. Kress. 1984. "Practical Cone-Beam Algorithm." *Journal of the Optical Society of America A* 1 (6): 612–619. doi:10.1364/JOSAA.1.000612.
- Ionita, C. N., K. R. Hoffmann, D. R. Bednarek, R. Chityala, and S. Rudin. 2008. "Cone-beam Micro-CT System Based on LabVIEW Software." *Journal of Digital Imaging* 21 (3): 296–305. doi:10.1007/s10278-007-9024-9.
- Kahl, W. A., and B. Ramming. 2012. "Non-Destructive Fabric Analysis of Prehistoric Pottery Using High-Resolution X-ray Microtomography: A Pilot Study on the Late Mesolithic to Neolithic Site Hamburg-Boberg." *Journal of Archaeological Science* 39: 2206–2219.
- Kak, A. C., and M. Slaney. 1988. *Principles of Computerized Tomographic Imaging*. New York: IEEE Press.
- Kozatsas, J., K. Kotsakis, D. Sagris, and K. David. 2018. "Inside out: Assessing Pottery Forming Techniques with Micro-CT Scanning. An Example from Middle Neolithic Thessaly." *Journal of Archaeological Science* 100: 102–119.
- Kulkova, M., and A. Kulkov. 2014. "Investigations of Early Neolithic Ceramics from Eastern Europe by X-ray Microtomography and Petrography." *Microscopy and Analysis* 136: 7–10.
- Landis, E. N., and D. T. Keane. 2010. "X-ray Microtomography." *Materials Characterization* 61 (12): 1305–1316.
- Lee, S. C., H. K. Kim, I. K. Chun, M. H. Cho, S. Y. Lee, and M. H. Cho. 2003. "A Flat-Panel Detector Based Micro-CT System: Performance Evaluation for Small-Animal Imaging." *Physics in Medicine & Biology* 48 (24): 4173–4185. doi:10.1088/0031-9155/48/24/014.
- Lliveras, A., I. Bonaduce, M. P. Colombini, C. Blaensdorf, and M. Tao. 2011. "A First Insight into the Asian Clay Sculptures Painting Technique and Materials: Western and Eastern Buddha of the Bamiyan Valley (Afghanistan) and Sculptures from Shuilu'an (Shaanxi province, China)." In *Art'11 – 10th International Conference on Non-Destructive Investigations and Microanalysis for the Diagnostics and Conservation of Cultural and Environmental Heritage, Florence 13–15 April*, edited by AIPnD - Associazione Italiana Prove non Distruttive.
- López-Prat, M., B. Carrascosa, D. Miriello, J. Simón-Cortés, and S. R. Bandyopadhyay. 2021. "An Ethnographic Approach to Developing New Conservation Strategies for the Archaeological Clay-Based Sculpture of the Silk Road." In *Transcending Boundaries: Integrated Approaches to Conservation. ICOM-CC 19th Triennial Conference Preprints, Beijing, 17–21 May 2021*, edited by J. Bridgland. Paris: International Council of Museums.
- Luczanits, C. 2004. *Buddhist Sculpture in Clay. Early Western Himalayan Art, Late 10th to Early 13th Centuries*. Chicago: Serinda Publications.
- Munsell Soil Color Book. 2009. Revised, 2018 Production by Munsell Color X-rite.
- Ollion, J., J. Cochenec, F. Loll, C. Escudé, and T. Boudier. 2013. "TANGO: A Generic Tool for High-Throughput 3D Image Analysis for Studying Nuclear Organization." *Bioinformatics (Oxford, England)* 29 (14): 1840–1841. doi:10.1093/bioinformatics/btt276.
- Otsu, N. 1979. "A Threshold Selection Method from Gray-Level Histograms." *IEEE Transactions on Systems, Man, and Cybernetics* 9 (1): 62–66.
- Paiman, Z. 2005. "La Renaissance de L'archéologie Afghane. Découvertes à Kaboul." *Archeologia* 419: 24–39.
- Paiman, Z. 2017. "Archaeological Activity in Kabul." In *Preserving the Cultural Heritage of Afghanistan: Proceedings of The International Conference Held at Kabul University, November 2014*, edited by Gil J. Stein, Michael T. Fisher, Abdul Hafiz Latify, Najibullah Popal, and Nancy Hatch Dupree, 97–106. The Oriental Institute and The University of Chicago.
- Paiman, Z., and Michael Alram. 2010. "Tepe Narenj: A Royal Monastery on the High Ground of Kabul, with a Commentary on the Coinage." *Journal of Inner Asian Art and Archaeology* 5: 33–58.
- Park, K. S., R. Milke, E. Rybacki, and S. Reinhold. 2019. "Application of Image Analysis for the Identification of Prehistoric Ceramic Production Technologies in the North Caucasus (Russia, Bronze/Iron Age)." *Heritage* 2: 2327–2342.
- Reedy, C. L. 2020. "3D Documentation and Analysis of Porosity in Deteriorated Historic Brick." *Studies in Conservation* 65 (S1): P258–P261.
- Schindelin, J., I. Arganda-Carreras, E. Frise, V. Kaynig, M. Longair, T. Pietzsch, S. Preibisch, et al. 2012. "Fiji: an Open-Source Platform for Biological-Image Analysis." *Nature Methods* 9: 676–682. doi:10.1038/nmeth.2019.
- Schmid, B., J. Schindelin, A. Cardona, M. Longair, and M. Heisenberg. 2010. "A High-Level 3D Visualization API for Java and ImageJ." *BMC Bioinformatics* 11 (1): 1–7. doi:10.1186/1471-2105-11-274.
- Singh Gill, M., C. Priego Rendo, and Sreekumar Menon. 2014. "Materials and Techniques: Early Buddhist Wall Paintings and Sculptures at Sumda Chun, Ladakh." *Studies in Conservation* 59 (5): 300–313. doi:10.1179/2047058413Y.0000000090.
- Tarzi, Z. 1986. "La technique du modelage en argile en Asie Centrale et au Nord-Ouest de l'Inde sous les Kouchans: la continuité malgré les ruptures." *Ktéma* 11: 57–93.
- Varma, K. M. 1970. *The Indian Technique of Clay Modelling*. Santiniketan: Proddu.
- Wang, N., L. He, E. Egel, S. Simon, and B. Rong. 2014. "Complementary Analytical Methods in Identifying Gilding and Painting Techniques of Ancient Clay-Based Polychromic Sculptures." *Microchemical Journal* 114: 125–140. doi:10.1016/j.microc.2013.12.011.
- Wang, X., G. Zhen, X. Hao, T. Tong, F. Ni, Z. Wang, J. Jia, L. Li, and H. Tong. 2020. "Spectroscopic Investigation and Comprehensive Analysis of the Polychrome Clay Sculpture of Hua Yan Temple of the Liao Dynasty." *Spectrochimica Acta Part A: Molecular and Biomolecular Spectroscopy* 240: 1386–1425. doi:10.1016/j.saa.2020.118574.
- Wildenschild, D., and A. P. Sheppard. 2013. "X-Ray Imaging and Analysis Techniques for Quantifying Pore-Scale Structure and Processes in Subsurface Porous Medium Systems." *Advances in Water Resources* 51: 217–246. doi:10.1016/j.advwatres.2012.07.018.

FIGURES

| | |
|--|----|
| Fig. 1.1 The mass-attenuation coefficient as a function of photon energy in case of water. Based on the tables in Hubbell, J.H., Seltzer, S.M., 1989. Tables of X-Ray Mass Attenuation Coefficients and Mass Energy-Absorption Coefficients (Online). National Institute of Standards and Technology. http://www.nist.gov/pml/data/xraycoef/ | 11 |
| Fig. 1.2 Principle of photoelectric process responsible for photon absorption. The photon's energy E_γ is absorbed by an electron of the innermost shells, close to the nucleus. A fraction of such energy, E_b , unbounds the electron while the remaining part is gained as kinetic energy E_{kin} | 12 |
| Fig. 1.3 Principle of X-ray attenuation by Compton scattering and the theoretical relation between the scattered photon's energy and the scattering angle. | 12 |
| Fig. 1.4 Schematic illustration of a standard micro-CT setup. The sample is positioned on a rotational stage between the X-ray source and a two-dimensional (2-D) X-ray imaging device. | 13 |
| Fig. 1.5 Illustration of different beam configuration geometry. (Pacilè and Tromba 2018b) | 14 |
| Fig. 1.6 Illustration of the incident and acquired X-ray represented as a ray passing through the sample. the acquired intensity I is modeled as a line integral of X-ray absorption along the ray path. (Landis and Keane 2010) | 20 |
| Fig. 1.7 Schematic of X-ray radiography: (a) attenuation through homogenous medium and (b) summation of attenuation through heterogeneous medium. (Tatone and Grasselli 2014) | 21 |
| Fig. 1.8 Scanning of a single layer in the plane (x, y). Where z is the axis of rotation. (Kharfi 2013) | 23 |
| Fig. 1.9 Parallel beam geometry utilized in tomography and tomographic reconstruction. Each projection, resulting from tomography under a specific angle, is made up of the set of line integrals through the object. | 24 |
| Fig. 1.10 CT volume reconstruction: (a) original X-ray projection data; (b) simple back projection; and (c) Filtered Back Projection, after (Tatone and Grasselli 2014). | 27 |
| Fig. 1.11 Figure 1. Mechanism of in-line phase-contrast: A sample imposes a phase-shift on the X-ray beam, which distorts the X-ray wavefront. | 29 |

Fig. 1.12 The principle of inline phase-contrast imaging. The projection images of the computer phantom of the spheres are shown for different positions of the detector along the z axis. (Bronnikov 2006)..... 30

Fig. 2.1 Schematic diagram of the developed micro-CT system (Lee et al. 2003). .. 32

Fig. 2.2 X-ray microtomography measurement. 33

Fig. 2.3 (Top image) Main components of cone beam X-ray computed tomography: X-ray source (X-ray tube), rotary stage with specimen and a matrix detector (flat panel detector). (Bottom image) Typical geometry of cone beam micro-CT: Geometrical magnification is determined by the source-object distance (SOD) and source-detector distance (SDD), as well as the effective detector width D and the diameter d of the measuring volume. f is the focal spot size, p is the detector pixel size and Ug the geometric unsharpness in the penetration image in relation to the focal spot size f. (Kastner and Heinzl 2018)..... 35

Fig. 2.4 Sketch of the field of measurement. Radial and angular sampling is illustrated within the cross-sectional tomographic plane..... 38

Fig. 2.5 cone-beam geometry in CT 40

Fig. 2.6 The coordinate system for Feldkamp’s cone-beam algorithm (Zeng 2010) 42

Fig. 2.7 The coordinate system for Feldkamp’s cone-beam algorithm. (Zeng 2010) 43

$$f(r, \varphi, z) = \frac{1}{2} \int_0^{2\pi} \frac{D}{D-s} \int_{-\infty}^{\infty} \frac{D}{\sqrt{D^2 + l^2 + \hat{z}^2}} g(l, \hat{z}, \beta) h(l'-l) dl d\beta.$$

$$s = r \sin(\varphi - \beta), \text{ and } l' = \frac{Dr \cos(\varphi - \beta)}{D - r \sin(\varphi - \beta)}$$

Fig. 2.8 FDK Reconstruction Algorithm 44

Fig. 3.1 Sketch of the uTomo microtomography station at STAR-LAB..... 46

Fig. 3.2 The sketch zoomed shows in detail the alignment of the components of the tomographic system. X-ray source, sample and detector. 46

Fig. 3.3 μ Tomo@STAR-Lab. - University of Calabria..... 47

Fig. 3.4 Microfocus X-ray source Hamamatsu L12161-07 & the external control unit. 48

Fig. 3.5 The Graph shows the working curves of the microfocus X-ray source Hamamatsu L12161-07..... 49

| | | |
|------------------|--|-----------|
| Fig. 3.6 | Cross section of microfocus transmission x-ray tube..... | 50 |
| Fig. 3.7 | Geometric properties for a microfocus X-ray source..... | 50 |
| Fig. 3.8 | Fig. Spectra generated by microfocus x-ray sources Hamamatsu L12161-07 at different acceleration potentials and plotted for a range of voltages between 1 and 150 kV. The photon counts were normalized to 1 (relative). | 51 |
| Fig. 3.9 | Detector Hamamatsu C7942SK-05 | 52 |
| Fig. 3.10 | Skecth of Sample positioning: y sample holder structure: X-translator (1), Y-translator (2), ω -rotator (3), θ -goniometer (4) and φ -goniometer. | 53 |
| Fig. 3.11 | μ tomo@STAR-Lab. Sample positioning system. | 54 |
| Fig. 3.12 | Connection diagram for the remote control of the μ Tomo station..... | 56 |
| Fig. 3.13 | Front Panel panel of the Main Program | 57 |
| Fig. 3.14 | Block Diagram..... | 57 |
| Fig. 3.15 | Graphical User Interface (GUI) of the Software for X-ray source control provided by the hamamatsu company | 61 |
| Fig. 3.16 | Software for the control of the X-ray source made in the STAR-LAB laboratory. | 61 |

BIBLIOGRAPHY

- Bacci, Alberto, Dennis Palmer, L. Serafini, Valter Torri, Vittoria Petrillo, Paolo Tomassini, Ezio Puppini, D. Alesini, Maria Pia Anania, M. Bellaveglia, Fabrizio Bisesto, G. Pirro, Adolfo Esposito, Massimo Ferrario, Gallo Alessandro, G. Gatti, Andrea Ghigo, Spataro Bruno, Cristina Vaccarezza, and M. Marazzi. 2014. "The STAR Project." in *IPAC 2014: Proceedings of the 5th International Particle Accelerator Conference*.
- Bronnikov, Andrei. 2006. "Phase-Contrast CT: Fundamental Theorem and Fast Image Reconstruction Algorithms - Art. No. 63180Q." *Proceedings of SPIE - The International Society for Optical Engineering*.
- Cai, Ailong, Lei Li, Linyuan Wang, Bin Yan, Zhizhong Zheng, Hanming Zhang, and Guoen Hu. 2018. "Optimization-Based Region-of-Interest Reconstruction for X-Ray Computed Tomography Based on Total Variation and Data Derivative." *Physica Medica* 48:91–102.
- Cai, Weixing. 2009. "Feasibility Study of Phase-Contrast Cone Beam CT Imaging Systems."
- Curatolo, C., I. Drebot, V. Petrillo, and L. Serafini. 2017. "Analytical Description of Photon Beam Phase Spaces in Inverse Compton Scattering Sources." *Phys. Rev. Accel. Beams* 20(8):80701.
- Faridani, Adel, David V Finch, Erik L. Ritman, and Kennan T. Smith. 1997. "Local Tomography II." *SIAM Journal on Applied Mathematics* 57(4):1095–1127.
- Faridani, Adel, Erik L. Ritman, and Kennan T. Smith. 1992. "Examples of Local Tomography." *SIAM Journal on Applied Mathematics* 52(4):1193–98.
- Gureyev, T. ~E., Ya. I. Nesterets, and S. ~C. Mayo. 2007. "Quantitative Quasi-Local Tomography Using Absorption and Phase Contrast." *Optics Communications* 280(1):39–48.
- Hanke, R., T. Fuchs, M. Salamon, and S. Zabler. 2016. "3 - X-Ray Microtomography

- for Materials Characterization.” Pp. 45–79 in *Materials Characterization Using Nondestructive Evaluation (NDE) Methods*, edited by G. Hübschen, I. Altpeter, R. Tschuncky, and H.-G. Herrmann. Woodhead Publishing.
- Hanke, Randolph, Theobald Fuchs, and N. Uhlmann. 2008. “X-Ray Based Methods for Non-Destructive Testing and Material Characterization.” *Nuclear Instruments and Methods in Physics Research Section A: Accelerators, Spectrometers, Detectors and Associated Equipment* 591:14–18.
- Hounsfield, G. N. 1973. “Computerized Transverse Axial Scanning (Tomography). 1. Description of System.” *The British Journal of Radiology* 46(552):1016—1022.
- Kak, A. C. and M. Slaney. 1988. “Principles of Computerized Tomographic Imaging IEEE Press.” *New York*.
- Kastner, Johann and Christoph Heinzl. 2018. “X-Ray Tomography.” Pp. 1–72 in *Handbook of Advanced Non-Destructive Evaluation*, edited by N. Ida and N. Meyendorf. Cham: Springer International Publishing.
- Kharfi, F. 2013. “Mathematics and Physics of Computed Tomography (CT): Demonstrations and Practical Examples.”
- Landis, Eric N. and Denis T. Keane. 2010. “X-Ray Microtomography.” *Materials Characterization* 61(12):1305–16.
- Lee, Sang Chul, Ho Kyung Kim, In Kon Chun, Myung Hye Cho, Soo Yeol Lee, and Min Hyung Cho. 2003. “A Flat-Panel Detector Based Micro-CT System: Performance Evaluation for Small-Animal Imaging.” *Physics in Medicine and Biology*.
- Mayo, Sheridan C., Andrew W. Stevenson, and Stephen W. Wilkins. 2012. “In-Line Phase-Contrast X-Ray Imaging and Tomography for Materials Science.” *Materials* 5(12):937–65.
- Noori-Asl, Mahsa and Alireza Sadremomtaz. 2013. “Analytical Image Reconstruction Methods in Emission Tomography.” *Journal of Biomedical Science and Engineering* 06:100–107.

- Pacilè, Serena and Giuliana Tromba. 2018a. “Introduction to X-Ray Micro-Tomography.” Pp. 19–39 in *Advanced High-Resolution Tomography in Regenerative Medicine: Three-Dimensional Exploration into the Interactions between Tissues, Cells, and Biomaterials*, edited by A. Giuliani and A. Cedola. Cham: Springer International Publishing.
- Pacilè, Serena and Giuliana Tromba. 2018b. “Introduction to X-Ray Micro-Tomography BT - Advanced High-Resolution Tomography in Regenerative Medicine: Three-Dimensional Exploration into the Interactions between Tissues, Cells, and Biomaterials.” Pp. 19–39 in, edited by A. Giuliani and A. Cedola. Cham: Springer International Publishing.
- Paleo, Pierre, Michel Desvignes, and Alessandro Mirone. 2017. “A Practical Local Tomography Reconstruction Algorithm Based on a Known Sub-Region.” *Journal of Synchrotron Radiation* 24(1):257–68.
- Paleo, Pierre and Alessandro Mirone. 2017. “Efficient Implementation of a Local Tomography Reconstruction Algorithm.” *Advanced Structural and Chemical Imaging* 3(1):5.
- Pogany, A., Dachao Gao, and Stephen Wilkins. 1997. “Contrast and Resolution in Imaging with a Microfocus X-Ray Source.” *Review of Scientific Instruments* 68.
- Sodini, Nicola, Diego Dreossi, Rongchang Chen, Marco Fioravanti, Alberto Giordano, Peter Herrestal, Luigi Rigon, and Franco Zanini. 2012. “Non-Invasive Microstructural Analysis of Bowed Stringed Instruments with Synchrotron Radiation X-Ray Microtomography.” *Journal of Cultural Heritage* 13:S44–S49.
- Tatone, Bryan and Giovanni Grasselli. 2014. “Characterization of the Effect of Normal Load on the Discontinuity Morphology in Direct Shear Specimens Using X-Ray Micro-CT.” *Acta Geotechnica* 10:31–54.
- Zeng, Gengsheng. 2010. *Medical Image Reconstruction: A Conceptual Tutorial*.

